



HAL
open science

Development of an innovative U-shaped steel-concrete composite beam solution: experimental and numerical studies on the mechanical behaviour

Maxime Turetta

► **To cite this version:**

Maxime Turetta. Development of an innovative U-shaped steel-concrete composite beam solution: experimental and numerical studies on the mechanical behaviour. Materials Science [cond-mat.mtrl-sci]. Université de Lorraine; Université du Luxembourg, 2019. English. NNT : 2019LORR0203 . tel-02527858

HAL Id: tel-02527858

<https://hal.univ-lorraine.fr/tel-02527858v1>

Submitted on 1 Apr 2020

HAL is a multi-disciplinary open access archive for the deposit and dissemination of scientific research documents, whether they are published or not. The documents may come from teaching and research institutions in France or abroad, or from public or private research centers.

L'archive ouverte pluridisciplinaire **HAL**, est destinée au dépôt et à la diffusion de documents scientifiques de niveau recherche, publiés ou non, émanant des établissements d'enseignement et de recherche français ou étrangers, des laboratoires publics ou privés.



AVERTISSEMENT

Ce document est le fruit d'un long travail approuvé par le jury de soutenance et mis à disposition de l'ensemble de la communauté universitaire élargie.

Il est soumis à la propriété intellectuelle de l'auteur. Ceci implique une obligation de citation et de référencement lors de l'utilisation de ce document.

D'autre part, toute contrefaçon, plagiat, reproduction illicite encourt une poursuite pénale.

Contact : ddoc-theses-contact@univ-lorraine.fr

LIENS

Code de la Propriété Intellectuelle. articles L 122. 4

Code de la Propriété Intellectuelle. articles L 335.2- L 335.10

http://www.cfcopies.com/V2/leg/leg_droi.php

<http://www.culture.gouv.fr/culture/infos-pratiques/droits/protection.htm>

PhD-FSTC-2019-66
The Faculty of Sciences, Technology and Communication

DISSERTATION

Defence held on 17/10/2019 in Luxembourg

to obtain the degree of

DOCTEUR DE L'UNIVERSITÉ
DU LUXEMBOURG ET DE LORRAINE

EN SCIENCES DE L'INGÉNIEUR

by

Maxime TURETTA

Born on 22nd July 1992 in Sainte-Foy-Lès-Lyon (France)

DEVELOPMENT OF AN INNOVATIVE U-SHAPED STEEL-CONCRETE COMPOSITE BEAM SOLUTION: EXPERIMENTAL AND NUMERICAL STUDIES ON THE MECHANICAL BEHAVIOUR

Dissertation defence committee

Dr Christoph ODENBREIT, dissertation supervisor
Professor, Université du Luxembourg

Dr Abdelouahab KHELIL, dissertation co-supervisor
Professor, Université de Lorraine

Dr Danièle WALDMANN, Chairman
Professor, Université du Luxembourg

Dr Marion MARTINY, Vice Chairman
Professor, Université de Lorraine

Dr Hugues SOMJA,
Professor, INSA Rennes

Dr Hervé DEGÉE,
Professor, Universiteit Hasselt



UNIVERSITÉ DU
LUXEMBOURG



UNIVERSITÉ
DE LORRAINE

G2MP



With the presence of experts in advisory capacity

Pierre-Olivier MARTIN

Research Director, CTICM

Dr. Bin ZHAO

Director of the Research & Valorisation Department, CTICM

Acknowledgements

The present thesis was realised in the frame of the PhD project “COMINO” (CIFRE grant 2017/0048) at CTICM (Centre Technique Industriel de la Construction Métallique) and in cotutelle between the University of Luxembourg and the University of Lorraine.

Je souhaite remercier grandement le CTICM pour m’ avoir donné la chance de réaliser cette thèse. En particulier, je souhaite remercier très chaleureusement Monsieur Pierre-Olivier MARTIN, Directeur de Projets de Recherche au CTICM, avec qui nous avons discuté, à la fin d’un cours au CHEM (Centre des Hautes Etudes de la Construction Métallique), de la possibilité de réaliser une thèse en construction métallique. Grâce à ton encadrement et tes conseils d’expert, il s’en est suivi trois belles années de collaboration aboutissant sur un succès. Je te remercie également d’ avoir fait partie de mon jury de thèse et surtout pour toutes les remarques constructives que tu m’as apportées.

I would like to express my special thanks to Professor Christoph Odenbreit, Professor at the University of Luxembourg, holder of the ArcelorMittal Chair of Steel and Façade Engineering and the co-director of my thesis. Thank you for giving me the opportunity to do the thesis in a European context. Thank you for your time, your supervision and your expertise in steel and composite structures. The completion of the thesis would not have been possible without your many advice and guidance. You gave me the opportunity to successfully conduct two completely different full-scale experimental tests. It was a pleasure and an honor to work with you.

Je tiens à remercier Professor Abdelouahab KHELIL, Professeur de l’ Université de Lorraine, co-directeur de cette thèse, pour son investissement personnel et pour toute l’ aide qu’ il m’ a apportée afin de résoudre des problèmes techniques et administratifs. Vous avez contribué au bon déroulement de cette thèse grâce à votre encadrement durant ces trois années. Je vous remercie pour tout votre soutien, c’ était un plaisir et un honneur de travailler à vos côtés.

Je souhaite également remercier Docteur Bin ZHAO, Directeur du Service Recherche du CTICM, pour m’ avoir permis d’ intégrer le Service et d’ effectuer cette thèse en étant un des initiateurs du projet avec la collaboration de la société BRIAND. Merci d’ avoir pris le temps de me prodiguer tes conseils d’ experts sur le calcul en situation d’ incendie et merci d’ avoir pris part à mon jury de thèse.

J’ en profite pour remercier Monsieur Jean Michel BOISSEAU, Directeur Technique chez BRIAND Construction Métallique, pour avoir impliqué l’ entreprise BRIAND dans ce projet et avoir apporté ses solutions techniques.

Je souhaite également remercier Monsieur Alain BUREAU, Chef du Département Construction Métallique du CTICM, pour m’ avoir encadré au sein du Département et pour tous tes conseils.

ACKNOWLEDGEMENTS

Je souhaite remercier très chaleureusement, mon collègue et voisin de bureau, Dr André BEYER, Ingénieur Chef de Projet au CTCIM, pour toute l'aide que tu m'as apportée durant ces trois années de thèse notamment sur la modélisation numérique de problèmes complexes.

Je souhaite également remercier toutes les personnes du CTCIM pour leur accueil et pour leur participation de près ou de loin à ce projet.

I would also like to express my gratitude to the laboratory team of the University of Luxembourg, special thanks to Logan Freitas, Ed Weyer, Marc Seil, Gilbert Klein, Vicente Reis, Ralph Reiter, Claude Collé and Cedric Bruyère.

I also want to thank Valter de Matos and Alfredo Romero, students at University of Luxembourg, for their assistance during the preparation and the execution of the experimental tests.

The steel sections for the tests were supplied by the company BRIAND. The steel fasteners for the tests were supplied by the company HILTI. Their supports are gratefully acknowledged.

I would like to express my gratitude to the reporters of this thesis, Professor Hugues SOMJA, Professor at INSA de Rennes, and Professor Hervée DEGEE, Professor at Universiteit Hasselt. I would like to thank you for your reports and for the interesting discussions we had during the PhD defence.

I am also grateful that Professor Danièle WALDMANN, Professor at the University of Luxembourg, Chairman of my defence committee, and Professor Marion MARTINY, Professor at University of Lorraine, Vice-chairman of my defence committee, accepted to be part of the jury and dedicated their time to discuss the outcomes of my work. Thank you for all the comments you made on the thesis manuscript, it helped me to improve the quality of my work.

I would like to thank my colleagues at University of Luxembourg; Andras Kozma, Valentino Vignieri, Matthias Braun and Maciej Chrzanowski. Thank you for your advice on many topics and for your help with the experimental tests. I would especially like to thank Andras and Valentino for their homemade steel hat that I will keep as a great souvenir!

I would like to thank all the people who participated in the thesis project during these three years of intense work.

Enfin, je voudrais exprimer ma profonde gratitude à toute ma famille pour son soutien sans faille durant ces trois années de ma thèse de doctorat; en particulier à ma fiancée Anne-Sophie, mes parents Nicole et Gérard, ma sœur Julie et ma fille Léa.

Maxime Turetta

November 2019

Abstract

An innovative solution of steel-concrete composite beam was developed taking into consideration the fire situation and the construction stage. The beam is composed of a U-shaped steel part connected to a reinforced concrete part. In the construction phase, the beam is supporting the slab and constitutes a formwork for the reinforced concrete part. The U-shaped beam withstands the construction loads without any temporary propping system. When casting concrete, the steel beam is filled at the same time as the slab, this allows considerable time savings on site. In the exploitation stage, the beam behaves as a steel-concrete composite beam. The connection between the two materials is made by welded headed studs on the lower part of the U-shaped beam. In a fire situations, the composite beam satisfies conventional fire stability durations due to the longitudinal reinforcements inside the concrete downstand part with sufficient covers.

Historical solutions are briefly reviewed and then the literature review focuses on modern solutions that fulfil the criteria in the construction stage and the fire situation, which are grouped into two categories; the integrated beams (Slim-floor) and the "composite formwork beams" which are in the centre of interest of several international research projects. This thesis comes within the second category. A state of the art also reviews the research carried out on the connection in a tension zone and on the minimum thickness required to ensure an efficient connection.

During the development of this innovative solution, two major issues were identified concerning the mechanical behaviour of this solution. In the construction stage, the U-shaped steel beam without restraints is prone to lateral torsional buckling instability. In order to characterise the stability of the beam, a full-scale test is carried out at the Laboratory of the University of Luxembourg. The test clearly showed the lateral torsional buckling of the steel beam. The test results are compared with numerical simulations and analytical studies. A parametrical study, covering 200 geometrical configurations of the U-shaped beam, is carried out to validate the use of the curve "b" for the design of the steel beam for lateral torsional buckling according to Eurocodes 3.

In the exploitation phase, once the concrete hardens, the beam has a steel-concrete composite behaviour provided by the shear connection between the two materials. For manufacturing reasons, the connection is located in a zone where the concrete is subjected to tension forces induced by the bending of the beam. The concrete in this zone is potentially cracked, thus the efficiency of the connection and therefore the mechanical steel-concrete composite behaviour is investigated. Another test is therefore carried out in the Laboratory of the University of Luxembourg, this time the specimen tested is made of concrete and steel. The failure mode is a shear mechanism of the composite beam at very large displacements. However, the beam specimen exhibited a real steel-concrete composite behaviour with high ductility, the

connection was therefore efficient.

The test results are compared with numerical simulations in order to validate the finite element model developed. From numerical results and test results, an analytical method, based on EN 1994-1-1, is proposed to find the bending resistance of this composite beam by taking into account the partial yield of the side plates of the U-shaped steel section.

From the conclusions on each investigation, a global analytical design method is proposed for the developed solution based on the Eurocodes with additional considerations and constructional guidelines.

Résumé étendu

Une nouvelle configuration de poutre mixte-acier béton a été développée dans le cadre de la thèse afin de répondre à des problématiques de résistance au feu et de montage sur chantier. La poutre se compose d'une partie métallique en U et d'une partie en béton armé en T (dalle comprise). En phase de construction, la poutre métallique en U sert de support pour la dalle et de coffrage de la partie en béton armé. Elle résiste seule aux charges de construction sans la présence d'étais temporaires. Lors du coulage du béton, la poutre métallique est remplie en même temps que la dalle, ceci permet un gain de temps considérable sur chantier. En phase d'exploitation, la poutre devient mixte acier-béton, la connexion entre les deux matériaux s'effectue par des goujons à tête soudés sur la partie inférieure de la poutre métallique en U. En situation d'incendie, la poutre mixte acier-béton satisfait les durées conventionnelles de stabilité au feu (jusqu'à 2 heures) grâce à la disposition d'armatures longitudinales à l'intérieur de la retombée en béton armé et suffisamment éloigné des bords.

Chapitre 1 – Motivation, objectifs et méthodologie

Pour les structures de bâtiments, une résistance au feu est couramment requise notamment pour les structures de planchers. Les durées de résistance dépendent surtout du temps nécessaire à l'évacuation des personnes. La construction métallique permet de construire des structures légères et très rapides à installer, réduisant ainsi les délais et les coûts. Lorsque les durées de résistance au feu sont trop importantes, les éléments de structures doivent être protégés et la solution métallique peu perdre en intérêt. Cependant, grâce aux structures mixtes acier-béton il est possible de proposer des solutions non protégées avec les parties métalliques partiellement enrobées de béton. Pour les structures de planchers, ces solutions sont difficiles à mettre en œuvre. Ainsi, des solutions mixtes acier-béton font l'objet de travaux de recherches afin de tirer le plus profits des avantages de chacun des matériaux et c'est l'objet de cette thèse.

Trois objectifs sont identifiés pour cette thèse :

- Proposer une solution de poutre de plancher résistante en situation d'incendie pour des durées d'exposition importantes (jusqu'à 2 heures) sans protection additionnelle.
- La poutre métallique doit être stable et résistante en phase de construction sans étalement.
- La poutre mixte acier-béton doit résister aux sollicitations en phase d'exploitation.

La méthodologie mise en place dans cette thèse pour atteindre ses objectifs a suivi les étapes suivantes :

1. Une première phase de recherche d'une solution comprenant de la conception, des dimensionnements et des échanges avec un constructeur métallique. La solution pro-

posée s'inspire de recherches scientifiques récentes et recensées dans l'état de l'art présenté au Chapitre 2.

2. S'assurer que la solution remplisse les critères de résistance au feu à l'aide de modèles analytiques et de simulations numériques en situation d'incendie présentés au Chapitre 3.
3. Identifier les phases critiques de la solution et les aspects techniques qui ne sont pas ou partiellement couverts par les normes européennes (Eurocodes). Ces aspects sont étudiés par des essais expérimentaux et présentés aux Chapitre 4 (pour la poutre métallique) et 6 (pour la poutre mixte acier-béton).
4. Analyser par des méthodes analytiques et des modèles numériques éléments finis le comportement mécanique des poutres testées afin de l'étendre à des cas plus généraux (Chapitre 5 et 7).
5. Finalement, proposer des recommandations pour le dimensionnement de la solution développée dans le cadre de la thèse en accord avec les normes (Chapitre 8).

Chapitre 2 – Etat de l'art

Une recherche bibliographique a été réalisée sur les solutions qui ont été développées et qui répondent en parties aux problématiques de la thèse. Les solutions historiques sont brièvement passées en revue pour montrer que les considérations d'incendie et de mixité des matériaux étaient déjà une préoccupation, à l'époque, parmi les recherches scientifiques. La recherche bibliographique se concentre ensuite particulièrement sur les solutions modernes qui remplissent les critères de montage et d'incendie. Ces solutions sont regroupées en deux grandes catégories. La première catégorie concerne les poutres intégrées (Slim-floor) qui sont des poutres mixtes de plus en plus utilisées de nos jours pour faire face à ces enjeux. La deuxième catégorie concerne les « poutres mixtes coffrages » qui sont sujets à de nombreux projets de recherche internationaux. Pour ce type de solution, la partie métallique sert de coffrage en phase de construction, puis participera en phase d'exploitation par un comportement mixte avec la partie béton (souvent également armée). Cette thèse vient s'inscrire dans cette seconde catégorie.

Afin de concevoir la solution présentée dans cette thèse, un état de l'art a été également réalisé sur les recherches effectuées au sujet de la connexion mixte acier béton. Plus particulièrement sur la connexion en partie tendue et sur les épaisseurs minimales requises pour s'assurer du bon fonctionnement de la connexion à l'aide de goujons à tête.

Chapitre 3 – Etudes analytiques et numériques du comportement en flexion en situation d'incendie

Un des objectifs de la thèse est de développer une solution de poutre de plancher résistante en situation d'incendie. Ainsi, les dimensions géométriques de la poutre, principalement la hauteur de la retombée en béton armé, dépendent fortement de la résistance nécessaire dans cette phase. Une étude analytique est conduite sur le comportement de la solution exposée à un feu ISO suivant les recommandations de la norme EN 1992-1-2 (2005). La hauteur de retombée nécessaire est déterminée en fonction de la quantité d'armatures longitudinales inférieures et des sollicitations de cette phase.

Une étude numérique sur le comportement thermomécanique de la solution est conduite. Tout d'abord, une simulation numérique 2D de l'échauffement thermique est réalisée suivi d'une analyse mécanique prenant en compte la réduction des caractéristiques des matériaux suivant leur degré d'échauffement. La simulation numérique de l'échauffement thermique permet de positionner les armatures loin des bords et ainsi de limiter leur échauffement. Il en résulte une optimisation de l'ordre de 40% de la hauteur de retombée nécessaire en situation d'incendie en comparaison à la précédente étude analytique. L'étude numérique a permis également de mettre en évidence qu'une poutre métallique non protégée supplémentaire positionnée sous la retombée en béton, pour atteindre de grande portée, n'était pas une bonne solution. En effet, l'échauffement de la poutre non protégée est si grand par rapport à la retombée que sa dilatation thermique va entraîner l'ensemble vers le bas plus rapidement que pour une solution sans poutre additionnelle.

Chapitre 4 – Propre essai de laboratoire sur la poutre métallique en forme de U

Lors de la phase de conception et de développement de cette solution innovante, des problèmes ont été identifiés. Un point majeur a soulevé des interrogations sur le comportement mécanique de cette poutre en phase de construction concernant sa résistance et surtout sa stabilité au déversement sans maintien latéral.

La poutre métallique, en forme de U, est formée de trois parties assemblées entre-elles à l'aide de vis autoperceuse (il n'y a aucune soudure). Les parois latérales et supérieures de la poutre sont en tôles minces formées à froid, la partie inférieure est constituée d'un plat formé à chaud d'épaisseur plus importante. Ce plat de plus forte épaisseur permet d'assurer une connexion adéquate d'après les recherches bibliographiques préalablement effectuées. Il se situe également à la fibre extrême inférieure de la section mixte acier-béton et ainsi contribue de manière efficace au moment résistant de la poutre en phase d'exploitation. Cependant, en phase de construction, sans présence de maintien, la poutre métallique seule en forme de U est sujette à l'instabilité globale de déversement. Afin de caractériser le déversement de la poutre et son comportement mécanique en phase de construction, un essai de déversement a été réalisé à échelle réelle au Laboratoire de l'Université du Luxembourg.

Les dimensions de l'échantillon sont présentées dans cette thèse, ainsi que la méthode de fabrication de la poutre (réalisé au Laboratoire). Les imperfections ont été mesurées et des essais de traction ont été réalisés sur des éprouvettes prélevées dans la poutre métallique afin d'obtenir leurs caractéristiques mécaniques. Le déversement d'une poutre est caractérisé par un déplacement latéral et une rotation de torsion de sa section transversale s'ajoutant au déplacement vertical. Ainsi, le système de chargement de l'essai et les systèmes de mesures ont été spécialement conçus pour cet essai. L'essai a bien mis en évidence le déversement de la poutre métallique et les résultats obtenus sont présentés au sein de cette étude. L'assemblage par vis autoperceuse a également bien fonctionné, formant une section monolithique.

Chapitre 5 – Etudes analytiques et numériques de la poutre métallique en forme de U

Le moment critique de déversement de la poutre métallique préalablement testée est évalué à l'aide de méthodes analytiques. Celles-ci ne permettent pas de prendre en compte les conditions aux limites particulières de l'essai. Ainsi un modèle numérique élément finis a été créé afin de reproduire le plus fidèlement possible l'essai au déversement réalisé. L'influence des imperfections géométriques équivalentes initiales, englobant l'effet des contraintes résiduelles, et l'influence des conditions aux limites ont été étudiées. Un modèle numérique élé-

ments finis a été retenu et validé sur la base des résultats de l'essai. Suite à une comparaison avec les méthodes de dimensionnement proposée par l' EN 1993-1-1 (2005), le choix de la courbe de déversement « b » semble décrire le comportement réel de la solution tout en gardant une marge de sécurité.

Une étude paramétrique a été conduite pour valider cette hypothèse. L'étude porte sur 200 configurations géométriques de la solution de poutre en U développée. Les résultats valident l'utilisation de la courbe « b » pour le dimensionnement de la poutre métallique prenant en compte le déversement.

Le précédent modèle numérique de la poutre métallique est complété avec la modélisation de bacs aciers cloués sur les semelles supérieures de la poutre. La modélisation du clouage est réalisée avec des hypothèses conservatrices et l'imperfection géométrique initiale est la plus défavorable. Les résultats de l'étude montrent que la poutre métallique est stabilisée, en phase de construction, par la présence de bacs aciers disposés perpendiculairement à l'axe de la poutre.

Chapitre 6 – Propre essai de laboratoire sur la poutre mixte

Lors de la phase d'exploitation, une fois le béton durci, la poutre a un comportement mixte acier-béton à condition que la connexion entre les deux matériaux soit efficace. Pour faciliter la fabrication, cette connexion se situe dans une zone où le béton est soumis à des efforts de traction induits par la flexion de la poutre dans le cas d'une poutre simplement appuyée. Le béton de cette zone peut être potentiellement fissuré et l'utilisation de connecteurs à cet endroit soulève une interrogation quant à l'efficacité de cette connexion et donc du comportement mixte acier-béton désiré. Un tout autre essai a été donc réalisé au laboratoire de l'Université du Luxembourg, cette fois-ci la poutre testée était composée de béton et d'acier et sa mixité a été étudiée. Cet essai en flexion 4 points est plus conventionnel et suit les recommandations de l' EN 1994-1-1 (2005).

La géométrie de la poutre, ainsi que son mode de fabrication, dont le placement des armatures et le coulage sont présentés dans cette thèse. Des essais de traction et de compression ont été réalisés sur des éprouvettes de chaque matériau utilisés (acier des plats formés à froid, acier des plats formés à chaud, acier des armatures et béton) afin de déterminer leurs caractéristiques mécaniques. Les résultats de l'essai sont présentés, le mode de ruine obtenu est une rupture de la poutre mixte par effort tranchant à de très grands déplacements. Toutefois, la poutre a montré un réel comportement mixte acier-béton présentant une importante ductilité, la connexion a été donc bien efficace.

Chapitre 7 – Etudes analytiques et numériques de la poutre mixte

A partir des résultats d'essais, des méthodes analytiques basées sur l' EN 1994-1-1 (2005) ont été proposés afin de retrouver le moment résistant de cette poutre mixte acier-béton. Une méthode de dimensionnement est retenue prenant en compte la plastification partielle des parois latérales de la section métallique en U.

Un second modèle numérique élément finis a été créé afin de reproduire l'essai mixte-acier béton. La poutre métallique en U est modélisée en éléments plaques de manière similaire au Chapitre 5. Le béton est quant à lui modélisé par des éléments volumiques et les armatures par des éléments filaires. La connexion en zone tendu est réalisée à l'aide de ressorts non linéaires. Chaque matériau est contrôlé par des lois élasto-plastiques. Les résultats des

simulations numériques à l'aide de ce modèle sont comparés aux résultats de cet essai afin d'en valider les hypothèses sur les lois des matériaux utilisés, les conditions aux limites et la modélisation de la connexion.

La capacité résistante de la connexion est validée en comparant le moment résistant obtenus numériquement à l'essai. Une valeur de connexion est déterminée.

Chapitre 8 – Ligne directrice de conception et de construction

A partir des conclusions provenant des résultats des deux essais et des simulations numériques, une méthode analytique de dimensionnement de la solution développée est proposée. Cette méthode repose principalement sur les normes européennes EN 1992, EN 1993 et EN 1994 avec quelques considérations supplémentaires à prendre en compte ainsi que des dispositions constructives.

Les recommandations en phase de construction :

1. La construction de la section en U peut être réalisé à l'aide de vis autoperceuse. Le nombre de vis est déterminé à partir du flux de cisaillement à l'ELU en phase de construction.
2. La poutre métallique étant formé de tôles minces formés à froid, les effets de voilement local et de flambement par distorsion doivent être pris en compte à l'aide de l' EN 1993-1-3 (2007). Il en résulte une section efficace déterminé selon l' EN 1993-1-5 (2007).
3. Le moment résistant de la poutre mixte est le moment élastique de la section efficace préalablement déterminée.
4. La stabilité globale de la poutre au déversement doit être vérifiée selon l' EN 1993-1-1 (2005). La courbe de déversement a utilisé est la courbe "b".
5. La stabilisation au déversement par le maintien latéral des bacs aciers disposés perpendiculairement à l'axe de la poutre peut être pris en compte.
6. La flèche de la poutre doit être vérifiée. Sans étais, la flèche de la poutre sera définitive une fois le béton durci.
7. Des barrettes de maintiens latérales doivent reliées les deux semelles supérieures de la poutre U afin de limiter l'ouverture de la section de la poutre tant que le béton n'est pas durci. Les barrettes peuvent être fixées à l'aide de vis autoperceuse. Les barrettes doivent être disposées tous les mètres.

Les recommandations en situation d'incendie:

1. Afin de limiter l'échauffement des armatures, il est conseillé de placer les armatures à une distance d'au moins 45 mm des bords de la retombée en béton armé.
2. Le moment résistant de la poutre peut être déterminé en suivant la méthode des valeurs tabulées proposées par l' EN 1992-1-2 (2005), en négligeant la partie métallique. Ces résultats sont sécuritaires et peuvent être améliorés par des simulations numériques thermomécaniques.

Les recommandations en phase d'exploitation:

1. Afin d'assurer une bonne connexion, le plat sur lequel les goujons sont soudés doit être au moins égal à 0.4 fois le diamètre du goujon.
2. La connexion à l'aide de goujon à tête est efficace même en zone tendue. Après avoir satisfait les critères de montage et d'incendie, la poutre mixte est souvent sur résistante en phase d'exploitation, une connexion partielle peut être adoptée. Ainsi, une méthode analytique de dimensionnement en connexion partielle est proposée. Dans cette méthode, la plastification partielle des tôles minces latérales de la section en U est déterminée en fonction de la capacité en cisaillement de la connexion.
3. Suite aux observations de l'essai mixte, la résistance à l'effort tranchant de la poutre mixte ne tient pas compte de la contribution des parois latérales de la poutre métallique en U. Il semble que la résistance à l'effort tranchant dépend principalement de la retombée en béton armé. Ainsi, de manière sécuritaire, le dimensionnement de la poutre mixte à l'effort tranchant est réalisé en ne tenant compte que de la partie en béton armée selon l'EN 1992-1-1 (2005).
4. L'essai a aussi mis en évidence que le béton autour des goujons était écrasé et n'était peut-être pas suffisamment armé. Il est donc proposé de disposer d'une armature d'effort tranchant dans le cône de compression de béton sous la tête de chaque goujon.

Un exemple de dimensionnement d'un cas réel est donné prenant en compte toutes ces recommandations. Il s'agit d'une poutre de plancher pour un centre commercial (catégorie D) d'une portée de 8 m avec des poutres espacées de 2 m.

Chapitre 9 – Conclusions et perspectives

L'objectif de cette recherche était de développer une solution de poutre acier-béton résistant au feu et stable en phase de construction. À partir de l'état de l'art sur les recherches internationales précédentes, une solution de poutres composites acier-béton en forme de U a été choisie. La poutre développée est innovante par la disposition de la tôle d'acier, sa résistance en phase de construction et l'emplacement de la connexion mixte.

Finalement, sur la base des travaux de recherche effectués dans le cadre de la thèse, pour chaque phase critique (construction, incendie et exploitation), des recommandations de conception et construction sont données pour l'utilisation de cette solution dans les bâtiments. Un exemple de cas réel détaillé est proposé et remplit tous les objectifs de la thèse.

La résistance au feu semble être de plus en plus nécessaire pour de nombreux bâtiments. Bien que cette solution de poutre ne fonctionne que pour les structures de planchers, il semble que ce type de solution peut augmenter la part de marché de la construction métallique et mixte.

En effet, grâce au comportement mixte, la structure peut tirer le meilleur parti des avantages des différents matériaux (ici l'acier et le béton). Afin d'optimiser les coûts, cette solution innovante peut être associée à la méthode FRACOF. Ainsi, la structure du plancher peut être composée de la solution développée pour les poutres périphériques et les poutres intérieures peuvent être non protégées si elles sont connectées à la dalle.

Les simulations thermomécaniques en situation d'incendie ont également montré que la hauteur ou la quantité de ferrailage peuvent être réduites si les armatures sont suffisamment éloignées des bords de la poutre. Ce n'est pas pris en compte dans les recommandations car

cela est spécifique à chaque configuration. Cependant, il pourrait être intéressant pour une utilisation ultérieure de construire une base de données et des abaques avec ces simulations pour différentes configurations sans utiliser de simulations numériques compliquées.

L'assemblage des trois tôles, formant la section en U, se fait par des vis autoperceuse pour éviter le soudage sur les tôles d'acier formées à froid pré-galvanisées. Cet assemblage prend du temps et augmente les coûts. En fait, les plaques latérales sont pliées en forme de Z après la galvanisation, la soudure est alors déconseillée. Une optimisation de la solution pourrait être un changement de procédé de fabrication permettant de souder ensemble les trois plaques d'acier et d'éviter ainsi l'utilisation de vis autoperceuse.

Nomenclature

Acronyms

FE	Finite Element
GMNIA	Geometrical and Material Non-Linear Analysis including Imperfections
LBA	Linear Buckling Analysis
LTB	Lateral Torsional Buckling
RC	Reinforced Concrete
Rebars	Reinforcement bars

Notations

The notations of the Eurocodes (principally 2, 3 and 4) are used in the thesis as far as possible.

General for steel, concrete and steel-concrete composite structures:

$x - x$	Longitudinal axis of a member
$y - y$	Lateral axis of a cross-section
$z - z$	Vertical axis of a cross-section
b	Width of a section
h	Height of a section
t	Thickness of a plate
A	Cross-sectional area
L	Length; span
I	Second moment of area
EI	Flexural stiffness
δ	Central deflection
μ	Coefficient of friction
M_{Ed}	Design bending moment
$M_{el,Rd}$	Design value of the elastic resistance moment of the section

NOMENCLATURE

$M_{pl,Rd}$	Design value of the plastic resistance moment of the section
M_{cr}	Elastic critical moment for lateral-torsional buckling
$M_{b,Rd}$	Design value of the buckling resistance moment
L_e	Equivalent span
b_{eff}	Effective width of the composite slab
F_l	Design longitudinal force per stud
P_{Rd}	Design value of the shear resistance of a single connector
h_c	Depth of the concrete above the profiled steel sheeting of the composite slab
h_p	Overall depth of the profiled steel sheeting excluding embossments
h_{sc}	Overall nominal height of a stud connector
n_0	Modular ratio for short-term loading
γ_V	Partial factor for design shear resistance of a headed stud
R_{eH}	Yield strength to product standards
R_m	Ultimate strength to product standards
ε_y	Yield strain
ε_u	Ultimate strain

For the structural steel part used in the composite section:

A_a	Cross-sectional area of the structural steel section
E_a	Modulus of elasticity for the structural steel
G_a	Shear modulus of structural steel
ν_a	Poisson's ratio in elastic stage for the steel
I_a	Second moment of area of the structural steel section
f_y	Yield strength of structural steel
f_{yd}	Design value of the yield strength of structural steel
f_u	Ultimate tensile strength
t_{hr}	Thickness of the hot rolled steel plate
b_{hr}	Width of the hot rolled steel plate
$f_{y,hr,m}$	Mean measured value of the yield strength of the hot rolled steel plate
$f_{u,hr,m}$	Mean measured value of the ultimate strength of the hot rolled steel plate
t_{cf}	Thickness of the cold-formed steel plate
$b_{cf,top}$	Width of the top flanges of the cold-formed steel plate
$b_{cf,inf}$	Width of the bottom flanges of the cold-formed steel plate

$h_{cf,w}$	Height of the webs of the cold-formed steel plate
c_{cf}	Height of the edge stiffeners of cold-formed steel plate
t_{bat}	Thickness of the battens
b_{bat}	Width of the battens
l_{bat}	Length of the battens
$f_{y,cf,m}$	Mean measured value of the yield strength of the cold-formed steel plate
$f_{u,cf,m}$	Mean measured value of the ultimate strength of the cold-formed steel plate
γ_{M0}	Partial safety factor for structural steel for cross-section resistance
γ_{M1}	Partial safety factor for structural steel for members resistance subject to instability
$\bar{\lambda}$	Relative slenderness
$\bar{\lambda}_{LT}$	Relative slenderness for lateral-torsional buckling
χ_{LT}	Reduction factor for lateral-torsional buckling

For the concrete part used in the composite section:

A_c	Cross-sectional area of concrete
E_{cm}	Secant modulus of elasticity of concrete
I_c	Second moment of area of the un-cracked concrete section
f_{ck}	Characteristic value of the cylinder compressive strength of concrete at 28 days
f_{cd}	Design value of the cylinder compressive strength of concrete
f_{cm}	Mean value of the measured cylinder compressive strength of concrete
f_{ctm}	Mean value of the axial tensile strength of concrete
$A_{s,slab}$	Area of the reinforcement in the composite slab in both direction
b_{rc}	Width of the downstand reinforced concrete beam
h_{rc}	height of the downstand reinforced concrete beam
A_s	Area of the longitudinal reinforcement in the downstand reinforced concrete beam
$f_{s,m}$	Mean measured value of the yield strength of the rebars
$f_{t,m}$	Mean measured value of the ultimate strength of the rebars
γ_c	Partial factor for concrete

For the reinforcement bars used in the composite section:

A_s	Cross-sectional area of reinforcement bars
E_s	Modulus of elasticity for the reinforcing steel
I_s	Second moment of area of the steel reinforcement

NOMENCLATURE

f_{sk}	Characteristic value of the yield strength of reinforcing steel
f_{sd}	Design value of the yield strength of reinforcing steel
$f_{s,m}$	Mean measured value of the yield strength of the rebars
$f_{t,m}$	Mean measured value of the ultimate strength of the rebars

Contents

Acknowledgements	3
Abstract	5
Résumé étendu	7
Nomenclature	15
Introduction	25
1 Motivations, Objectives and Methodology	27
1.1 Motivations	27
1.2 Objectives	27
1.3 Methodology	28
2 State of the art	29
2.1 Historical solutions	30
2.2 Integrated steel-concrete composite beams	31
2.2.1 Top-hat beams	32
2.2.2 Slimflor beams	32
2.2.3 Composite Slim Floor Beam (CoSFB)	36
2.2.4 Ultra Shallow Floor Beam (USFB)	37
2.2.5 Deltabeam	37
2.2.6 iTECH beam	39
2.3 Formwork steel-concrete composite beams	39
2.3.1 Composite Profiled Beam	40
2.3.2 Modular composite profiled beam	43
2.3.3 Thin walled composite beam	45
2.3.4 Checkered steel-encased composite beam	47
2.3.5 U-shaped steel-concrete composite beams	48
2.3.6 Others	58
2.4 Shear connection	59
2.4.1 Headed stud shear resistance	59
2.4.2 Connection in tension zone	61
2.4.3 The minimum plate thickness for headed stud welded	63
2.5 Conclusion	65
3 Analytical and numerical studies of the flexural behaviour in the fire situation	67
3.1 Objectives of this study	68

3.2	Fire design in building	68
3.2.1	Definition of a fire	68
3.2.2	The European fire classification of structural elements	69
3.2.3	Methods of analysis in fire safety engineering	69
3.3	Partial safety factors	70
3.4	Combination of actions	70
3.5	Materials characteristics	70
3.6	Parameters of the study	71
3.7	Configuration of longitudinal rebars	72
3.8	Loading	72
3.8.1	Permanent loads	72
3.8.2	Live loads	73
3.9	Analytical evaluation of the fire resistance of the reinforced concrete part	74
3.9.1	Design procedure	74
3.9.2	Evaluation of the internal moment	75
3.9.3	Moment resistance of the reinforced concrete section	75
3.9.4	Required height of the downstand beam for the flexural resistance	76
3.9.5	Results example	77
3.10	Numerical simulations of the thermo-mechanical behaviour of the reinforced concrete part	80
3.10.1	Thermal analysis	80
3.10.2	Mechanical analysis with the heated section	83
3.10.3	Results comparison	85
3.11	Conclusions	85
4	Conducted steel beam test	87
4.1	Objectives of the test	88
4.2	Test specimen	88
4.2.1	Geometry	88
4.2.2	Material	88
4.2.3	Fabrication	91
4.2.4	Imperfections	93
4.3	Layout	97
4.4	Setup	100
4.4.1	Test frame	100
4.4.2	Specific application of the load	100
4.4.3	Supports	103
4.5	Instrumentation	103
4.5.1	Displacement sensors	103
4.5.2	Displacement targets	104
4.5.3	Strain gauges	106
4.6	Test procedure	106
4.7	Test results	107
4.7.1	Observations during the test	107
4.7.2	Equivalent moment	112
4.7.3	Force-displacement of the hydraulic cylinder	112
4.7.4	Cross-section representation by the targets	113
4.7.5	Measurement point on the targets during the test	113

4.7.6	Deformed shape of the section	114
4.7.7	Displacement of the section at mid-span	115
4.7.8	Rotation of the section	119
4.7.9	Strains	119
4.8	Conclusions	122
5	Analytical and numerical investigations of the U-shaped steel beam	123
5.1	Objective of the investigations	124
5.2	Cross-section resistance	124
5.3	Analytical evaluation of the elastic critical moment for LTB	124
5.4	Evaluation of the elastic critical moment with LTBeamN	126
5.5	Evaluation of the elastic critical moment with ANSYS	126
5.5.1	Geometry and elements	126
5.5.2	Ideal support conditions	127
5.5.3	Effect of the bottom plate welds at the supports	130
5.5.4	Effect of the loads introduction	131
5.5.5	Recap of the elastic critical moment of the beam specimen	133
5.6	Validation of the FE model	134
5.6.1	Imposed displacements	134
5.6.2	Materials properties	134
5.6.3	Influence of equivalent geometrical imperfections	134
5.6.4	Effect of combined global and local imperfections	137
5.6.5	Numerical results compared to the test results	138
5.7	Comparison to EN 1993	142
5.8	Parametric study on the LTB of the U-shaped steel section	144
5.8.1	The finite element model	144
5.8.2	The varied parameters	144
5.8.3	Methodology	144
5.8.4	Results	146
5.9	Modeling of the lateral restraint provided by perpendicular steel decks	148
5.10	Conclusions	150
6	Conducted composite beam test	151
6.1	Objectives of the test	152
6.2	Test specimen	152
6.2.1	Geometry	152
6.2.2	Material	154
6.2.3	Fabrication	156
6.3	Layout	163
6.4	Test setup	164
6.5	Measurements	165
6.5.1	Displacement sensors	165
6.5.2	Strain gauges	169
6.6	Test procedure	169
6.7	Test results	170
6.7.1	Observations during the test and failure mode	170
6.7.2	Effect of the self-weight	172
6.7.3	Moment-displacement curve	174

6.7.4	Evolution of the deflection	174
6.7.5	Slip at the steel-concrete interface	176
6.7.6	Strain	179
6.8	Investigation on the failure mode of the composite beam	183
6.9	Conclusions	186
7	Analytical and numerical investigations of the composite beam	187
7.1	Objective of the investigations	188
7.2	Analytical evaluation of the flexural stiffness	188
7.3	Analytical evaluation of the bending resistance	190
7.3.1	Elasto-plastic bending moment resistance by integrating the stress distribution	190
7.3.2	Plastic bending resistance considering a full plastic distribution	193
7.3.3	Plastic bending resistance considering a full plastic distribution neglecting the contribution of the cold-formed part	197
7.3.4	Plastic bending resistance with a full plastic distribution limited by the maximum shear force of the connection	198
7.3.5	Compared to the test curve	200
7.4	Numerical study	202
7.4.1	Model	202
7.4.2	Elements	205
7.4.3	Materials properties	206
7.4.4	The boundary conditions	213
7.4.5	Local geometrical imperfection	213
7.4.6	Validation of the FEM compared to the test	214
7.5	Conclusions	217
8	Design and constructional guideline	219
8.1	Construction stage	220
8.2	Fire situation	220
8.3	Exploitation stage	221
8.4	Real case example	222
8.4.1	Case study	222
8.4.2	Section properties	222
8.4.3	Design in the construction stage	222
8.4.4	Design in the fire situation	228
8.4.5	Design in the exploitation stage	230
8.4.6	Summary	235
9	Conclusions and outlooks	237
9.1	Conclusions	237
9.2	Outlooks	238
9.3	Scientific publications	239
A	Tensile tests reports	241
A.1	Coupon B1	241
A.2	Coupon B2	242
A.3	Coupon B3	243
A.4	Coupon W1	244

A.5	Coupon W2	245
A.6	Coupon W3	246
A.7	Coupon T1	247
A.8	Coupon T2	248
A.9	Coupon T3	249
A.10	Coupon C1	250
A.11	Coupon C2	251
A.12	Coupon C3	252
A.13	Coupon C4	253
A.14	Coupon C5	254
B	Compression tests reports	255
B.1	Test on concrete cylinders	255
B.2	Test on concrete cubes	257
C	Effective Cross-section calculation of the specimen	259
C.0.1	Effect of the local buckling of the edge stiffeners	260
C.0.2	Effect of the local buckling of the top flanges	260
C.0.3	Effect of the local buckling of the webs	260
C.0.4	Effect of distortional buckling	261
D	Parametric study – Data and results	263
E	Concrete material law implemented in ANSYS	269
F	Technical drawings	271
	Bibliography	281

Introduction

Composite structures are the mechanical association of materials with different properties. The aim of this kind of structure is to take advantage of the different materials. In civil engineering, steel-concrete composite construction is the most popular, but it exists other composite structures like steel-wood or wood-concrete structures and others. Because this thesis project is dedicated to steel-concrete composite structures, in the following paragraphs the term “composite structures” will refer only to the mechanical association of steel and concrete.

Concrete has high compressive strength but lower tensile strength and has to be reinforced or pre-stressed to be used in structures subject to tension. Although reinforced concrete structures are now more prefabricated, this type of structure is still propped often, the time of installation is then dependent of concrete hardening. This material also has good properties for thermal, acoustic and vibration considerations. In a fire situation, reinforced concrete structures with correct cover can satisfy the regulatory requirement for two hours without additional protection.

Steel has high compressive and tensile strength but it is sensitive to instability under compression. Although this material is heavier than concrete, due to its high resistance, the elements are thinner and so the global structure is much lighter compare to a reinforced concrete solution. One of the biggest advantage of the steel construction is the rapidity of installation; the structural elements are prefabricated and are quickly assembled on site with bolts. In a fire situation, a steel element without protection can satisfy the requirement for a duration of only fifteen minutes.

Composite elements in buildings are beams, slabs and columns. The steel part and the concrete part are mechanically connected at the interface of the two materials. The two connected materials act as a global composite element with a higher stiffness and resistance.

For horizontal elements, in case of bending, to use ideally the two materials, the concrete is used as possible in compression zone and the steel in tension. The floor of a composite building is realised with steel beams connected to a concrete or composite slab. Composite slab is composed of a profiled steel decking which acts as formwork during construction and as reinforcement at the final stage. For an unpropped construction, the maximum span of composite slab limits the space between the beams (around 2.5 m). There are different types of steel beams supporting the slab, their use depends on the span and the frame of the floor. For vertical elements, the composite columns are composed of steel column cased or filled with concrete.

Many constructions are now requiring a global stability in a fire situation to evacuate the building and for emergency response (residential, tall building, car parks ...). The solutions

on the market to protect the steel beam are expensive and some are not sustainable. Beside the economic advantage of reducing the size of the steel beam, the composite construction can also bring a protection by encasing the steel beam with concrete for fire design. In the case of composite beams, there is a solution of a partially encased beam with concrete. This solution is often realised on site, the beam is laid and the concrete is cast on one side, the operation is repeated on the other side after concrete hardening. This process slows down the installation which is the main advantage of steel and unpropped composite structures!

From this statement, the objective of the thesis is to develop a new fire resistant steel-concrete composite beam while keeping the advantage of fast installation (unpropped structure). The solution development is done in collaboration with the CTICM, University of Luxembourg, University of Lorraine and with the participation of the company BRIAND on practical aspects like fabrication and constructional phases.

Chapter 1

Motivations, Objectives and Methodology

Contents

1.1 Motivations	27
1.2 Objectives	27
1.3 Methodology	28

1.1 Motivations

In a building's construction, a structural fire resistance is commonly required for categories of buildings that receive people or store specific products. The required duration of stability strongly depends on the time needed for the evacuation of the persons. Steel construction provides many advantages like a very fast on-site erection of light structures, reducing the delay of the construction, but for some structural floors, when the fire resistance requirements are too important, the steel beam must be protected by additional painting like intumescent coating. These additional protections often lead to uneconomic solutions compared to ones with others materials.

However, thanks to composite structures, it is possible to overcome this problem. In particular with steel-concrete composite beam with steel profile encased in concrete. Nowadays, steel-concrete composite solutions are investigated to take the most benefits of the different material and this is the aim of the solution's development in the present thesis.

1.2 Objectives

The objectives of the thesis is to develop a steel-concrete beam solution for building floors with the following characteristics:

- Fire resistant without any additional protection against high standard duration of fire exposure

- Stable and resistant in the construction stage to avoid any propping system and keep one of the biggest advantage of steel structures
- Resistant in the exploitation stage

A smart use of the material's characteristics and an easy fabrication is also required to be economically competitive.

1.3 Methodology

In order to achieve the mentioned objectives, the methodology of the solution's development was:

1. Finding a potentially adequate solution, during almost 1 year, comprising drawings, concepts and exchanges with a steel constructor. The proposed solution was inspired on a state of the art on the researches already made (presented in Chapter 2).
2. Ensuring that the solution would meet one of the objectives (fire resistance) by analytical and numerical study in a fire situation, almost 1/2 year (presented in Chapter 3).
3. Identifying the critical phases of the beam and the technical aspects that are not well-covered by the standards, and investigating experimentally the different mechanical behaviour of the beam in its critical phase, during almost 1 year (presented in Chapter 4 and 6).
4. Analysing with analytical and numerical model the mechanical behaviour of the tested beam and extending it to more configurations, during almost 1/2 year (presented in Chapter 5 and 7).
5. Finally proposed design guideline referring to the standards with additional recommendations (presented in Chapter 8).

Chapter 2

State of the art

Contents

2.1	Historical solutions	30
2.2	Integrated steel-concrete composite beams	31
2.2.1	Top-hat beams	32
2.2.2	Slimflor beams	32
2.2.3	Composite Slim Floor Beam (CoSFB)	36
2.2.4	Ultra Shallow Floor Beam (USFB)	37
2.2.5	Deltabeam	37
2.2.6	iTECH beam	39
2.3	Formwork steel-concrete composite beams	39
2.3.1	Composite Profiled Beam	40
2.3.2	Modular composite profiled beam	43
2.3.3	Thin walled composite beam	45
2.3.4	Checkered steel-encased composite beam	47
2.3.5	U-shaped steel-concrete composite beams	48
2.3.6	Others	58
2.4	Shear connection	59
2.4.1	Headed stud shear resistance	59
2.4.2	Connection in tension zone	61
2.4.3	The minimum plate thickness for headed stud welded	63
2.5	Conclusion	65

2.1 Historical solutions

Although it is difficult to determine the exact beginning of steel-concrete composite construction, it seems that the first developments of structures including concrete and iron preceded the first patent of reinforced concrete construction of Monier (1867). In fact, in 1808, Dodd (1808) patented an invention where iron tubular members were filled by “condensed earth or artificial stone” as related by James (1974). This patent consisted of a hollow metal section, column or beam, filled with a similar material as concrete. This system was already designed for fire consideration!

In the second part of the 19th century, different systems of fireproof flooring used steel joist encased with cement and plaster. Henry Hawes Fox and James Barrett proposed their suspended floor with inverted “T” section cast iron joist. Ward (1883) proposed a global “T” beam with concrete and an encased steel joist in the tension zone as shown in Figure 2.1. The manner that they used the two materials shows that the inventors were aware of the stress distribution in their solution. At this time, there is still no shear connection between the two materials as related by Pelke and Kurrer (2015).

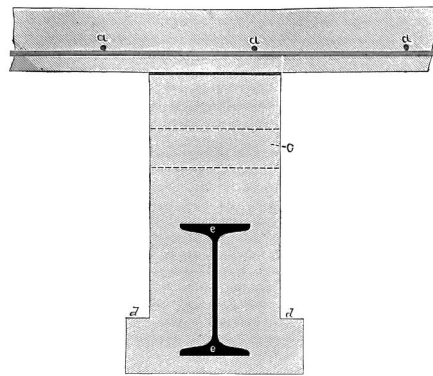


Figure 2.1 – “The re-enforced beam of béton supporting a section of the floor” (Ward, 1883)

At the beginning of the 20th century, Fritz Pohlmann patented a steel-concrete composite beam with a shear connection. The steel beam is an asymmetric rolled section with perforated holes, “when embedded in the concrete, the filled holes transmit the sheering stress” (Pohlmann, 1904). Additional steel plate loops were used as shear connectors near the supports of the beam, a representation of the beam patented is shown in Figure 2.2. This system is interesting for its similitudes with modern composite solution like USFB system (§ 2.2.4) a hundred years later.

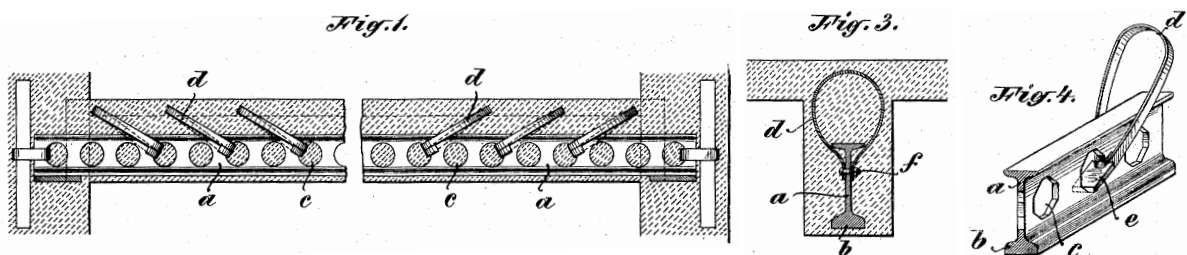


Figure 2.2 – The composite beam of Fritz Pohlmann (Pohlmann, 1904)

In 1926, Kahn (1926) patented a new steel-concrete composite beam system using angled tab flanges welded on steel beams as shear connectors (see Figure 2.3) (Pelke and Kurrer,

2015). This solution is very close to a modern steel-concrete composite beam. This type of shear connectors also looks like the nailed connectors X-HVB (HILTI) used nowadays.

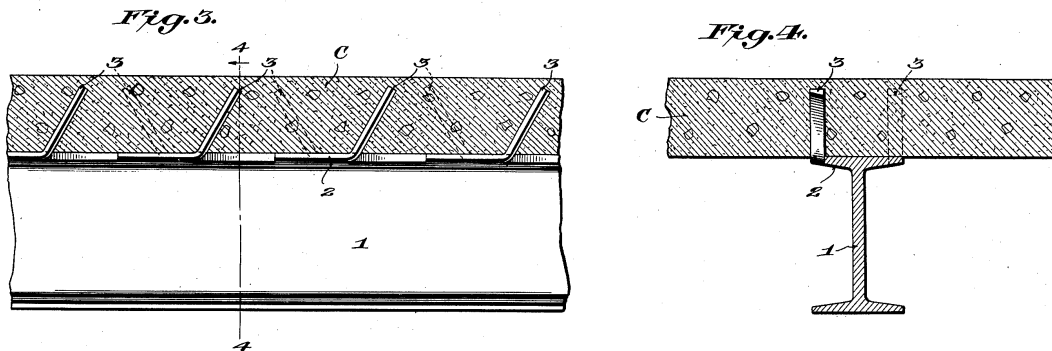


Figure 2.3 – The composite beam of Julius Kahn (Kahn, 1926)

2.2 Integrated steel-concrete composite beams

Since the increase of composite structure in buildings, constructors and researchers have developed new solutions of steel-concrete composite beams. The purpose is to take even more benefits from the two materials. In the context of the thesis project, two categories of floor beams that tend to meet the needs of the thesis (see Chapter 1) are presented. The first category, presented in this section, concerns the composite beams integrated within the slab of the floor (also called slim floor). The second category concerns the “formwork” steel-concrete composite beams, presented in the next section (see § 2.3), where a steel section is used as a formwork that withstands the load in the construction stage and acting compositely with the hardened concrete in the exploitation stage.

In order to reduce the height of the plenum, thus reducing the total height of the building, a solution is to partially integrate the steel profile in the concrete slab. This is often called a slim floor system. The lower flange of the steel section is wider than the upper one, this enables the floor slab to lie on either side of the beam. Then, the steel beam is completely encased in concrete, except for the lower flange. This confer to the beam a great behaviour against fire action and also corrosion. To increase the fire resistance, protection can be applied on the bottom flange not embedded in concrete or/and longitudinal rebars can be added to the lower part of the section. The installation can be unpropped, the steel part is then resistant during the construction stage. Depending on the propping, the slim floor system is used in the span range of 5 to 12 m according to Hicks (2003).

There are many products of slim floor beams, most of them come from Scandinavia (the “hat beams”, see Figure 2.4) and the United Kingdom developed their own products (the “Slimflor” beams, see Figure 2.5). More recent integrated beams have been developed and are also presented in this section : the Composite Slim-Floor Beam (CoSFB), the Deltabeam and the Ultra Shallow Floor Beam (USFB).

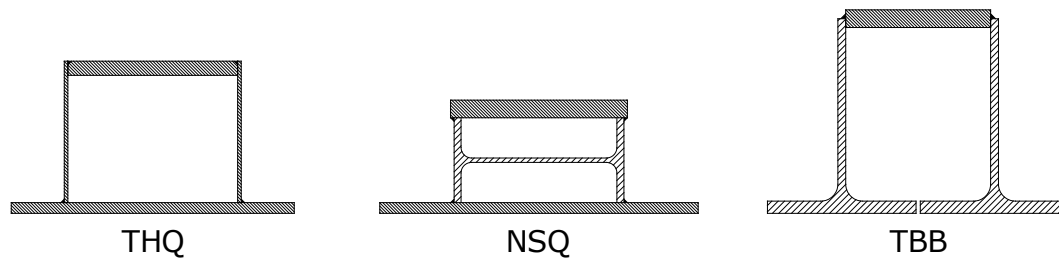


Figure 2.4 – Typical “Hat” beams sections

The benefits of using slim floor construction are listing in Mullett (1992):

- The overall floor construction depth can be reduced. This leads to significant economies (reduce cladding costs, more floors for the same height).
- It offers a flat soffit to the floor and a passage for services.
- It improves the fire resistance of the section. The concrete that surrounds the beam partially insulates the section.
- In the case of local instability, the concrete that surrounds the beam will improve its load carrying characteristics.

2.2.1 Top-hat beams

In Nordic countries the first integrated beams that have been developed are called “hat beams” because of their shaped sections, typical “hat beams” are shown in Figure 2.4.

Mullett (1992) described the arrangements of theses internal “hat beams”:

- **THQ**: The cross-section of the beam consists of four plates, two vertical and two horizontal giving the classic “hat” shape.
- **NSQ**: The beam consist of an “I” shaped section with the web horizontal and the flanges vertical. Horizontal plates are welded to the top and bottom flanges of the section.
- **TBB**: This section is fabricated using two structural T sections with the flange edges touching. The webs of the T are vertical with a horizontal plate welded across the tops of them.

2.2.2 Slimflor beams

Following the success of slim floor beams in Scandinavia, British Steel and Steel Construction Institute (SCI) developed in the United Kingdom a new type of integrated beams called Slimflor. Three types of Slimflor beams are proposed as shown in Figure 2.5. These beams can be used with pre-cast units or deep composite slabs marketed as the Slimdek system.

The Slimflor beam

The original Slimflor beam is composed of a UC (British Universal Column) and a plate welded to the bottom flange. The support of the slab is the rest of the bottom plate. Mullett (1992) proposed three floor construction concepts with precast unit: “non-composite”,

“semi-composite” and “composite”. The first one is when the concrete is not covering the Slimflor beam, the “semi-composite” is when the concrete is covering the beam without shear connection, the “composite” is when there is a concrete cover and a shear stud connector welded on the top flange of the beam to ensure the composite action. The author recommend to keep the precast unit depth and the Slimflor height similar.

The design guidance proposed by Mullett (1992) is limited to plastic (Class 1) and compact sections (Class 2), the sections of higher class limiting the design to the elastic moment capacity are not considered and are uneconomical. The design procedures are based on BS 5950-1 (1990) and BS 5950-3 (1990) with restricted values for conservative calculation.

During the construction stage, Lateral Torsional Buckling (LTB) has to be considered taking into account eventual lateral restraints. Also the disposal of precast units could induce torsion in the beam. The combination of these two effects has to be considered. The author advises the designer also to verify the biaxial stress effects in the flange plate. In fact, the welded flange plate is subjected to longitudinal stress from global bending and stress from transverse bending induced by the precast unit laying on this cantilever plate.

For “semi-composite”, although the concrete surrounding the Slimflor beam seems to enhance the resistance capacity of the section, the design guidance is not taking it into account for the evaluation of the moment capacity, only the steel part is considered.

For composite construction, the effective width (b_{eff}) of the T-shaped beam formed between the beam and the concrete is limited to the $l/4$ (where l is the span). The characteristic strength of the precast units (usually around 60 MPa) is assumed to be the same as the *in situ* concrete (around 30 MPa) in a conservative approach. Furthermore, the concrete stress is limited to $0.5f_c$ instead of $0.85f_c$ in common plastic design. The calculation can be done with full or partial connection. For partial connection, the *in situ* concrete depth in compression is limited to 50 mm below the top flange in order to be sure that the concrete is mobilised without additional shear connectors and transverse reinforcement.

The fire resistance of the Slimflor beam is good because of concrete encasement, all systems presented by Mullett (1997) achieve 30 minutes of fire resistance without additional protection. After 60 minutes of exposure, the temperature of the bottom plate is 150 °C below the fire temperature, the bottom flange is 60 °C to 80 °C below the plate, and at mid-height of the web the temperature is sufficiently reduced and the steel strength is unaffected according to Mullett (1997).

The “non-composite” and “semi-composite” Slimflor can even reach 60 minutes of fire resistance without protection, but not the “Composite” Slimflor which require additional protection. The reason is “composite” Slimflor beam at ambient temperatures are carrying much

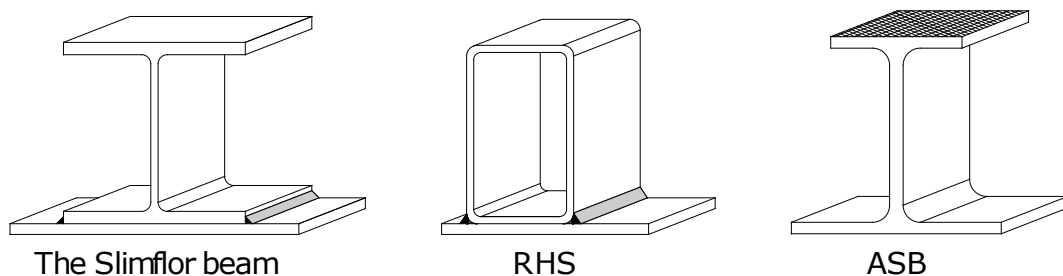


Figure 2.5 – Slimflor beams

Table 2.1 – Comparison of non-composite and composite performance [SCI-110 1992]

Design type	M_{Rd} [kN.m]	$M_{Rd,fi}$ [kN.m]	Load ratio (R)
Non-composite	333	218	0.65
Composite	930 (+180 %)	389 (+78%)	0.42

more loads than the other types. At an ambient temperature (20 °C), the “composite” Slimflor section is more symmetric than the other types, the steel beam is asymmetric but the part of the slab in compression balances the composite section. In fire, the bottom plate loses strength and unbalances the section. Conversely, for “non-composite” and “semi-composite” Slimflor, the asymmetric steel beam at ambient temperature become more efficient with the reduced strength of the bottom plate due to the temperature.

To illustrate this, Mullett (1992) introduced a load ratio (see Equation 2.1) and compared the performance of a “non-composite” and a “composite” Slimflor composed of 254x254x73 UC section (Table 2.1).

$$R = \frac{M_{Rd,fi}}{M_{Rd}} \quad (2.1)$$

Where :

$M_{Rd,fi}$ is the moment capacity of the section at fire limit state

M_{Rd} is the moment capacity of the section at ambient temperature (20 °C)

For composite Slimflor beams with 60 minutes of fire resistance, the author suggests designers to over-design the beam for the normal design situation if they want to avoid adding fire protection. For more than 60 minutes of fire resistance, for all types of Slimflor beams, it is necessary to fireproof the bottom plate.

Rectangular Hollow Section (RHS) Slimflor beam

The use of the Slimflor beam for edge beams is problematic because the open section is weak in torsion. A solution is to use a classical downstand composite beam for edge beams then the loads are assumed to be on the shear centre of the downstand beam. But this leads to a loss in the advantages of the integrated beams construction (saving space by reducing the ceiling). That is why, the RHS Slimflor has been developed, its good torsional properties minimise the stress induced by eccentric loads. The other advantage of this solution is to offer a smooth external face compared to classical Slimflor beam providing easier cladding connection. The RHS Slimflor beam is composed of a standard RHS section with a welded bottom plate 15 mm thick. The bottom plate is not centred providing a longer part to support the slab and a small part to facilitate welding. It can be used with precast units and deep decking. The fire resistance of a RHS Slimflor beam is weaker than that of a classical Slimflor beam, the temperature increases more in the section because the bottom flange, the inner webs and the edge of the outer web of the RHS section are not in contact with concrete. However, fire tests were carried out at TNO in Netherlands and prove, like the classical Slimflor beam, that the RHS, without protection, is fire resistant during 60 minutes exposure with a load ratio

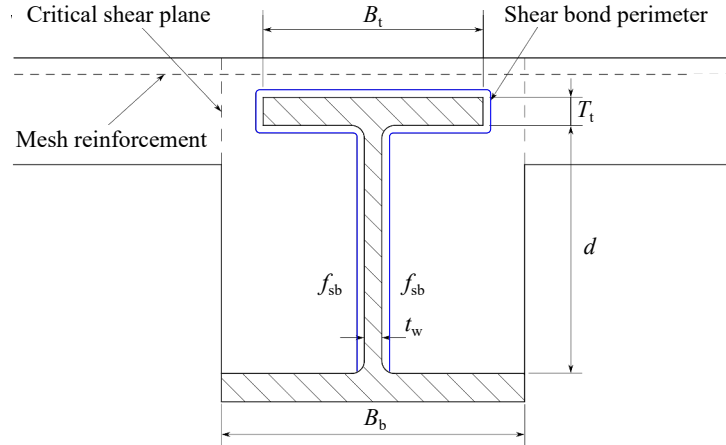


Figure 2.6 – Shear bond transfer around internal surface of the section (Lawson et al., 1997)

$R \approx 0.5$ (see Table 2.1 for comparison with other solutions). The exposed side of the edge beam has to be protected, the cladding material can be used as a protection with a particular attention on any gap between the beam and the cladding.

Asymmetric Slimflor Beam (ASB)

The last Slimflor product developed by SCI is the Asymmetric Slimflor Beam (ASB). It is a hot rolled section with asymmetric flanges. The shorter upper flange has an embossed surface to increase the composite action between the beam and the concrete slab. The beam was originally developed for use with deep decking (Slimdek system) but it can also be used with precast concrete slab.

Lawson, Mullett, and Rackham (1997) present a design guidance for ASB with deep deck composite slabs according to BS 5950-1 (1990) and BS 5950-3 (1990). The publication presents two full-scale load tests on two specimens: 280ASB and 300ASB sections. One of the objectives was to estimate the shear-bond strength developed between the embossed surface and the surrounding concrete. Although only the top of the upper flange is embossed, the authors make the assumption that the longitudinal shear force occurs by shear-bond stresses on a perimeter around the upper flange and the web as illustrated in Figure 2.6. From the tests results, it is concluded that there is a shear connection and the average value of the design shear-bond strength is $f_{sb} = 0.6 \text{ MPa}$. For beams subjected to distributed load, the authors proposed the Equation 2.2 to evaluate the shear capacity of the connection (the parameters used are described in Figure 2.6). Finally if the capacity of the connection (F_{sb}) is greater to the concrete compressive resistance (R_c), the composite connection is considered full. Like for the other method of design for Slimflor beams, the concrete strength is limited to $0.45 f_{cu}$. Fire tests were also carried out and showed that the solution is fire resistant during 60 minutes of exposure with a load ratio $R \approx 0.5$ as well.

$$F_{sb} = (B_t + T_t + d - 0.5t_w) \frac{L}{2} f_{sb} \quad (2.2)$$

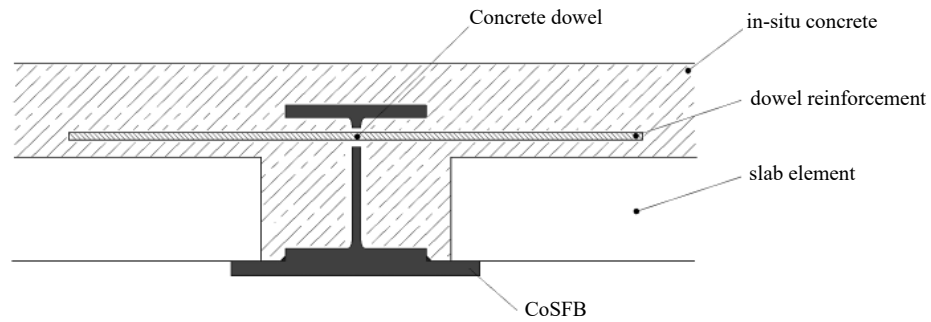


Figure 2.7 – CoSFB cross-section details (Braun et al., 2015)

2.2.3 Composite Slim Floor Beam (CoSFB)

The Composite Slim Floor Beam (CoSFB) system uses Slim-Floor beams with transverse dowel reinforcement passing through the web of the profile used for the shear connection (See Figure 2.7). CoSFB fulfils the requirements for fire resistance classes R60 and R90 without fire protection. Coupling this solution with deep decking (Cofraplus 220) allow this solution to reach 14 m span with 5.4 m space between the beams for unpropped construction.

Braun (2018) presented the fundamental investigations of the load-bearing behaviour of CoSFB-Dowels comprised of experimental push-out tests, numerical simulations, and analytical comparisons. Different failure modes were observed with the experimental investigations and the concrete strength was the most influencing parameter. Braun (2018) identified that the concrete, the dowel action of the dowel rebar and the friction were determinant for the load-bearing behaviour of CoSFB as illustrated by Figure 2.8.

Braun et al. (2015) performed a test campaign comprising 2 flexural tests, 2 shear tests and 27 push-out tests on the "CoSFB-Betondübel" (deep-embedded concrete dowel). All flexural tests showed a very ductile behaviour with large deformation up to failure. All push-out tests reached slip values greater than 6 mm, the limit value for ductile connection according to EN 1994-1-1 (2005). The failure of push-out tests were characterized by the maximum elongation of the dowel rebar. The authors concluded that full composite action can be achieved between the concrete chord and the steel section.

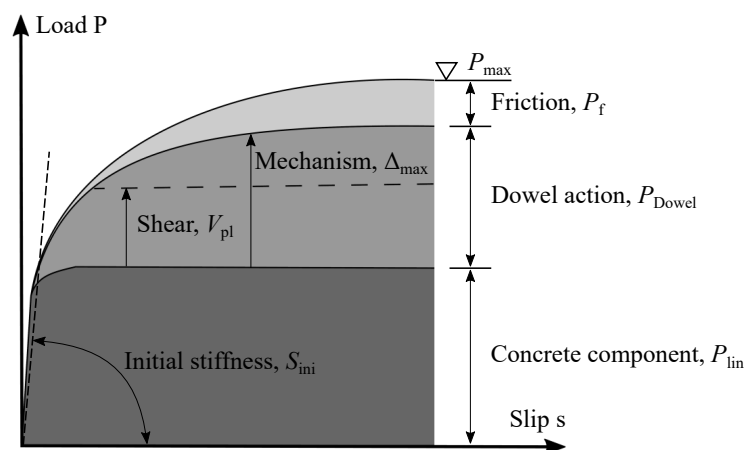


Figure 2.8 – Load-bearing behaviour of a CoSFB-Dowel (Braun, 2018)

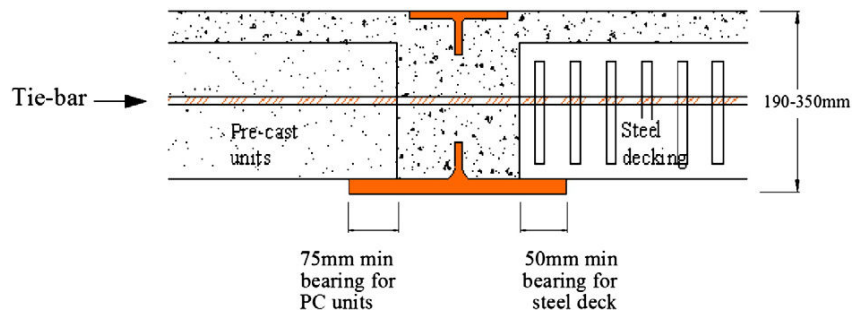


Figure 2.9 – Schematic drawing of the composite shallow cellular floor beam (Huo, 2012)

2.2.4 Ultra Shallow Floor Beam (USFB)

An alternative system is the Ultra Shallow Floor Beam (USFB) (see Figure 2.9), the system is a slim floor beam with, this time, large web opening coupling to a reinforcement bar integrated in the slab. This system is similar to the CoSFB by its shear connection.

Huo (2012), Huo and D’Mello (2013) carried the push-out tests on 24 full-scale specimens with different shear connections : Concrete-infill-only, with tie-bar, with headed studs welds on the web and with ducting passage. The authors found that the shear resistance of the USFB beams increased with the web opening diameter. The additional shear connectors like transverse tie-bar or headed studs welded on the webs increased also significantly the shear resistance and also the slip capacity and ductility of the composite connection. A brittle failure appeared with concrete infill only in the web openings with a low slip capacity below 6 mm. Local shear failure of the tie-bar occurred if the bars are too close to the perimeter of the web openings.

Huo (2012) carried out two flexural tests on the same composite shallow cellular floor beam with a span of 6 m. The specimen was composed of an asymmetric steel profile with web openings embedded in a concrete solid slab. The shear connection was different in the two shear spans, in fact on one side the shear connection was only done by the concrete infill through web openings whereas, on the other side, the connection was composed of $\varnothing 16$ mm tie-bars inserted through the web openings. The author carried out a symmetrical four-point bending test until the plastification of the section at mid-span without failure and then a three-point asymmetric test up to the ultimate failure. The author compared the test results to an analytical study and finite element analysis for the shear connection and analytical study for the flexural tests. The two tests showed significant composite action, the moment resistance was 1.5 times the plastic moment resistance of the steel section. The four-point bending test clearly identified a difference between the two shear connections tested, without the tie-bars the connection was brittle and more slip were observed. Huo (2012) finally recommended to use USFB with additional elements like tie-bars or headed studs. For the use of tie-bars, the authors recommended to place them away for the perimeters to avoid a shear failure. The ducting passage should be used only in region of low shear forces.

2.2.5 Deltabeam

Nádaský (2012) presented the advantages of the Deltabeam as shown in Figure 2.10. Deltabeam is an optimized solution for minimizing structural height with high load bearing capacity and provides a simple and very fast on-site erection. This type of beam can be also fire resistant up to R180 according to Nádaský (2012).

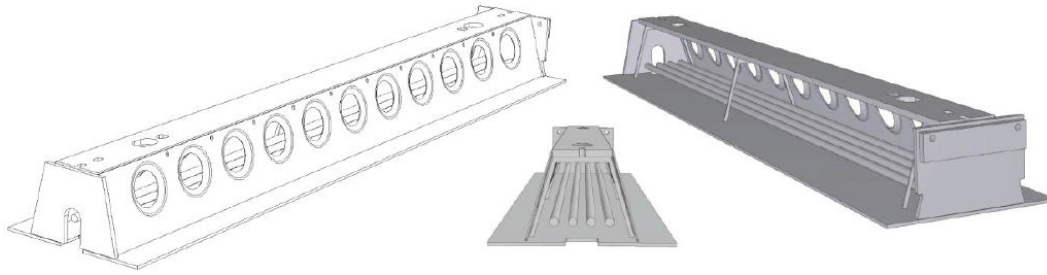


Figure 2.10 – Typical standard Deltabeam of D32-400 cross-section type with 4 F32 fire reinforcement bars inside (Nádaský, 2012)

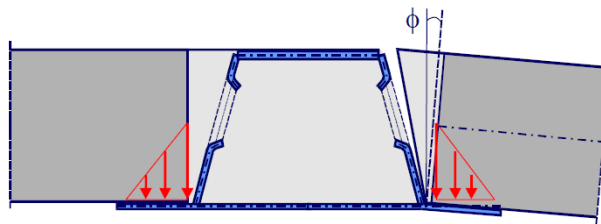


Figure 2.11 – Twisting of the bottom flanges (Schäfer, 2007)

Peltonen and Leskelä (2004) carried out 74 push-out tests to find out the shear-slip properties of the concrete dowel. They investigated the influence of the web hole diameter, the geometry of the lip and the concrete class on the doweling effect. The connection behaviour was ductile, the maximum average slip between steel and concrete was varying from 6 to 9 mm. Peltonen and Leskelä (2004) proposed Equation 2.3 for determining the shear resistance of this connection.

$$P_{\max} = k_R(f_{\text{ctm}})f_{\text{ctm}}A_{\varnothing_w} \quad (2.3)$$

Where:

f_{ctm} is the mean tensile strength of the concrete

$k_R(f_{\text{ctm}})$ is a resistance factor that also depends on the geometry of the hole

A_{\varnothing_w} is the area of the web hole

Schäfer (2007) carried out numerical simulations and analytical study on Deltabeams. The author considered three stages of investigations, the construction stage, the fire situation and the exploitation stage. During the construction stage, the effect of transverse loading due to the precast concrete element (for instance) applied on the bottom flanges induced transverse bending moments on the bottom plate as represented in Figure 2.11. According to Schäfer (2015), this effect reduced the global moment resistance of the Deltabeam.

Leskela, Peltonen, Iliopoulos, and Kiriakopoulos (2014) investigated numerically and experimentally the shear resistance of the steel-concrete composite Deltabeams. They found that the failure of Deltabeams in vertical shear was very ductile.

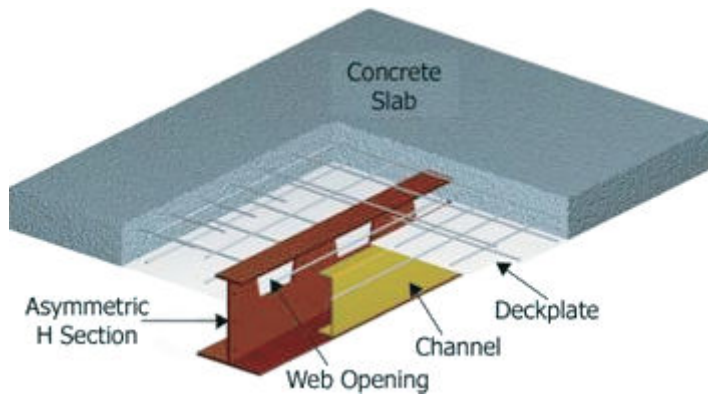


Figure 2.12 – Conceptual view of the proposed iTECH system (Ju et al., 2005)

2.2.6 iTECH beam

Ju, Kim, and Kim (2005) developed a new solution of steel-concrete composite beams called iTECH system (see Figure 2.12). An asymmetric H-shaped section with trapezoidal web opening is encased by concrete, C channels on both sides of the beam are supporting the steel decks. According to Ju et al. (2005), the span of the iTECH beam varies from 7.5 m to 15 m. Ju et al. (2005) carried out four tests to quantify the shear strength of 4 different iTECH specimens with a short span of 1 m:

- The steel beam only with trapezoidal web openings (S-C0S0)
- The steel beam plus inner concrete (S-C1S0)
- The steel beam plus inner concrete and outer concrete (S-C2S0)
- The steel beam plus inner concrete, plus outer concrete and stirrups rebars (S-C2S1)

From the test results, the authors recommended to consider only the steel web and the inner concrete panel for the design of the shear resistance of iTECH beams.

2.3 Formwork steel-concrete composite beams

The second category presented in this section regroups steel-concrete composite beam that comprises a steel part used as a formwork connected to a reinforced concrete part. The steel parts comprises top flanges supporting the steel decking of a composite slab or pre-cast concrete slab. The shaped of the steel part (often “U” or “C”) is then filled with concrete at the same time as the slab.

These types of solution can be used for concrete as well as steel building because their advantages are numerous compared to a classical reinforced concrete (RC) beam, a classical steel or a steel-concrete composite beam. The main advantages of these solutions are:

- The composite beam is fire resistant because of the reinforced concrete part. The duration of exposure to ISO fire can reached 2 hours.
- The steel formwork can withstand the loads during the construction phase, the beam can be unpropped, which reduces construction delay and therefore costs.

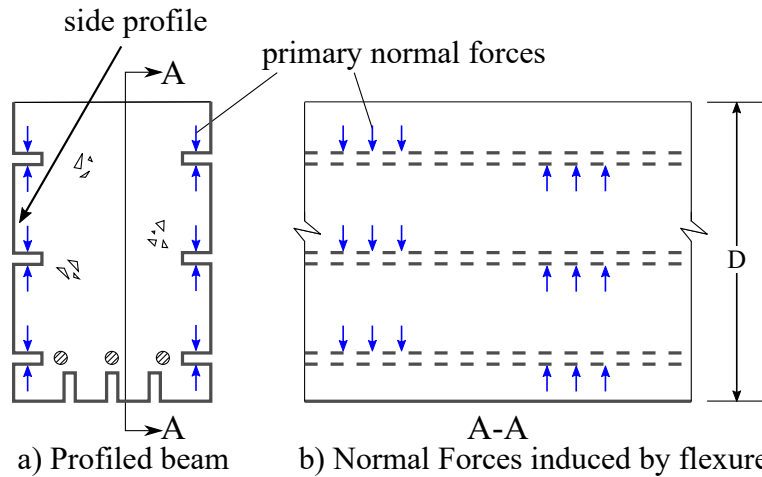


Figure 2.13 – Composite Profiled Beam behaviour (Oehlers, 1993)

- Compared to RC beams, this type of composite beams, with the same size, achieved higher bearing capacity and ductility thanks to the external steel parts.
- The steel part, used as formwork, is prefabricated and thus increases the quality of the concrete implementation phase.
- The amount of steel used is low, the external steel part is often composed of thin-walled plates, which reduces costs.
- The hardened encased concrete can limit the buckling of the external steel.

If the beam is unpropped in construction phase, the formwork steel-concrete composite beam are used in the span range of 5 to 12 m. If the beam is propped, the span can achieved 15 m.

2.3.1 Composite Profiled Beam

Inspired by the developments of composite slab made of steel decking used as permanent formwork, Oehlers (1993) investigated the behaviour of composite beams made of a reinforced concrete part with steel profiled sheets on its sides. The solution developed is called "Composite Profiled Beam". The formwork is made of profiled sheets and are assembled to form an open-box girder. The steel beam reduces the number of propping systems and thus reduces the site labor costs; the wet concrete is then poured inside the steel box. Once the concrete has hardened, the profiled section acts compositely with the reinforced concrete beam. The shear connection between the steel and the concrete parts is ensured by shear bond (like for composite slab) and mainly by forces normal to the side of the ribs of the profiles sheets. These vertical forces are induced by shear forces and by the curvature of the overall composite beam as shown in Figure 2.13.

In order to characterize the composite action and the mechanical behaviour of this innovative solution, Oehlers (1993) carried out 3 flexural tests and 3 shear tests on large-scale beams. For each flexural and shear test, the 3 specimens were : a classical reinforced concrete (RC) beam (F1, S1), a profiled composite beam with the same amount of rebars (F2, S2), a profiled composite beam with a reduced amount of rebars with a strength similar to the RC beam (F3, S3). The flexural test was a four-point bending, the span was 6.5 m and for the shear test the span was 2.4 m.

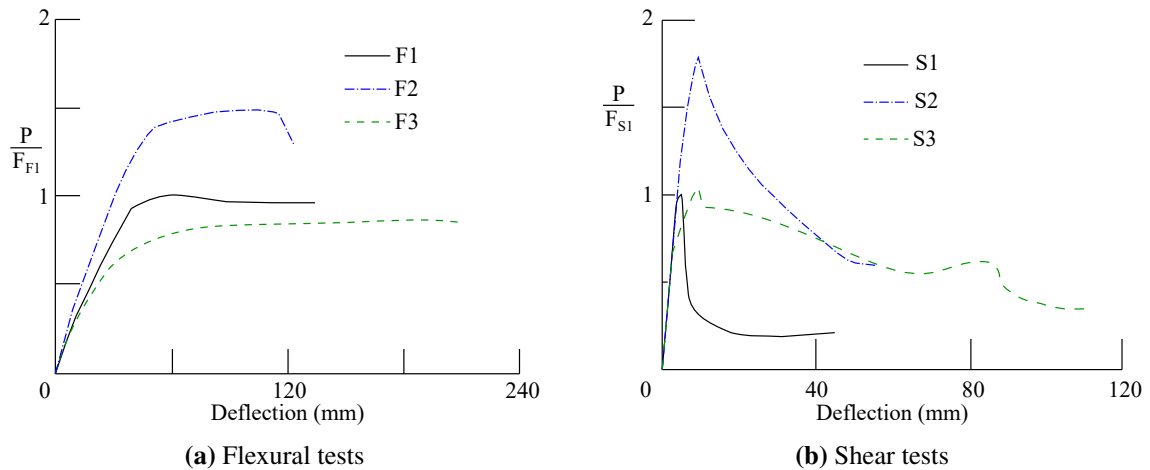


Figure 2.14 – Ductility of tests carried out by Oehlers (1993)

From the flexural tests (see Figure 2.14a), no particular slip between steel and concrete were observed, the beam failed by concrete crushing and the top of the external steel buckled due to compression forces after reaching the maximum load. Thanks to the side profiles, the load-bearing capacity of the profiled Composite Beam increased by 50% compared to the same RC beam without the external steel. A Composite Profiled Beam with the same flexural strength of a classical RC beam exhibited a greater ductility.

For the shear tests (see Figure 2.14b), the Composite Profiled Beam were more ductile with a large ductile plateau after reaching the peak load compared to a classic RC beam where the forces decreased immediately after the peak load. Oehlers (1993) suggested to sum the shear resistance of each component (side profiles + RC part) of the Profiled Composite beams for the evaluation of the shear strength of this innovative solution. In comparison with RC beams, the Composite Profiled Beams can allow an increase of the span/depth ratio of about 20%.

Oehlers, Wright, and Burnet (1994) investigated how the buckling of the external steel of Composite Profiled Beam can affect their flexural strength. One advantage of this type of solution is that one side of the steel plate are restrained by the encased concrete and thus the buckle can form only on the other side (see Figure 2.15). The authors found that the width of the external steel plates can be increased about 70% thanks to the presence of encased concrete.

Following these investigations, Uy and Bradford (1996) developed a finite strip model for

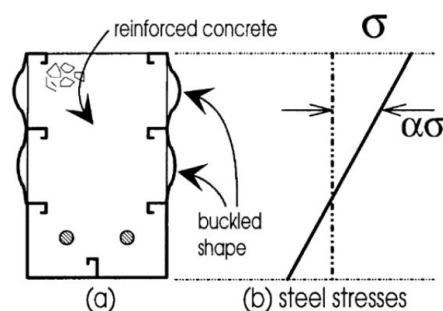


Figure 2.15 – Stress gradient and buckled shapes in Composite Profiled Beams (Oehlers and Bradford, 1995)

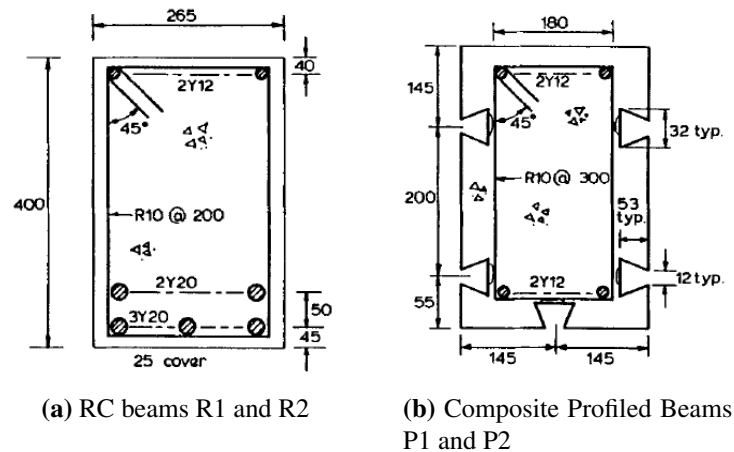


Figure 2.16 – Specimens cross-section tested by Uy and Bradford (1995a)

elastic local buckling to take into consideration the local buckling of a steel plate in contact with a rigid restraint like concrete. The method is applicable for many usages of composite structures like walls, slabs columns and particularly Profiled Composite Beams and was validated against "local buckling push tests" carried out by Uy (1995).

Oehlers et al. (1994) then proposed analytical equations to determine the flexural strength of Composite Profiled Beams in case of full, partial or no shear connection using rigid plastic analysis. They underlined that the loss of the longitudinal shear strength did not induce a high loss in term of flexural capacity for this type of beam compared to the reduction obtained for a classical composite beam (with an I-shaped profile underneath the slab).

Uy and Bradford (1995a,b) proceeded further investigations on the ductility of this type of beam by experimental and analytical studies. The authors carried out large-scale flexural tests on two Composite Profiled Beams (P1 and P2) and on two RC beams (R1 and R2) as represented in Figure 2.16. The beam specimens (RC and composite) are supposed to have the same flexural strength. It was a four-point bending test with a span of 6 m, the two-point loads were applied at 2 m from the supports.

The Profiled Composite Beams exhibited ductility until the same failure load at 230 kN for the two identical specimens (P1 and P2). The beams were loaded for 500 days before this test with different serviceability loads level. Since the load-deflection responses for ultimate flexural tests were really similar for both P1 and P2, the authors indicated that the previous service-loading had no effect on the final response of the beams. For both specimens (P1 and P2), local buckling of the steel sheeting appeared at the top of the section at a load between 20-40 kN. This corresponds to 9-17% of the ultimate load of the tests. Uy and Bradford (1995a) underlined that the local buckling could have a significant effect for this type of beam as the sheeting pulls away from the encase concrete, this leads to a reduction of the load bearing capacity of the composite section. However, according to the authors, the tests showed that the local buckling obtained did not have consequences on the ductility of the beam specimens.

Finally, Uy and Bradford (1995b) proposed an analytical method for calculating the short-term moment-curvature response of the profiled Composite Beams integrating many parameters that can affect the ductility of this type of composite beams. The authors found that the parameters that influenced most the ductility of Profile Composite Beams were the yield

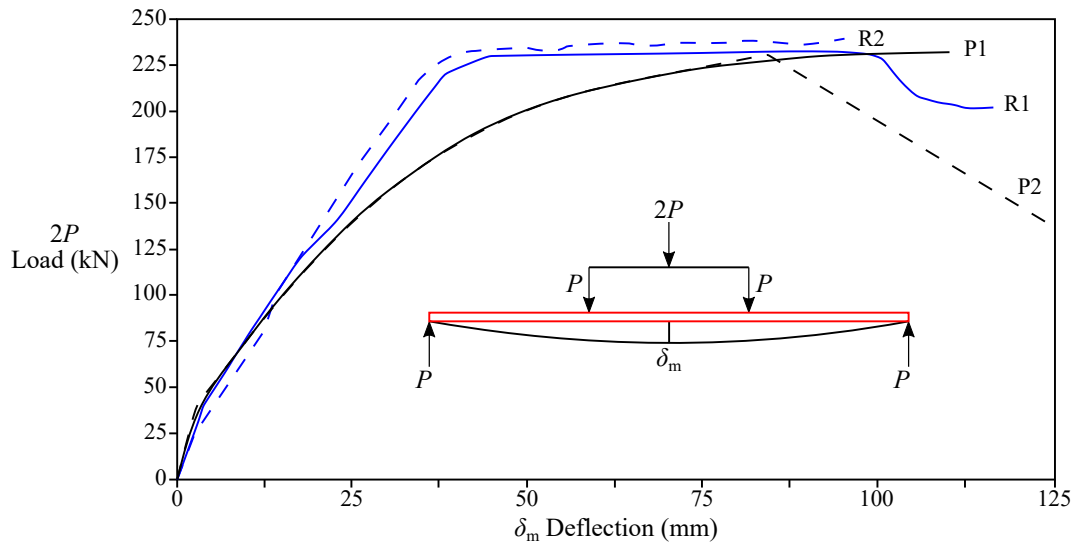


Figure 2.17 – Load deflection of the flexural tests carried out by Uy and Bradford (1995a)

strength of the steel, area of rebars and the slip. The increase of the yield strength of the steel decking (f_{yp}) increased the ultimate moment of the beam but reduced its ductility. Similarly, like for classical RC beams, the increase of the ratio of the area of longitudinal rebars on the concrete section ($\frac{A_{st}}{BD}$) results in an increase of strength and stiffness but a loss of ductility. Uy and Bradford (1995b) underlined that the increase in the slip strain (ϵ_s) can decrease the flexural strength of the composite beam for low values of curvature whereas at high displacements, with higher value of curvature, the increasing of slip strain can increase substantially the ductility of the beam.

2.3.2 Modular composite profiled beam

Following these investigations, Ahn and Ryu (2007) experimentally studied the flexural strength of C-type and Lip-type Modular Steel Concrete (MSC) beams. The concept consists in the arrangements of external steel modules connected to a concrete part as represented in Figure 2.18. The authors tested 6 types of specimens with different arrangements in four-point bending with a span of 2 m. The specimens can be sorted in two groups, 3 were composed of C-type steel modules (-C) and 3 with Lip-type steel modules (-L). In each group, 1 specimen was without connection between the modules (N), 1 with bolt connection between modules (B) and 1 with bolt connection plus an additional bottom plate which reinforced the section (RB).

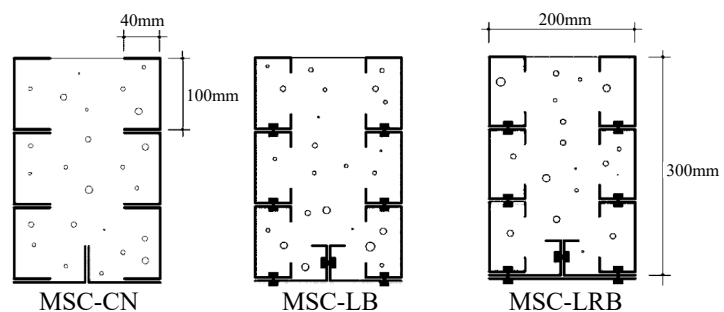


Figure 2.18 – Example of specimens tested by Ahn and Ryu (2007)

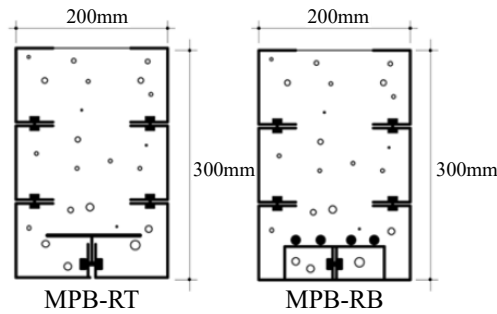


Figure 2.19 – Specimens tested by Ahn and Ryu (2008)

The modules not connected to each other by bolts exhibited slip between the modules and a lower stiffness and strength compared to the others. For the modules connected by bolts, local buckling appeared in the compression part. Specimen CB (with bolts) and CRB (with bolts and additional plate) displayed plastic behaviour but not a ductile plateau after reaching the peak load. The Lip-Type modules had lateral buckling of the upper modules, this resulting in an important decrease of the load after reaching the maximum strength followed then by a very ductile plastic plateau. Ahn and Ryu (2007) underlined that if the beam is used with a slab as a T-shaped section, the compression part would be in the slab and thus the buckling would be limited.

Ahn and Ryu (2008) improved their solution by reinforcing the bottom of the section of the Modular composite Profiled Beam (MPB formerly MSC). The authors investigated two types of reinforced specimens as represented in Figure 2.19; by welding T-type section (MPB-RT) and by adding deformed bars supporting longitudinal rebars (MPB-RB). The authors carried out four-point bending tests with a span of 2 m on 7 specimens: 3 MPB-RB with different area of rebars, 3 MPB-RT with plate having equivalent areas compared to the rebars used for MPB-RB and 1 MPB-CB (not reinforced as already investigated by Ahn and Ryu (2007)).

The MPB-RT series exhibited similar stiffness compared to a not reinforced MPB section whereas MPB-RB series showed higher stiffness. All specimens had slip between the modules and at high load level this became sever and prevent the section to achieve full plastic behaviour. The authors found experimental results lower than theoretical values in average about 32% for the MPB-RT series and about 28% for MPB-RB series.

Finally, Ryu (2010), studied the behaviour of a T-section modular composite profiled beams (TMPB) which considers the concrete slab as the flange of the T-section in order to improve the ductility of the composite beam and avoid buckling instability in the top of the steel modules. The authors carried out four-point bending tests with a span of 2.35 m on 7 specimens regrouped in two series. The first series comprises 4 specimens (T1 to T4) of TMPB without stirrups (see Figure 2.20a) and the second series (TS2 to TS4) are TMPB with stirrups (see Figure 2.20b). The number following the section name is the thickness of the steel modules, for instance T1 has steel modules with a thickness of 1 mm. Except for specimen T1, all the T-type specimens had separation between modules before reaching the maximum load. At the maximum strength for all T-type specimens diagonal tension cracks occurred in the shear span until failure. However, the TS-type (with stirrups) did not exhibit diagonal cracks and failed due to more severe separation between the steel modules. The TMPB-TS specimens showed more ductility. Ryu (2010) compared the test results to theoretical results based on analytical methods with full plastic distribution, the precision was good when the specimen has less separation between the modules (like T1). The shear strain measured in both series

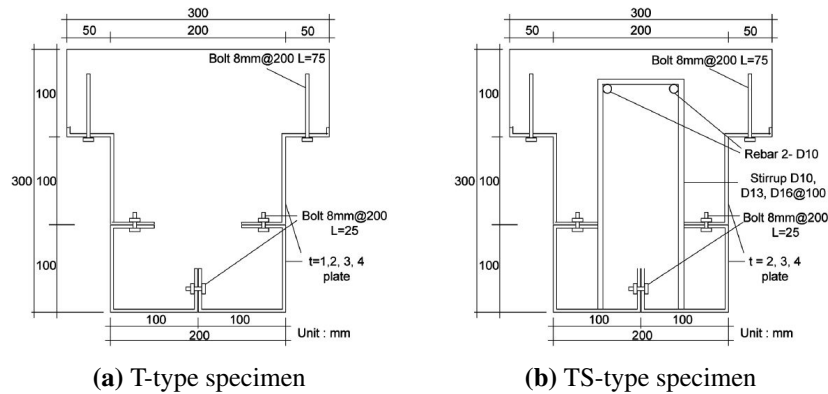


Figure 2.20 – Specimens cross-section tested by Ryu (2010)

also showed that the section without stirrups (T-type) were more solicited about 50% and the authors indicated **the use of shear reinforcement (TS-type) could avoid any reduction of bending resistance in case of important shear forces**. Finally, the authors concluded that the behaviour of TMPB was clearly dependent on the separation between steel modules and therefore dependent to the bolt connection between them. The authors proposed to conducted new flexural test with the bolt connection as a parameter.

2.3.3 Thin walled composite beam

Hossain (2003) proposed new types of formwork steel-concrete composite beams called Thin Walled Composite (TWC) beams. According to the author, the advantages of TWC sections are that they allow easy casting of concrete (due to the open box section) and they do not need any propping system in the construction stage; the steel beam resists in this phase the loads of wet concrete, workmen and tools.

The abbreviation of the TWC sections represented in Figure 2.21 are :

OS : Open Section

WE : Welded Extension on the opens section

WER : Welded Extension linked with Rods

BS : Braced open Section

RC : open section filled with Reinforced Concrete part (stirrups and longitudinal rebars)

CS : Closed Section

Hossain (2003) tested 3 series of beam specimens, series A and C were tested in four-point bending whereas series B was tested with one-point loading:

- Series A : 4 OS with a span of $L = 1500$ mm with lightweight and normal concrete in order to study their performances with this type of beam
- Series B : 3 OS, 4 CS, 2 BS, 2 WE with a span of $L = 600$ mm in order to study the effect of the different connections (1 BS and 1 OS were unfilled to compare with the other composite beams)
- Series C : 4 WE, 2 WER, 2 RC with a span of $L = 990$ mm in order to study the effect of the welded rods and the reinforcement bars

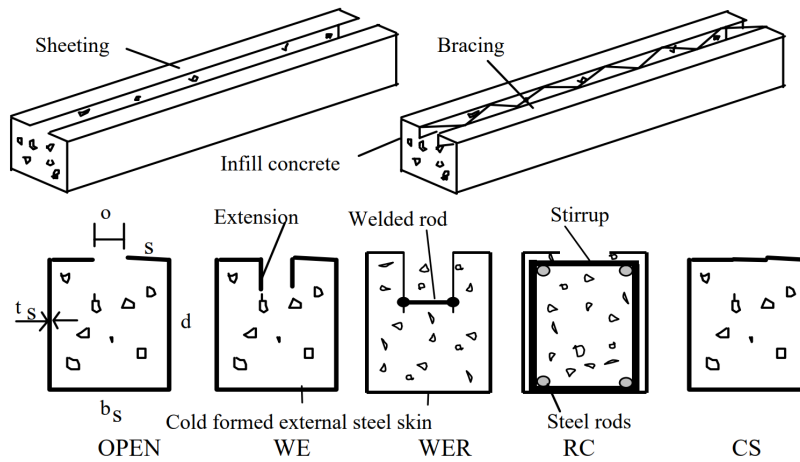


Figure 2.21 – Proposed beam section by Hossain (2003)

The behaviour of all beams was affected by the separation of the side plates with the concrete (see Figure 2.22). The WER specimens had less separation due to the presence of the rods and has the higher strength compared to other sections. At failure the side steel plates buckled outward the encase concrete. Like from the previous study with Composite Profiled Beam (CPB) and Modular CPB of Oehlers (1993), Ahn and Ryu (2008), the strength of TWC sections is limited by the buckling resistance of the external plates at the top of the section. It was found that the flexural strengths of CS, WE and WER were higher compared to OS. The ductility of the beam was found higher for WE sections (increase of 250% compared to OS), the authors also underlined that the WER exhibited more strength than WE but with less ductility. When comparing the performance between unfilled and filled beams, the strength of composite beam increased about 50% in average compared to unfilled sections. It can be noted that the bracing of the open section (BS) did not improve the strength of the unfilled beam (only 0.5% increase).

Hossain (2003) validated theoretical analysis based on the models proposed by Oehlers et al. (1994) with the experimental results of series A and B. For series C, according to the author, the results may differ because buckling of the steel occurred before yielding. Therefore the assumption of plastic stress distribution in the analytical model was not reached. Additionally the steel plates used for series C were more slender (4 to 5 times greater than in other series) and thus the buckling stress should be much lower than series A and B. Hossain (2003) proposed to estimate the buckling stress in the plate by Equation 2.4.

$$\sigma_b = \frac{k_b \pi^2 E_s}{12(1 - \nu^2)} \left(\frac{t_s}{d}\right)^2 \quad (2.4)$$

Where:

k_b is the bending buckling coefficient depending on the ratio span/depth (L/d) of the plate and the degree of rotation restraint

E_s is the Young modulus of the plate

t_s is the thickness of the plate

d is the depth of the plate

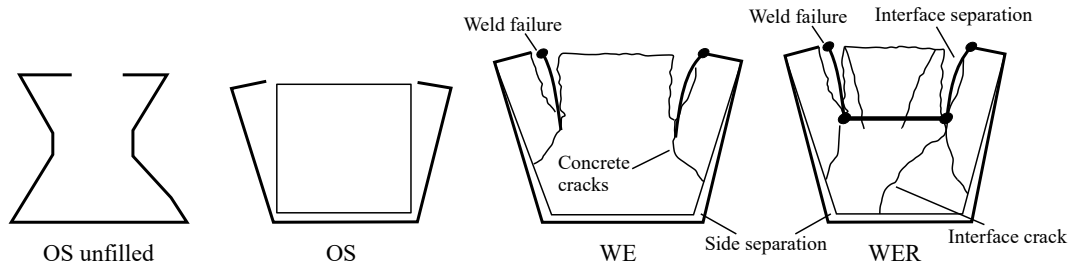


Figure 2.22 – Failure mode of TWC beams (Hossain, 2003)

Hossain (2005) developed design guidelines for TWC beams with an analytical model for determining the flexural strength of WE sections in partial or full shear connection. This type of beam is generally in partial shear connection because of the limited bond strength at the steel-concrete interface. The authors gave design considerations and design examples. Hossain (2005) sent surveys to steel constructors in order to know their preferences on the different TWC sections accompanied with their mechanical performances. Although WER beams had the highest strength and a good ductility, the constructors preferred OS beams because of its easier fabrication.

2.3.4 Checkered steel-encased composite beam

Chen, Li, Zhang, and Wu (2018) proposed a new solution similar to the OS section proposed by Hossain (2005) but with checkered plates in order to strengthen the bonding effect between steel and concrete (see Figure 2.23). This effect can reduce the number of shear connectors. The previous studies carried out by Oehlers (1993), Ahn and Ryu (2007), Hossain (2003) underlined that the bond action between the external steel and the concrete have a great influence on the mechanical behaviour of this type of composite beam. Therefore Chen et al. (2018) developed a composite beam with checkered surfaces in contact with the concrete. In addition to the checkered plates, the authors also provided bolt shear connectors on the top flange of the section embedded in the concrete slab. The authors tested 6 specimens, 2 were "full anti-slipping" and the 4 others were "partial anti-slipping". The authors proposed to calculate the anti-slipping shear capacity of the steel-concrete interface with checkered plate by Equation 2.5.

$$F_R = \tau L_s U + n V_{sb} \quad (2.5)$$

Where:

τ is the bonding strength between checkered steel and concrete determined by push-out tests on checkered steel tube with concrete carried out by Chen, Dai, Jin, Chen, and Liu (2015).

L_s is the length of the shear span

U is the inner perimeter of the C-shaped steel beam

n is the number of bolts connectors on the steel flanges

V_{sb} is the ultimate bearing capacity of a single bolt connector

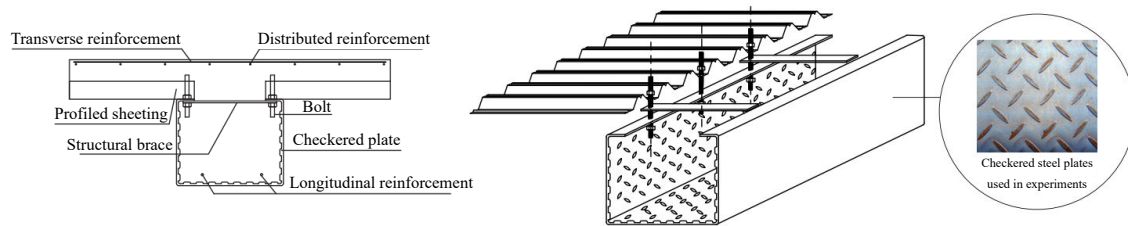


Figure 2.23 – Checkered steel-encased composite beam proposed by Chen et al. (2018)

The tests were four-point bending tests with a span of 3400 mm. The checkered plates were 4.7 mm thick. The top flanges widths of the steel beam were 50 mm and they were folded inward. Structural braces spaced by 480 mm were set on the top flanges. For two specimens, longitudinal rebars ($\varnothing 16$ mm) were inserted in the encased concrete part.

Chen et al. (2018) obtained two different failure modes depending on the degree of shear connection (also called "anti-slipping" capacity by the authors). The two specimens "full anti-slipping" exhibited a bending failure whereas the others, in partial shear connection ($\eta \approx 0.6$), had shear slip failure. The bending failure was characterized by the crushing of top concrete slab and the yielding of the whole steel section (even the rebars if present), the slip was very small. The slip failure was characterized by very important slip between steel and concrete, most of the steel section yielded but no damage were found in the concrete slab. However, even in partial shear connection, the checkered composite beam showed a good bearing capacity and ductility. Chen et al. (2018) finally concluded that the checkered pattern of steel improves the bonding effect and can reduce the number or diameter of shear connectors. The "anti-slipping" connection degree influenced the load bearing capacity, the ductility and the failure mode of the composite beam. The authors validated an analytical calculation method for the design of such composite beam with the experimental results.

2.3.5 U-shaped steel-concrete composite beams

In the continuity of the developed concepts, recent studies have been carried out on innovative steel-concrete solutions where a U-shaped steel section is filled with concrete.

Nakamura (2000) presented new forms of structural steel-concrete composite section used for bridges and one of them was a "Partially Prestressed Cold-Formed Steel U-Girder". The cold-formed U-section was used as the main girder of a double-tee bridge and can be formed from only one steel sheet. In the hogging moment region of the continuous beam, near to the intermediate supports, concrete was poured inside the U-section and prestressed. Static bending tests were carried out on this section with a span of 4 m on two specimens, one unfilled for the sagging region and one filled and reverse for the test for the hogging region. The shear connection between steel and concrete was ensured by shear studs welded on the top flanges of the steel U-section. The specimens tested exhibited very good ductility after reaching the yield point of the steel. A continuous road bridge with three span of 60 m was designed. The height of the steel U-shaped section was 2.5 m high with a thickness of 25 mm. Although, the U-shaped was made in two parts welded together, Nakamura (2000) indicated that this type of beam limit the welding and reduced the fabrication cost about 20-30% compared to bridges with I-shaped girders.

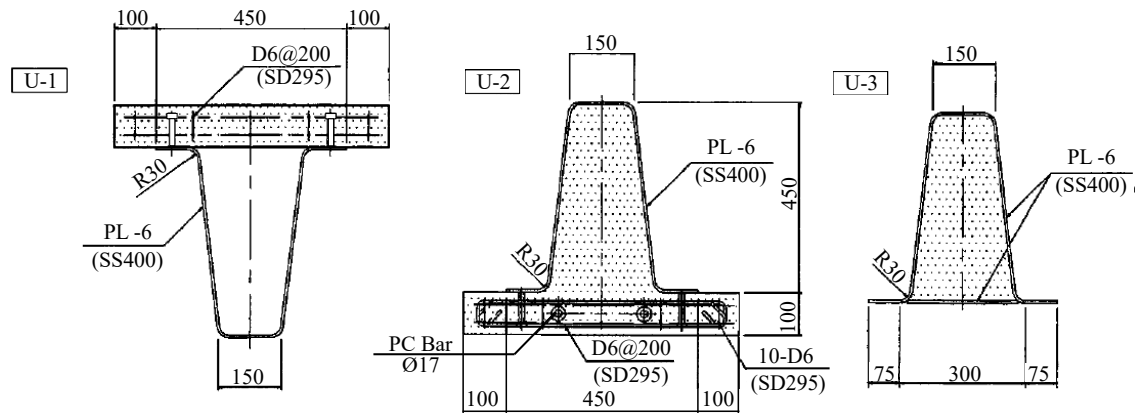


Figure 2.24 – Specimens tested by Nakamura (2000)

Nakamura (2002) carried out four-point bending tests on 3 U-shaped steel-concrete specimens (U1, U2 and U3 as represented in Figure 2.24) with a span of 3.8 m. The thicknesses of the steel plates were 6 mm. The specimen U1 was dedicated for positive bending region, the section is not filled with concrete and the connection is realized through shear studs welded to the top flanges. The specimen U2 was dedicated for negative bending region, the section is filled with concrete prestressed and the connection is also realized through shear studs welded to the top flanges. The specimen U3 is an alternative solution of U2 for negative bending region, instead of prestressed concrete, an additional bottom plate is welded to the top flanges to resist the tension forces. Therefore, for U3, the concrete slab in tension is not considered. Specimens U2 and U3 (filled with concrete) exhibited the highest ductility probably due to the restraint of local plate buckling due to the presence of encased concrete. The authors proposed a method of design for such a beam assuming Bernoulli-Euler principle and verified the method with the tests. The author finally concluded that this type of cold-formed U-shaped steel-concrete composite beam had sufficient strength, good rotation and deformation; thus they provide a suitable and economical solution for bridges.

Liu, Guo, Qu, and Zhang (2017) investigated steel-concrete composite beams with U-shaped steel girders with a shear connection realised through angles welded on the U-shaped beam (see Figure 2.25). According to the authors, the use of welded angles for the connection reduced the cost compared to a classical connection with headed stud. The U-shaped filled with hardened concrete formed a box girder and thus is also providing a higher torsional resistance compared to a classical composite beam with an open steel section underneath the concrete slab. The angle connectors are composed of a vertical and a horizontal leg, according to Liu et al. (2017) the vertical leg resists the longitudinal shear force between the concrete slab and the steel girder whereas the horizontal leg is limiting the separation between the slab and the downstand beam. Two positions of the angles connectors were investigated, the angles can be welded to the webs or to the top flanges. The authors underlined that the option of connection to the webs would facilitate the installation of the low layer of longitudinal rebars in the slab compared to the connection welded on the top flanges. Liu et al. (2017) carried out four-point bending tests on 5 U-shaped steel-concrete composite specimens (CB1 to CB5), the span of each beam was 8.4 m. The specimens were identical except for the composite connection, the varied parameters were the spacing, the position and the length of the shear connectors. The specimens CB1 to CB3 had the shear connectors welded to the webs (see Figure 2.25b), CB4 also had the connectors welded to the webs but

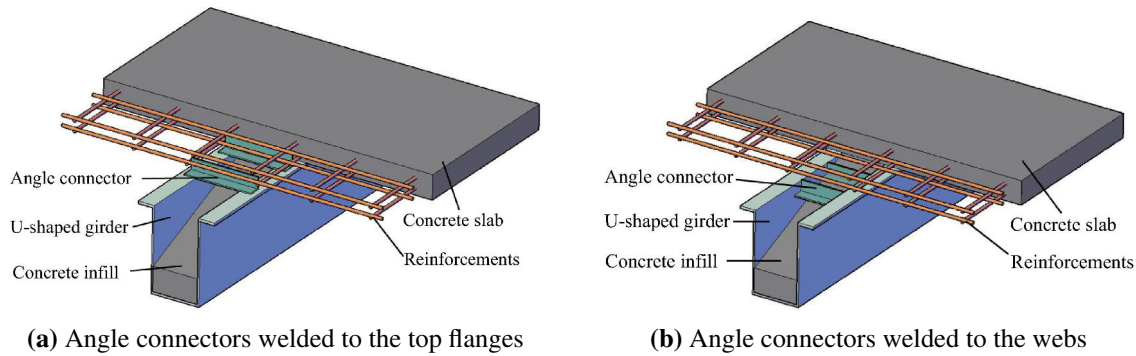


Figure 2.25 – U-shaped steel-concrete composite beams investigated by Liu et al. (2017)

4 angles connectors were replaced by 14 headed shear studs and finally CB5 had the connectors welded to the top flanges (see Figure 2.25a). All the specimens were 400 mm height, 250 mm wide plus the top flanges 80 mm wide (oriented outwards) and the thickness of the external steel was 6 mm for the webs and 10 mm for the flanges. For the connection, 3 specimens were in partial shear connection and 2 in full connection. The shear strength of these connectors were assumed by Equation 2.6 proposed in the Chinese Code GBJ 17-88 (1995) for channel connectors (not angle connectors as investigated). Three spacings of connectors were tested: 230 mm, 300 mm and 400 mm.

$$N_v^c = 0.26(t + 0.5t_w)l_c(E_c f_c)^{0.5} \quad (2.6)$$

Where:

t is the thickness of channel connectors flanges

t_w is the thickness of channel connectors webs

l_c is the length of channel connectors

E_c is the modulus of Elasticity of concrete

f_c is the compressive strength of concrete

From the conducted experimental study, Liu et al. (2017) obtained two failure modes depending on the slip at the steel-concrete interface. Specimens CB1 to CB3 exhibited very high slip at the end (around 20 mm) whereas specimens CB4 and CB5 had a very small slip deformation (less than 1 mm). The authors underlined that the connection used for specimen CB4 (with the replacing headed stud) was more ductile than the one used for the same specimen without headed studs (CB1). The degree of shear connection was assumed full for the two specimens, this shows that Equation 2.6 cannot approximate precisely the shear strength of angle connectors. The authors underlined that the inclusion of headed studs (in CB4) improved the deformation capacity of the beam because they had better anchorage in the concrete slab and, as they were welded to the top flanges, they were directly connected to the slab and this is a more effective location for the shear transfer. That was confirmed by specimen CB5 which exhibited the highest flexural strength and deflection, as a reminder, for CB5 the angle connectors were welded to the top flanges and not to the webs.

Finally, Liu et al. (2017) concluded that the U-shaped steel-concrete composite beams investigated should have the angle connectors welded to the top flanges instead of the webs.

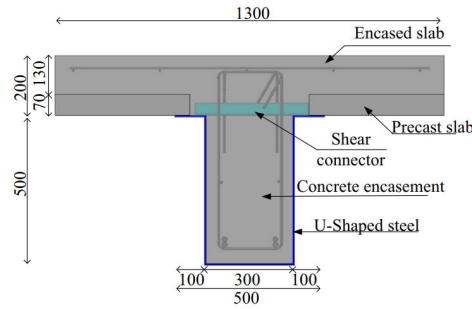


Figure 2.26 – Specimens cross-section proposed by Keo et al. (2018)

The experimental results showed that the connection located in the top flanges, directly embedded in the concrete slab, had a higher shear strength capacity. Therefore this confers a higher ductility to the composite beam and limits the slip between steel and concrete. The connection to the webs had the advantage of facilitating the installation of the low layer of longitudinal rebars in the concrete slab, thus if it is used, the authors advised to replace part of them with headed studs.

Keo, Lepourry, Somja, and Palas (2018) investigated a U-shaped steel-concrete solution with L-shaped or square sections used as connectors and conducted asymmetrical push-out tests. An advantage of this connection is that the L-shaped, welded to the two top flanges, maintains the shape of the steel cross-section during the casting of the concrete. The authors adapted the classical symmetrical push-out test of EN 1994-1-1 (2005) for this type of beam where the symmetry is not possible. They carried out 2 push-out tests with square (20x20 mm) and L-shaped connectors (40x40x4 mm) in order to determine the best connectors; which appears to be the L-shaped connector. Then, they carried out 3 other push-out test with this retained connection (L-shaped 50x50x5 mm) comparable to the proposed solution of Liu et al. (2017). For all specimens, the spacing of the shear connectors were 300 mm. The specimen tested had the dimensions presented in Figure 2.26.

From the first comparison between the two first push-out tests, the square connectors leads to a failure by crushing the surrounding concrete whereas for L-shaped connector it is a fracture of the connector by plastic deformation due to shear forces leading to a large ductility in the force-slip behaviour. In fact, for L-shaped connectors, after reaching the peak load, the load capacity decreases slower than with square connector. Therefore Keo et al. (2018) retained the connector with L-shaped. The authors carried out finite element simulations of the push-out tests with the U-shaped specimens with L-shaped connectors and validate it with the experimental results. They performed a parametric study to investigate the parameters that influence the shear connection proposed (like dimensions of the L-shaped connector). Previously, Liu et al. (2017) assumed the shear capacity of such a connection with the Equation 2.6 proposed in the Chinese Code GBJ 17-88 (1995) without great satisfaction. Therefore, Keo et al. (2018) proposed Equation 2.7 for predicting the shear capacity of the L-shaped connector for U-shaped steel beams.

$$P_u = 2(A_{s1} + A_{s2}) \times \frac{f_u}{\sqrt{3}} + 2K_c \times A_c \times f_c \quad (2.7)$$

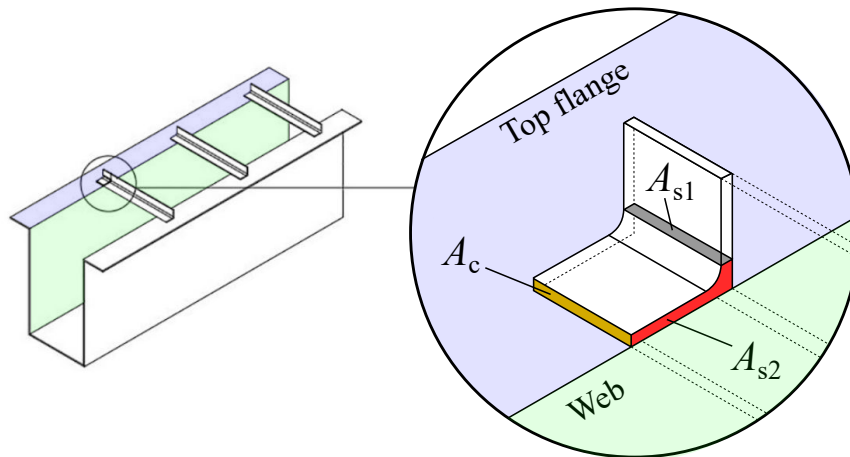


Figure 2.27 – Shear failure plans and concrete local pressure zone (Lepourry et al., 2018)

Where:

A_{s1} is the shear plan of the vertical leg located on the top flanges (see Figure 2.27)

A_{s2} is the shear plan of the horizontal leg located on the top flanges (see Figure 2.27)

A_c is the area of concrete subjected to pressure on the thickness of the horizontal leg located on the top flanges (see Figure 2.27)

f_u is the ultimate strength of the shear connector

f_c is the compressive strength of concrete

K_c is a calibration factor for concrete strength ($K_c = 19 - 38.1h_a/H_c$)

h_a is the height of the L-shaped cross-section

H_c is the height of the concrete slab

From the push-out test of Keo et al. (2018), the L-shaped (or angle) connectors exhibited a ductile behaviour greater than the square bar, the slip at load level descending to 90% of ultimate load was larger than 6 mm (the limit to classify a connector "ductile" according to EN 1994-1-1 (2005)).

Following the investigations of Keo et al. (2018), Guo, Liu, and Qu (2018) carried out new four-point bending on six other full-scale specimens (SCB1 to SCB6) with the angle connectors welded only to the top flanges, this time (see Figure 2.25a). The beam's specimens were all fully composite and the span was 7.2 m. No longitudinal rebars and stirrups were inserted into the encased concrete. The authors varied different parameters between specimens: the height of the U-shaped, the width of the U-shaped, the thickness of the U-shaped top flanges, the spacing between the connectors and the width of the slab. The angle connectors used were L50x50x5. For specimen SCB3, **headed shear stud were welded at the bottom of the U-shaped section**. The slips between steel and concrete recorded at the ultimate load were below 0.1 mm indicating that the full composite action was reached for every specimen. The specimen which exhibited the highest ductility from the load-deflection response was the specimen with additional shear studs at the bottom flange (SCB3), the others showed also a good ductile flexural behaviour. The specimen which had the highest flexural strength was the specimen with the highest downstand beam (SCB5, $H = 390$ mm instead

of 350 mm for the others) whereas the lowest flexural strength was obtained with the specimen with the lowest slab width (SCB6, $B_e = 320$ mm instead of 1400 mm for the others). The authors compared the results with analytical methods of design of EN 1994-1-1 (2005) with good agreement, they also developed a 3-D finite element model validated with the test results. The authors carried out a parametrical study to see the influence of the parameters on the flexural strength. They concluded that the depth of the U-shaped beam had the most influence on the flexural strength of the composite beam. The authors also indicated that the external steel part of the specimens were made by welding steel plates instead of cold-forming the section from one steel plate. This induces residual stresses, the authors assumed their distribution in their analysis and found that the effect is a reduction of the flexural stiffness of about 30% but not the flexural strength (as they carried out plastic analysis).

Lepourry, Heng, Somja, Boissonnade, and Palas (2019) proposed a portal frame using this solution, achieving a span of 13.5 m with a height of 3.07 m (including the slab height). The authors in their proposed solution divide the U-shaped beam in three parts. Thus, the connection beam to beam is investigated, Lepourry et al. (2019) carried out two experimental tests in order to validate the design of this connection. The connection beam to column of the portal frame has also been investigated through four full-scale experimental test and numerical simulations on a finite element model.

Lepourry et al. (2019) proposed Equation 2.8 for the shear force-slip relationship of L50 angles.

$$P = P_u \left[1 - \exp(-1.8\delta^{0.5}) \right] \quad (2.8)$$

Where:

P_u is the ultimate strength of the connector calculated by Equation 2.7

δ is the slip in millimeter

Lepourry et al. (2019) carried out a 6-point bending test on one specimen with a span of 10.6 m. The specimen exhibited a large ductile plateau after the elastic stage in full shear connection. The slip and the uplift between steel and concrete were relatively small.

Lepourry et al. (2019) underlined that the use of this type of beam avoids employments of bolts and welding on site which reduces the cost. However, this construction choice supposes to prop the beam in the construction stage and keeps the delay of concrete hardening as for classical reinforced concrete structures. The authors indicated that the use of headed studs were not suitable with the developed solution due to the low thickness of the steel plates, this is also explained in paragraph § 2.4.3. Therefore, they preferred welding L-shaped on the top flanges and this is also used as bracing in order to prevent the opening of the steel section.

Nevertheless, Liu, Zhao, Chen, Xu, and Yang (2018) presented a novel configuration where a cold-formed steel U-shaped section, stiffened by a rebar truss on its top flanges, is connected to a reinforced concrete part with **welded headed shear stud at the bottom of the section**. They named this section RCUCB and a detailed representation is in Figure 2.28. The cold-formed thin plates (3-4 mm) are folded in a U-shaped section with the top flanges directed inward (also called "varus" top flanges), reducing the number of welding and residual stresses (as already mentioned by Nakamura (2002), Guo et al. (2018)). The rebar truss can transform the open steel U-section into a considered closed section and restrain the outward opening

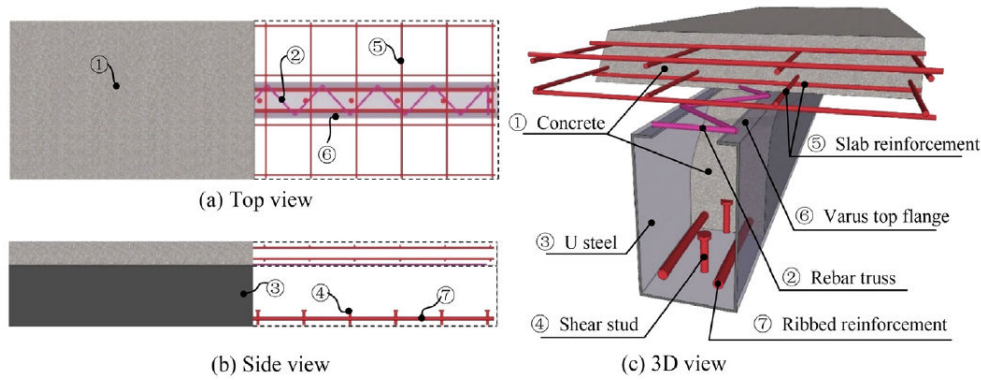


Figure 2.28 – RCUCB beam details (Liu et al., 2018)

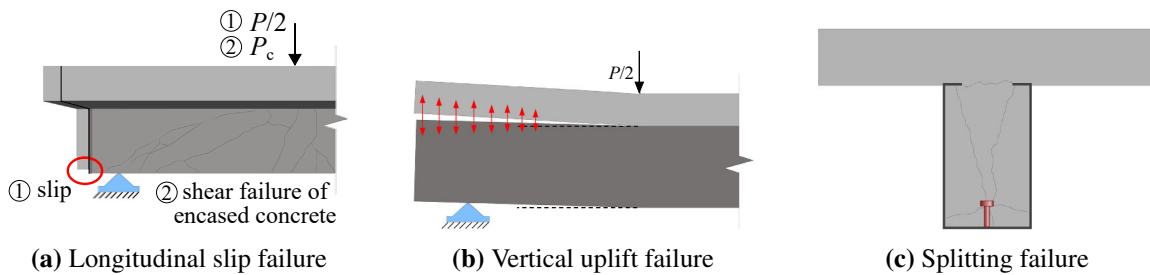


Figure 2.29 – Different failure mechanism obtained by Liu et al. (2018)

of the external steel in bending as it was found, for instance, by Hossain (2003) with OS section (see Figure 2.22). Good bending capacity and ductility can be expected with this type of beam as already found by previous authors. The authors carried out four-point bending test on 10 specimens varying different parameters to see their influences on the mechanical behaviour: the beam's depth, the presence of longitudinal rebars and the degree of shear connection.

The RCUCB showed three distinct failure modes: longitudinal slip failure, vertical uplift failure and splitting failure. They were defined as:

- The longitudinal slip failure was characterized by an important slip between the encased concrete and the U-shaped beam after the yielding of the bottom of the U-shaped steel. Then the composite action decreased gradually with the slip and finally a shear failure of the encased concrete was obtained. This failure occurred for specimens without longitudinal rebars inserted in the encased concrete and when the shear connection was partial (see Figure 2.29a).
- The vertical uplift failure was characterized by the apparition of micro-cracks at the neck (between the slab and the downstand beam) before reaching the peak load. Then, after the peak load, the micro-cracks developed in all the shear span and the slab is uplifted from the downstand beam. This failure occurred for specimens with longitudinal rebars (see Figure 2.29b).
- The splitting failure was characterized by splitting cracks radiating in the encased concrete from the cap of the headed shear studs to the edges of the external U-shaped section. This failure occurred for specimens with full shear connection in addition to the uplift failure (see Figure 2.29c).

From the flexural tests, comparison between specimens can underline the influence of different parameters. It appeared that the presence of shear studs only increase the bending capacity of 5%. This result is surprising, the composite connection for specimens without shear studs might have been done thanks to the "varus" top flanges and the rebar truss embedded in concrete. The presence of longitudinal rebars increased significantly the flexural stiffness (more than 20%) and slightly the bending capacity (around 7-10%). The specimens with full shear connection and longitudinal rebars had the highest flexural strength (12% greater compared to specimens in partial shear connection without rebars). The authors underlined that the presence of rebars influenced more the bending capacity than the presence of shear studs. The ductility found for the RCUCB was high and the ultimate bending capacity can be determined by EN 1994-1-1 (2005) in conjunction with three reduction coefficients (λ_b , λ_c and λ_h), where :

λ_b is a reduction coefficient for the effective slab width (= 0.87 for all specimens)

λ_h is a reduction coefficient for the effective depth of steel web (= 1.0 without rebars, = 0.7 with rebars)

λ_c is a reduction coefficient for the concrete compressive strength (= 1.0 without rebars, = 0.8 with rebars)

Liu et al. (2018) suggested to install a proper anti-uplift detailing in order to avoid the vertical uplift failure.

Therefore, Zhou, Zhao, Liu, Chen, and Yang (2019), Liu, Zhao, Yang, and Chen (2019) proposed an updated configuration of the RCUCB with additional inverted U-shaped rebar (stirrups) as presented in Figure 2.30. With this new configuration, the authors investigated the influence of the reinforcement ratio, the steel ratio, the beam depth and the spacing of shear studs on the flexural behaviour of the composite beam. They carried four-point bending test on 10 new specimens, with a span of 2.8 m or 3.6 m depending on the specimen. The beam depths were 300 mm or 400 mm. The thickness of external steel was 3 mm or 4 mm. All the specimens had longitudinal rebars inserted in the encased concrete with diameters of 12 mm or 16 mm. This time, **two end steel plates were welded at the both ends of the steel U-shaped beam**, this must play an important role in the slip distribution of the composite beam. The authors justified the use of these end plates to simulate a column boundary. However, following this assumption, the column should also restrained the face of the slab, here a separation would appear between the downstand beam and the slab. If the beam is later used without these end plates, the slip behaviour may differ.

According to Liu et al. (2019), all specimens showed the same flexural failure characterized by the yielding of the bottom of the U-shaped steel beam before the peak load and by the crushing of the concrete slab, at mid-span, at the peak load. Zhou et al. (2019) indicated that all materials reached their yield strength (concrete, structural steel and reinforcing steel). The flexural concrete cracks were mainly located in the pure bending region (between the two-point loads). Although the steel plates were slender (exceeding the local buckling limit specified in GB 50017 (2017)), no local buckling was found in the steel plates of the U-shaped steel beam. This is due to the restraint given by the encased concrete beam as already mentioned by Oehlers and Bradford (1995). The inverted U-shaped rebars insert in the new configuration prevent the uplifting failure as expected and enhanced the weak neck between the slab and the downstand beam as previously found by Liu et al. (2018). Zhou et al. (2019) found that the increase of the reinforcement ratio or the steel thickness increase the bending

capacity. The contribution of the headed studs welded at the bottom of the section was small. In fact, the varus top flanges embedded in the encased concrete and braced with the rebars truss participate already in the composite action. In addition, the two end plates (to simulate the column boundary according to Zhou et al. (2019)) restricted the slip between the encased concrete and the U-shaped beam where the connectors should be used for. Thus, **the authors underlined that the shear studs welded at the bottom of the section could be removed.** Once more, this is only possible if the two ends plate are welded at the both ends of the beam. In fact, with this new bending test, the slip was located between the downstand beam and the slab. Therefore, the shear connection is no longer ensured by the shear studs, but instead by the inverted U-shaped rebars linking the concrete slab to the downstand beam. Liu et al. (2019) found a full connection behaviour with an estimated very low degree of connection by the Chinese code GB 50017 (2017) ($\eta = 0.24 - 0.36$). Thus, the authors proposed to revise the method for the calculation of the shear connection resistance. Liu et al. (2019) proposed to consider in the calculation of the total shear resistance (F_{VR}), the sum of the following contributions:

- the shear resistance of the inverted U-shaped rebar $F_{vr} = A_{ri}f_{vr}$
- the longitudinal shear capacity of the concrete $F_{vc} = A_{cv}f_{tk}$
- the interlocking resistance of the concrete $F_{vo} = 0.6A_{cc}f_{ck}$

Where:

A_{ri} is the cross-sectional area of the inverted U-shaped rebar

f_{vr} is the shear strength of the inverted U-shaped rebar (often $f_{yr}/\sqrt{3}$)

A_{cv} is the shear surface area at the neck in the shear span

f_{tk} is the concrete tensile strength

A_{cc} is the "squeezing" area between the reinforcement truss longitudinally projected

f_{ck} is the concrete compressive strength

Finally, Liu et al. (2019) obtained with this new shear resistance, a modified degree of shear connection between $\eta = 0.77 - 1.06$ in accordance with the full composite behaviour of the specimens.

The RCUCB showed very good ductility (up to a deflection of $L/20$ at mid-span), the author used the ductility factor (μ), which is the ratio of the ultimate deflection on the deflection at the yielding, to quantify it and found values between 15 to 24 which is significantly higher compared to classical composite beam (often around 5). According to Zhou et al. (2019), the RCUCB also showed excellent plastic deformability quantifying by a plastification factor ($\gamma \geq 1.44$), higher than classical composite beam ($\gamma \leq 1.43$). Liu et al. (2019) recommended to calculate the elastic bending stiffness of the RCUCB beams by transforming the beam into an equivalent steel beam and proposed a simplified method for determining the bending capacity based on the plasticity analysis.

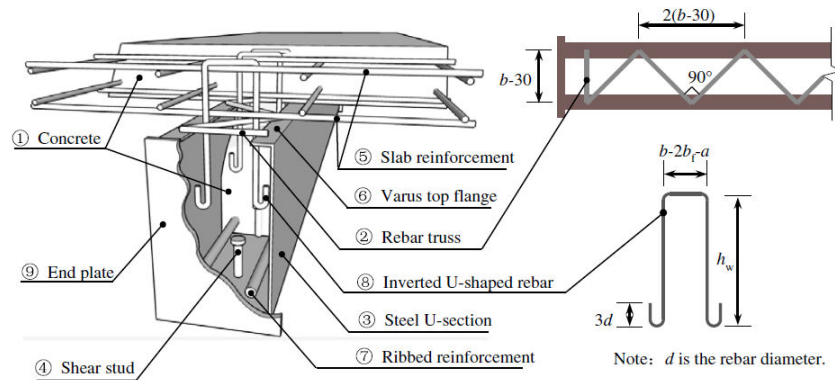


Figure 2.30 – New RCUCB beam details (Liu et al., 2019)

Lawson and Taufiq (2019) studied the use of partial shear connection with other types of U-shaped sections with bolts shear connectors. This also underlined the problem of stud welding for light steel plate. The thickness of the steel plates may not be sufficient for welding, thus bolt connectors can avoid this problem. Kozma, Odenbreit, Braun, Veljkovic, and Nijgh (2019) reviewed different types of bolt connectors and carried out 15 push-out tests in order to evaluate their mechanical behaviour.

Lawson and Taufiq (2019) investigated two forms of composite beam using an assembly of cold-formed C-shaped sections connected together with self-drilling screws. The C sections are used as tensile and shear reinforcement. The authors underlined that longitudinal reinforcement can be added inside the encased concrete for a fire situation but this configuration was not tested. The two type of beams tested were :

- Type 1 are composite beams with C sections at the bottom. The shear connection was ensured through the lips of the C section, or increased by horizontal screws, or with vertical bolts, or with perforated plates.
- Type 2 (see Figure 2.31) are composite beams with C sections at the bottom plus higher C sections on the sides forming a U-shaped steel concrete beam. The shear connection was ensured through the horizontal screws and can be increased with perforated plates.

The authors carried out three-point bending tests on 18 Type 1 specimens and 4 on Type 2 specimens with the different shear connections mentioned with a span varying from 800 mm to 1700 mm. The load-deflection curves for the U-shaped steel concrete composite beam are represented in Figure 2.31. Lawson and Taufiq (2019) found an important increase of the failure about 80% with the side C section (Type 2) compared to the same test without (Type 1). The flexural stiffness also increased about 80% for Type 2 compared to Type 1 specimens. This showed the important participation of side sections. The use of perforated plates in the side sections increased about 30% the bending resistance of the U-shaped composite beams. However, as shown in Figure 2.31, the use of perforated plates seems to decrease the ductility behaviour of the composite beam.

Lawson and Taufiq (2019) proposed to determine the shear force resisted by the side C-shaped sections as a function of their span and the elastic bending resistance of a C section. For instance, for uniform loading, the shear force resisted by the pair of side C section is $8M_{el}/L$ where M_{el} is the elastic bending resistance of a C section and L is the span. The authors concluded from the tests that the mechanical shear connectors (screws, bolts, perforated plates) had small influences on the composite behaviour.

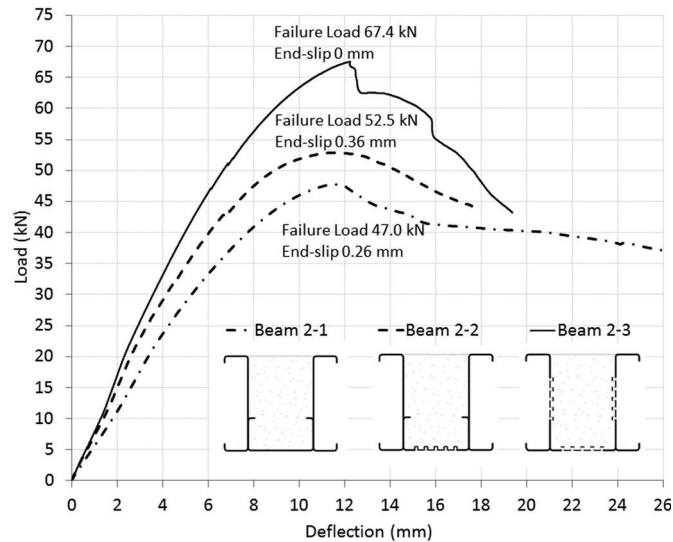


Figure 2.31 – Load-deflection curves for 1.7 m span light steel composite beam with side C section (Lawson and Taufiq, 2019)

2.3.6 Others

Two other industrial concepts are presented in this section. Their solutions also meet the requirements of the thesis.

Gagnepark beam

Gagnepark is a French company specialist in car parks buildings. In order to improve the fire resistance for their floor, the company patented a steel-concrete composite beam (Dejean and Fraud, 2013). As represented in Figure 2.32, the solution comprises a closed steel box girder made of welded plates. In the construction stage the steel box girder support the load of fresh concrete and workers. The top flange of the steel section has holes regularly spaced to allow the concrete casting on site. A reinforcement cage is inserted inside the steel box girder and an inverted U-shaped rebars is linking this part to the concrete slab, similarly to the inverted U-shaped rebars of Zhou et al. (2019), Liu et al. (2019).

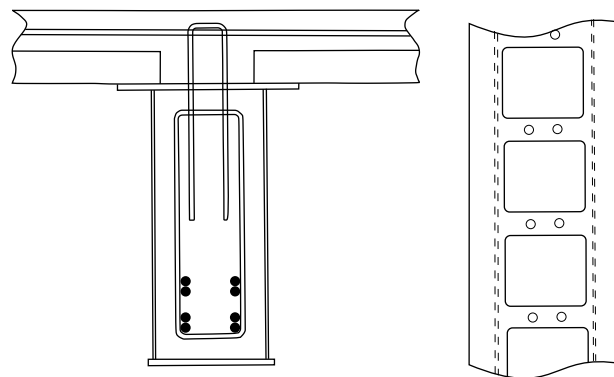


Figure 2.32 – Cross-section and top view of the patent concept (Dejean and Fraud, 2013)

Diversakore Versa :T: beam

Diversakore is a US company in the field of structural engineering, fabrication and construction. They developed a patented solution that also respond in part to the problematic of the thesis: the "Versa :T: beam" (Rahimzadeh, 2002) (see Figure 2.33). This solution is also fire resistant through the inserted longitudinal rebars. In the construction stage the beam is propped but the steel is providing a formwork prefabricated and facilitates the on site execution. This type of composite connection is realized through headed shear studs welded on the bottom flange of the U-shaped section as investigated by Liu et al. (2018).

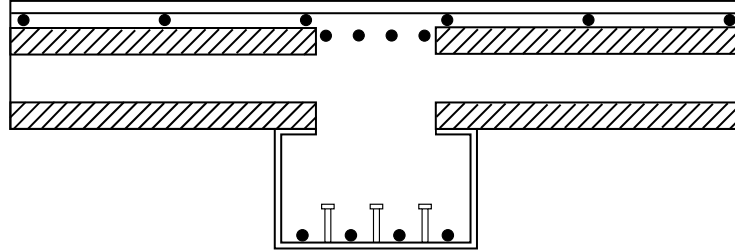


Figure 2.33 – Cross-section of the patent concept (Rahimzadeh, 2002)

2.4 Shear connection

2.4.1 Headed stud shear resistance

The shear connection is a key factor that influences the mechanical behaviour of steel-concrete composite structures. Different shear connection type have been reviewed in this chapter by presenting the innovative beam solutions that fulfill some requirements of the thesis. For instance, some solutions where using headed stud (which is the most common shear connection type), concrete dowel (like Deltabeam see § 2.2.5) or even angles connectors (like RCUCB by Zhou et al. (2019)).

In the frame of the thesis, the innovative solution proposed would use headed stud for the shear connection. This was chosen because, in addition to the high ductile behaviour provided, since they are the most common connector they are cheap and well known by the steel constructors, they are used to fabricate composite beam with shear stud welding.

EN 1994-1-1 (2005) proposed to evaluate the design shear resistance of welded headed studs connectors in solid slabs by Equation 2.9.

$$P_{Rd} = \min \left(\frac{0.8f_u\pi d^2/4}{\gamma_v}; \frac{0.29\alpha d^2\sqrt{f_{ck}E_{cm}}}{\gamma_v} \right) \quad (2.9)$$

Where:

$$\alpha = 0.2 \left(\frac{h_{sc}}{d} + 1 \right) \quad \text{for } 3 \leq h_{sc}/d \leq 4$$

$$\alpha = 1 \quad \text{for } h_{sc}/d > 4$$

h_{sc} is the overall nominal height of the stud

d is the diameter of the shank of the stud, $16 \text{ mm} \leq d \leq 25 \text{ mm}$

f_u is the ultimate strength of the stud material but not greater than 500 N/mm^2

γ_v is the partial factor

f_{ck} is the concrete characteristic cylinder compressive strength

E_{cm} is secant modulus of elasticity of concrete

In buildings, for the use of shear stud with steel decking, EN 1994-1-1 (2005) proposed to reduce the design shear resistance (P_{Rd}) previously calculated by Equation 2.9 by reduction factors depending on the orientation of the profiled steel sheeting.

When the profiled steel sheeting is parallel to the beam:

$$k_1 = 0.6 \frac{b_0}{h_p} \left(\frac{h_{sc}}{h_p} - 1 \right) \leq 1.0 \quad (2.10)$$

When the profiled steel sheeting is perpendicular to the beam:

$$k_t = \frac{0.7}{\sqrt{n_r}} \frac{b_0}{h_p} \left(\frac{h_{sc}}{h_p} - 1 \right) \leq 1.0 \quad (2.11)$$

Where:

h_p is the height of the profiled steel sheeting

b_0 is the mean width of a concrete rib or minimum width for re-entrant sheeting profiles

n_r is the number of stud connectors in one rib at a beam intersection, not to exceed 2

However, the welding positions in the steel decking have a significant influence on the shear capacity, even more with deep decking, and new formulations were proposed to take into account these effects by Nellinger, Eggert, Kuhlmann, Odenbreit, and Obiala (2018). The authors carried out push-out tests and ten short-span composite beam tests with small degree of shear connection. They showed that the shear connectors resistance with headed shear studs with new forms of steel decking calculated by the methods of EN 1994-1-1 (2005) might be insufficiently safe.

This confirms that the close environment around the shear stud plays a major role in their mechanical behaviour. In the present thesis project, the headed studs would be welded located at the bottom of the downstand part of an U-shaped section (similarly as for RCUCB developed by Zhou et al. (2019)). It can be considered that the steel side plates are far enough to not reduce the shear capacity and thus the calculation recommended by EN 1994-1-1 (2005) for solid slab could lead to accurate results.

However, the cold-formed plates might not be sufficiently thick and the connector location would be in tension zone due to simple bending. That is why these two points are investigated through the following literature review.

2.4.2 Connection in tension zone

In the thesis project, due to fabrication constraints and the innovative design of the steel beam section, the connection of the composite beam between the steel and the concrete is in the lower part of the section. In this case, in positive bending moment, the concrete surrounding the shear connectors will be subjected to tensile forces. This could cause micro-cracks around the shear connectors and affect the connection strength. In this section, different works related to the connection in tension zone are described in order to propose an adequate connection for the project.

According to Fabbrocino and Pecce (2000), experimental tests of steel-concrete composite beams under negative bending are very few, therefore the authors carried out three-point bending tests on a reversed composite beam to obtain information about the efficiency of shear connection when the slab is under tension (see Figure 2.34). Three specimens were tested with a span of 3610 mm. The steel beams were all identical, it was HEB180 profile, classify as a compact section (Class 1) according to EN 1993-1-1 (2005) and therefore the steel beams can reach full plastic moment and a good rotation capacity. Web stiffeners were welded on the steel beams under the support and the load introduction. Only the arrangement of the headed shear studs were varied on three types of beams:

- Type A had 20 shear studs on a single row uniformly distributed along the beam (spacing of 190 mm)
- Type B had 20 shear studs concentrated at the ends of the beam on two rows (same spacing of 190 mm)
- Type C had 8 shear studs on a single row uniformly distributed along the beam (spacing of 515 mm)

Type A and Type B have the same degree of connection whereas type C is in partial shear connection. For type A and B, the tests were stopped due to local buckling of the steel beam. For type C the load decreased abruptly at the end corresponding to fracture of the headed studs and a failure of the composite connection. The authors used the ductility factor (μ) and found a ductility factor around $\mu \approx 10 - 11$ for type A and B and $\mu = 6$ for type C (in partial shear connection). The three type of beams showed a ductile behaviour, for composite beam in positive bending the ductility factor is $\mu \approx 5$.

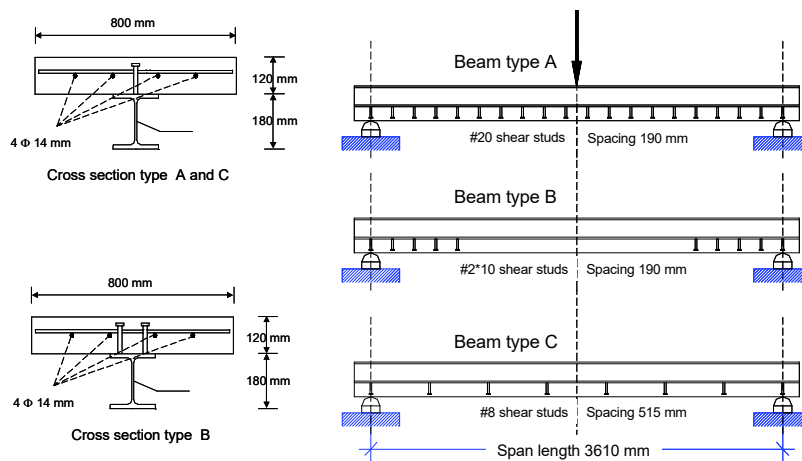


Figure 2.34 – Beam specimens tested by Fabbrocino and Pecce (2000)

Nie, Fan, and Cai (2004) also carried out bending tests on three specimens (SB6 to SB8) under negative bending. This time, it was four-point bending tests, the beam were not reversed, the hydraulic jack was pushing the composite beam up. The authors varied the area of reinforcement bars (A_r) installed in the composite slab and the degree of shear connection. All the specimens showed a large plateau after the yielding of steel and reinforcement indicating a great ductile behaviour. The specimen with the highest area of longitudinal reinforcement (SB8) exhibited the highest failure load but with a reduced ductility. The reason behind is that the compressive height of the steel beam in negative bending increase with the increase of reinforcement and thus the steel beam buckle earlier.

Loh, Uy, and Bradford (2004a,b) investigated the behaviour of composite beam in partial shear connection subjected to hogging moment (negative bending). The authors underlined that partial shear connection in building in hogging moment regions is not permitted by EN 1994-1-1 (2005). This is due to a potential reduction in strength of the surrounding concrete subjected to tensile force in negative bending. However, "**no evidence of a reduced strength in the connectors was found, albeit the concrete was severely cracked**" (Loh et al., 2004a). The authors indicate that the presence of a confining compressive stress on the concrete located at the base of the stud can avoid any reduction of the connector resistance due to concrete cracking.

The authors conducted negative bending tests on 8 composite specimens with composite slab. The main parameters investigated were the degree of shear connection, the reinforcement ratio and the effect of repeated loading. The composite beam specimens were reversed, the test were three-point bending with a span of 2.5 m, the load was applied on the bottom flange of the steel beam. Two modes of failure were obtained; local buckling of the steel beam or fracture of the shear connectors. The beam specimens with the higher degree of shear connection and higher amount of reinforcement had local buckling failure of the steel beam limiting the ductility of the composite beam. The beam with a low degree of shear connection were subjected to connector failure but were able to achieved significant ductility and a higher rotation capacity. The load-deflection responses of three specimens CB1, CB2 and CB3 with a degree of shear connection of 83%, 50% and 33% respectively is represented in Figure 2.35. It can be seen that specimens with a higher degree of shear connection were able to exhibit a higher moment resistance but with a reduced ductility.

Finally, **the shear connectors placed in concrete subjected to tension did not shown any reduction in resistance.** Although the concrete was severely cracked due to negative bending, Loh et al. (2004a) indicated that the reinforcement were yielded and able to transfer considerable tensile force even in partial shear connection.

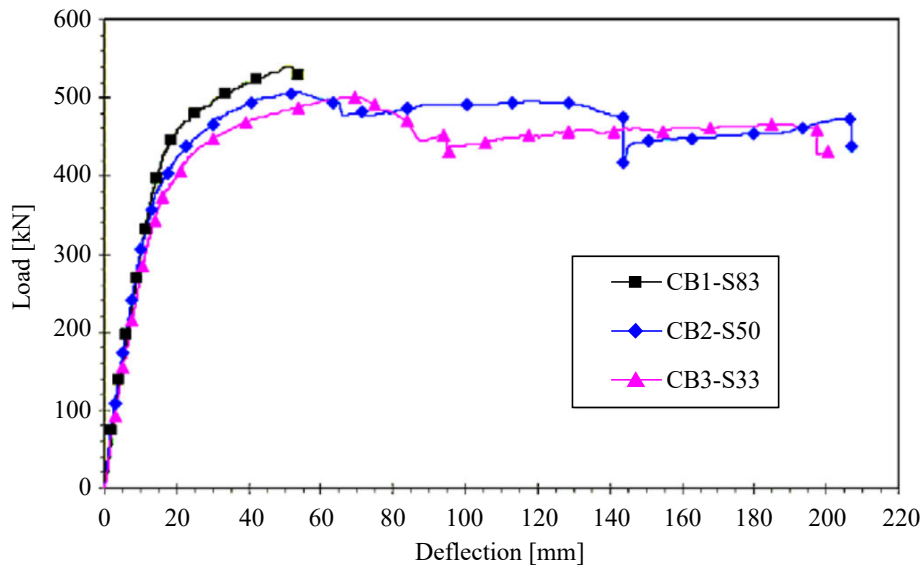


Figure 2.35 – Load-deflection response of beams CB1 to CB3 (Loh et al., 2004a)

2.4.3 The minimum plate thickness for headed stud welded

The developed U-shaped steel beam is made of three parts; two cold-formed side plates (folded in an asymmetric Z-shaped section) and a hot rolled central bottom plate. In order to activate the mechanical composite behaviour of the section, it was decided to use headed studs welded on the hot rolled bottom central plate. This solution gives two advantages. First, the plate located at the extreme fibre of the section would confer a great contribution to the bending resistance of the composite beam. Secondly, the thickness of the central plate can be designed in order to respect the criterion of Goble (1968) to prevent a pull out failure of the welded studs.

In fact, as the use of light steel sections are increasing with the composite beam, Goble (1968) carried out push-out tests on 41 specimens in order to find a minimum plate thickness for headed stud welded and solicited in shear. The tests were conducted in the structural laboratory of Case Western Reserve University at Cleveland, United states. The following results are all taken from the paper of Goble (1968), only the units were converted into the International System of Units (SI).

Goble (1968) tested three diameters of headed shear studs ($d_{sc} = 13$ mm, 16 mm and 19 mm) welded on different flanges thickness (from $t_f = 3.3$ mm to 11.2 mm). The author underlined with this experimental program that if a very thin steel flange is used, the risk is to obtain a failure mode characterized by the pull-out of the connector from the steel flanges. The pull-out failure of the connector leads to a reduction in the ultimate failure load of the connection as shown in Figure 2.36. For each stud diameter, if the flanges were sufficiently thick, the ultimate loads of the push-out tests were almost constant and limited by the shear failure of the studs. However, if the flanges were not thick enough, the ultimate load decreased following the reduction of the thickness (see Figure 2.36).

The author expressed the nominal stud shear stress at failure against the ratio of the stud diameter on the flange thickness of the 41 specimens results (see Figure 2.37). A limit where the failure shift between the shear failure to the pull-out failure was identified at a ratio $d_{sc}/t_f = 2.7$. The author underlined that this limit is dependent on the material strengths used for the test. Even if the test were carried out in 1968, the materials strength used were com-

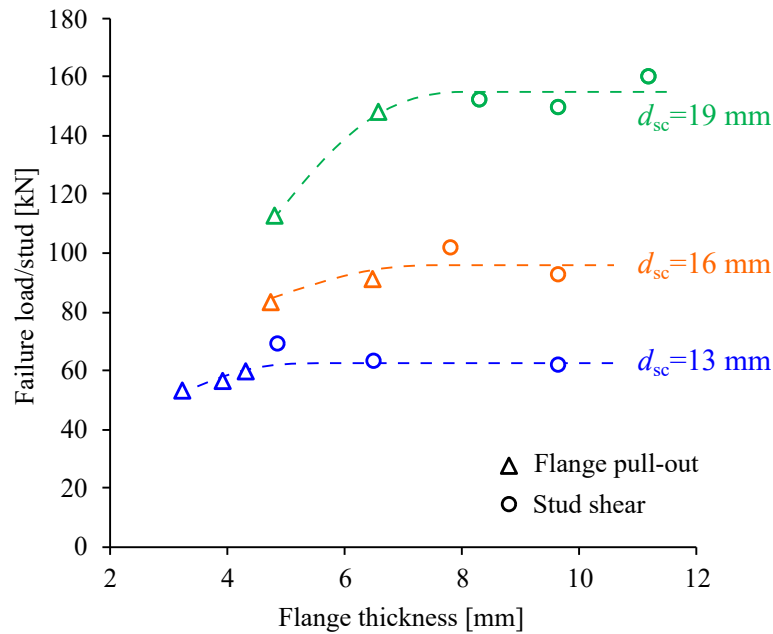


Figure 2.36 – Failure load versus flange thickness Goble (1968)

prised between $f_y = 248$ to 438 MPa for the yield strength and between $f_u = 308$ to 531 MPa for the ultimate strength which is still in accordance with modern steel. This confirms that the criterion is still in accordance with modern design.

For instance, based on the work of Goble (1968), according to AISC 360-16 (2016) § 18.1 and EN 1994-1-1 (2005) § 6.6.5.7(5), when the headed studs are not welded over the web, the diameters of the steel headed studs should not be greater than 2.5 times the flange thickness. Indeed, the webs of an I or H-shaped section stiffen the flange and can prevent pull-out failure of the studs but it is not the case for the developed U-shaped section in the thesis project, so this criterion has to be respected. For common headed stud diameter, the minimum thickness is presented in Table 2.2. It can be seen that the standards are slightly on the safe side compared to the recommendations of Goble (1968), this is potentially due to the fact that some points in Figure 2.37 were below the limit and also some failures were a mixed of shear and flange pull-out (called Partial Flange Pull-out).

Table 2.2 – Minimum thickness for common headed stud diameters

Headed stud diameter d_{sc} [mm]	According to Goble (1968) $t_{f,min}$ [mm]	According to the standards ¹ $t_{f,min}$ [mm]
13	4.8	5.2
16	5.9	6.4
19	7.0	7.6
22	8.1	8.8

¹ AISC 360-16 (2016) and EN 1994-1-1 (2005)

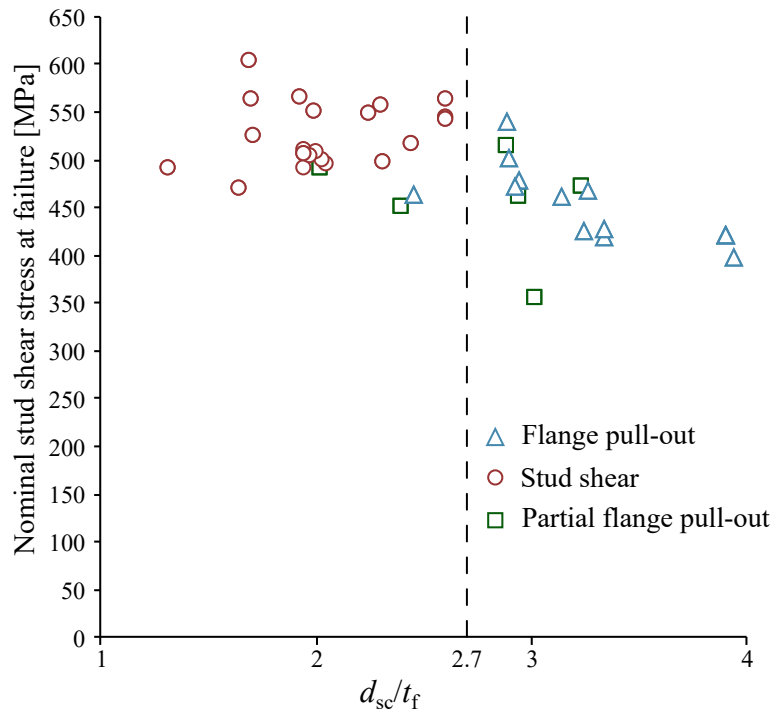


Figure 2.37 – Nominal stud shear stress versus d_{sc}/t_f Goble (1968)

2.5 Conclusion

The objective of this state of the art was to review all the solutions that fulfill some of the requirements of the thesis project in order to propose a guideline for the development of an innovative solution. The solutions were presented with their different advantages and with international research works that have been carried out on them. The modern solutions were classified in two categories:

1. **The integrated beam** : This solution can resist in the construction stage, can be fire resistant without additional protection and provide flat floor but it often used an important amount of steel (very compact section) especially if the solution is designed for the fire situation (see the loading ratio of Mullett (1992))
2. **Formwork steel-concrete composite beams** : This alternative solution can resist in the construction stage and can be fire resistant without additional protection as well but with a downstand part and is often accompanied with heavier loads due to a high quantity of concrete. However, very recent researches (2018/2019) carried out on U-shaped steel-concrete composite beams with very light external cold-formed steel are very interesting for economical aspect. These solutions are taking the most benefits of the reinforced concrete and steel structures and can be the future of building construction more and more using composite materials. This type of solution will be retained for the solution development.

From fabrication constraints, and investigations made by the authors on the U-shaped steel-concrete composite beam it was decided to use headed studs to ensure the shear connection of the composite beam. The state of the art on the researches made on the shear connection resistance in tension zone and on the minimum plate thickness to avoid pull-out failure lead to a specific solution design.

In fact, the use of cold-formed thin plates for the U-shaped steel beam limit the welding of shear connectors. Therefore it was decided to locally use a thicker plate assembled with two cold-formed side plates. The thicker plate will be the bottom of U-shaped section, this allows the possibility of forming the U-shaped beam in two parts leading to higher beams. The state of the art of the shear connection in tension zone (see § 2.4.2) allows the assumption of an effective connection at this location. Indeed, although the concrete was severely cracked in negative bending, the authors found out that the shear connectors, placed in the concrete subjected to tension, did not exhibited any reduction in strength and were able to transfer the shear forces to the rebars. Additionally, the highest amount of steel (due to this thicker plate) would be located at the extreme fiber of the section leading to the highest lever arm with the concrete in compression. Therefore the contribution of the thicker plate to the bending resistance of the composite beam would be very efficient. A schematic representation of the developed solution is represented in Figure 2.38.

Experimental, numerical and analytical investigations of the proposed solution were carried out and are presented in the following chapters.

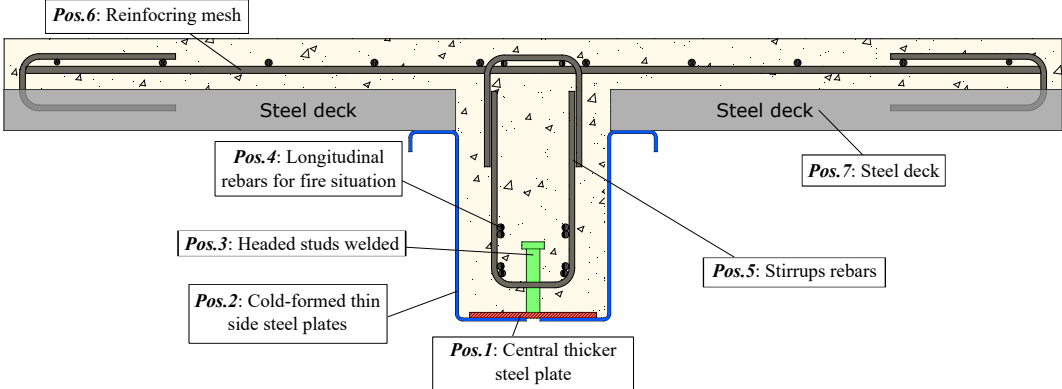


Figure 2.38 – Schematic cross-section of the developed solution

Chapter 3

Analytical and numerical studies of the flexural behaviour in the fire situation

Contents

3.1 Objectives of this study	68
3.2 Fire design in building	68
3.2.1 Definition of a fire	68
3.2.2 The European fire classification of structural elements	69
3.2.3 Methods of analysis in fire safety engineering	69
3.3 Partial safety factors	70
3.4 Combination of actions	70
3.5 Materials characteristics	70
3.6 Parameters of the study	71
3.7 Configuration of longitudinal rebars	72
3.8 Loading	72
3.8.1 Permanent loads	72
3.8.2 Live loads	73
3.9 Analytical evaluation of the fire resistance of the reinforced concrete part	74
3.9.1 Design procedure	74
3.9.2 Evaluation of the internal moment	75
3.9.3 Moment resistance of the reinforced concrete section	75
3.9.4 Required height of the downstand beam for the flexural resistance	76
3.9.5 Results example	77
3.10 Numerical simulations of the thermo-mechanical behaviour of the reinforced concrete part	80
3.10.1 Thermal analysis	80
3.10.2 Mechanical analysis with the heated section	83
3.10.3 Results comparison	85
3.11 Conclusions	85

3.1 Objectives of this study

One of the main objectives of the thesis project is to find a fire resistant composite solution for buildings without any additional protection (like intumescent paint). After investigating different propositions of design, the retained solution was a steel formwork beam supporting a reinforced concrete part inspired by the reviewed solutions in the chapter “State of the art” § 2.3. The reinforced concrete part is the only resisting part of the composite beam in the fire situation.

The first developments carried out in the frame of the thesis were to find the geometrical proportions of the reinforced concrete solution, in particular, the height of the downstand beam under the slab and the amount of longitudinal rebars. Numerical and analytical investigations, presented in this chapter, were performed on the reinforced concrete part subject to ISO fire defined by the curve ISO834 as presented in § 3.2.1.

3.2 Fire design in building

3.2.1 Definition of a fire

A fire is a physical phenomenon induced by the combination of heat, fuel and an oxidizing agent (the fire triangle). A confined fire that takes place in a compartment of a building can be characterised by three steps according to Purkiss (2007):

1. The “Pre-flashover” period is the initial phase where the fire is local and a part of the fuels present in the compartment burns. The increase of temperature is local and the average temperature of the compartment is low. Often, the starting fire does not get beyond this step because of a lack of fuel in the compartment or a lack of oxidizing agent. However, when those ingredients are in a sufficient quantity, the fire can spread throughout the compartment. The human activity is often responsible of this spread by inserting oxygen with the opening of a windows or a door. Then flashover occurs when the fire is extended to all the compartment and the combustibles gases are at high temperature.
2. The “Post-flashover” period is characterised by a fast rise of temperature until a peak that can be over 1000 °C. The structural elements are subjected to the worst thermal actions.
3. The “decay” period is, after the peak, the decreasing of temperature as the rate of fuel combustion decreases. Because of thermal inertia, the temperature stays at a level far from ambient temperature during a certain amount of time.

A standard curve to represent the evolution over time of the gas temperature in the fire compartment, in case of fully developed fire, is proposed by EN 1991-1-2 (2002). This temperature-time curve is taken from the ISO 834 standard. This standard curve is given by Equation 3.1.

$$\theta_g = 20 + 345 \log_{10}(8t + 1) \quad (3.1)$$

Where θ_g is the gas temperature in °C and t is the time in minutes.

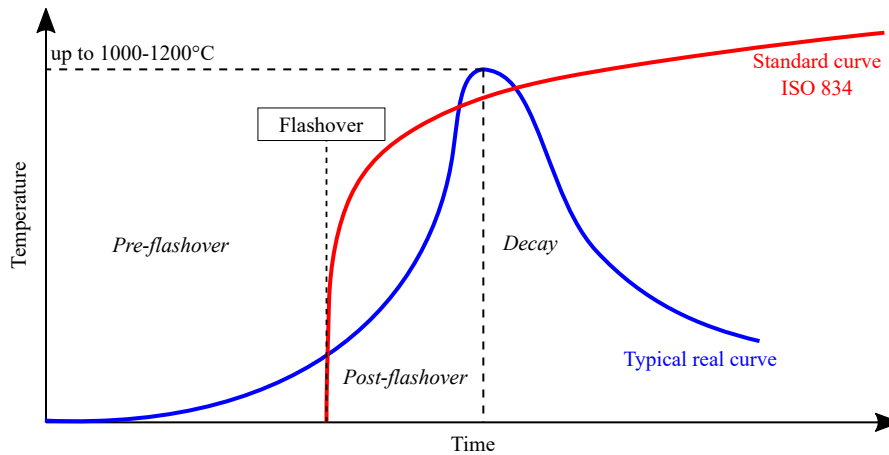


Figure 3.1 – Comparison between a standard (ISO 834) and a “typical” real fire

The standard and a “typical” real fire curves are compared in Figure 3.1. It shows that the standard curve ignores the “pre-flashover” and the “decay” phases. The standard curve is characterised by a really fast rise of the gas’ temperature and keeps on increasing with the time. Although sometimes the “real” fire causes an elevation of temperature higher than the standard curve, this curve is still conservative by its instant high rise of temperature and with its infinite growth without cooling.

3.2.2 The European fire classification of structural elements

For buildings, the regulation of European countries impose steps to prevent from the apparition of a fire, to limit its propagation and its effect, to protect and evacuate the people and to allow the intervention of the rescue services. These objectives depend on the category of buildings defined by the regulation of the country. The engineer has to take into account all the requirement of the regulation for its building’s project. For the structural elements, they are classified by the European fire standards with three performance criteria:

- (R) The load bearing capacity of the element against fire action without losing its structural ability.
- (E) The integrity of the element to prevent transmission of flames and hot gas from a compartment to another.
- (I) The insulation of the element to limit the propagation of high temperature from a compartment to another (the temperature of the cold face as to be inferior to 140 °C).

The classification of the structural element is expressed with these letters followed by the time (in minutes); the element satisfies the criteria on the standard curve (ISO 834). For example, a composite floor with steel decking can be classified REI90, that means the floor withstands accidental loads and isolates the compartment where the fire started from the rest of the structure for 90 minutes ($\approx 1000^{\circ}\text{C}$ on ISO 834 curve). Steel structures without protection are able to resist, in average, 15 minutes, the elements are then classified R15.

3.2.3 Methods of analysis in fire safety engineering

Since the standard curves are not supposed to represent a real fire, the fire safety engineering allows the user to optimise its structure with other fire design methods, because of various

scenarios and advanced calculation model methods. These methods are taking more time and investigations but compared to the gain of material it can be economic.

3.3 Partial safety factors

According to EN 1992-1-2 (2005), for the fire situation, the partial safety factor for all the composite material are fixed to $\gamma_{M,fi} = 1.0$.

3.4 Combination of actions

According to EN 1990 (2003), the combination of actions for the fire situation considered as an Accidental Limit State (ALS) is defined by Equation 3.2.

$$E_{fi} = \sum_{j \geq 1} G_{k,j} + \psi_1 Q_{k,1} \quad (3.2)$$

Where :

$G_{k,j}$ is the characteristic value of permanent action j

$Q_{k,1}$ is the characteristic value of the leading variable action 1¹

ψ_1 is the factor for frequent value of a variable action depending on the building category (see Table 3.1)

Table 3.1 – Recommended values of ψ_1 depending on the building category (EN 1990, 2003)

Building category	ψ_1
Category A: domestic, residential areas	0.5
Category B: office areas	0.5
Category C: congregation areas	0.7
Category D: shopping areas	0.7
Category E: storage areas	0.9
Category F: traffic area, vehicle weight ≤ 30 kN	0.7
Category F: traffic area, vehicle weight ≤ 160 kN	0.5
Category H: roofs	0.0

3.5 Materials characteristics

For the concrete, the characteristic compressive strength of concrete at 28 days is $f_{ck} = 30$ MPa (C30/37) and its volumetric mass density is $\rho_c = 2500$ kg/m³. For the steel, the characteristic yield strength of reinforcement is $f_{yk} = 500$ MPa and its volumetric mass density is $\rho_a = 7850$ kg/m³.

¹In this case study, the characteristic value of the leading variable action Q_k is always the imposed load in buildings depending on the category according to EN 1991-1-1 (2003)

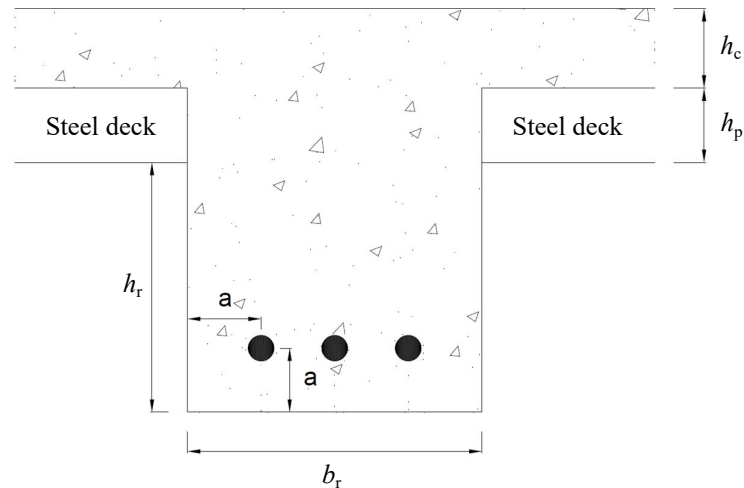


Figure 3.2 – Cross-section of the reinforced concrete part studied

3.6 Parameters of the study

In the fire situation, the section resistance is ensured by the reinforced concrete part as represented in Figure 3.2. **The parameters which are not followed by constant values were variants in the study.**

The composite slab is made with steel decks (Cofraplus60) perpendicular to the beam studied, with the following parameters:

b_{slab} : width of the slab

h_c : height of the concrete on top of the steel decks ($h_c = 62 \text{ mm}$)

h_p : height of the steel deck ribs ($h_p = 58 \text{ mm}$)

e_0 : space between the steel deck ribs ($e_0 = 207 \text{ mm}$)

b_1 : minimum width of the steel deck ribs ($b_1 = 62 \text{ mm}$)

b_2 : maximum width of the steel deck ribs ($b_2 = 101 \text{ mm}$)

b_0 : average width of the steel deck ribs ($b_0 = \frac{b_1+b_2}{2} = 81.5 \text{ mm}$)

t_d : nominal thickness of the steel deck ribs: ($t_d = 0.75 \text{ mm}$)

Γ_d : weight of the steel decks: ($\Gamma_d = 8.53 \text{ daN/m}^2$)

The downstand reinforced concrete beam studied has the following geometrical parameters:

b_r : width of the downstand RC beam

h_r : height of the downstand RC beam

a : average distance from the centre of the rebars to the closest edge

The study covers a variation of the frame of the floor between:

- The space between the adjacent beams: $1.5 \text{ m} \leq e \leq 3 \text{ m}$
- The span of the beam: $5 \text{ m} \leq l \leq 20 \text{ m}$

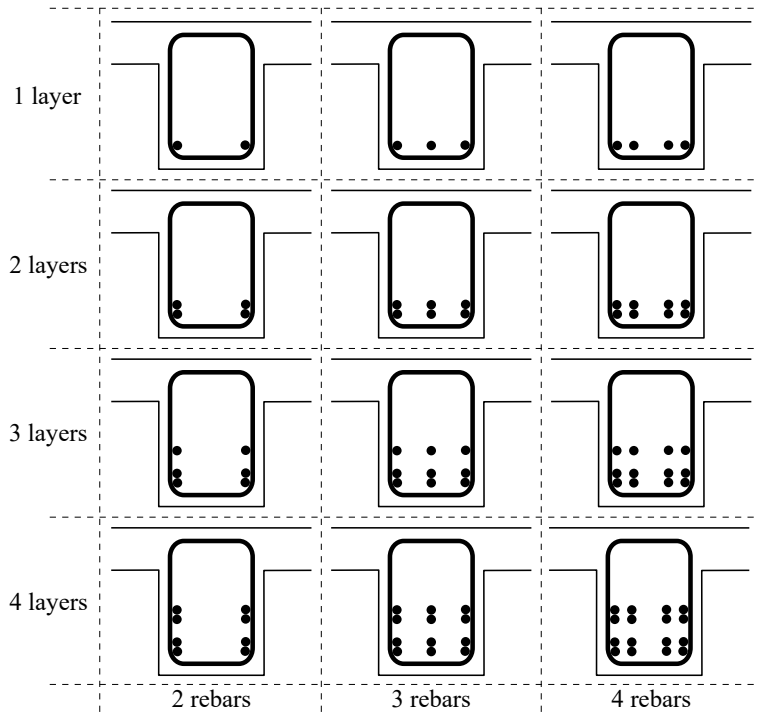


Figure 3.3 – Scheme of the possible arrangements of rebars studied

3.7 Configuration of longitudinal rebars

In this study, different arrangements of rebars are considered as shown in Figure 3.3. The longitudinal rebars at the bottom of the downstand beam varies from HA8 to HA32. The arrangement can vary from 1 to 4 layers and with 2 to 4 rebars per layers. For each arrangement, the area (A_s) and the centre of gravity from the bottom fibre of the section ($z_{g,s}$) are calculated. The concrete covers and the spacings of rebars are respecting the recommendations of EN 1992-1-1 (2005).

3.8 Loading

3.8.1 Permanent loads

The permanent loads are defined by the self-weight of the structural elements and an additional load for non-structural permanent element (like flooring):

- concrete slab: $g_{1,c,slab} = \rho_c \times h_c \times b_{slab}$
- concrete inside the steel decks: $g_{1,c,deck} = \rho_c \times \frac{h_p b_0}{e_0} \times (b_{slab} - b_r)$
- concrete between the steel decks: $g_{1,c,btw} = \rho_c \times h_p \times b_r$
- concrete downstand beam: $g_{1,c,r} = \rho_c \times h_r \times b_r$
- steel decks: $g_{1,d} = \Gamma_d \times (b_{slab} - b_r)$
- U-shaped steel beam: $g_{1,a} = \rho_a \times 2 \times t_c \times (b_{sup} + h_r + b_r/2)^*$
- non-structural element: $g_2 = 1.5 \times e$

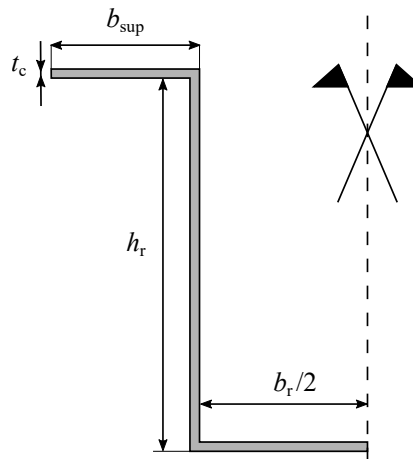


Figure 3.4 – Approximation of the U-shaped cross-section

(*) : The dimensions of the U-shaped steel beam are dependent on the height and width of the downstand concrete part. For this study, in order to simplify the calculation of the load $g_{1,a}$, the U-shaped cross-section is approximated as shown in Figure 3.4.

3.8.2 Live loads

The live load is the imposed load depending on the category of the building according to EN 1991-1-1 (2003):

– imposed load: $q_1 = 1.5 \times q_k$

Where q_k is the surface load depending on the building category proposed in Table 3.2 according to EN 1991-1-1 (2003) and the French National Annex NF P 06-111-2 (2004).

Table 3.2 – Imposed loads for floors depending on the building category (NF P 06-111-2, 2004)

Categories of loaded areas	q_k [kN/m ²]
Category A (floors)	1.5
Category B	2.5
Category C	
– C1	2.5
– C2	4.0
– C3	4.0
– C4	5.0
– C5	5.0
Category D	5.0
Category E1	7.5
Category F (PTAC \leq 30 kN)	2.3

3.9 Analytical evaluation of the fire resistance of the reinforced concrete part

3.9.1 Design procedure

The beam is considered simply supported. The design method follows the tabulated data method proposed in EN 1992-1-2 (2005), the bending resistance must verify the Equations 3.3 and 3.4.

$$\frac{M_{\text{Ed,fi}}}{M_{\text{Rd,fi}}} \leq 1.0 \quad (3.3)$$

$$M_{\text{Ed,fi}} \leq 0.7M_{\text{Ed,ULS}} \quad (3.4)$$

Where :

$M_{\text{Ed,fi}}$ is the internal moment in the fire situation obtained by the ALS combination (see Equation 3.2)

$M_{\text{Rd,fi}}$ is the moment resistance of the section in the fire situation considering a critical temperature of 500 °C applied on the steel longitudinal rebars which correspond to a reduction of the yield strength (f_{sk}) of 40%. The moment is also determined with partial safety factors in the fire situation (see § 3.3)

$M_{\text{Ed,ULS}}$ is the internal moment obtained by the ULS combination

Furthermore, the downstand width (b_r) and the distances of the rebars from the edges (a) have to be compatible with this assumption of a critical temperature of 500 °C in the rebars. In order to do so, depending on the time of fire exposure, minimum geometrical arrangements are proposed in EN 1992-1-2 (2005) and shown in Table 3.3.

Table 3.3 – Minimum width (b_r) and covering distances (a) according to Table 5.5 (EN 1992-1-2, 2005)

Standard fire resistance	Minimum dimensions [mm]		Possible combinations of a and b_{min}		
	b_{min}	a			
R30	b_{min}	80	120	160	200
	a	25	20	15	15
R60	b_{min}	120	160	200	300
	a	40	35	30	25
R90	b_{min}	150	200	300	400
	a	55	45	40	35
R120	b_{min}	200	240	300	500
	a	65	60	55	50

The width of the downstand beam (b_r) is determined by taking into account the diameters of the rebars used, the diameters of the stirrups, the required horizontal space between them at ambient temperature, the minimum width (b_{\min}) and the minimum distance from the edges (a) as requested by Table 5.5 of EN 1992-1-2 (2005) (see Table 3.3).

The height of the downstand beam (h_r) is obtained by calculating the height necessary between the concrete in compression and the longitudinal steel rebars in tension for equilibrating the internal moment (see § 3.9.4). In addition to this, the height must be sufficient for the diameters of the rebars used, the diameter of the stirrups, the required vertical space between them at ambient temperature and the minimum distance from the edges (a) as requested by Table 5.5 of EN 1992-1-2 (2005) (see Table 3.3).

3.9.2 Evaluation of the internal moment

The loads are combined as related in § 3.4:

$$p_{fi} = g_1 + g_2 + \psi_1 q_1 \quad (3.5)$$

The internal moment of the simply supported beam is then obtained by:

$$M_{Ed,fi} = \frac{p_{fi} l^2}{8} \quad (3.6)$$

3.9.3 Moment resistance of the reinforced concrete section

The section resistance is evaluated by considering that the downstand beam and the slab are forming a T-shaped section. The height of the flange of the T-shaped section is h_c , the contribution of the concrete in the steel decks is neglected. In the fire situation, under positive bending moment, a part of the flange of the T-shaped section is in compression and the longitudinal rebars are in tension.

Assuming that the stress distribution in the concrete is rectangular instead of parabolic, the resultant design value of the compressive normal force in the concrete flange is:

$$F_c = 0.8 b_{eff} x_{fi} f_{cd,i} \quad (3.7)$$

Where :

b_{eff} is the effective width of the concrete flange of the T-shaped section

x_{fi} is the height of the concrete subject to compression force

The effective width is determined according to § 5.3.2.1 in EN 1992-1-1 (2005) :

$$b_{eff} = \sum_i b_{eff,i} + b_r \leq b_{slab} \quad (3.8)$$

Where:

$b_{eff,i} = 0.2b_i + 0.1l_0 \leq 0.2l_0$ (l_0 : the distance between points of zero moment, here $l_0 = l$)

Finally :

$$b_{eff} = 2 \times \min \left[0.2 \frac{b_{slab} - b_r}{2} + 0.1l; 0.2l; \frac{b_{slab} - b_r}{2} \right] + b_r \quad (3.9)$$

In order to determine the height of the concrete in compression (x_{fi}), the equilibrium between tension and compression is made:

$$F_c = F_{s,fi} \quad (3.10)$$

Where $F_{s,fi}$ represents the maximum resistance in tension of the heated longitudinal rebars, in the fire situation, expressed by :

$$F_{s,fi} = \frac{k_{y,\theta} A_s f_{yk}}{\gamma_{s,fi}} \quad (3.11)$$

Where :

$k_{y,\theta}$ is the reduction coefficient taking into account the heated rebars, in the study $k_{y,\theta} = 0.6$ for $\theta = 500^\circ\text{C}$

A_s is the area of longitudinal reinforcements bars

f_{yk} is the characteristic yield strength of reinforcement, here $f_{yk} = 500\text{MPa}$

$\gamma_{s,fi}$ is the partial safety factor in the fire situation for the rebars, here $\gamma_{s,fi} = 1.0$

The compressive height of the concrete is then expressed by:

$$x_{fi} = \frac{A_s k_{y,\theta} f_{yk}}{0.8 b_{eff} f_{ck,i}} \frac{\gamma_{c,fi}}{\gamma_{s,fi}} \leq h_c \quad (3.12)$$

The resistance moment of the concrete section can be expressed by :

$$M_{Rd,fi} = F_{s,fi} \times z_{fi} \quad (3.13)$$

Where z_{fi} is the lever arm between the two resultants $F_{s,fi}$ and $F_{c,fi}$.

3.9.4 Required height of the downstand beam for the flexural resistance

From the previous analytical expressions it is possible to find the minimum height of the downstand beam in order to justify the resistance of the section in the fire situation:

$$M_{Rd,fi} = M_{Ed,fi} \quad (3.14)$$

Thus, the height of the reinforced concrete downstand beam can geometrically determined by :

$$h_r = z_{g,s} + z_{fi} + x_{fi}/2 - (h_c + h_p) \quad (3.15)$$

Where $z_{g,s}$ is the vertical position of the gravity centre of the longitudinal rebars from the bottom extreme fibre of the section.

The lever arm (z_{fi}) is directly linked to the internal moment and so to the loading. Some loads depend on the height of the downstand beam (see § 3.8.1). From Equations 3.14 and 3.13, the lever arm (z_{fi}) can be expressed with the loading by:

$$z_{fi} = \frac{p_{fi} l^2}{8 F_{s,fi}} \quad (3.16)$$

As related in § 3.8, p_{fi} can be decomposed in :

$$p_{fi} = p_{cst} + \rho_c \times \mathbf{h}_r \times b_r + \rho_a \times 2 \times t_c \times (b_{sup} + \mathbf{h}_r + b_r/2) \quad (3.17)$$

Where p_{cst} regroups all the loads that are not dependent of the height of the downstand beam.

That means : $p_{cst} = g_{1,c,slab} + g_{1,c,deck} + g_{1,c,btw} + g_{1,d} + g_2 + \psi_1 q_1$

Then the lever arm (z_{fi}) can be expressed by :

$$z_{fi} = \frac{l^2}{8F_{s,fi}} \times (p_{cst} + \rho_c \times \mathbf{h}_r \times b_r + \rho_a \times 2 \times t_c \times (b_{sup} + \mathbf{h}_r + b_r/2)) \quad (3.18)$$

Finally the minimum height of the downstand beam required to equilibrate the internal bending moment in the fire situation due to the ALS loading is obtained by :

$$h_r = \frac{Fz + p_{cst} + 2\rho_a t_c (b_{sup} + b_r/2)}{F - \rho_c b_r - 2\rho_a t_c} \quad (3.19)$$

Where:

$$F = \frac{8F_{s,fi}}{l^2} \text{ [N/m}^2\text{]}$$

$$z = z_{g,s} + x_{fi}/2 - (h_c + h_p) \text{ [m]}$$

3.9.5 Results example

The height of the downstand concrete beam required for the fire situation is analytically obtained by Equation 3.19. An example of a result is shown in this paragraph with the input parameters presented below. The detailed results are presented in Tables 3.4, 3.5 and plotted in Figure 3.5.

Building category	F (car parks)
Standard fire resistance	R90
Spacing between adjacent beams	$e = 2.5 \text{ m}$
Number of rebars layers	2
Number of rebars per layers	3
Combination (a, b_{min})	1

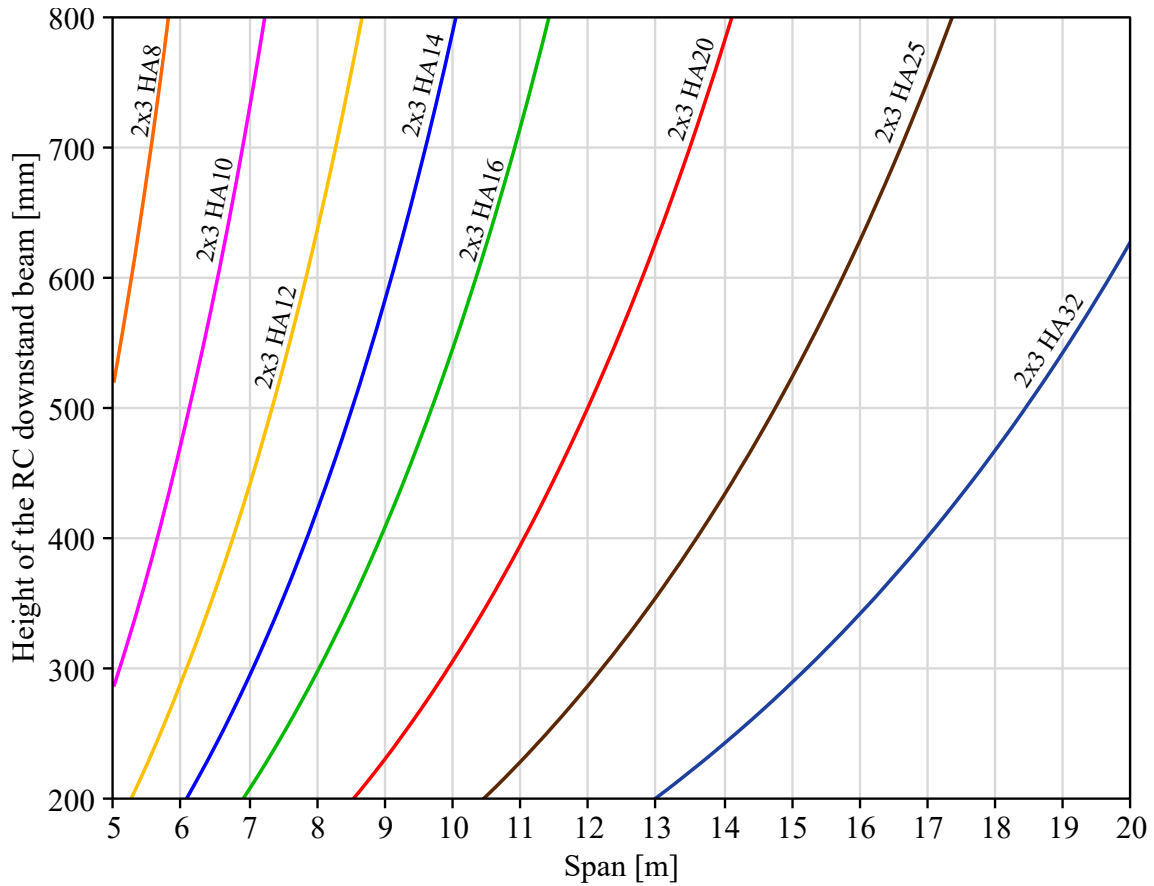


Figure 3.5 – Required RC downstand beam height in the fire situation (R90) depending on the span (Building Cat. F)

Table 3.4 – Detailed results of the example - Part 1

Arrangement :	2x3HA8	2x3HA10	2x3HA12	2x3HA14
A_s [cm ²]	3.02	4.71	6.79	9.23
b_r [mm]	197	204	211	218
$z_{g,s}$ [mm]	57	59	61	64
l [m]	h_r [mm] and ($M_{Rd,fi}$[kN m])			
6	881 (85.4)	474 (75.4)	291 (70.8)	194 (68.3)
8	-	-	638 (141.5)	422 (131.7)
10	-	-	-	789 (233.5)
12	-	-	-	-
14	-	-	-	-
16	-	-	-	-

Table 3.5 – Detailed results of the example - Part 2

Arrangement :	2x3HA16	2x3HA20	2x3HA25	2x3HA32
A_s [cm ²]	12.07	18.85	29.45	48.25
b_r [mm]	226	240	258	283
$z_{g,s}$ [mm]	66	71	77	85
l [m]	h_r [mm] and ($M_{Rd,fi}$[kNm])			
6	135 (66.8)	- -	- -	- -
8	297 (126.0)	168 (119.9)	- -	- -
10	546 (215.9)	306 (198.2)	178 (188.6)	- -
12	- -	502 (308.9)	287 (285.4)	165 (271.9)
14	- -	782 (467.0)	433 (414.5)	244 (385.3)
16	- -	- -	629 (587.3)	343 (528.9)

3.10 Numerical simulations of the thermo-mechanical behaviour of the reinforced concrete part

In order to analyse precisely the flexural behaviour of the RC part subject to fire and to validate or even optimise the results of the analytical study, two numerical analysis were conducted successively :

1. A thermal analysis on the 2D reinforced concrete section subject to fire with the software (ANSYS, 2017)
2. A mechanical analysis on the heated beam with the program SISMEF developed by CTICM

3.10.1 Thermal analysis

As related in § 3.2.1, the “ISO” fire is often conservative and the use of numerical thermal analysis can be relevant for a more realistic fire in order to obtain a more economical solution. However, in this numerical study, the fire situation considered is only defined by the curve ISO834 (see Equation 3.1). Thus, the numerical results will be compared to analytical results obtained by the method proposed in EN 1992-1-2 (2005) for ISO fire. The reinforced concrete part could be optimised by following the same numerical procedure but with more realistic fires depending on the exploitation of the building (this is not considered in the thesis).

For the thermal analysis, only the cross-section of the reinforced concrete beam and the concrete slab are modelled. In fact the contribution of the steel is neglected because, after around 30 minutes, the steel is heated at very high temperature and its resistance is practically null.

However, a particular attention has to be paid in regards to the amount of structural steel used for the formwork steel part. Indeed, during the solution development, for longer span (around 16 meters), a solution was studied with an unprotected I-shaped steel profile underneath the reinforced concrete part. This solution was rejected because due to the high amount of unprotected steel heated at very high temperatures, the deflection of the overall composite beam was increased in the fire situation compared to the same solution without the I-shaped profile underneath. A greater amount of unprotected structural steel can lead to a poorer flexural behaviour in the fire situation. This phenomenon is produced because of bi-material thermal expansion. The coefficient of thermal expansion of the two materials are comparable but the unprotected steel is subjected to much higher temperatures compared to the concrete part, thus the steel part underneath is extended more than the concrete part and tends to bring the overall composite section down. An example illustrating this effect is shown in Figure 3.6, a thermo-mechanical study was carried out on two different sections for a span of 16 meters subjected to an ISO fire during 90 minutes. The first section is a reinforced concrete beam (RC) in the fire situation (as it is the case for the developed solution in the thesis) whereas the second section is a composite solution for high span with an additional I-shaped profile underneath. At an ambient temperature, the solution with the I-shaped profile had a smaller deflection compared to the simple RC beam, this is due to a greater flexural stiffness. However, after 90 minutes of ISO fire exposure, the deflection for the section with the I-shaped profile is greater than the RC section; this is due to the high differential in thermal expansion between the two materials.

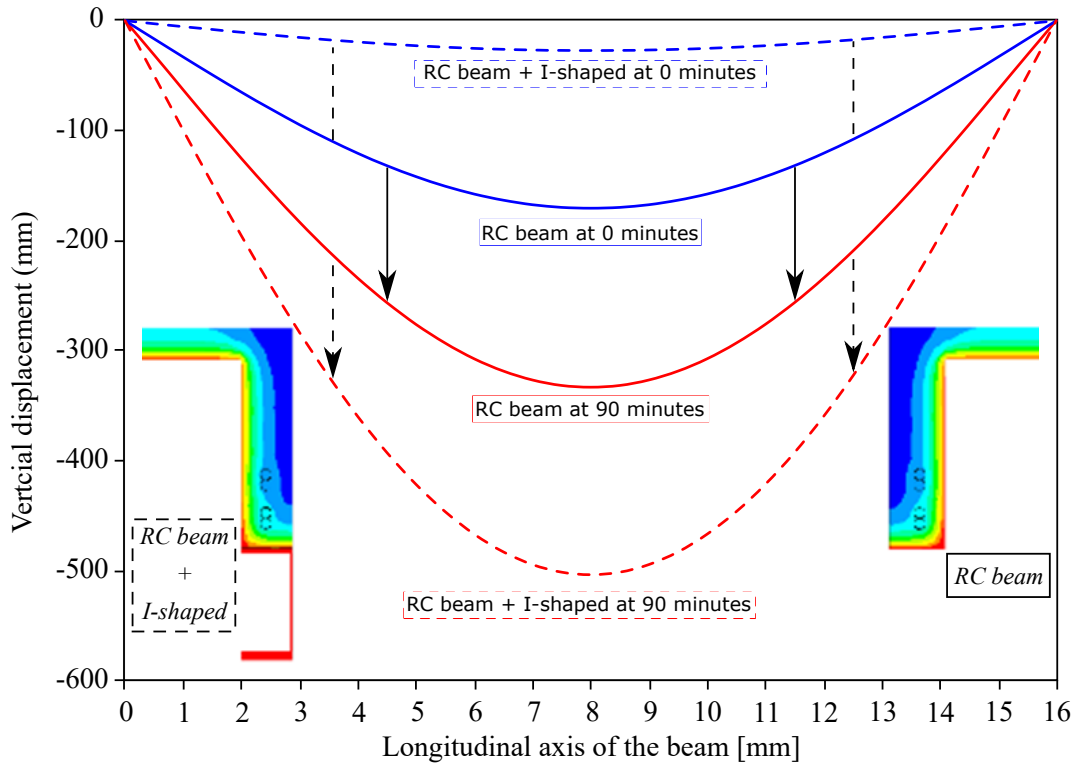


Figure 3.6 – Comparison between two sections highlighting bi-material thermal expansion

Thermal finite element model

For the thermal analysis, the 2D finite element model was created as represented in Figure 3.7. The cross-section of the concrete beam and the concrete slab were modelled by rectangular elements PLANE55 (in purple on Figure 3.7). Due to the circular shape, the longitudinal rebars were modelled by triangular elements PLANE55 (in red on Figure 3.7). These elements are 2D Thermal Solid of ANSYS (2017) defined by three nodes (triangular option) or four nodes with only one degree of freedom, the temperature, at each node.

The temperature is introduced with line elements SURF151 on the external surfaces of the section. These elements are 2D Thermal Surface Effect defined by a line between two nodes and with one extra nodes, away for the element location, used for convection. The temperature, introduced by SURF151 elements, is set to ambient (20 °C) on the top of the concrete slab (the blue line on Figure 3.7) whereas the elevation of temperature, according to ISO834 fire (governed by Equation 3.1), was introduced on the lower side of the model (the red line on Figure 3.7). The steel decks were not modelled and the concrete inside was not considered in the analysis. This assumption is conservative. Every two minutes, the temperatures at the nodes of the section were output in files for the analysis with SISMEF as well as the location of every node of the 2D model.

The three modes of heat transfer (conduction, convection and radiation) are taken into account in this thermal analysis. According to EN 1922-1-2, the emissivity of the concrete surface is taken at 0.7 and the coefficient of convection is taken at 25 W/m²K.

* Extra node for convection

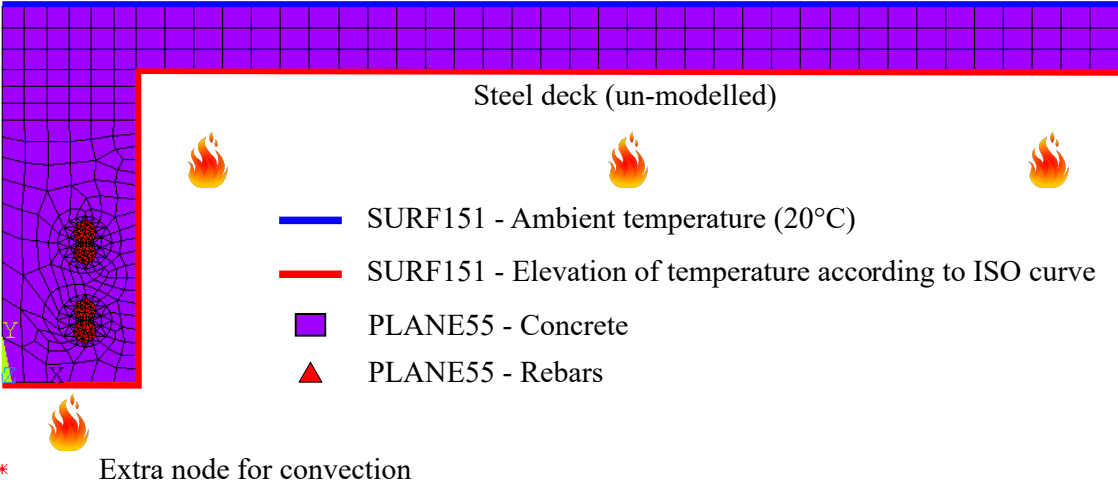


Figure 3.7 – Model 2D for thermal analysis with ANSYS (2017)

Thermal distribution in the section

Every two minutes, the distribution of the temperature is calculated in the section. For example, the distribution after 90 minutes of exposure to ISO fire is represented in Figure 3.8. The temperatures of the concrete near the edges reach around 1000°C. In order to keep the rebars below 350°C, a reinforcement cover of 45 mm is retained for every section of the parametrical study (Figure 3.8). In fact, under 350°C, according to EN 1992-1-2 (2005), for ductile rebars in tension ($\epsilon_{s,fi} \geq 2\%$), the resistance (f_{yk}) is not reduced (see Figure 3.11).

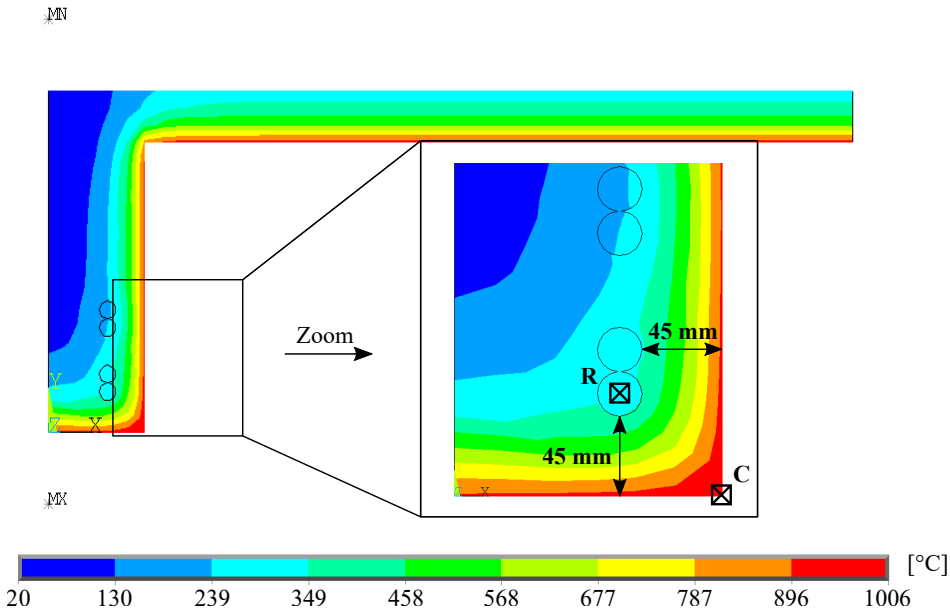


Figure 3.8 – Temperature distribution in the section at 90 minutes of ISO fire

Figure 3.9 below illustrates the evolution of the temperature in the concrete corner that is the most exposed to high temperature (indicated “C” in Figure 3.8) and the evolution of temperature in the middle of the lowest rebars (indicated “R” in Figure 3.8). The graphic underlines that the most exposed rebars stayed below 350°C until 90 minutes of ISO fire.

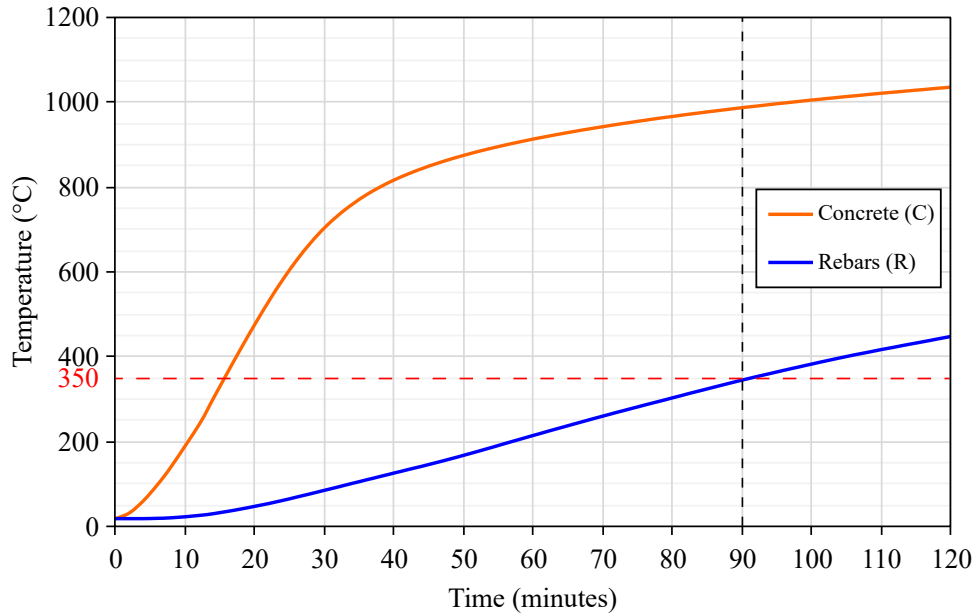


Figure 3.9 – Evolution of the temperature in the concrete and in the rebars during ISO fire

3.10.2 Mechanical analysis with the heated section

The program SISMEF has been developed by CTICM to evaluate the mechanical behaviour of a steel-concrete composite beam or portal frame in large displacement with taking into account the slip at the interface between the two materials.

With the file containing the results of the distribution of the temperature in all the sections studied (every two minutes in this parametrical study) and with the file containing the location of every node of the 2D section modelled with ANSYS (2017), the program is able to calculate the mechanical behaviour of the structure (resisting moment, strains and stresses, displacements).

Every minute, the temperature increases in the different elements thus their characteristic strengths decrease with the time. In order to have an idea of the expected strength at each time, EN 1992-1-2 (2005) gives the strength reduction of concrete and rebars depending on the temperature.

The curves in Figure 3.11 are in accordance with the strength reduction of 40% used in the analytical study for an assumption of 500°C in the rebars : when $\theta = 500^\circ\text{C}$, then $k_s(\theta) = 0.6$). However, in this numerical study, the temperature is now known and the rebars are placed to be subjected, at the end of the exposure time required (like 90 minutes), at 350°C. Thus there should be no reduction in strength for the rebars and this would lead to an increase in bending resistance in the fire situation.

The beam studied is a secondary simply supported beam defined by 33 nodes as shown in Figure 3.12. Each node contains the informations of the 2D thermal model: geometry of the section and the temperature distribution depending on time.

The aim of the numerical study is to compare the bending resistance moment in the fire situation ($M_{Rd,fi}$) with a realistic distribution of the temperature to the ones obtained with the analytical method related in § 3.9.

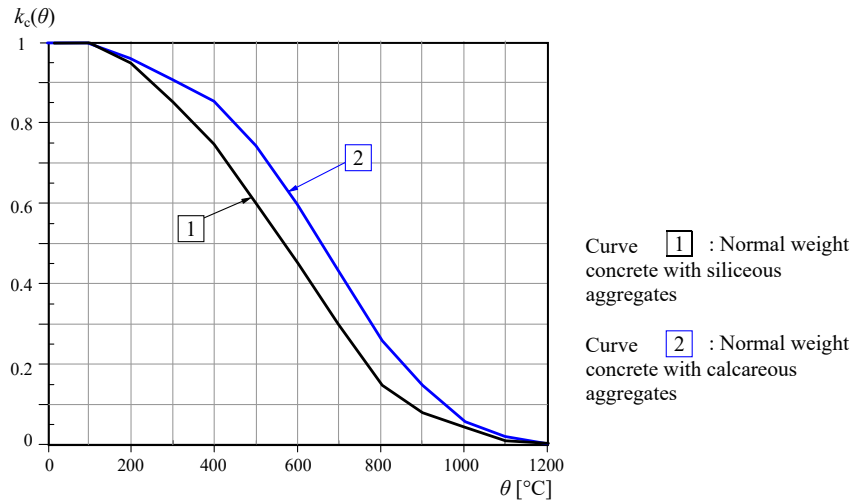


Figure 3.10 – Coefficient $k_c(\theta)$ allowing for decrease of characteristic strength (f_{ck}) of concrete (EN 1992-1-2, 2005)

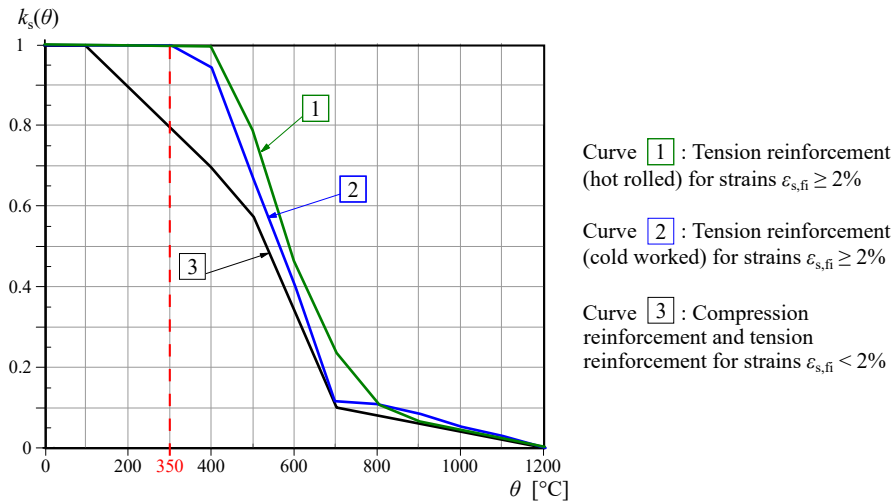


Figure 3.11 – Coefficient $k_s(\theta)$ allowing for decrease of characteristic strength (f_{yk}) of reinforcement (EN 1992-1-2, 2005)

The beam resistances were calculated with the maximum temperature distribution corresponding to the required time of exposure to ISO fire, obtained with the thermal analysis. The evolution of the temperature over time of exposure is not taken into account in this study. Only the heated section after the required time of fire exposure is considered (like in Figure 3.8 for R90).

The heated beam is subjected to a constant bending moment $M_{Ed,fi}$ by applying two opposite moments at both extremities of the beam (see Figure 3.12). The applied moments were increased gradually until the ultimate bending resistance moment ($M_{Rd,fi}$).

Note: During this parametrical study, the vertical displacement is not controlled. During a fire, the deflections of a composite floor is usually limited by the value $d_{lim} = (L + l)/30$ when in a floor grid, L is the span of the primary beam and l is the span of the secondary beam. To limit the deflection during fire, a sufficient second moment of area is needed, that means a short concrete rib with a great amount of reinforcement (ex: 4x2HA 25 + $h_r = 200$ mm) is often exceeding the limit of deflection.

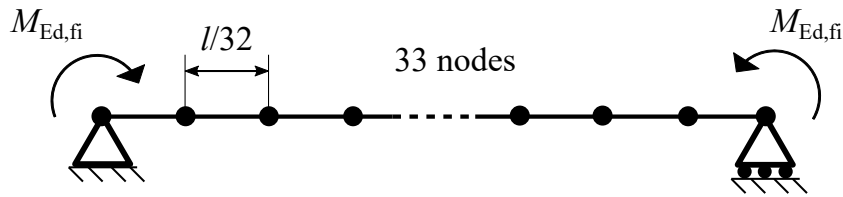


Figure 3.12 – Boundary conditions and loading

3.10.3 Results comparison

The configuration of the example used for the analytical study (see § 3.9.5) is used along with the numerical study. Only the arrangements of rebars is different this time; 2 rebars per layers and the layers varied from 1 to 4. This arrangement of rebars would be recommended for the use of the developed solution. The calculations of the required heights of the RC downstand beams depending on the span for a defined configuration were carried out analytically and numerically with the methods presented in this chapter. Some of the results are shown and compared in Figure 3.13.

Building category	F (car parks)
Standard fire resistance	R90
Spacing between adjacent beams	$e = 2.5$ m
Number of rebars layers	1 to 4
Number of rebars per layers	2

With the same arrangement of rebars, the numerical simulations provided a reduction of the required concrete height of about 40% for each case compared to the analytical study. For the analytical study, a reduction of 40% was applied to the characteristic strength of the rebars (f_{sk}), this was to take into account a critical temperature in the rebars of 500 °C. However, the numerical thermal analysis had shown that if the rebars were placed with a cover of 45 mm from the edges, the temperature after 90 minutes of ISO fire stayed below 350 °C. With this temperature in the rebars, the characteristic strength is not reduced (see Figure 3.11) and this explained the optimisation.

3.11 Conclusions

- The reinforced concrete part of the steel-concrete composite solution, developed in the thesis, is the only part resisting in the fire situation. In fact, numerical thermal simulations underlined that with standard fire, the U-shaped steel section was too heated to participate in the resistance. The required height of the RC downstand beam, in the fire situation, associated to the amount of rebars, is linked to the height of the U-shaped section. So this phase has a strong impact on the final form of the developed solution.
- The height of the RC downstand beam needed for the fire situation can be analytically evaluated according to EN 1992-1-2 (2005). The heights obtained with this method are acceptable for a use of this solution in buildings. The reinforced concrete part is designed for the fire situation in ALS and is not sufficiently resistant for the exploitation stage at ULS. However, in the exploitation stage, the U-shaped steel beam designed for the construction stage will provide the rest of resistance, by composite action.

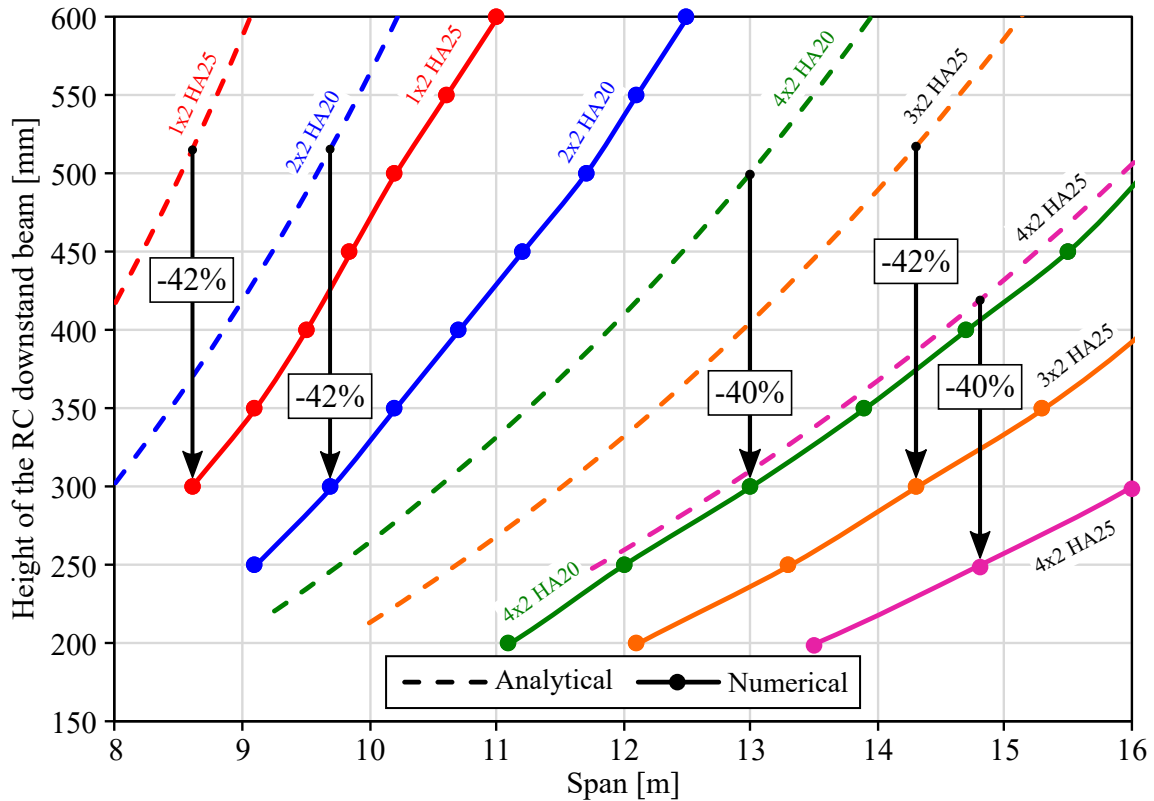


Figure 3.13 – Required RC downstand beam height in the fire situation (R90) depending on the span (Building Cat. F)

- The combined thermal and mechanical numerical simulations are giving a reduced height of RC downstand beam (about 40%). This gain principally comes from the positions of the rebars. In fact, with the thermal simulations, it is possible to place the rebars with sufficient covers and limits the heating of them and then limits the reduction of their characteristic strength. However the combined numerical methods are more complicated and would not be necessary except for a very precise optimisation. For a later use, some abacus for different load levels could be realised. This numerical methods also showed that the analytical method gave conservative results.
- In the development phase of the solution, it was planned to add an unprotected I-shaped steel profile underneath the reinforced concrete downstand part for very high span. The numerical simulations had proved that this idea for high span would not meet the fire requirements due to the too high differential in heating which leads to a terrible increase in the deflection of the overall composite beam in the fire situation. That means the developed solution is suitable for the fire situation as long as the amount of unprotected steel is not too important.

Chapter 4

Conducted steel beam test

Contents

4.1	Objectives of the test	88
4.2	Test specimen	88
4.2.1	Geometry	88
4.2.2	Material	88
4.2.3	Fabrication	91
4.2.4	Imperfections	93
4.3	Layout	97
4.4	Setup	100
4.4.1	Test frame	100
4.4.2	Specific application of the load	100
4.4.3	Supports	103
4.5	Instrumentation	103
4.5.1	Displacement sensors	103
4.5.2	Displacement targets	104
4.5.3	Strain gauges	106
4.6	Test procedure	106
4.7	Test results	107
4.7.1	Observations during the test	107
4.7.2	Equivalent moment	112
4.7.3	Force-displacement of the hydraulic cylinder	112
4.7.4	Cross-section representation by the targets	113
4.7.5	Measurement point on the targets during the test	113
4.7.6	Deformed shape of the section	114
4.7.7	Displacement of the section at mid-span	115
4.7.8	Rotation of the section	119
4.7.9	Strains	119
4.8	Conclusions	122

4.1 Objectives of the test

The U-shaped steel beam withstands the load in the construction stage without any temporary propping system. In the development phase, it appeared that this section type was prone to the global instability of Lateral Torsional buckling (LTB). However, as the beam is not a classic section, the standards (Eurocodes) do not clearly define how to take into account this effect precisely. In fact, the beam is an assembly of cold-formed and hot rolled plates. According to EN 1993, the buckling curve used for the design could be “b” or “d” depending, if the section is considered as a cold-formed section (“b”) or if it classified in “other section” (“d”). Thus, the objective of this test is to underline the LTB instability of the beam and characterize more precisely its mechanical behaviour in the construction stage.

Additionally, the beam is assembled with self-drilling screws instead of welding, the monolithic behaviour of the section would also be investigated by this test.

4.2 Test specimen

4.2.1 Geometry

The specimen tested has the same dimensions of the solution proposed for a normal use with the same span. This means the cross-section geometry of the specimen, associated with the materials characteristics, is optimized as for an industrial use with the same span (6 m). The span of the tested beam at the laboratory was 6 m due to the maximum allowable support spacing of the test frame. The total length was 6.3 m as the beam extended beyond the supports by 150 mm at each side.

The developed U-shaped section is composed of three steel parts; a hot rolled steel plate (180x8x6300 mm, see (1) in Figure 4.1) and two cold-formed steel plates (470x4x6300 mm before folding, see (2, 3) in Figure 4.1). The section was assembled together with four self-drilling screws (S-MD 25 GZ, $\Phi = 5.5$ mm) longitudinally spaced of 150 mm (see (4) in Figure 4.1).

The hot rolled central steel plate forms the bottom of the steel section. The cold-formed steel plates are folded in an asymmetric Z-shaped section with an edge stiffener on their top flanges. These side folded plates constitute the webs and the top flanges of the steel section. In addition, eight steel battens longitudinally spaced of 825 mm connected the top flanges of the section (see (5) in Figure 4.1). These battens prevented the section from excessive distortion and assured, at their locations, the constant spacing between the top flanges.

The beam tested was 270 mm high and 220 mm wide without considering the width of the top flanges or 352 mm in total. The main dimensions of the section are presented in Table 4.1. A representation of the cross-section is shown in Figure 4.1a and its principal mechanical properties are presented in Table 4.2.

4.2.2 Material

For the steel beam, two different steel grades have been used for the central bottom plate and for the folded side plates, respectively S355 and S235. At the ordering, their minimum expected yield strength were $f_{y,hr} = 355$ MPa for the central plate and $f_{y,cf} = 235$ MPa for the side plates. After the test, tensile specimens were cut out in the steel beam according

Table 4.1 – Main dimensions of the cross-section specimen

Designation	Symbol	Values
Hot rolled central plate (1)		
- Thickness	t_{hr}	8 mm
- Width	b_{hr}	180 mm
- Steel grade	S355	
- Mean measured yield strength	$f_{y,hr,m}$	417 MPa
- Mean measured tensile strength	$f_{u,hr,m}$	558 MPa
Cold-formed side plates (2, 3)		
- Thickness	t_{cf}	4 mm
- Top flanges width	$b_{cf,top}$	70 mm
- Webs height	$h_{cf,w}$	270 mm
- Bottom flanges width	$b_{cf,inf}$	100 mm
- Edge stiffeners height	c_{cf}	30 mm
- Steel grade	S235	
- Mean measured yield strength	$f_{y,cf,m}$	322 MPa
- Mean measured tensile strength	$f_{u,cf,m}$	406 MPa
Steel battens (5)		
- Thickness	t_{bat}	4 mm
- Width	b_{bat}	30 mm
- Length	l_{bat}	320 mm

Table 4.2 – Principal mechanical properties of the gross cross-section specimen

Definition	Symbol	Value	Units
Total area of the section	A	50.2	cm ²
Vertical position of the gravity centre (G) in yOz	z_G	96.4	mm
Second moment of area /GY (major axis)	I_y	5325	cm ⁴
Second moment of area /GZ (minor axis)	I_z	4809	cm ⁴
Section modulus upper fibre (Z+) /GY	$W_{el,y,sup}$	306.8	cm ³
Section modulus bottom fibre (Z-) /GY	$W_{el,y,inf}$	552.3	cm ³
Vertical position of the shear centre (S) in yGz	z_S	-191.1	mm
Torsion constant	I_t	10.50	cm ⁴
Warping constant	I_ω	289 151	cm ⁶

to the ISO standard for tensile testing for metal (EN ISO 6892-1, 2016) in order to measure their yield and ultimate strengths. For the cold-formed side plates, nine coupons were cut out in the beam, three in the bottom flange (B1 to B3), three in the web (W1 to W3) and three in the top flange (T1 to T3). For the central plate, five coupons were cut out (C1 to C5) (see Figure 4.2). The tensile tests were performed by the technical team at the laboratory of the University of Luxembourg (see Annex A for the reports). The main results of the tensile tests are presented in Table 4.3 and in Table 4.4.

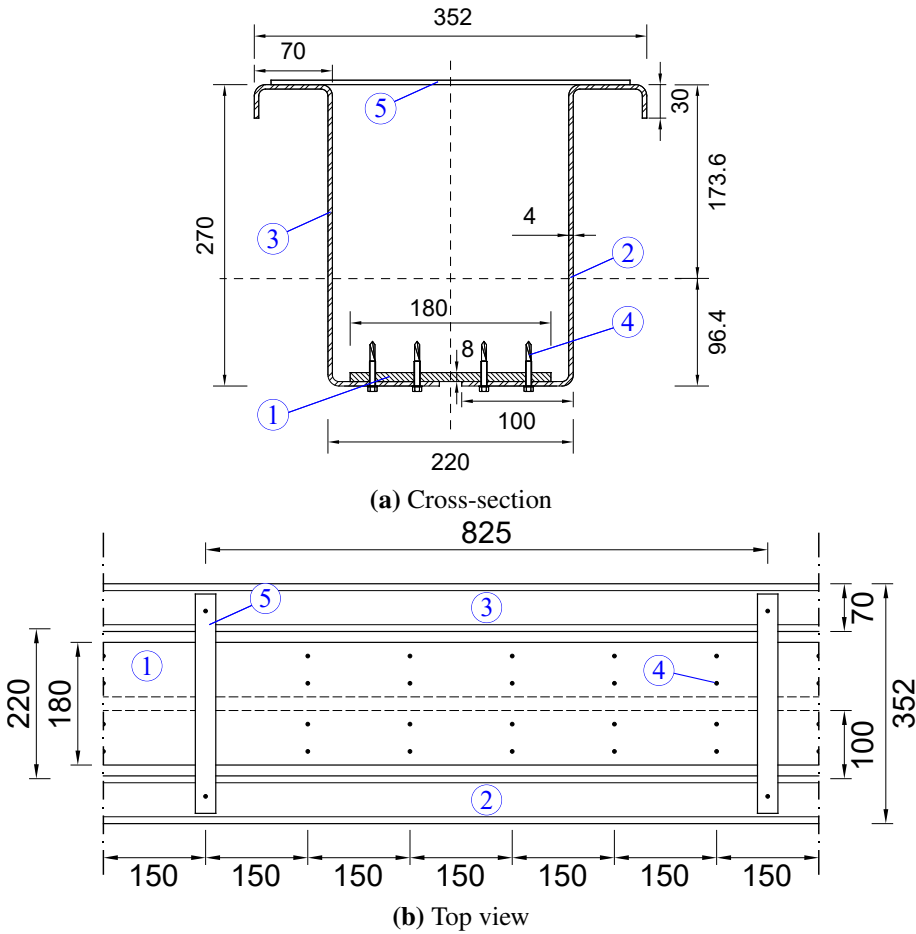


Figure 4.1 – The steel beam specimen

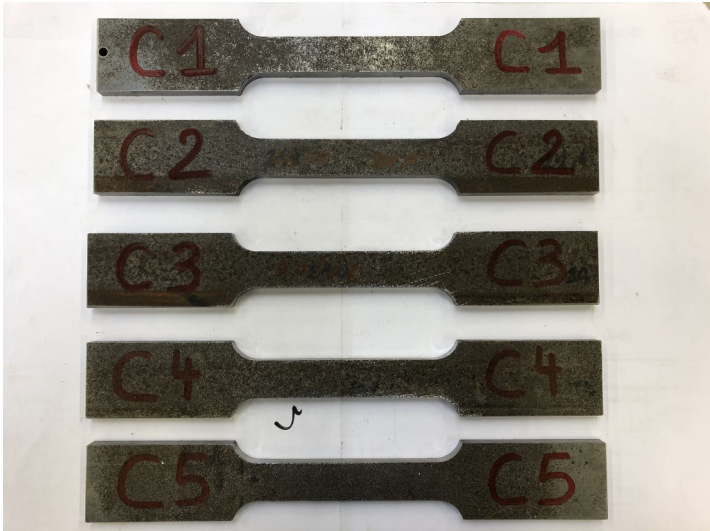


Figure 4.2 – Tensile specimens of the central plate (C1 to C5)

From these results, the mean yield and ultimate strengths of the cold-formed side plates were:

$$f_{y,cf,m} = 322 \text{ MPa}$$

$$f_{u,cf,m} = 406 \text{ MPa}$$

Table 4.3 – Tensile tests results of the cold-formed steel plates

Specimens	Grade	ReH [MPa]	Rm [MPa]
B1	S235	325	410
B2	S235	338	410
B3	S235	331	409
W1	S235	316	407
W2	S235	316	402
W3	S235	314	406
T1	S235	320	404
T2	S235	317	407
T3	S235	323	405

Table 4.4 – Tensile tests results of the hot rolled steel plates

Specimens	Grade	ReH [MPa]	Rm [MPa]
C1	S355	413	560
C2	S355	410	558
C3	S355	420	558
C4	S355	419	557
C5	S355	423	560

From these results, the mean yield and ultimate strengths of the hot rolled central plate were:

$$f_{y,hr,m} = 417 \text{ MPa}$$

$$f_{u,hr,m} = 558 \text{ MPa}$$

For both steel grades, the experimental values were in accordance with the recommended values in the Table 7 of EN 10025-2 (2005).

4.2.3 Fabrication

The beam cross-section was composed of three distinct steel parts. At the delivery, two central plates were delivered with shear studs and two central plates were delivered without any (Figure 4.3a). For the test on the steel beam in the construction stage, the presence of the shear studs were not needed. That is why two central plates do not have them. In a real situation, the central plates always have shear studs. The plates with the shear studs were dedicated for the second test where the beam has a composite behaviour. The cold-formed side plates that were delivered to the laboratory were pre-folded (Figure 4.3b). The central plate was then placed between the two side plates. The general shape of the beam developed in the thesis project was appearing (Figure 4.3c). The positioning of the three plates was done carefully by using clams and a timber template (see Figure 4.4b).

In order to avoid local plate buckling at the supports during the test, additional plates and stiffeners were welded on the beam at the exact position of the supports (see Figure 4.4a). These plates were welded early during the fabrication process because they helped in maintaining the two side plates alignment before the final assembly with the self-drilling screws.

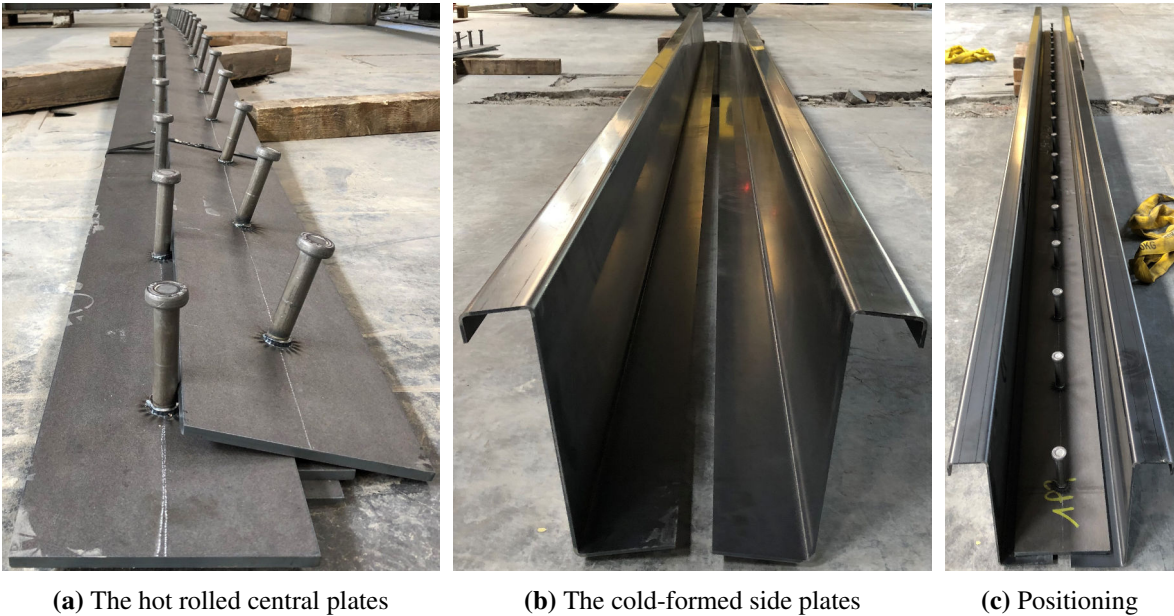


Figure 4.3 – Preliminary assembly of the steel beam



Figure 4.4 – Assembly of the supports and positioning of the side plates

The final assembly of the entire steel beam was done with self-drilling screws at the bottom of the section. The screws were fixed in a direction towards the interior of the section. Thus, the end of the screws, which are quite long because of the drilling part, were not visible from underneath the beam (see Figure 4.1a). The beam should be rotated to proceed to this final assembly (see Figure 4.6b). In order to rotate the beam easily and keep the three plates in position, some lines of screws (every meter) have been fixed before the rotation in the “wrong” direction (see Figure 4.5). These lines of screws were then cut after the rotation of the beam (see Figure 4.6a).

The final assembly was done after the rotation of the beam. A line of screws is comprised of 4 screws, the lines were spaced 150mm apart. 41 lines were drilled along the beam, which means 164 screws in total. The screws were designed with the estimated maximum shear flow during the test with a security factor of 2.0 to avoid any failure in these structural elements. For real applications, the beam will carry lighter loads and the security factor can be reduced to 1.0, so that the total number of screws will be significantly reduced.



Figure 4.5 – The self-drilling screws in the “wrong” direction before being cut

4.2.4 Imperfections

As the geometrical imperfections have a significant effect on the LTB, they were measured before the test. The imperfections were measured along the longitudinal direction of the beam. The imperfections were measured at the top and bottom of the section from both sides and at the space between the cold-formed steel plates at the bottom (see Figure 4.7).

For the positions at the top and the bottom of the section, distances (d_1 , d_2 , d_4 and d_5) were measured between the section and a cable taut between the supports (see Figure 4.8). With all the measured values, an average distance is calculated. Then, the relative gap between the real shape of the section and this average value is determined and presented in Table 4.5.

As it can be observed, geometrical imperfections were relatively small and the maximum gap was about 2mm equivalent to $L/3000$. The real shape of the beam, according to the measures, is also presented in Figure 4.9. From this top view, it is also confirmed that the tested beam specimen do not present important geometrical imperfections (like $L/500$).

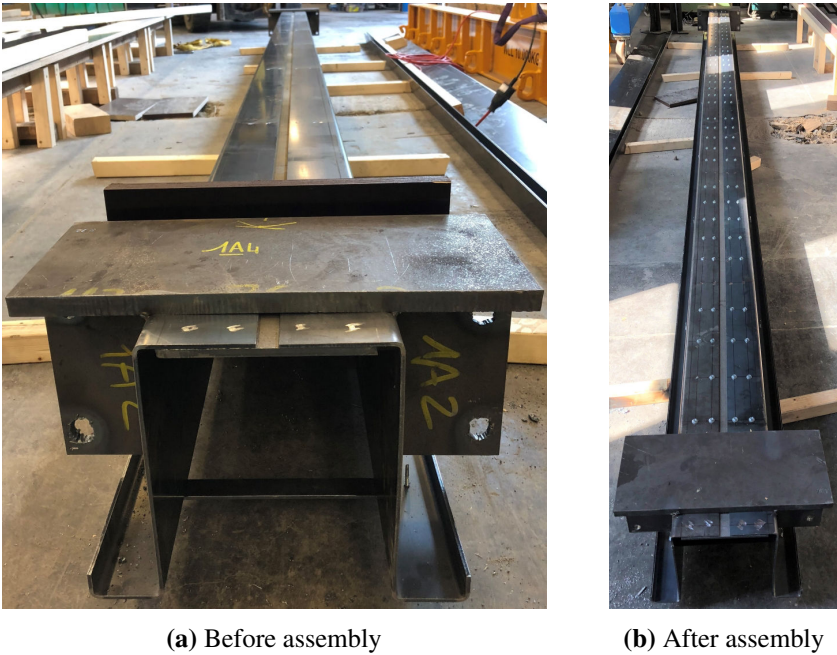


Figure 4.6 – The steel beam assembly

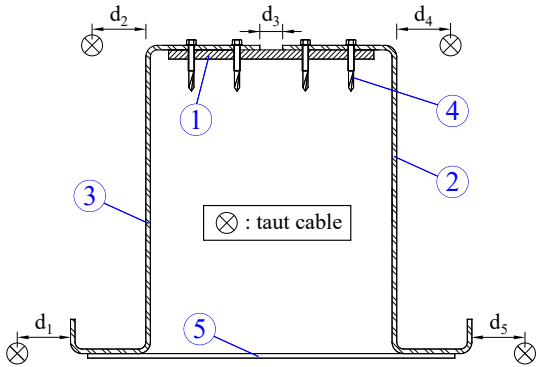


Figure 4.7 – Positions of the measured imperfections

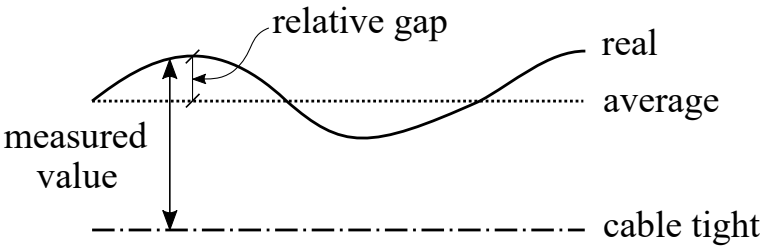


Figure 4.8 – How the imperfections were measured

Table 4.5 – Relative gap to the average shape

Longitudinal position [mm]	Relative gap [mm]				
	x	d1	d2	d3	d4
0	-	-	-	-	-
150	-	-0.2	0.0	2.0	-
300	0.8	-1.1	0.0	1.4	0.1
450	-	-1.4	0.6	0.7	-
600	0.3	-1.4	1.0	0.6	-0.3
750	-	-1.2	1.3	0.0	-
900	0.2	-0.9	1.2	0.1	-0.3
1050	-	-1.3	1.3	-0.4	-
1200	-0.2	-1.0	1.2	-0.6	-0.5
1350	-	-1.0	1.2	-0.3	-
1500	0.1	-0.8	1.0	-0.5	-0.1
1650	-	-0.5	0.6	-0.1	-
1800	-	-0.6	0.6	-0.1	0.0
1950	-0.2	-0.5	0.1	-0.1	0.4
2100	-	0.1	0.1	-	-
2250	-	0.4	0.0	0.2	-0.2
2400	-0.3	0.5	0.0	0.4	-
2550	-	0.6	-0.3	0.0	-0.1
2700	-0.3	0.3	-0.4	0.3	-
2850	-	0.5	-0.4	0.4	0.0
3000	-0.2	0.6	-0.6	0.3	-
3150	-	0.5	-0.6	0.0	-0.5
3300	-0.1	0.7	-0.6	0.3	-
3450	-	0.3	-0.7	0.2	-0.1
3600	-0.4	0.6	-0.6	0.2	-
3750	-	0.2	-0.7	0.0	0.2
3900	-0.1	1.0	-0.2	-0.1	0.0
4050	-	0.1	-0.2	-0.2	0.0
4200	-	0.4	-0.3	-0.2	-
4350	-	0.2	-0.1	-0.3	-
4500	0.2	0.7	0.0	-0.5	0.0
4650	-	0.6	-0.1	-0.7	-
4800	-0.1	0.3	0.0	-0.5	0.2
4950	-	0.3	-0.3	-0.3	-
5100	0.2	0.5	-0.4	-0.5	0.2
5250	-	0.1	-0.4	-0.3	-
5400	0.1	0.1	-0.8	-0.1	0.7
5550	-	0.1	-1.0	-0.1	-
5700	-0.1	0.8	-1.4	0.2	0.8
5850	-	0.6	-1.9	0.2	-
6000	-	-	-	-	-

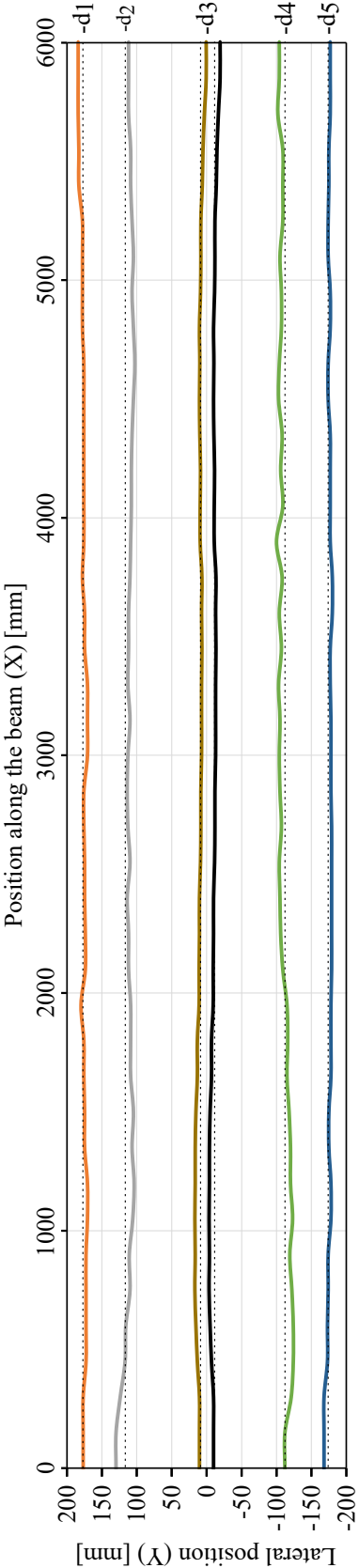


Figure 4.9 – Real geometrical imperfections (amplified x10) of the beam specimen (Top view)

4.3 Layout

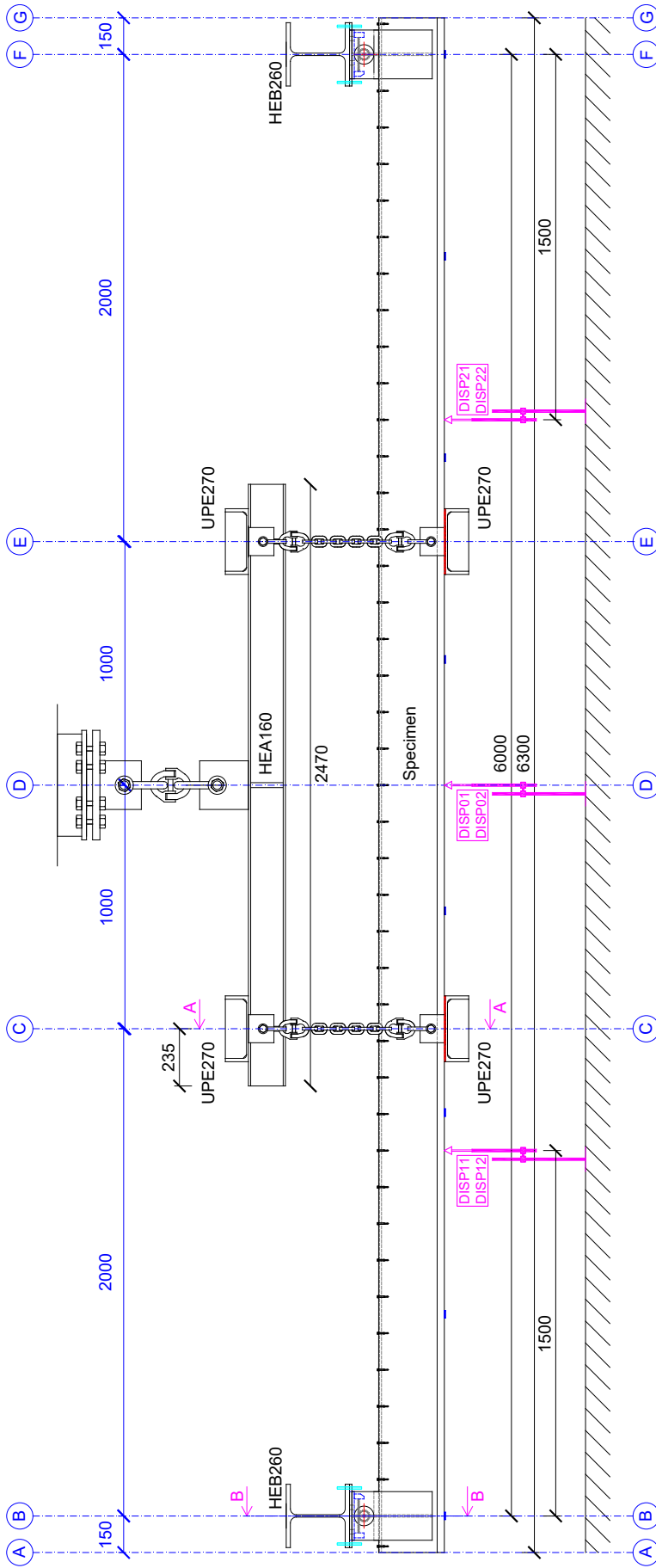


Figure 4.10 – Layout of the steel beam specimen placed in test frame - (main view)

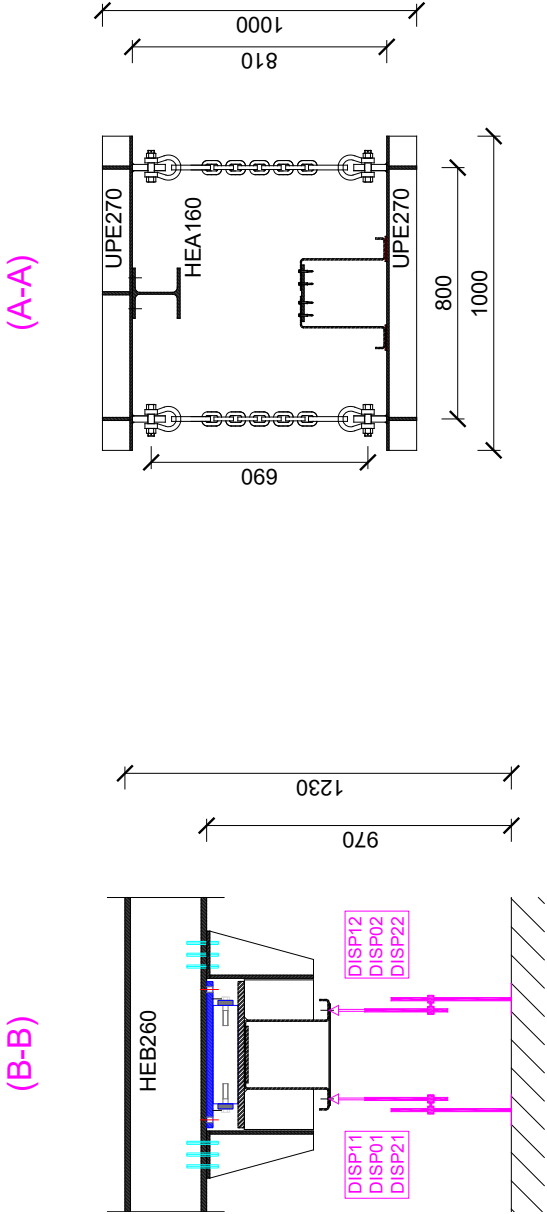


Figure 4.11 – Layout of the steel beam specimen placed in test frame - (sectional views)

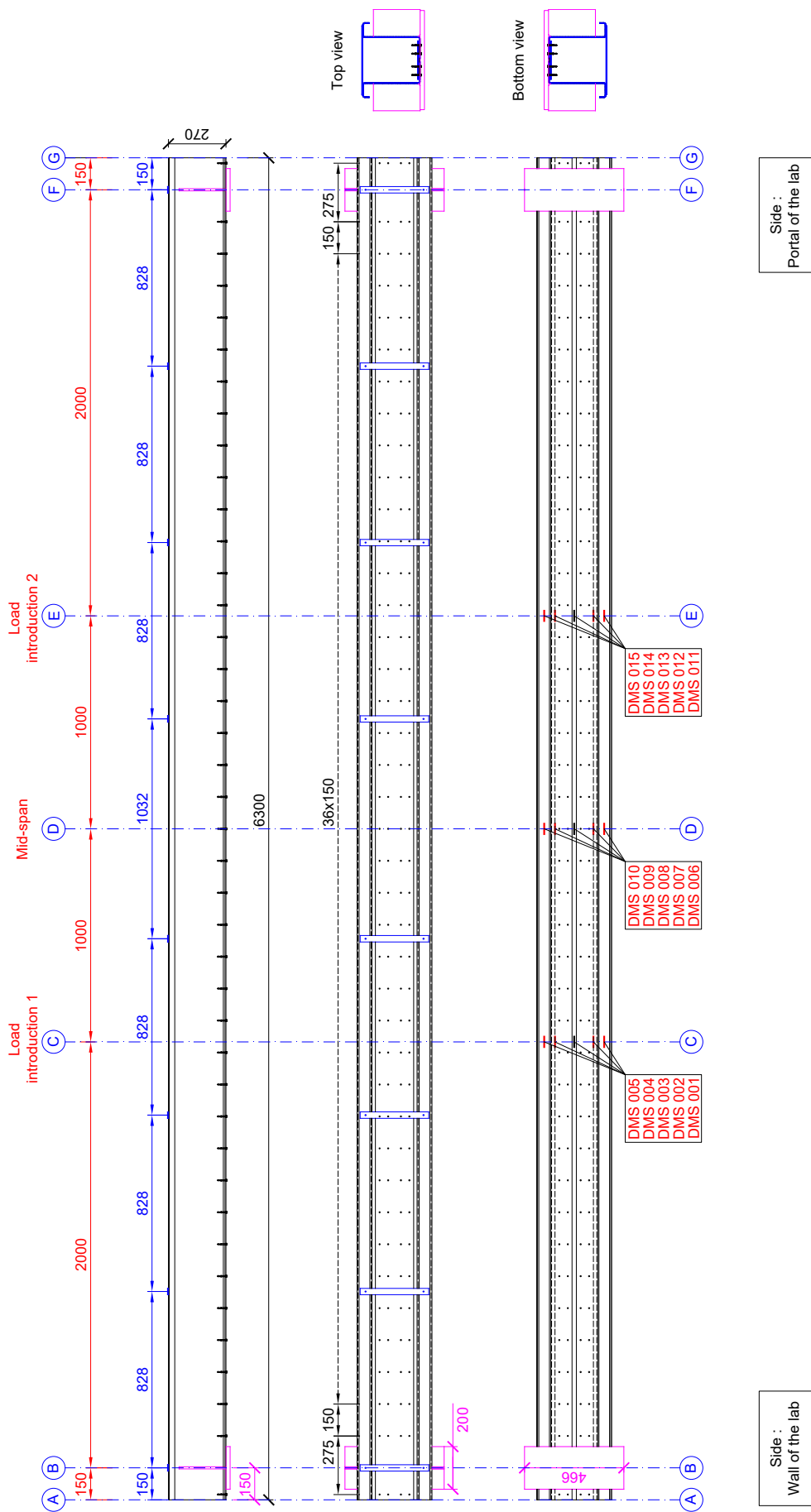


Figure 4.12 – Layout of the steel beam specimen with the strain gauges

4.4 Setup

4.4.1 Test frame

As presented by Yang, Kang, Xiong, Nie, Hu, Wang, Bai, and Dai (2017), it is possible to test the LTB instability of a beam with one-point loading applied at mid-span, and the cross-section is restrained at the load introduction. However, the main loads at the construction stage are equally distributed (due to the concrete weight) therefore it was preferred to have a 4-points bending test with two-point loading without any restraint to obtain a bending moment closer to the real situation (see Figure 4.10).

The test conducted at the laboratory of the University of Luxembourg was a 4-points bending test as shown in Figure 4.10 and 4.11. The beam was on fork supports, the span was 6 m. The beam was turned upside down and placed on the test frame in order to use a specific loading introduction (see § 4.4.2). The hydraulic cylinder was used in tension to reproduce a positive bending as it will be in reality. The maximum available force of the hydraulic actuator was 1000 kN, the force and the stroke were measured throughout the test. The cylinder was controlled in displacement.

4.4.2 Specific application of the load

In order to obtain the instability of LTB during the test, the application of the loads has been carefully studied. In fact, at a defined moment during the test, the global instability was expected to occur. The instability of LTB is characterized by a vertical displacement (U_z), a transversal displacement (U_y) and a torsional twist (θ_x) of the cross-section. In order to obtain the instability of LTB during the test, the application of the loads should not prevent the beam cross-section from these movements.

The beam was installed upside-down on two roller supports, a tension force was applied in order to produce a tension force at the bottom of the section and compression at the top. The force of the jack was distributed in two-point loads by a longitudinal beam (HEA160, (9) in Figure 4.10). The point loads were both constituted of deformable rectangular frames allowing the specific LTB movements in (YZ) plane (U_z , U_y and θ_x).

These rectangular frames were made of two parallel members (UPE270 oriented horizontally, (6, 8) in Figure 4.10) linked to each other by metal chains ((7) in Figure 4.10). Therefore, the shape of the initially rectangular loading frame could be transformed into a parallelogram during the test and allows the LTB instability to occur (see Figure 4.10).

The horizontal members (UPE270) were stiffened at the location of the chains and at the connection with the longitudinal beam (HEA160). These horizontal members transfer the load from the longitudinal beam (HEA160) through the chains to the beam specimen by a normal contact on the top flanges. Neoprene plates were inserted between the members (UPE270) and the top flanges of the beam specimen, in order to have a better distribution of the forces avoiding any local buckling due to a very narrow surface loaded (see Figure 4.10 and 4.11).

An additional pin was designed at the top of the loading frames to avoid any moment in the hydraulic cylinder. This was also done with a link (see Figure 4.14). During the test, the rotation of torsion of the loading system appeared mainly around the pin at the top and formed the angle θ in Figure 4.13. The chains of the loading system had a very small

inclination α in Figure 4.13), it can be admitted that the chains remained vertical during the test.

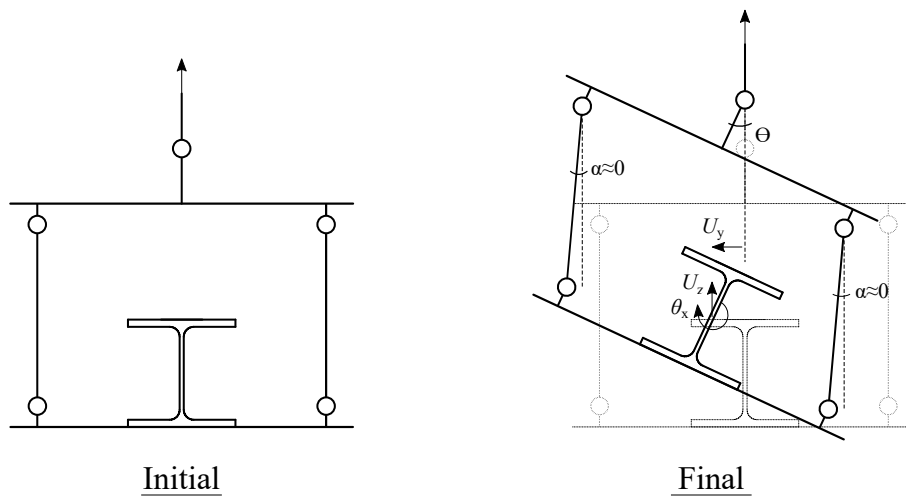


Figure 4.13 – Schematic representation of the loading system



Figure 4.14 – The beam specimen reversed and placed in the test frame



Figure 4.15 – The loading system – side view



Figure 4.16 – The U-shaped beam reversed and placed in the test frame

4.4.3 Supports

The reversed beam was simply supported on two roller supports (see Figure 4.17a). The aim was to reproduce as far as possible a fork bearing support, that means the vertical displacement (U_z) and the torsional twist (θ_x) should be restrained whereas the rotation about the major (θ_y) and the minor (θ_z) axis and the warping (θ'_x) should be free.

In the conducted test, the vertical displacement (U_z) was restrained on the contact line between the thicker plate underneath the U-shaped section and the roller. This system also restrains the torsional twist (θ_x). The three stops visible on Figure 4.17 (two on each side of the section and one at the end of the beam) were not in contact with the beam specimen during the instability. Their presence provided security in the case where the beam specimen during the instability might get out of the test frame. The lateral displacement (U_y) was not restrained because there was a gap between the stops and the side stiffeners (see Figure 4.17b). The longitudinal displacement (U_x) was not restrained because there was a space between the stop and the end of the beam. The rotation about the major and minor axis (θ_y and θ_z) and the warping (θ') were not restrained.

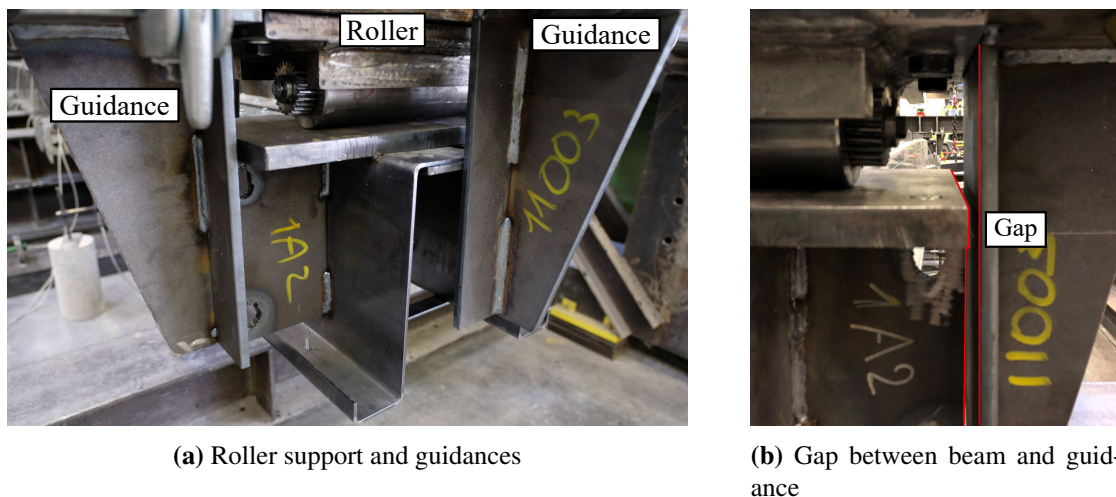


Figure 4.17 – Supports of the test

4.5 Instrumentation

4.5.1 Displacement sensors

The vertical deflection of the beam specimen was measured during the test thanks to six displacement sensors (LVDT) placed underneath the reversed beam. The vertical displacement was measured between the ground and the centres of the top flanges of the section (see DISP00i on Figure 4.10 and 4.11). The deflection of the beam was measured in three sections along the longitudinal axis: at mid-span and at $L/4$ (1500 mm) from each support.

These measures gave information on the deflection of the beam at the beginning of the test. When the twist and the lateral displacement of the section induced by LTB occurred during the test, the measured points moved and the measures were no longer accurate.

4.5.2 Displacement targets

During the LTB, the displacement of the cross-section is a combination of vertical and lateral displacements. The classical displacement sensors (LVDT) are only able to record a movement in 1D. For this reason, it was decided to measure the 3D displacements of the cross-section with displacement targets. The targets have been glued to the beam specimen on the left and right side at four points in three sections at the locations of the two load introductions and at mid-span. That means at $x = 2000$ mm, $x = 3000$ mm and $x = 4000$ mm, respectively section C, D and E in Figure 4.10. The positions of the targets on the section are indicated as “DISP” in Figure 4.21. The targets positions could not be closer to the top flanges for visibility reason. During the test, at defined steps (see Figure 4.32), the survey engineer from the laboratory team measured the positions of targets displaced with the help of a total station (Leica Geosystems AG, 2009). With this measurement system, the complex movements of the cross-section during the LTB instability were recorded during the test.



Figure 4.18 – The targets displacements were measured during the test by the survey engineer

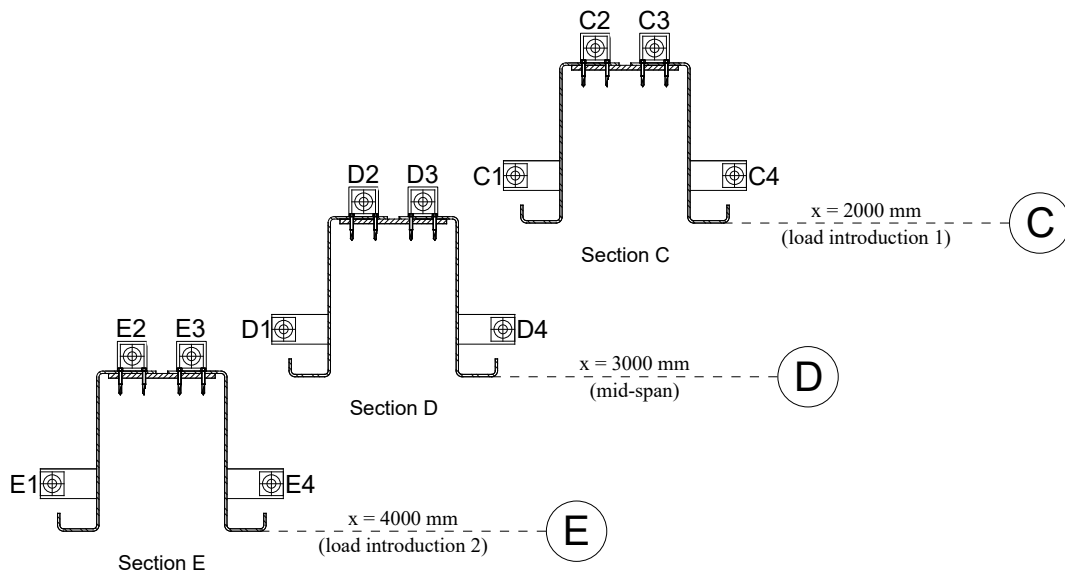


Figure 4.19 – Positions of the targets on the cross-section

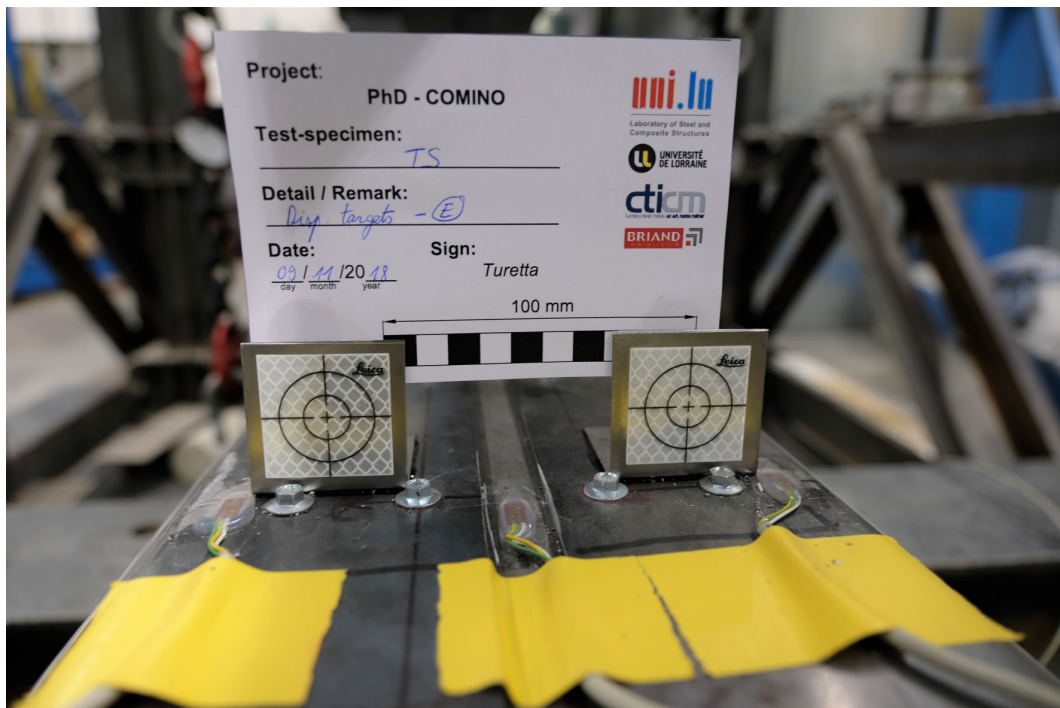


Figure 4.20 – The targets glued on the beam specimen

4.5.3 Strain gauges

The strain was measured with strain gauges (DMS) at the same three cross-sections on the beam specimen (positions C, D and E in Figure 4.10). Five DMS per section were used, three DMS on the bottom flange and two at the top flanges; they are indicated as “DMS” in Figure 4.21. At the bottom flange, the central DMS was placed on the hot rolled central plate, the others were placed on the cold-formed steel part.

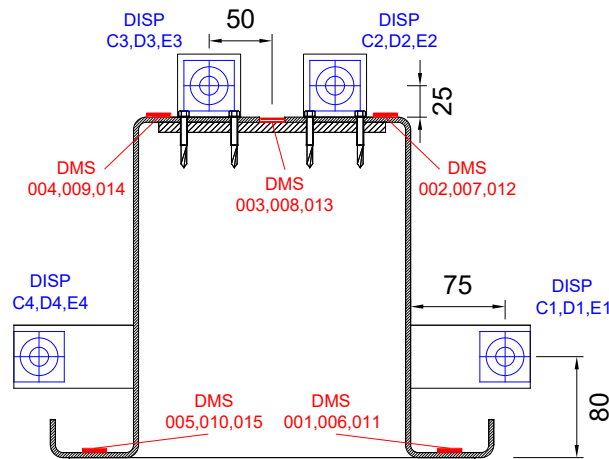


Figure 4.21 – Position of the strain gauges and targets on each cross-section measured

4.6 Test procedure

The hydraulic jack was operated in displacement-controlled mode during the test. The position of the beam on the supports and the position of the loading points were carefully checked. Before contact between the two loading frames (UPE270) the force recorded was 4.4 kN. This load corresponds to the self-weight of all the loading system (actuator, HEA160, UPE270, chains, pins, plates and stiffeners). A small load was applied to place the loading profiles (UPE270 with neoprene plates) in contact with the top flanges of the beam specimen. The beam was lifted up until the contact with the roller supports appeared. At that time, the force applied was 8.3 kN, which corresponds to the self-weight of the specimen plus the loading system. Therefore, the self-weight of the beam and the roller supports lifted up should be 3.9 kN. This value suits well with the calculated self-weight of the specimen (92% compared to calculated value).

The test was a static test with the conduction of a loading ramp and some unloading steps to obtain information on the stiffness of the beam specimen at a defined time. The loading was applied with an average rate of 1 mm/min. The unloading and re-loading loops were applied with a rate of 5 mm/min. The first load step was applied until 5% of the peak load and then decreased to nearly zero, so that small gaps in the loading system could be closed. In the second step, the load was applied until 54% of the peak load and decreased to 13%. Thereafter, the load was increased continuously to the peak load ($P_{ult,test}$). In results, the displacement kept increasing while the load stayed at a constant level. At an average vertical displacement of 28 mm, a final unloading was done until 13% of the peak load was reached and afterwards a final loading until the failure was carried out. The test was stopped when the displacement continued increasing while the force was considerably decreasing and the torsional twist of the beam section was exceeding the setup capacity.

Table 4.6 – Summarized test procedure

Steps	Force reached [kN]	Compared to $P_{ult,test}$	Speed rate [mm/min]
Loading	2	5 %	0.5
Unloading	0	0 %	0.5
Loading	36	54 %	1.0
Unloading	9	13 %	5.0
Loading to pick load	67	100 %	1.0
Unloading	9	13 %	5.0
Loading to failure	50	75 %	3.0

4.7 Test results

4.7.1 Observations during the test

At the beginning of the test, the beam only displaced vertically with increasing load without any visible torsional twist (see Figure 4.22).

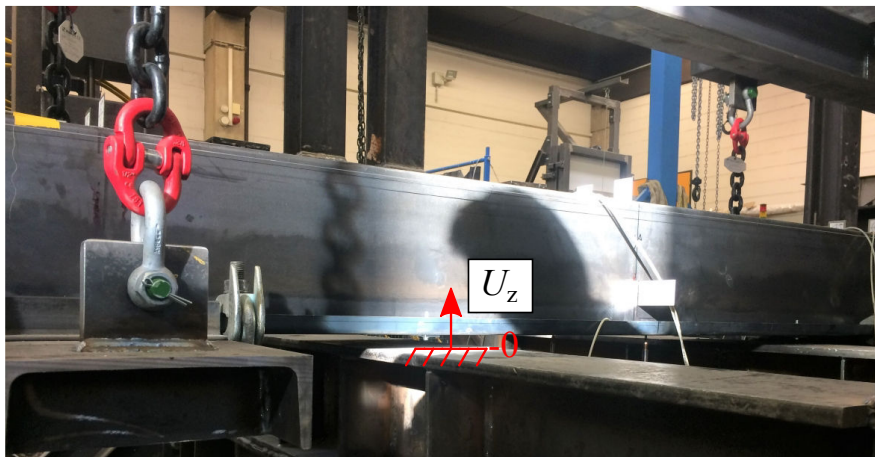


Figure 4.22 – The vertical deflection of the beam at the begin of the test

After a load of around 60% of the peak load, the lateral displacement and the torsional twist appeared, it was the beginning of the LTB instability (see Figure 4.23). As the loading increased, the section kept rotating and moving laterally because of the instability. The displacements of the targets were measured during the entire test at defined load steps, they gave the movement of three cross-sections (see Figure 4.24). During the test, the chains stayed apparently vertical (see Figure 4.23 to Figure 4.26).

The maximum bending moment during the test was $M_{ult,test} = 66.92 \text{ kN m}$. Finally, the failure mode of the beam was characterized by a high lateral displacement and a high torsional twist when no further load could be sustained. This failure mode is clearly a Lateral Torsional Buckling.

After the test, the beam was removed from the test frame. A residual deformed shape remains after failure due to the local buckling at high displacement (see Figure 4.28). A residual plate bulking in one web is shown in Figure 4.29 and a residual buckling in one flange is shown in Figure 4.27.

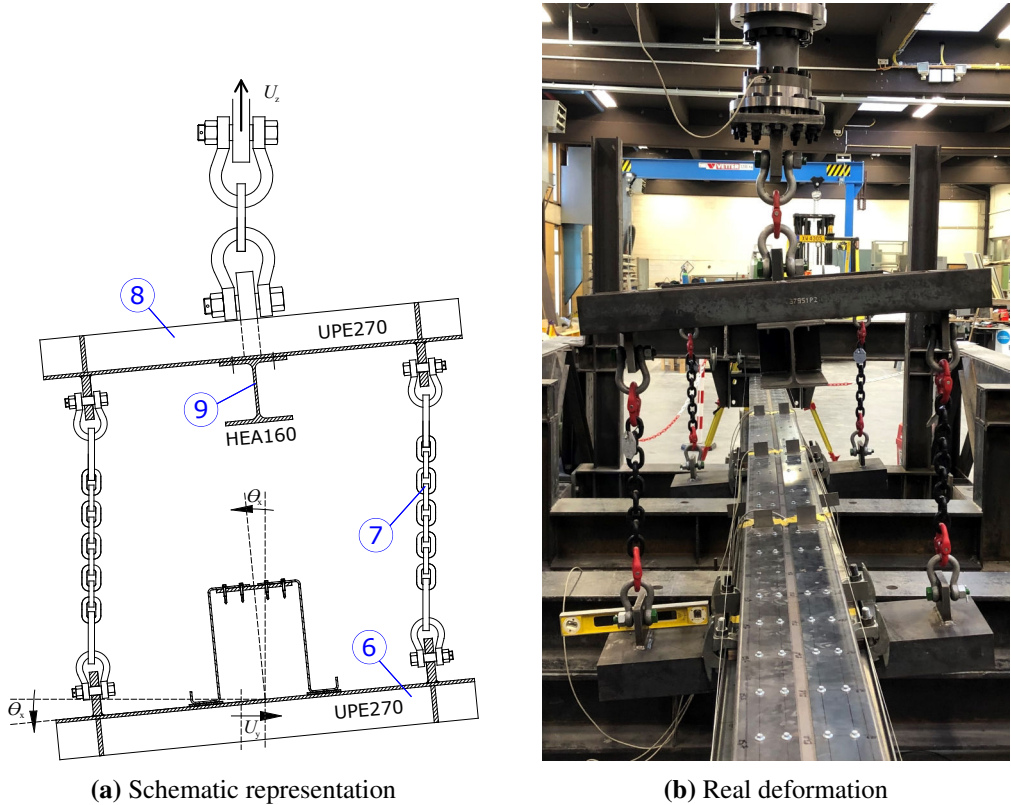


Figure 4.23 – Beginning of the LTB instability



Figure 4.24 – LTB instability followed with the targets



Figure 4.25 – Lateral view of the beam at failure (left side)



Figure 4.26 – Lateral view of the beam at failure (right side)

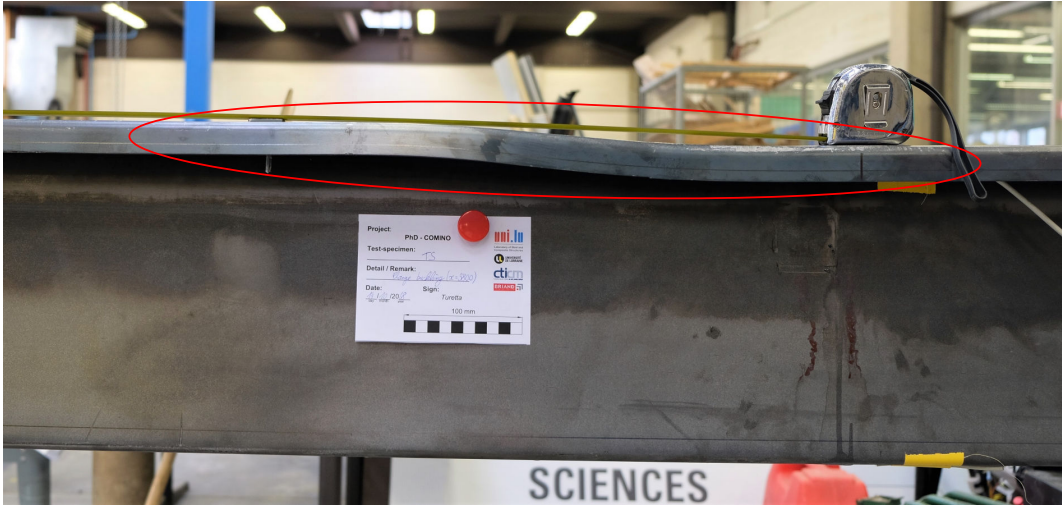
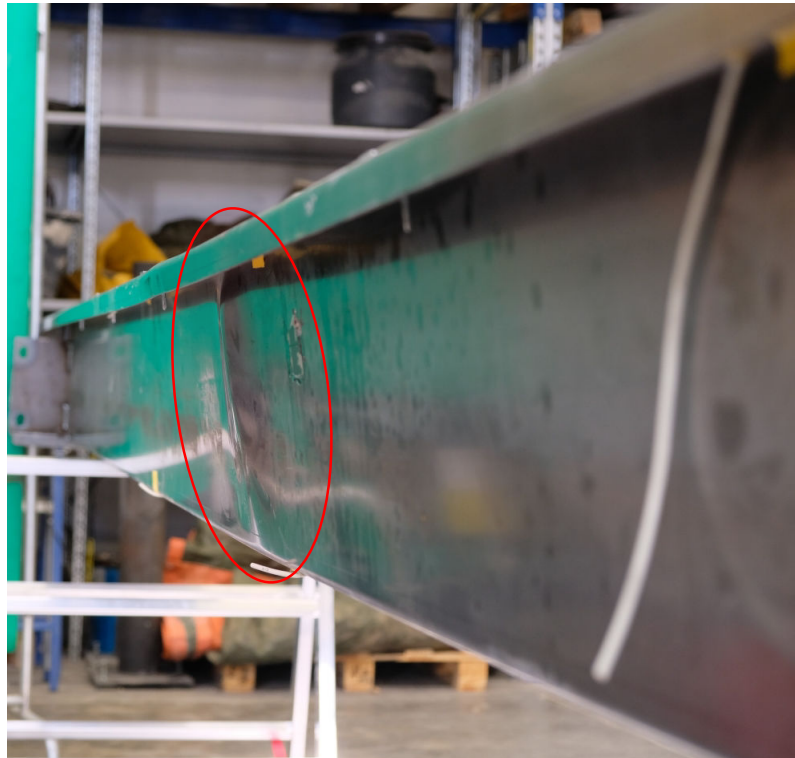


Figure 4.27 – Deformed shape in flange buckling after failure



Figure 4.28 – Global residual deformed shape after the test



(a) exterior view



(b) interior view

Figure 4.29 – Residual deformed shape after the test due to web buckling

4.7.2 Equivalent moment

As the loading was a symmetrical four points bending test with two points load at 2 m each from the support (1/3), the flexural bending moment is calculated by:

$$M_{\text{test}} = \frac{P_{\text{test}} L}{6} \tag{4.1}$$

With :

P_{test} : The load from the hydraulic cylinder

L : The span of the beam (6 m)

Finally, the bending moment value at mid-span was equivalent to the force value applied by the hydraulic jack. In all the graphics presented below, the solicitation is expressed in force but can be easily converted to the bending moment.

4.7.3 Force-displacement of the hydraulic cylinder

The force and the displacement of the hydraulic cylinder were measured during the test. The evolution of the resulting force with the increase of the vertical displacement is presented in Figure 4.30. As the section was reversed, the displacement of the cylinder is counted positive in the opposite direction of the gravity force. This measurement integrates the deflection of the beam and the deformation of the loading setup.

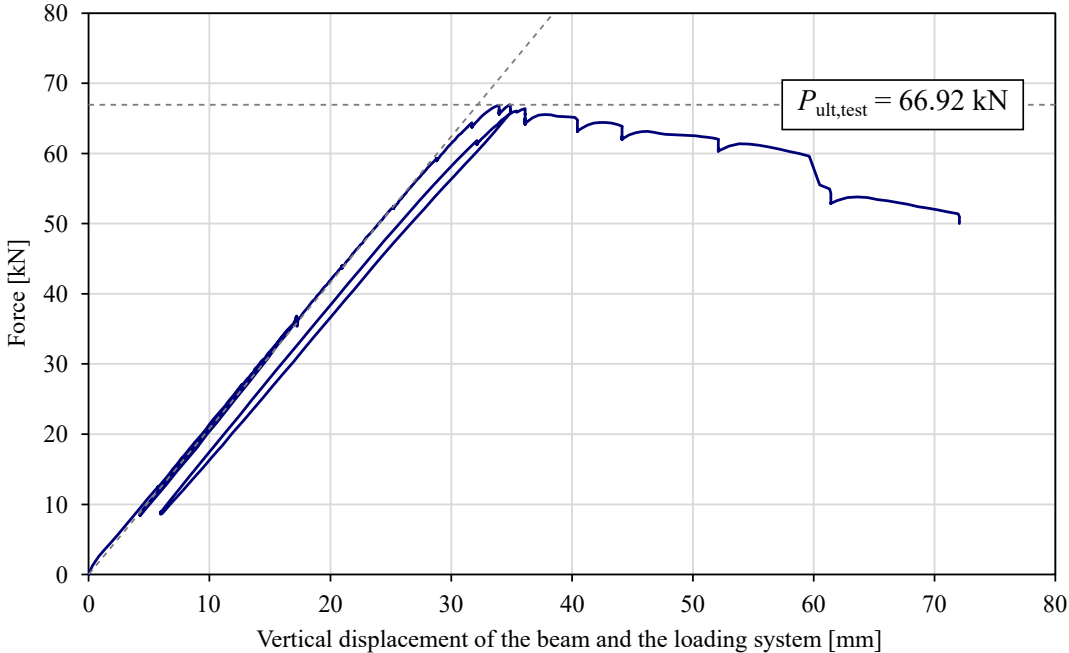


Figure 4.30 – Force displacement curve of the hydraulic cylinder

The structural behaviour was linear until around 90% of the peak load $P_{\text{ult,test}} = 66.92 \text{ kN}$. After this peak, the LTB instability occurred and the displacement continued to increase while the force decreased.

4.7.4 Cross-section representation by the targets

The targets were placed on the beam specimen in three sections (C, D and E see Figure 4.19). Their positions give a correct approximation of the cross-section's shape at the time of the measurement. The distances from a target to the angles of the U-shaped section are known. The targets placed on the webs near the top flanges (C1-C4, D1-D4 and E1-E4) are used to position the extremities of the top flanges and the angle between the webs and the top flanges. The targets at the bottom flange (C2-C3, D2-D3 and E2-E3) are used to position the angle between the webs and the bottom flanges. Then, for each section (C, D and E), the 2 extremities of the top flanges and the 4 folded angles are linked by straight lines in a (YZ) plan. This method gives a good approximation of the cross-section shape but cannot reflected any plate buckling during the test. The targets positions of the section D (at mid-span) are presented with circle marks in Figure 4.31 and are linked to each other with dotted lines. An average position called "CD" is the average of the four targets positions of the section D at the time of the measurement. From the targets positions, the approximate cross-section is drawn with lines called "Section D".

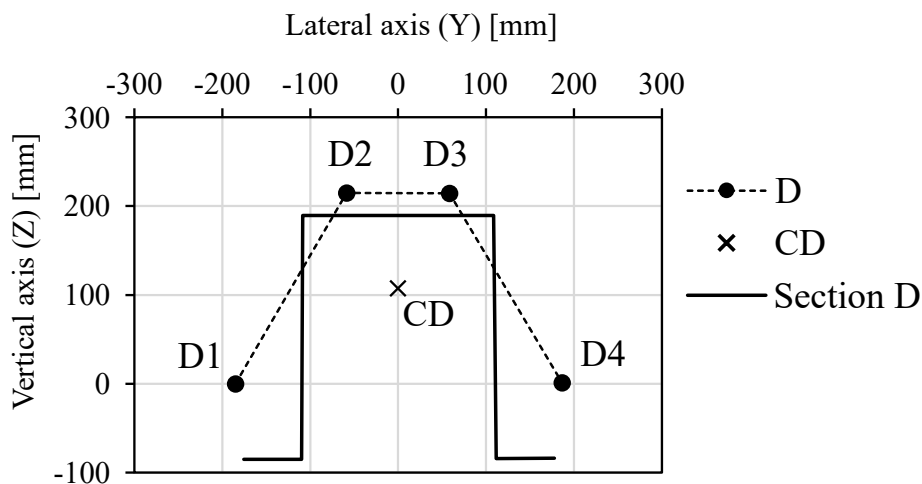


Figure 4.31 – cross-section linked to the targets positions

With the target displacement measurements, many results can be obtained and they are presented in the paragraphs below. For each section (C, D and E), all the targets stayed in their initial plan (YZ), no longitudinal displacement along X-axis were recorded.

4.7.5 Measurement point on the targets during the test

The displacement measurements of the targets was done during the test by a survey engineer. In total 20 measurement points were performed throughout the test at the time indicated in Figure 4.32. For the measurements n° 19 and n° 20, some targets of the sections were hidden due to too large deformations of the beam specimen. Therefore, the measurement n° 18 was the last step where all the targets can be measured.

All the results presented in the next paragraphs are related to the section D, the section at mid-span. This cross-section was the only one that was not in contact with the loading system. Thus, the top flanges of this section were not restrained by the contact with the UPE270 of the loading system.

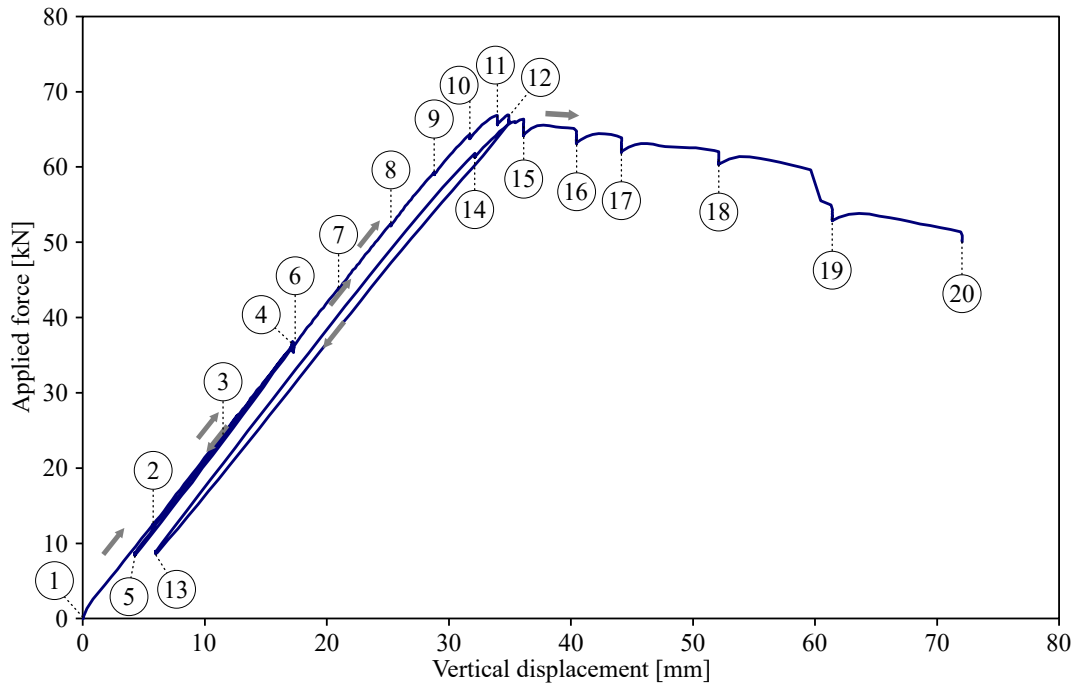


Figure 4.32 – Measurements performed on targets throughout the test

4.7.6 Deformed shape of the section

The measured displacements of the targets of the cross-section at mid-span (section D) give the evolution of the deformed shape of the section with the increase of the loading. Three displaced section shapes are presented in Figure 4.33; they correspond to the initial shape, the shape at the peak load and at the failure at a mean vertical displacement of $L/125$. The evolution of the torsional twist of the cross-section with the increase of the load during the test is presented in § 4.7.8. The maximum angle of torsional twist measured at the failure is $\theta_x = 279 \text{ mrad}$ (16°).

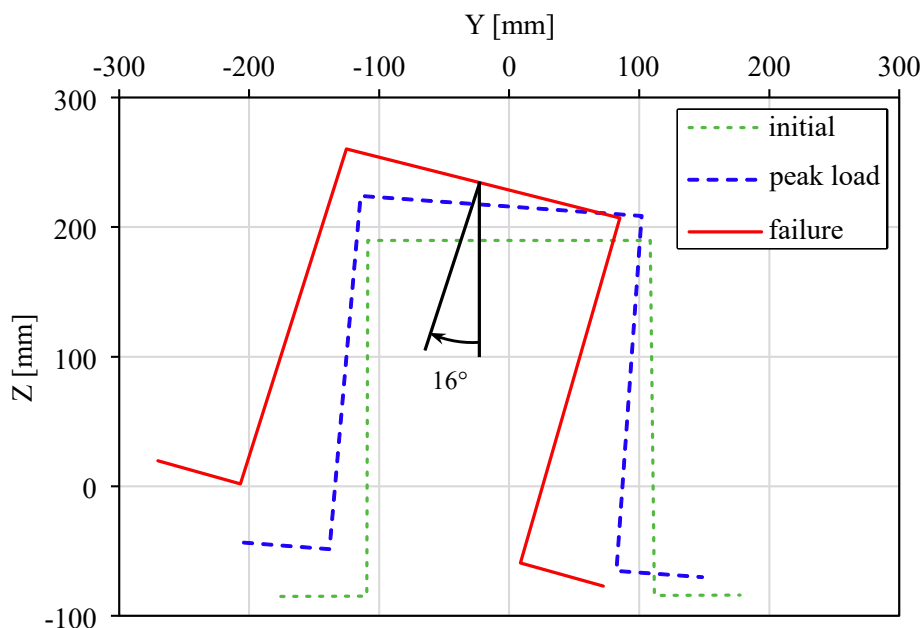


Figure 4.33 – Evolution of the deformed shape of the cross-section D



Figure 4.34 – Deformed shape of the beam during the test

The positions of the targets in the three sections (C, D and E) at the failure load are also plotted in 3D (see Figure 4.35). The sections are linked to each other by straight lines, so it is only an approximation of the deformed shape of the beam. The beam cross-section is reversed compared to the real position in the test.

4.7.7 Displacement of the section at mid-span

The evolution of the vertical and lateral displacements of the targets at mid-span (D1 to D4 in Figure 4.21) are respectively presented in Figures 4.38 and 4.36. As each point is presenting different quantities of movements, an average position called “CD” is created and is the average of the displacements of the targets D1 to D4. The evolution of the vertical and lateral displacements of the average position “CD” are respectively presented in Figure 4.37 and 4.39.

The maximum displacement were recorded at an applied load of 61.2 kN and they were :

- The maximum lateral displacement was for D4: $\delta_{y,\max,D4} = -82.3 \text{ mm (L/73)}$.
- The maximum vertical displacement was for D1: $\delta_{z,\max,D1} = 104.1 \text{ mm (L/58)}$.
- The maximum average lateral displacement was $\delta_{y,\max,CD} = 44.8 \text{ mm (L/134)}$.
- The maximum average vertical displacement was $\delta_{z,\max,CD} = 48.0 \text{ mm (L/125)}$.

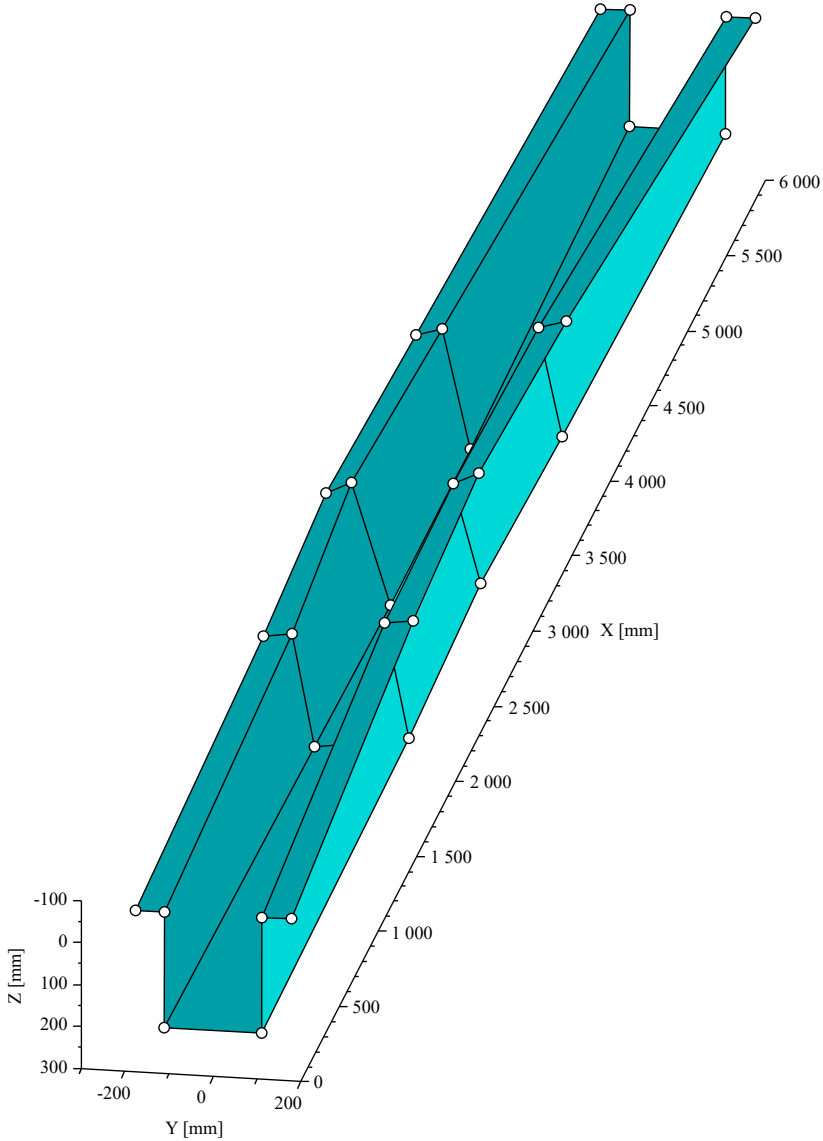


Figure 4.35 – Representation of the deformed shape of the beam specimen at the end of the test

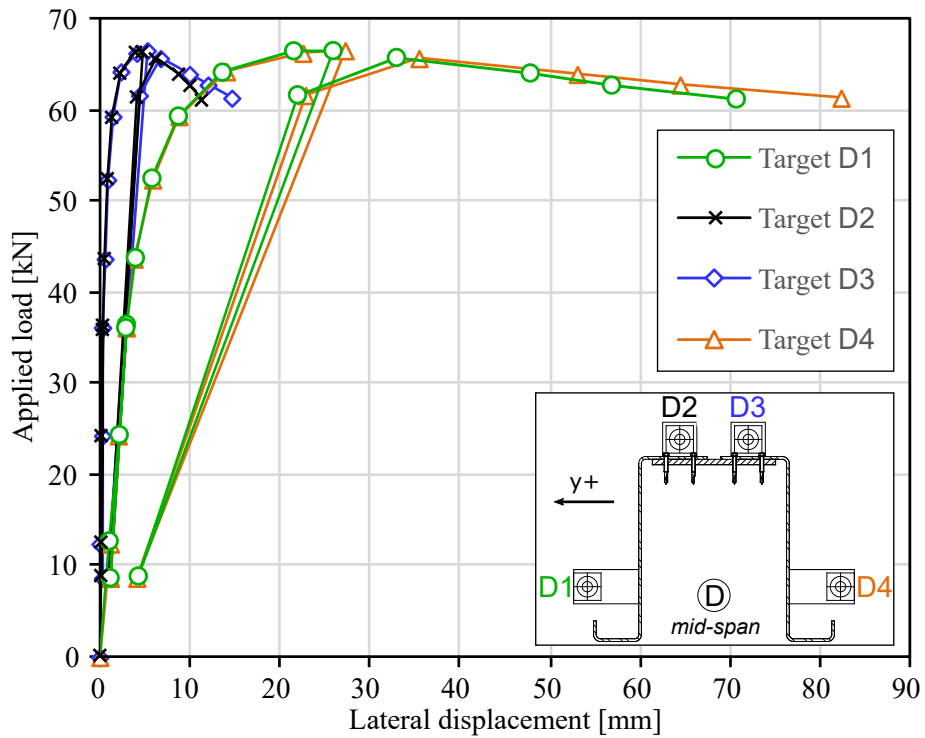


Figure 4.36 – Force - lateral displacement curves of the targets at mid-span

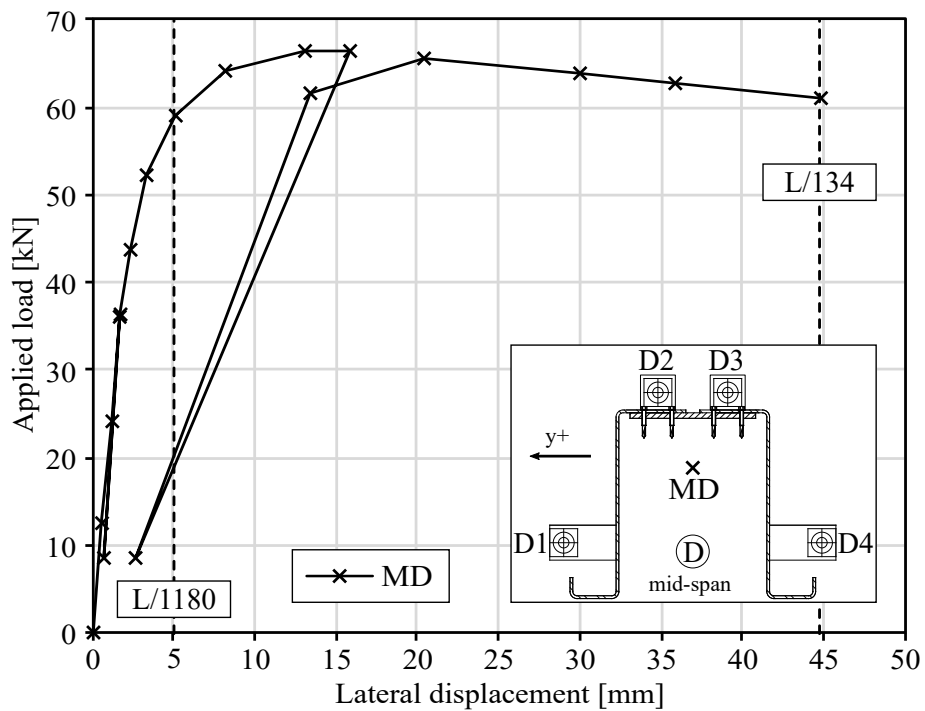


Figure 4.37 – Force - lateral displacement curve of the average position (CD) at mid-span

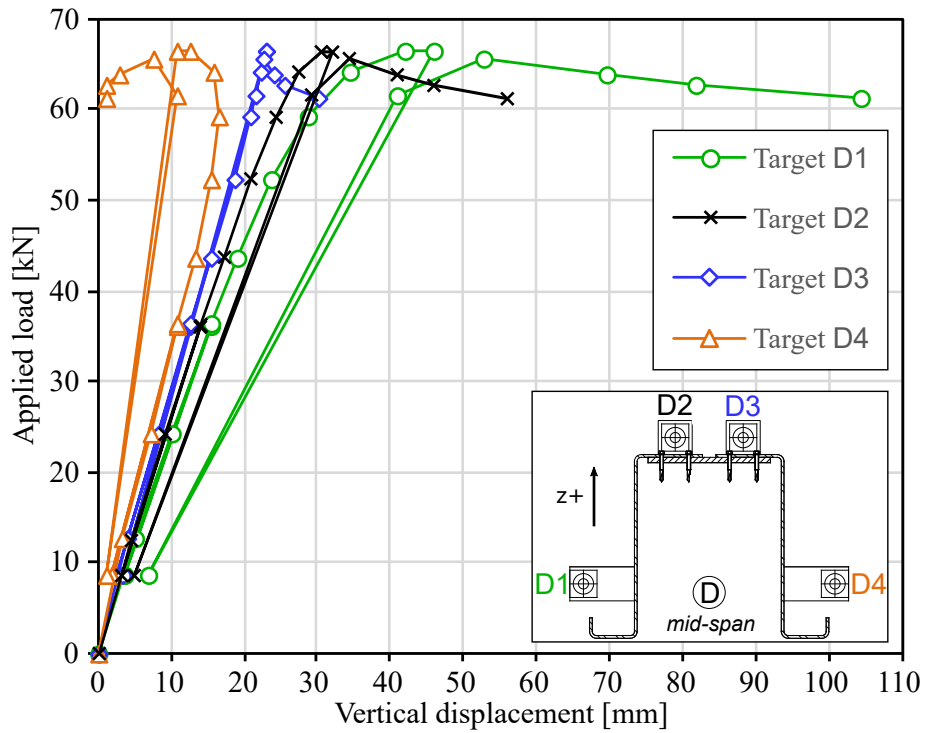


Figure 4.38 – Force - vertical displacement curves of the targets at mid-span

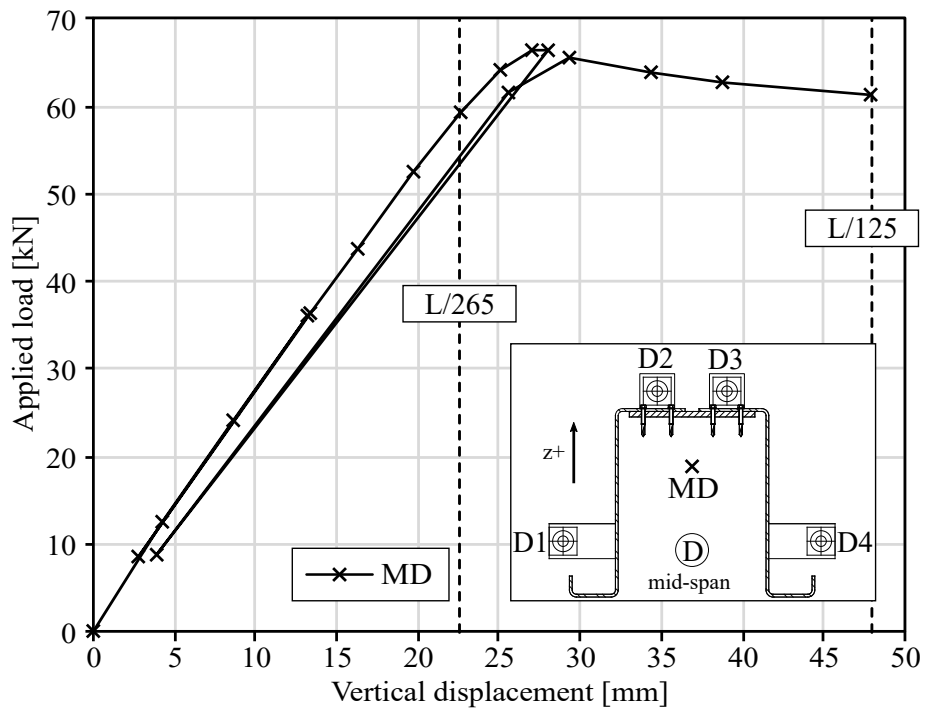


Figure 4.39 – Force - vertical displacement curve of the average position (CD) at mid-span

4.7.8 Rotation of the section

The angle of inclination of the section (θ) is measured between the lines (D1-D4)₁ of the initial shape and (D1-D4)_i of the deformed shape at a measured step “i”. The angle of inclination is equal to the torsional twist of the section (see Figure 4.23a).

At the failure, the angle of rotation is maximum between the lines (D1-D4)₁ and (D1-D4)₁₈. The maximum torsion twist of the section at mid span (Section D) is: $\theta_{x,\max,D} = 278.8\text{mrad} = 16.0^\circ$. The evolution of the rotation of the section D with the increase of the force is presented in Figure 4.40. The rotation of the section increases since the beginning of the loading but stays linear and not significant before 50% of the peak load ($\approx 35\text{kN}$). After 50% of the loading, the behaviour starts to be non-linear. At 90% of the peak load ($\approx 60\text{kN}$), the behaviour starts to be highly non-linear. After the peak load (66.92kN), the rotation continues increasing without increasing the force, it is the typical plateau for the LTB instability.

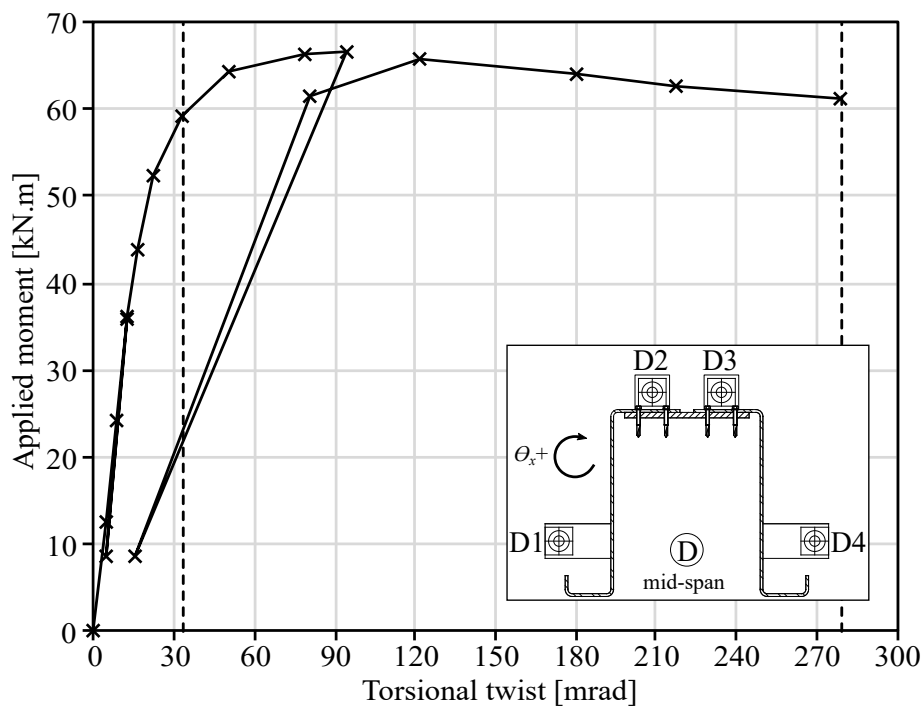


Figure 4.40 – Moment - torsional twist curve of the section at mid-span

4.7.9 Strains

The strain gauges were placed in three cross-sections along the beam at the two loads introduction points and at mid-span (see sections C, D and E in Figure 4.10). From the tensile test results (see § 4.2.2), the elastic limit strain can be determined by Hook’s law according to Equation 4.2 :

$$\epsilon_{\text{lim}}^{\text{el}} = \frac{f_{y,m}}{E_a} \quad (4.2)$$

The material mean values $f_{y,m}$ are given in Table 4.7. E_a is the Young’s modulus.

Table 4.7 – Estimated elastic limit strain

Material	Grade	$f_{y,m}$ [MPa]	ϵ^{el} [μdef]
Cold-formed side plates	S235	322	1533
Hot rolled central plate	S355	417	1986

The results shown in Figure 4.41 correspond to section D at mid-span (DMS006 to DMS010, see Figure 4.21). Before reaching around 60% of the peak load, the section had almost no torsional twist and the longitudinal strains measured in the different DMS position were linear. The strain gauges DMS007, DMS008 and DMS009 at the bottom of the section were in tension. The strain gauges DMS006 and DMS010 at the top of the section were in compression. The elastic neutral axis (ENA) was close to the bottom of the section (see z_G in Table 4.2) and the bigger strains were measured at the top of the section in compression. As shown in Figure 4.41, in the linear phase, the measured strains are in good accordance with calculated elastic strains according to Equation 4.3.

$$\epsilon^{el} = \frac{M_y}{EI_y}(z - z_G) \quad (4.3)$$

M_y is the applied moment during the test along the major axis y-y. z is the vertical position of the strain calculated on the cross-section. The mechanical properties of the cross-section I_y and z_G are given in Table 4.2. Young's modulus for both steel material is $E_a = 210\,000$ MPa.

After 60% of the peak load, with the beginning of the torsional twist of the section due to LTB instability, the relation between the applied load and the measured strains started to become non-linear, even if the elastic limit strain was not exceeded. This can be seen in the bottom-corner of the section at DMS007 and DMS009 in Figure 4.41. After reaching the peak load, the behaviour became fully non-linear for the bottom and top of the section. However, **in both tension and compression zones, the elastic limit strains of the two steel materials were not exceeded.** The load-strain relation was non-linear because of the torsional twist and the non-linear increase of the horizontal displacement induced by LTB. Some parts of the section that were in tension changed into compression, like for example the bottom corner of the section at DMS009. In the opposite bottom corner at DMS007, the strain increased respectively in a non-linear manner.

Before reaching the peak load, the strain distribution at mid-span, in section D, is shown in Figure 4.42. The results are presented with the section not reversed like in the test but like it would be the case in a normal use. The strain distribution is taken between the top (DMS006) and the bottom (DMS007) of the section.

Before the beginning of the LTB instability and the rotation of the section (at around $0.6P_{ult,test}$), the strain distribution in the section is perfectly elastic, see Figure 4.42. The strain is zero at the position of the ENA, see z_G in Table 4.2. When the torsional twist of the section started (after $0.6P_{ult,test}$), the strains still remained below the yield limit and the distribution of the strain was still linear but the position of the ENA was moving up. As already mentioned, the bending moment is no longer applied on the initial axis (y-y) of the section but on an inclined section and horizontally displaced. After this point, the strain distribution is no more symmetrical between the DMS006-DMS007 and DMS010-DMS009.

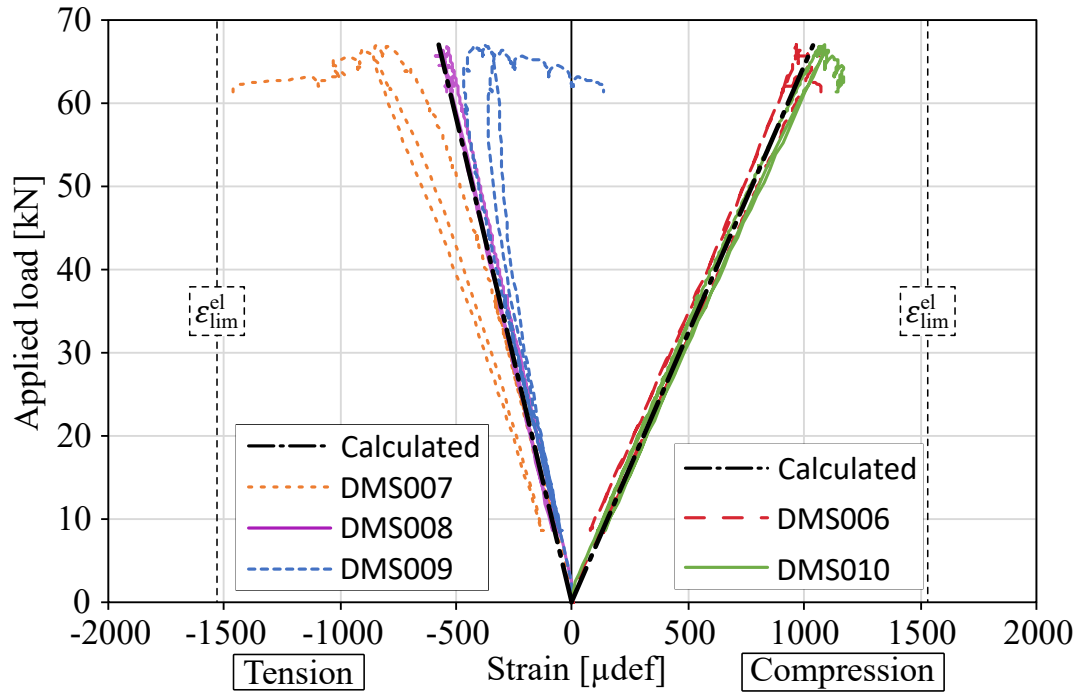


Figure 4.41 – Evolution of the strain with the force at mid-span

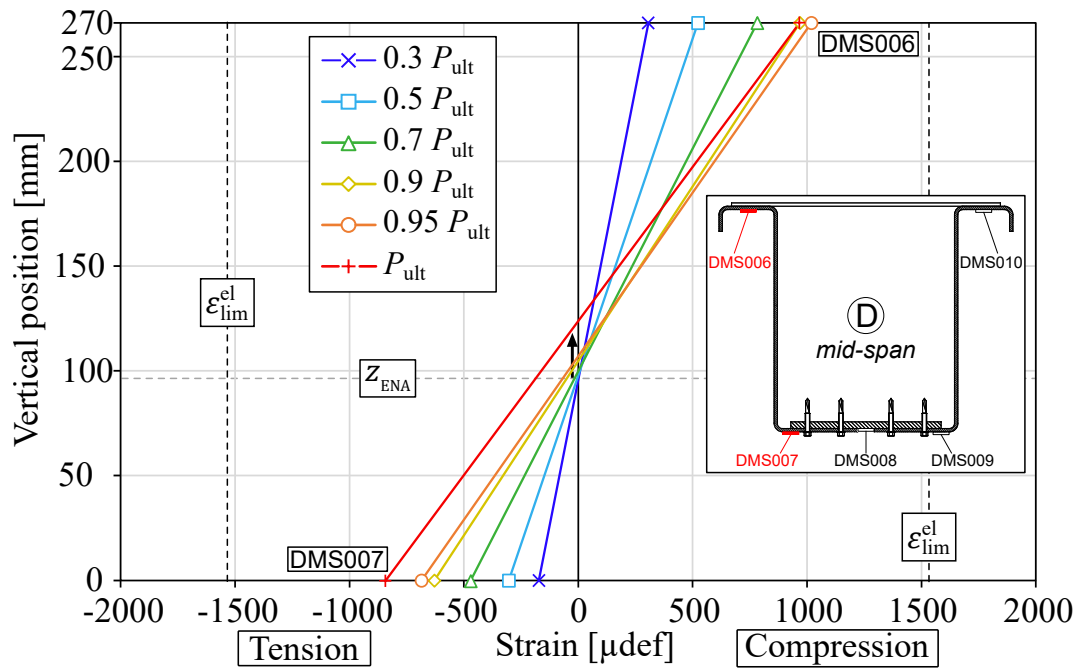


Figure 4.42 – Elastic strain distribution at mid span during the test

4.8 Conclusions

The test carried out at the laboratory of structural engineering of the University of Luxembourg to investigate the LTB behaviour of an assembled steel U-section developed in the frame of the thesis project allows the following conclusions:

- The assembly of three different steel plates with self-drilling screws instead of welding is possible and the screws did not fail or deform in the test.
- The open steel U-section is prone to the global instability of LTB which was shown in the test.
- The loading system designed for the test with the beam section reversed allows the LTB instability to occur.
- The displacements of the targets and the measurement with the “total station” during the test gave a good 3-dimensional picture of the cross-section’s movement during the entire test even after LTB had occurred.
- According the strain measurements, the elastic limit strains of the two steel materials were not exceeded, the section did not yield before failure.

Chapter 5

Analytical and numerical investigations of the U-shaped steel beam

Contents

5.1	Objective of the investigations	124
5.2	Cross-section resistance	124
5.3	Analytical evaluation of the elastic critical moment for LTB	124
5.4	Evaluation of the elastic critical moment with LTBeamN	126
5.5	Evaluation of the elastic critical moment with ANSYS	126
5.5.1	Geometry and elements	126
5.5.2	Ideal support conditions	127
5.5.3	Effect of the bottom plate welds at the supports	130
5.5.4	Effect of the loads introduction	131
5.5.5	Recap of the elastic critical moment of the beam specimen	133
5.6	Validation of the FE model	134
5.6.1	Imposed displacements	134
5.6.2	Materials properties	134
5.6.3	Influence of equivalent geometrical imperfections	134
5.6.4	Effect of combined global and local imperfections	137
5.6.5	Numerical results compared to the test results	138
5.7	Comparison to EN 1993	142
5.8	Parametric study on the LTB of the U-shaped steel section	144
5.8.1	The finite element model	144
5.8.2	The varied parameters	144
5.8.3	Methodology	144
5.8.4	Results	146
5.9	Modeling of the lateral restraint provided by perpendicular steel decks	148
5.10	Conclusions	150

5.1 Objective of the investigations

In the present chapter, analytical and numerical investigations of the U-shaped steel beam are presented. First, the test results are compared to analytical methods and to numerical simulations, in particular with FE model in order to reproduce the real boundary conditions of the test. By comparison with the methods of the standards (Eurocodes), recommendations for the design of the developed solution are proposed. After validating the results of the FE model to the test results, the model was extended through a parametric study to validate the choice of the buckling curve for LTB design. Finally, the effect of the lateral restraint provided by the perpendicular steel decking was investigated with the previous FE model.

5.2 Cross-section resistance

According to EN 1993, one of the roles of cross-section classification is to identify if the section resistance is limited by local buckling. Since the test was in simple bending, the parts of the section subjected to compression were the top part of the webs and the top flanges of the cold-formed side plates. The calculation of the effective cross-section according to EN 1993-1-3 (2007) combined with EN 1993-1-5 (2007) is given in Annex C.

Finally, according to EN 1993-1-3 (2007), there is **no reduction applied to the section**, the section is fully effective, considered as a class 3 cross-section according to EN 1993-1-1 (2005). That means the mechanical properties of the cross-section are equal to the characteristic of the gross section (see Table 4.2). The section is able to develop an elastic distribution of stresses and is allowed to reach the yield strengths with the respective elastic bending resistance. The bending resistance of the section is determined as $M_{el,R,m} = 98.8 \text{ kNm}$ according to Equation 5.1:

$$M_{el,R,m} = f_{y,cf,m} \frac{I_y}{h_{cf,w} - z_G} \quad (5.1)$$

The material mean value $f_{y,cf,m}$ and the geometrical parameter $h_{cf,w}$ are given in Table 4.1. The mechanical properties of the cross-section I_y and z_G are given in Table 4.2.

5.3 Analytical evaluation of the elastic critical moment for LTB

In the first step, simple analytical equations have been used to analyse the critical moment for LTB. These values serve to judge the accuracy of the numerical results. The elastic critical moment for LTB of a mono-symmetric beam subjected to a 4-points bending was evaluated analytically on the basis of Equation 5.2 proposed by ECCS (2006).

$$M_{cr,I} = C_1 \frac{\pi^2 E I_z}{(k_z L)^2} \left[\sqrt{\left(\frac{k_z}{k_\omega}\right)^2 \frac{I_\omega}{I_z} + \frac{(k_z L)^2 G I_t}{\pi^2 E I_z} + (C_2 z_g + C_3 \beta_z)^2} - (C_2 z_g + C_3 \beta_z) \right] \quad (5.2)$$

Where:

$$z_g = z_a - z_s$$

$\beta_z = \frac{1}{2I_y} \int_A z(y^2 + z^2) dA - z_s$, the Wagner's coefficient characterizing the mono-symmetry of the cross-section

With the principal mechanical properties defined in Table 4.2 and the other properties in Table 5.1, the elastic critical moment is evaluated analytically to $M_{cr,I} = 43.4 \text{ kNm}$.

According to de Ville de Goyet (1989), the equation for the elastic critical moment can include the effect of pre-buckling displacements. In order to do so, the equation for the critical moment is completed with the ratio $(1 - I_z/I_y)$. For mono-symmetric U-shaped members Beyer, Boissonnade, Khelil, and Bureau (2017) proposed to modify the Equation 5.2 with this factor and this leads to Equation 5.3.

$$M_{cr,II} = \frac{C_1 \pi^2 EI_z}{1 - \frac{I_z}{I_y} (k_z L)^2} \left\{ \sqrt{\left[\left(\frac{k_z}{k_\omega} \right)^2 \frac{I_\omega}{I_z} + \frac{(k_z L)^2 GI_t}{\pi^2 EI_z} \right] \left(1 - \frac{I_z}{I_y} \right) + (C_2 z_g + C_3 \beta_z)^2} - (C_2 z_g + C_3 \beta_z) \right\} \quad (5.3)$$

This improvement can be important if the ratio (I_z/I_y) is closed to 1.0, like in our case. However, the value obtained is $M_{cr,II} = 44.4 \text{ kNm}$, the improvement is only of 2%. This is explained by the important mono-symmetry of our section and the high destabilizing effect produced by the eccentricity of the loads.

Table 5.1 – Properties of the section for the calculation of M_{cr}

Definition	Symbol	Value	Unit
Young's modulus	E	210000	MPa
Shear modulus	G	80769	MPa
Torsion constant	I_t	10.504	cm ⁴
Warping constant	I_ω	289151	cm ⁶
Second moment of area about the minor axis	I_z	4809.6	cm ⁴
Length of the beam between lateral restraint	L	6000	mm
Factors depending on the loading and end restraint conditions	C_1	1.04	-
	C_2	0.42	-
	C_3	0.562	-
Effective length factors (no restraint at the end)	k_z, k_ω	1.0	-
Coordinate of the point of load application/G	z_a	173.59	mm
Coordinate of the shear centre/G	z_s	-191.07	mm
Distance between load and shear centre	z_g	364.66	mm
Wagner's coefficient	β_z	24.978	-

5.4 Evaluation of the elastic critical moment with LTBeamN

Thanks to the software LTBeamN described in Beyer, Galéa, and Nguyen (2015), the elastic critical moment is also calculated with the same section properties. The span was 6 m and the loads were applied in two points ($x_1 = 2$ m and $x_2 = 4$ m) at the top of the section. The beam is simply supported in (XZ) plan, the two supports block the vertical displacement (Z) and only one support blocks the horizontal displacement (X) and the rotation along the major axis (Y). The supports were considered as fork supports, the out of plane displacement (v) along Y-axis is blocked, the rotation of torsion (θ) along X-axis is blocked, the rotation (v') along the minor axis Z is free and the warping (θ') is free.

Finally, the elastic critical moment obtained is $M_{cr,LTBeamN} = 43.92$ kN m. This value is 1.1% below the value obtained with an analytical calculation ($M_{cr,II}$), this confirms the accuracy of Equations 5.2 and 5.3.

5.5 Evaluation of the elastic critical moment with ANSYS

The elastic critical moment is also evaluated with the software ANSYS (2017) by Linear Buckling Analysis (LBA). The simulations performed were carried out with linear material laws with Young's modulus of the steel ($E_a = 210000$ MPa). The boundary conditions have an important influence on the results and their effects are presented in this section.

5.5.1 Geometry and elements

The tested specimen was numerically modelled in ANSYS (see Figure 5.1) with the same geometrical properties. All the steel plates of the U-shaped cross-section, including the eight steel battens linking the top flanges together, are modelled with shell elements with the dimensions given in Table 4.1. The plates at the supports are also modelled with shell elements with their real dimensions. The shell element used is SHELL181 (ANSYS, 2017), it is a four-node element with six degrees of freedom at each node (UX, UY, UZ, ROTX, ROTY, ROTZ) well suited for large-deflection effects and supports elasticity and plasticity.

The central plate of the test specimen (1) was in reality assembled to the side plates (2, 3) with self-drilling screws (4) in Figure 4.1a. Instead of screws, in the numerical model a fully bonded contact was set between the bottom surfaces of the central plate (CONTA174) and the top surfaces of the folded side plates (TARGE170) (ANSYS, 2017). The element CONTA174 is used to represent contact and sliding between 3-D target surfaces and a deformable surface defined by this element. In the case of pair-based contact, the target surface is defined by the 3-D target element type, TARGE170. Contact occurs when the element surface penetrates an associated target surface. The element TARGE170 is used to represent various 3-D target surfaces for the associated contact elements CONTA174.

In the experimental test, the eight steel battens linking the top flanges together along the beam (see (5) in Figure 4.1a) were also connected to the top flanges with self-drilling screws. In the numerical model, these self-drilling screws are represented by small rigid beam element between their connection points (BEAM188) (ANSYS, 2017). The element BEAM188 is used as a linear two-node beam element with six degrees of freedom at each node (UX, UY, UZ, ROTX, ROTY, ROTZ) and it is well suited for large-deflection effects.

In addition, a contact surface (with a friction coefficient of 0.1) is set between the bottom

surfaces of the battens (CONTA174) and the top surfaces of the top flanges (TARGE170). The purpose of this contact is to avoid any penetration between the battens and the top flanges during the large displacements and rotations.

The plates at the supports were composed of one large plate underneath the beam (in contact with the roller) and two stiffeners welded to the webs of the section and on the mentioned large plate. In the numerical model, the welds between the stiffeners, the webs and the large plates underneath are simply modelled by meshing the elements with common nodes (see Figure 5.3).

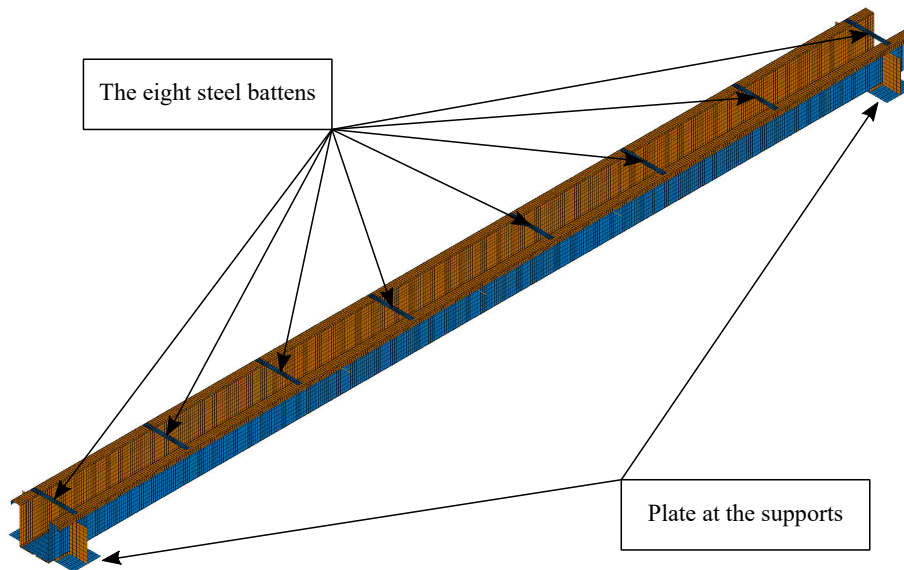


Figure 5.1 – The specimen modelled in ANSYS (ISO view)

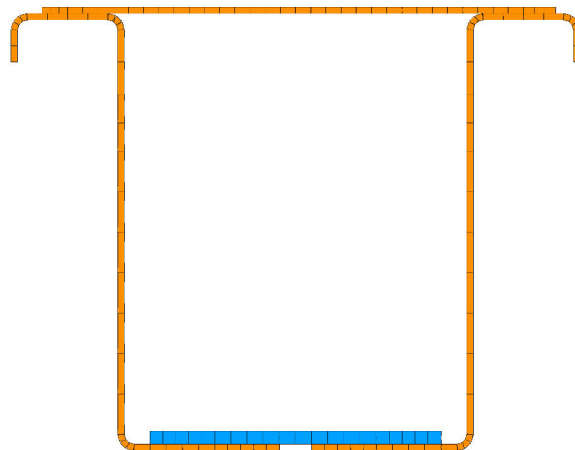


Figure 5.2 – The cross-section modelled with shell element with their thickness

5.5.2 Ideal support conditions

The ideal boundary conditions at the supports are fork supports. To consider this in the numerical model, the vertical displacements (U_z) are restrained on a line of nodes at the middle of the large plates underneath the beam (see Figure 5.3). The lateral displacement (U_y) is restrained only on one middle node of these plates. The longitudinal displacement was

not fixed to simulate the roller support. The longitudinal displacement (U_x) was restrained only at the middle of the beam in one node at the middle of the bottom central plate to ensure a perfect symmetry in order to meet the support conditions, which are explained in § 4.4.3. Thus, at the supports, the torsional twist (θ_x) is restrained whereas the rotation about the major and minor axis (θ_y and θ_z) are free and the warping (θ_x') is free. The symmetrical support conditions of the Finite Element (FE) model are shown in Figure 5.3.

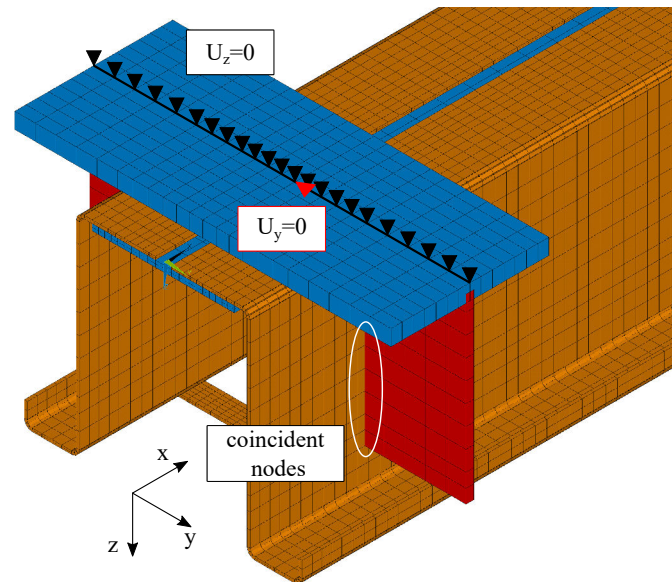


Figure 5.3 – Boundary conditions at the supports of the FEM

The loading is applied on the nodes of the top flanges at the position of the loading introduction of the test C ($x = 2$ m) and E ($x = 4$ m) (see Figure 4.10). The loading is applied with vertical nodal forces along Z-axis. The values of the two forces applied are $F_z = 500$ N. This leads to a bending moment of $M_y = 1$ kNm. This moment will be amplified by the critical factor to reach the elastic critical moment.

The loading is first applied with vertical nodal forces along Z-axis on the nodes of the top flanges at the position of the loading introduction of the test C ($x = 2$ m) and E ($x = 4$ m) in Figure 4.10. **The first Eigen mode of the simulation is clearly a mode of LTB. The ideal elastic critical moment of the numerical simulation is $M_{cr,FE,ideal} = 33.87$ kNm. The analytical value of the elastic critical moment obtained with Equation 5.3 was $M_{cr,II} = 44.4$ kNm and is **30% above the result from the numerical method**. This highlights that there is an additional phenomenon present in the model, which is not taken into account by the other methods. **This difference comes from the deformation of the cross-section.****

The analytical Equations 5.2 and 5.3 consider a warping deformation of the cross-section but the entire cross-section is assumed to stay rigid in its cross-sectional shape. However, the numerical simulation also considered this additional degree of freedom. The rotations of torsion (θ_x) of the nodes at mid-span resulting from the first Eigen mode are represented in Figure 5.5 and Figure 5.6. As it can be seen, the torsional rotations (θ_x) of the nodes are not constant along the cross-section. The nodes at the top of the section are rotated more than those of the bottom of the section. It shows the transversal deformations which are not considered in the previous methods for determining the elastic critical moment for LTB.

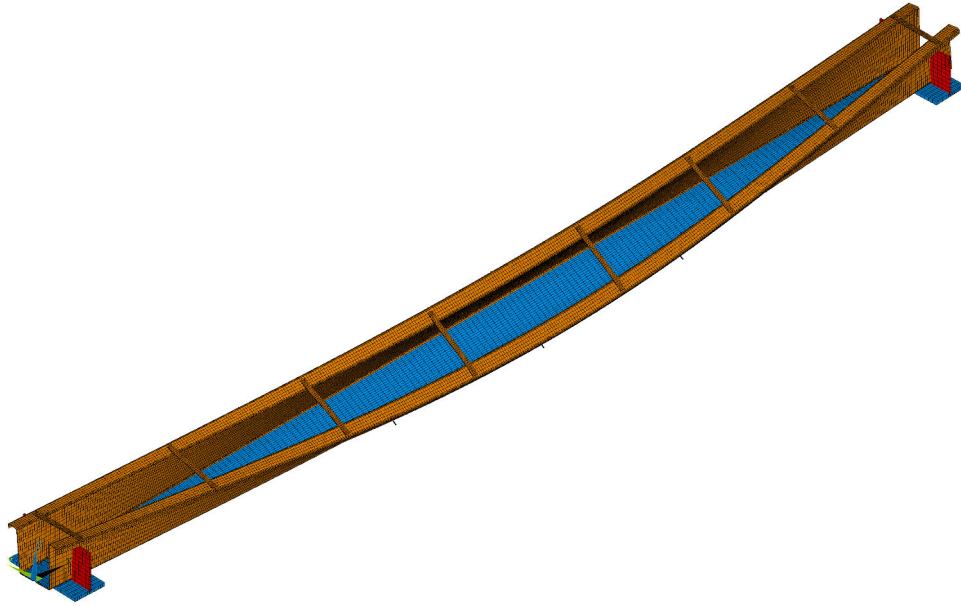


Figure 5.4 – The first Eigen mode of the numerical simulation

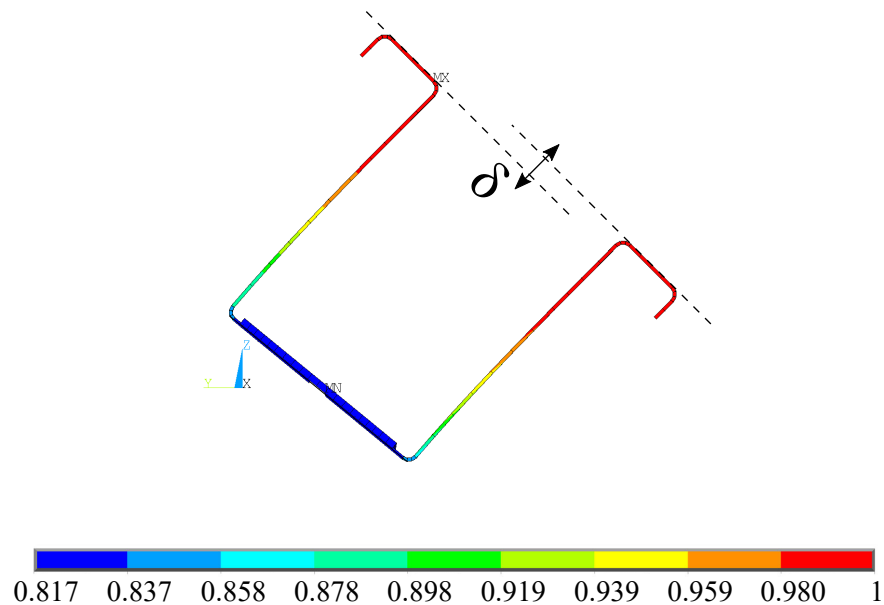


Figure 5.5 – Rotations of torsion of the nodes of the section at mid-span

Nevertheless, the elastic critical moment defines a theoretical limit for the maximum moment resistance of the cross-section subjected to LTB. Very slender sections fail elastically by LTB at an applied moment close to the elastic critical moment (M_{cr}). Intermediate slender sections fail inelastically by LTB at an applied moment (M_b) smaller than the elastic critical moment (M_{cr}) and smaller to the plastic resistance (M_{pl}). Compact sections fail at an applied moment close to the plastic moment resistance (M_{pl}), also smaller than the elastic critical moment (M_{cr}) which is very high for compact section. The specimen tested can be categorised as a very slender section and the beam failed by LTB during the test, therefore it should have failed at an applied moment close to the elastic critical moment (M_{cr}). **That is why, with this FE model and these boundary conditions, it is not possible that the elastic critical moment obtained is 50% inferior to the maximum measured moment during the test**

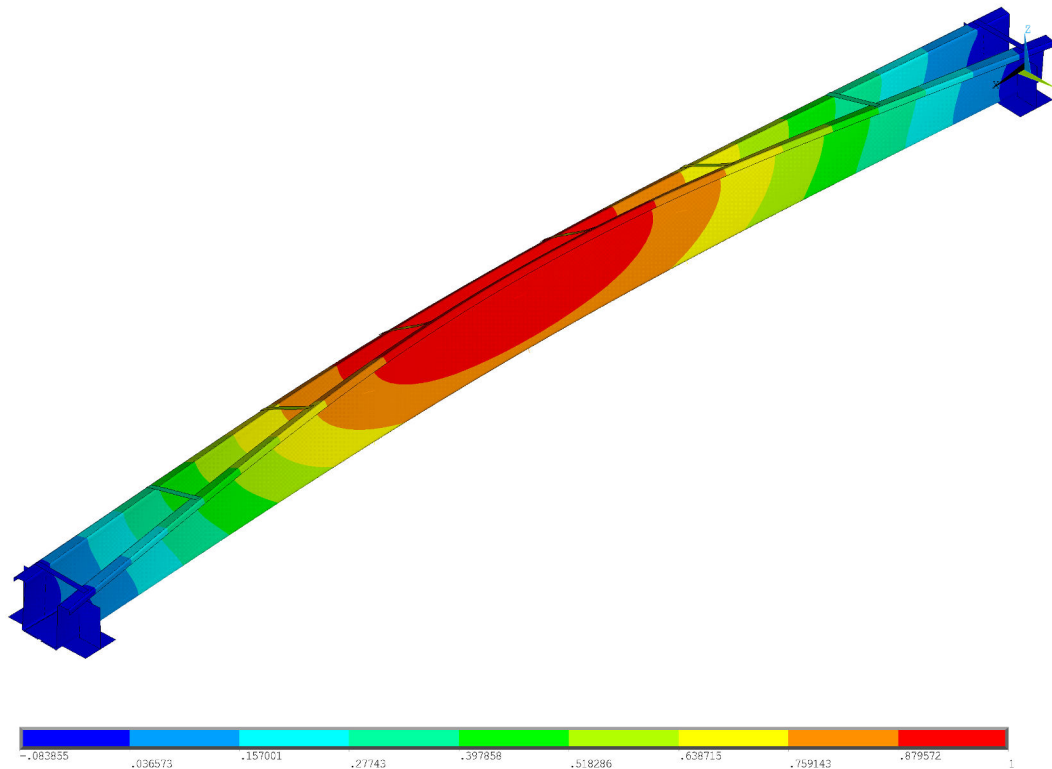


Figure 5.6 – Distribution of the rotation of torsion of the first Eigen mode

$(M_{ult,test})$. **The elastic critical moment (M_{cr}) must be closer to the maximum measured moment of the test ($M_{ult,test}$). It can be concluded that the boundary conditions of the test were more complex than this first model.**

5.5.3 Effect of the bottom plate welds at the supports

In reality, as it has already been described in § 4.2.3, the supports were also welded longitudinally between the large plate underneath the beam and the side plates of the beam (see Figure 5.7a).

These welded parts at the support restrained the rotation of the section around the longitudinal axis (θ_x , fork bearing) but add another restraint around the minor axis (θ_z) compared to the classical fork support. The welded parts added to the FE model are modelled with shell elements (see Figure 5.7b).

These shell elements link the plate underneath the beam to the side plates of the beam. The elements modelling the welding (SHELL181) have a thickness of 6 mm. **The elastic critical moment, with the consideration of welds to the bottom plate at the supports, is increased to $M_{cr,FE,weld} = 41.10\text{kNm}$. It is still 38.5% below the maximum measured moment of the test ($M_{ult,test}$ see Figure 4.40) and it clearly indicates the great sensitivity to the boundary conditions.**

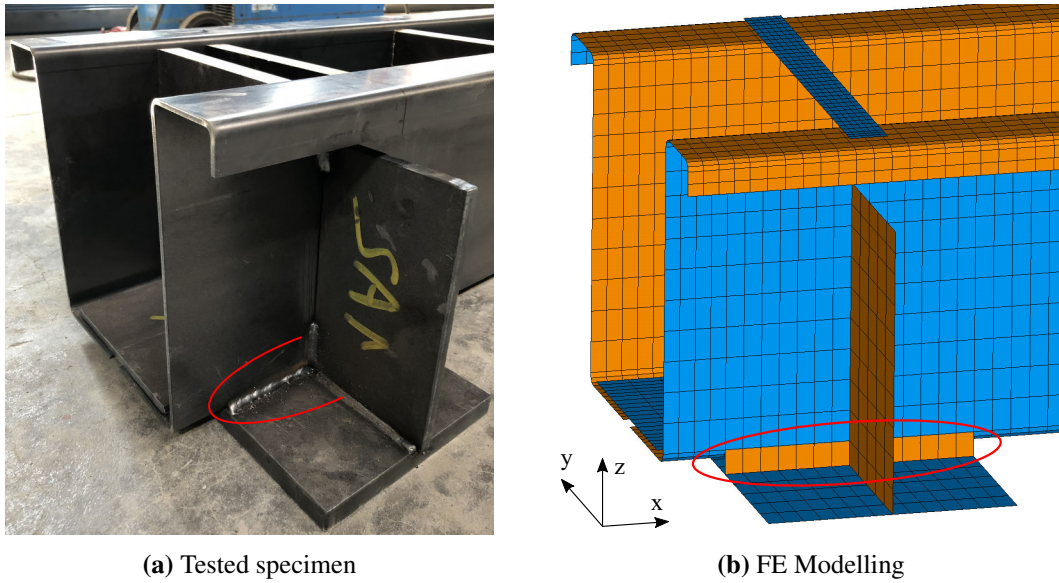


Figure 5.7 – Longitudinal welding at the supports

5.5.4 Effect of the loads introduction

During the test, the loads were introduced with two UPE270 in contact with the top flanges of the beam specimen at two positions (C and E, see Figure 4.10). Neoprene plates were placed between the top flanges of the section and the two UPE270 profiles. These neoprene plates were dedicated to spread the forces on all the surface contact and not only in one point load in order to avoid any issues due to too high concentrated stresses. Since the loading system with the chains was able to move easily in every direction, some stops were placed on both sides of the UPE and angle sections were welded to keep the position of the loads and to add more security (see Figure 5.8). **However, the warping of the top flanges of the steel specimen underneath the surface of pressure of the load introduction were restrained with a certain degree due to the high friction between steel and neoprene.**

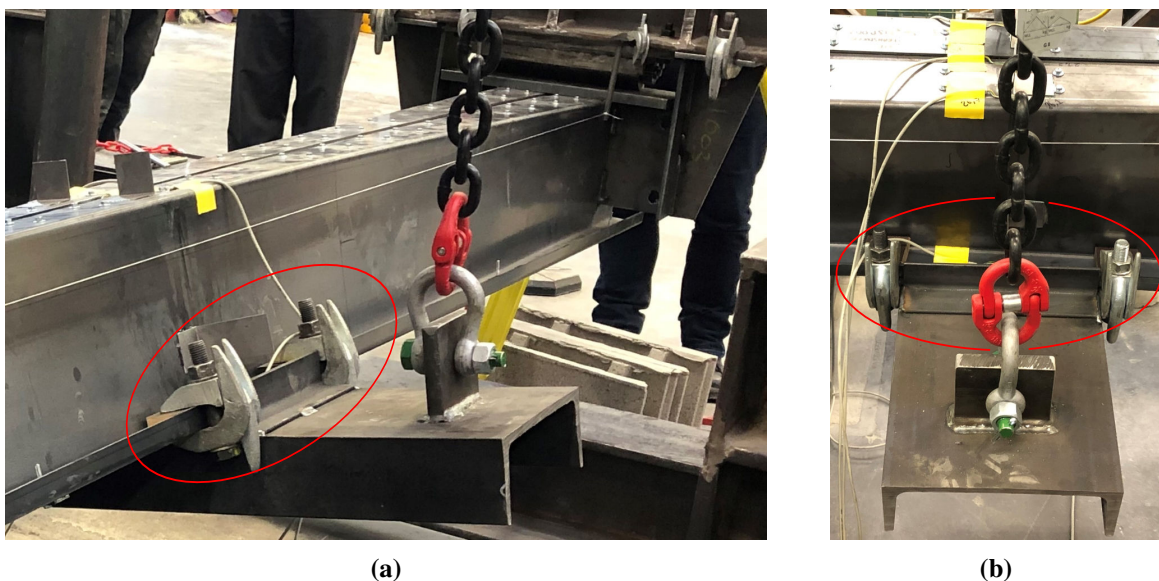


Figure 5.8 – The UPE in contact with the flanges of the beam specimen

This loading introduction, with the two UPE270 modelled with shell elements (SHELL181), is inserted in the model and a contact (“bonded always”) is set between the top flanges of the section and the two UPE270 profiles. That means the nodes are rigidly connected to consider this effect (see Figure 5.9). This assumption is strong but conceivable, as during the entire test the UPE270 stayed in contact, no slip between the loads introduction and the top flanges were observed.

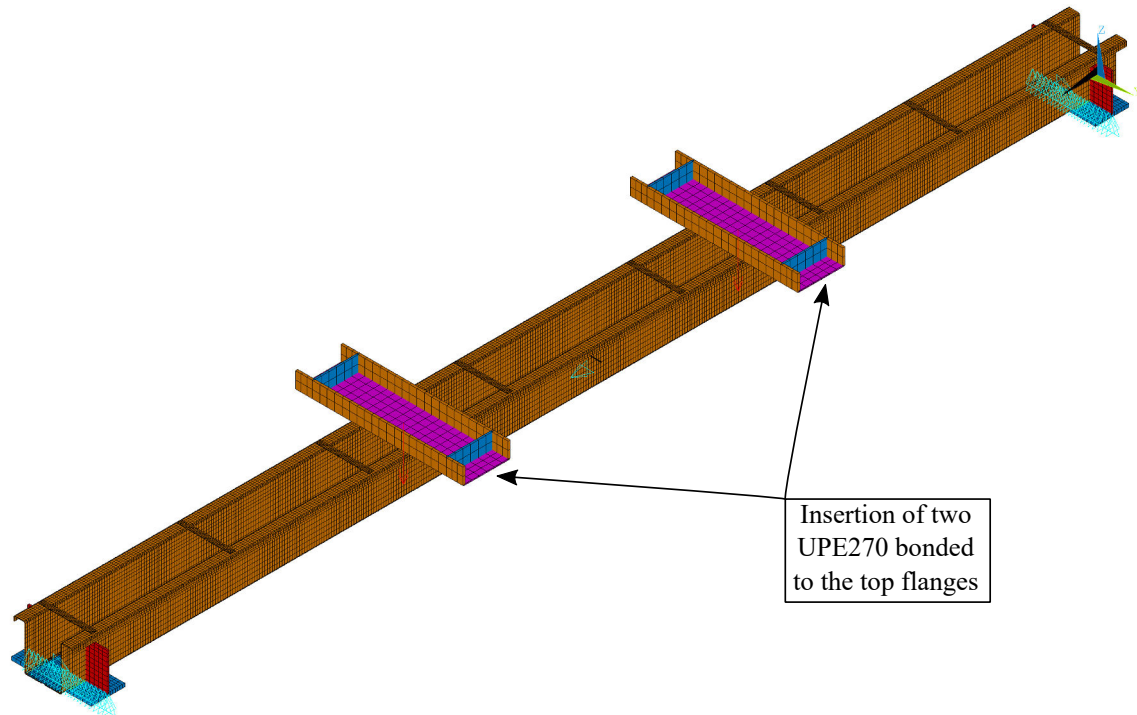


Figure 5.9 – The FEM with the loads introduction

The deformed shape obtained for the first Eigen mode with this assumption is no more the same (see Figure 5.10). In fact, the warping of the top flanges is restrained at the position of the load introduction as it is shown in Figure 5.11. Without the modelling of the loading system, the warping of the top flanges appears along the entire beam. With the restraints, the warping develops between the supports and the loading points, but is nearly zero at the middle part of the beam between the two loading points (see Figure 5.10).

The elastic critical moment increases to $M_{cr,FE,final} = 72.48 \text{ kNm}$ and it is 8.3% greater than the maximum measured moment during the test. This means the test specimen reacts very sensitively to this parameter of warping restraint.

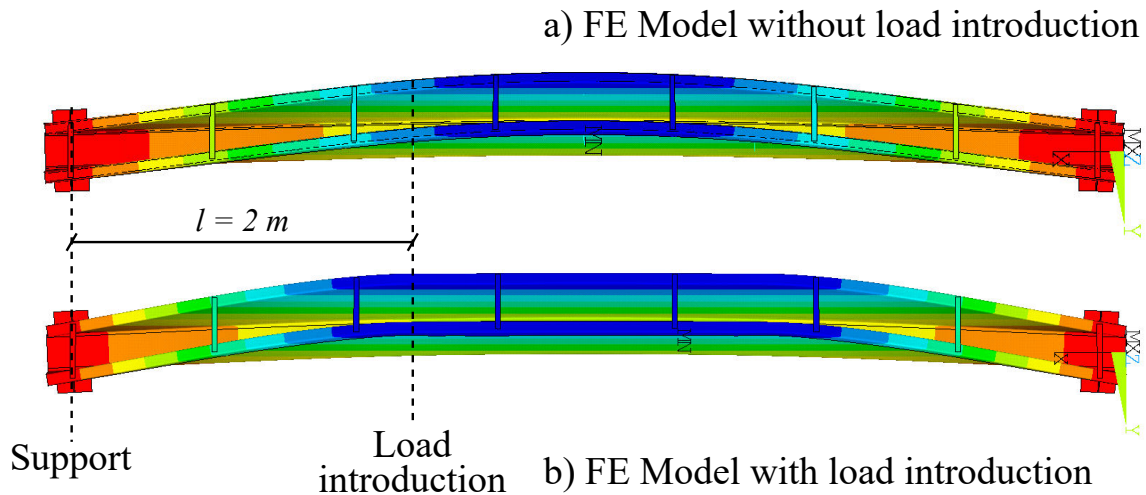


Figure 5.10 – Deformed shapes of the 1st mode a) with nodal forces b) with loads introduction

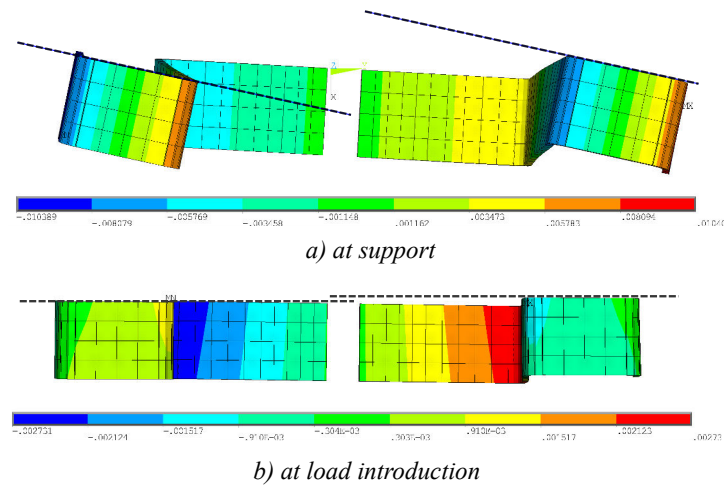


Figure 5.11 – Warping of the top flanges a) at the support and b) at load-introduction (Top view)

5.5.5 Recap of the elastic critical moment of the beam specimen

Finally, a recap of the elastic critical moment is presented in the Table 5.2.

Table 5.2 – Recap of the elastic critical moment

The maximum moment measured	Test	$M_{ult,test} = 66.92 \text{ kN m}$
Model	Method	Elastic critical moment
The beam specimen without distortion	Analytical	$M_{cr,II} = 44.4 \text{ kN m}$
	LBA (LTbeamN)	$M_{cr,LTbeamN} = 43.92 \text{ kN m}$
The beam specimen with distortion	LBA (ANSYS)	$M_{cr,FE,ideal} = 33.87 \text{ kN m}$
The beam specimen with distortion and welded supports	LBA (ANSYS)	$M_{cr,FE,weld} = 41.10 \text{ kN m}$
The beam specimen with distortion, welded supports and loads introduction	LBA (ANSYS)	$M_{cr,FE,final} = 72.48 \text{ kN m}$

As already mentioned, the elastic critical moment calculated analytically without taking into account the distortion of the section is a bit overestimated compared to the FEM model including the distortion. However, the boundary conditions are not taking into account the restraints produced by the welding and the loads introduction. When the assumptions on the boundary conditions are closer to the conditions of the test, the elastic critical moment is highly increased about 67%. This time the elastic critical moment is 8.3% above the maximum moment recorded during the test ($M_{ult, test} = 66.92 \text{ kNm}$) and this result is more logical. **For the next paragraphs, the boundary conditions are identical to the model taking into account the distortion, the welded supports and the loads introduction.**

5.6 Validation of the FE model

The geometry of the FE model and its boundary conditions are the same as proposed in § 5.5.4 : the boundary conditions include the effect of the welding at the support and the loads introduction, trying to represent the real conditions of the test.

5.6.1 Imposed displacements

Two vertical displacements are imposed on the middle of the UPE270 introducing the loads in the beam specimen. These vertical displacements are always vertical during the non-linear calculation like a destabilizing force in an analytical LTB calculation.

5.6.2 Materials properties

For both steel grades, the numerical simulations are now based on the multi-linear law proposed in ECCS-TC8 (1984) for an elasto-plastic material (see Figure 5.12). According to the tensile test results, the values are presented in Table 5.3.

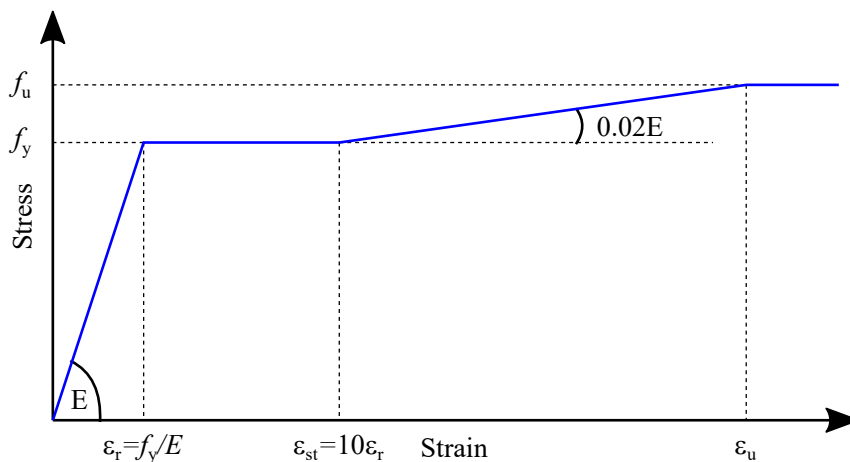


Figure 5.12 – Multi-linear material law for both steel materials

5.6.3 Influence of equivalent geometrical imperfections

The following analyses are numerical calculations taking into account geometrical and material non-linearities (GMNIA). Equivalent geometrical imperfections are added to the FE Model. The geometrical imperfections measured before the test were small (see § 4.2.4) but

Table 5.3 – Parameters of the multi-linear laws implemented in the FEM

Components	Grade	E [MPa]	f_y [MPa]	f_u [MPa]	ϵ_r	ϵ_{st}	ϵ_u
Cold-formed plates	S235	210000	322	405	0.15 %	1.53 %	3.51 %
Hot rolled plates	S355	210000	417	558	0.20 %	1.99 %	5.34 %

the equivalent geometrical imperfections in the FE model also include effects like residuals stresses, non-perfect load-application and supports (Beyer, Boissonnade, Khelil, and Bureau, 2018). That is why the imperfections in the model are higher to the imperfection measured.

According to EN 1993-1-5 (2007) § C.5, it is recommended to include global and local equivalent geometrical imperfections to the FE model. The equivalent global imperfection is in a bow shape with a magnitude e_0 . The local imperfections are in plate buckling shape with a magnitude $e_{0w} = \min(a/200; b/200)$, where a and b are the sides of the panels (see Figure 5.13).

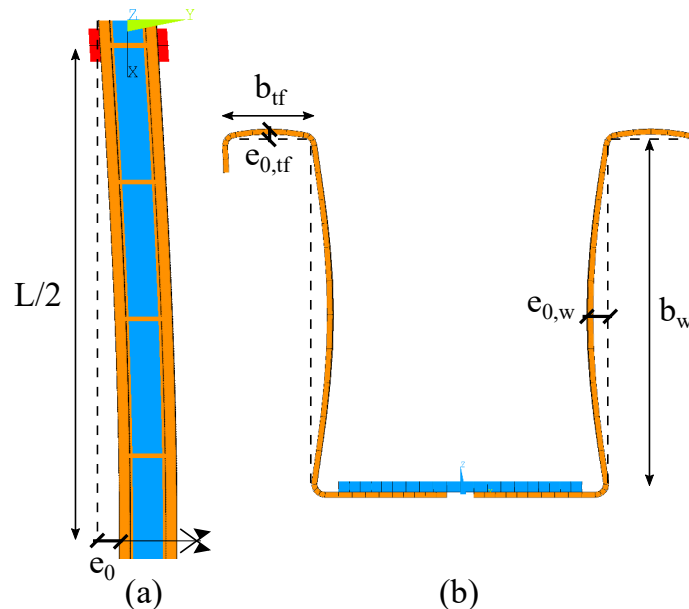


Figure 5.13 – Global and local imperfections included in the FEM model

According to EN 1993-1-5 (2007) Table C.2, the magnitude e_0 of the global imperfection can be chosen in EN 1993-1-1 (2005), table 5.1¹.

The U-section of the beam specimen is composed of plates produced by two different methods. The bottom central plate is produced out of hot rolled steel and the two side plates are cold-formed.

According to EN 1993-1-1 (2005), the cross-section should be classified in “other section”. This classification leads to the buckling curve “d”. Therefore, the magnitude e_0 should be equal to $L/100$ (see Table 5.4).

However, in simple bending, the cold-formed steel plates are the only plates in compression

¹According to EN 1993-1-1 (2005) § 5.3.4(3), the imperfections for LTB, for a second order analysis, may be adopted as ke_0 with a recommended value $k = 0.5$. For our comparison, with a non-conventional profile, it is assumed to choose a value of $k = 1.0$, that means with no reduction of the amplitude.

Table 5.4 – Design values of initial bow imperfection e_0/L (Table 5.1 of EN 1993-1-1 (2005))

Buckling curves acc. to Table 6.1	Elastic analysis	Plastic analysis
	e_0/L	e_0/L
a ₀	1/350	1/300
a	1/300	1/250
b	1/250	1/200
c	1/200	1/150
d	1/150	1/100

and on that basis, EN 1993-1-3 (2007) allows the use of the lateral buckling curve “b”. With this buckling curve, the magnitude e_0 should be equal to $L/200$ (see Table 5.4).

As the section is a mix of two cold-formed steel plates and one hot rolled steel plate, the numerical simulations are performed with different magnitudes of e_0 from $L/3000$ to $L/100$. The magnitude $L/100$ corresponds to the curve “d” and the imperfection $L/3000$ corresponds to the maximum geometrical imperfections measured on the specimen, before the test, without taking into account other effects like residual stresses.

The numerical results will give information on the initial magnitude e_0 of the equivalent geometrical imperfections that best fit with the test conducted. This can later be compared to the buckling curve recommended in EN 1993-1-1 (2005). A summary of the maximum load bearing capacity reached with the numerical simulations depending on the initial magnitude e_0 is presented in Table 5.5.

Table 5.5 – Influence of e_0 on the ultimate resisting moment

Referring to	e_0 [mm]	$M_{ult,FE,final}$ [kNm]	$\frac{M_{ult,FE,final}}{M_{ult,test}}$
curve d	$L/100 = 60$	53.4	0.80
curve c	$L/150 = 40$	58.2	0.87
curve b	$L/200 = 30$	61.2	0.91
curve a	$L/250 = 24$	63.2	0.94
curve a ₀	$L/300 = 20$	64.8	0.97
-	$L/500 = 12$	68.7	1.03
-	$L/750 = 8$	71.2	1.06
-	$L/1000 = 6$	72.6	1.09
-	$L/2000 = 3$	75.2	1.12
Measured	$L/3000 = 2$	76.1	1.14

The magnitude $L/200$ of the curve “b” (for cold-formed steel members) is slightly too conservative (ratio 0.91, see Table 5.5) compared to the laboratory test result. The ultimate bending moment of the test is reached in the numerical simulation with an initial magnitude e_0 between $L/300$ and $L/500$.

When the imperfection in the simulation is only the measured imperfection before the test ($\approx L/3000$), the peak load is overestimated by 13.7%. **This clearly shows that the equivalent geometrical imperfection covers not only the pure geometrical imperfection but also other effects** as the residual stresses due to the manufacturing process. Indeed, since the

residual stresses were not measured before the test, the role of the **equivalent** geometrical imperfection is to include this effect by a higher value compared to the measured geometrical imperfections before the test.

In addition to the comparison with the ultimate moment, the stiffness of the imperfect beam is also affected by the magnitude of the imperfection. The evolution of the lateral displacement of the target D1 in the numerical simulations depending on the initial imperfection is shown in Figure 5.14. It can be observed that the numerical model with the imperfection magnitude of $e_0 = L/1000$ describes best the experimental behaviour of the initial test phase up to a lateral displacement of 15 mm. Whereas the numerical model with the imperfection magnitude of $e_0 = L/300$ describes best the behaviour in the final test phase between 30 mm and 60 mm of lateral displacement including the assessment of the ultimate load.

A good compromise is delivered by the numerical simulation with the initial magnitude $e_0 = L/500$. The initial stiffness of the beam according to the numerical simulation is very close to the test and the ultimate moment is only 2.6% higher than the ultimate moment recorded during the test.

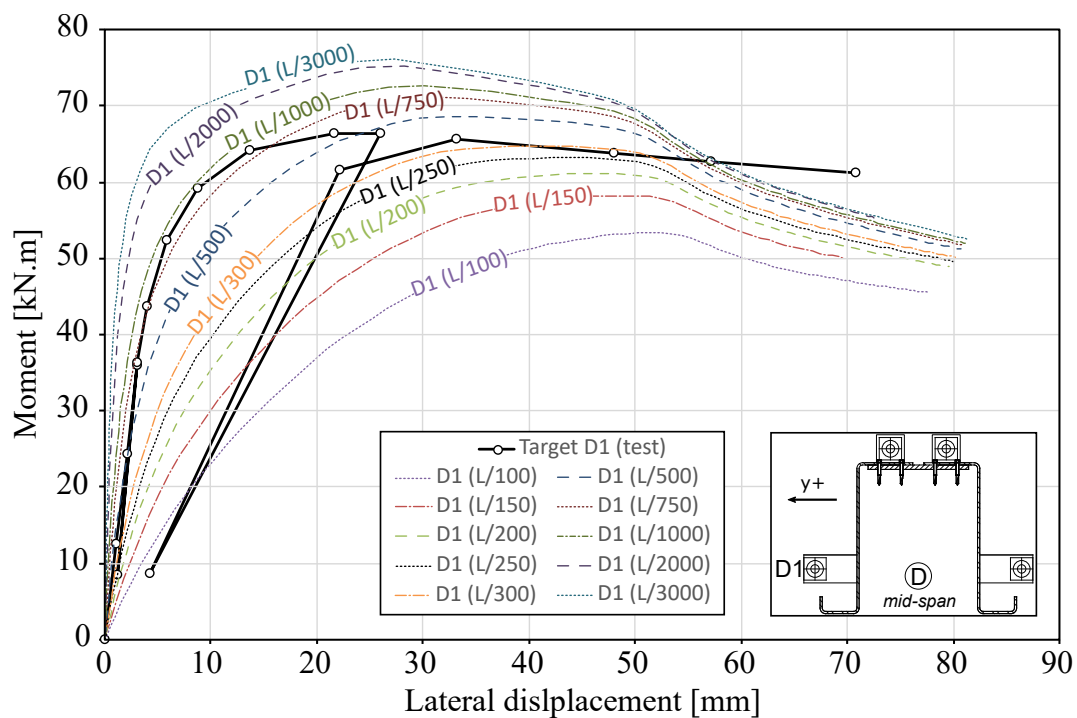


Figure 5.14 – Influence of the geometrical imperfection on the load - displacement curve

5.6.4 Effect of combined global and local imperfections

In order to evaluate the influence of local imperfections combined with the global imperfection, a comparison was carried out between a FE model with an equivalent global imperfection of $L/500$ (see Figure 5.13 (a)) compared to the same model with additional local imperfections in buckling shapes (see Figure 5.13 (b)). As it can be seen in Figure 5.15, the local imperfections do not affect significantly the result of the FE model concerning the LTB-Load, the numerical results depend only on the initial magnitude e_0 of the global imperfection. Therefore, they are not implemented in the following numerical simulations.

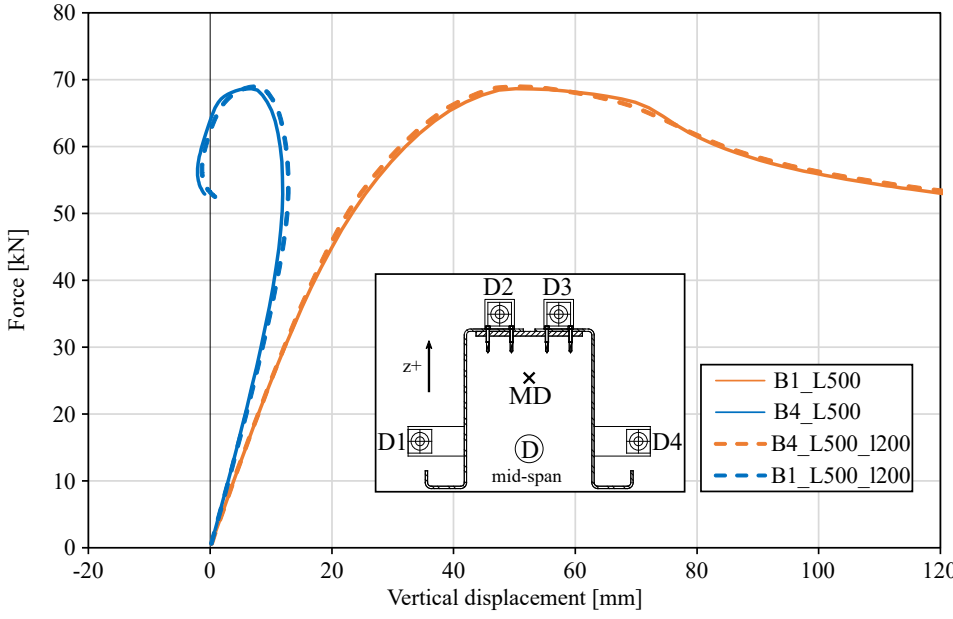


Figure 5.15 – Effect of combined global and local imperfections

5.6.5 Numerical results compared to the test results

For the comparison with the test, the imperfection magnitude e_0 is assumed to $L/500$ as explained in § 5.6.3. The deformed shape of the numerical model at the peak load is represented in Figure 5.16 (the beam is not reversed like in the test). The targets at mid-span (D1 to D4) are introduced in the model in order to compare their displacements to the test results. As shown in the Figures 5.17, 5.18, 5.19 and 5.20, the numerical results of the FE model, with the presented boundary conditions and equivalent imperfection, are in a great accordance with the test results.

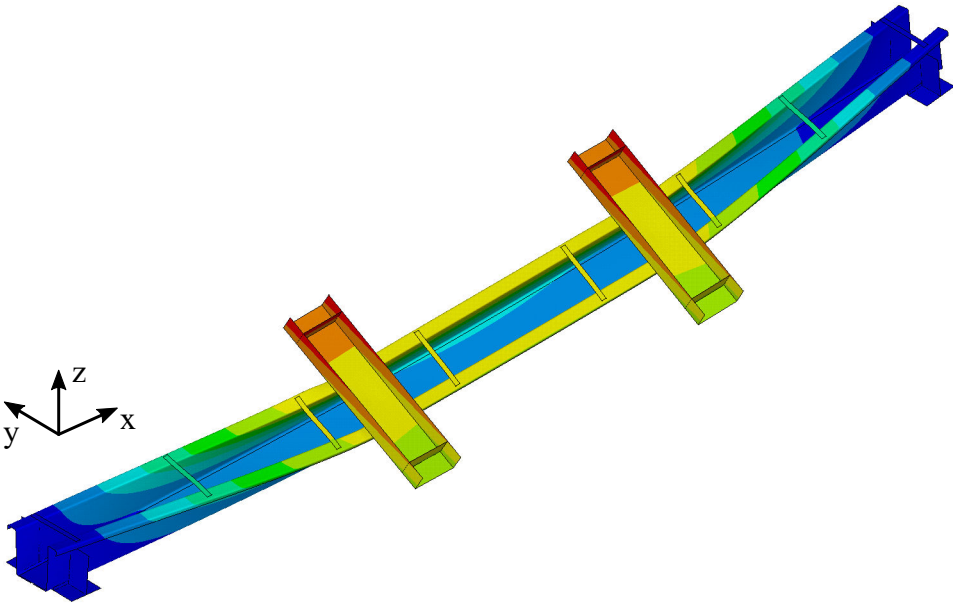


Figure 5.16 – Deformed shape at the time of the measurement n° 18 of the FE model

The displacements measured on the targets at mid-span are similar to the displacement of the numerical model. The twist of the section of the finite element model at the time of the

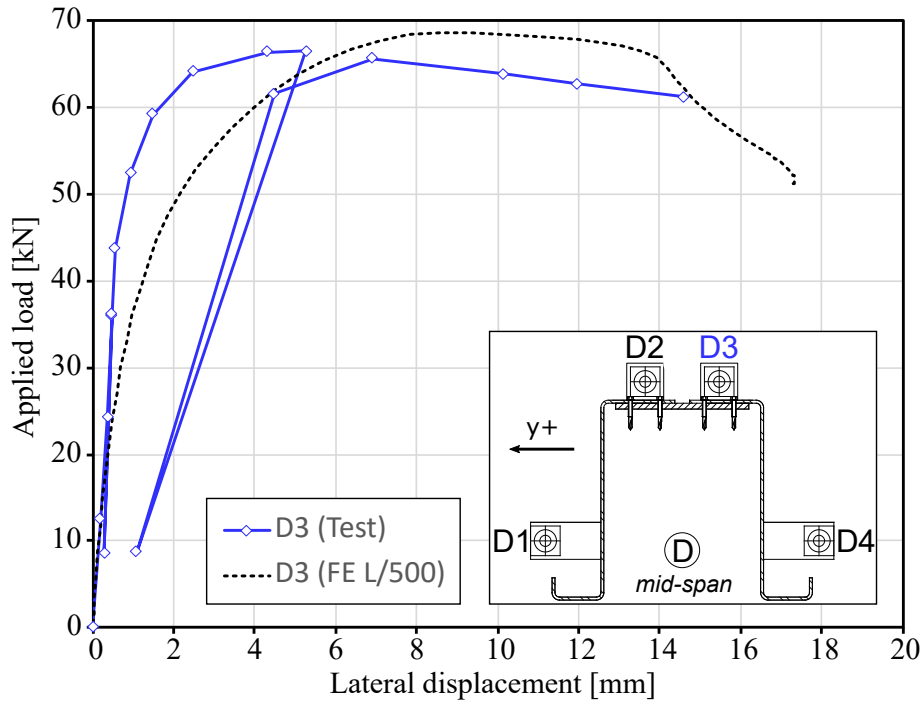


Figure 5.17 – Force - lateral disp. of the targets D3 compared to numerical results

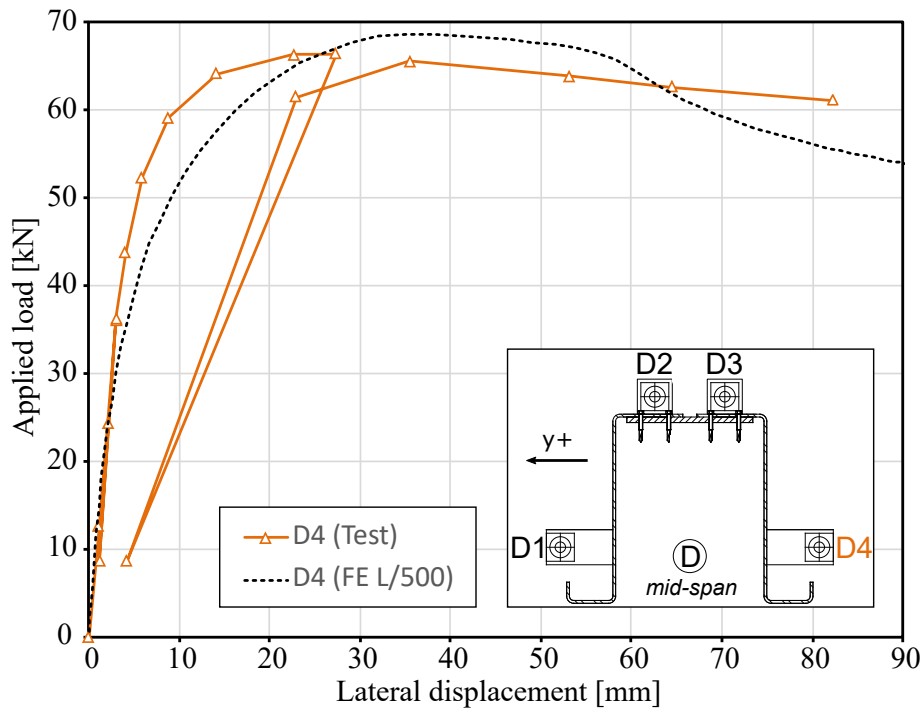


Figure 5.18 – Force - lateral disp. of the targets D4 compared to numerical results

last measurement (n° 18) is presented in Figure 5.21. Because of the small distortion of the section, the rotation is varying in the section between -0.31 rad to -0.28 rad. The maximum torsion twist of the section measured at mid span during the test was $\theta_{x,max,D} = 278.8$ mrad. The gap with the FE model is about 0.7% and 12.4% from the extrema.

Another view of the global deformed shape of the beam specimen is presented in the Figure 5.22.

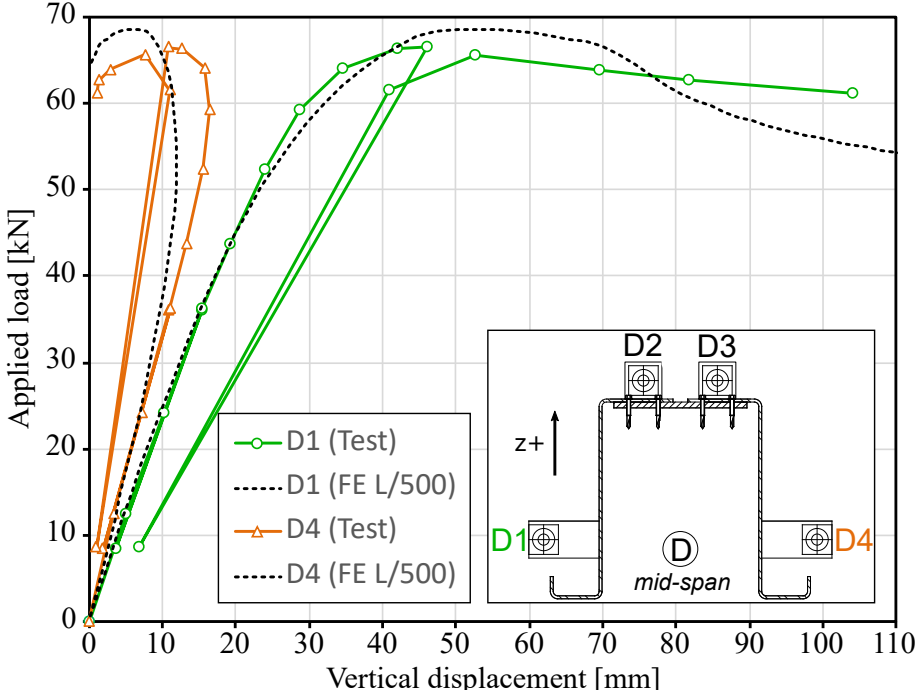


Figure 5.19 – Force - vertical disp. of the targets D1 and D4 compared to numerical results

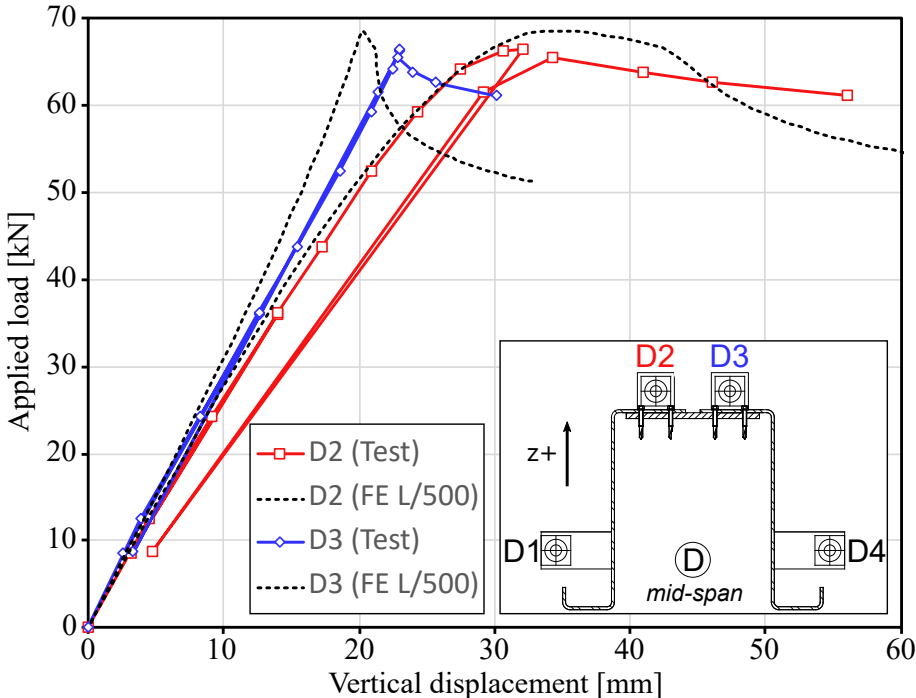


Figure 5.20 – Force - vertical disp. of the targets D2 and D3 compared to numerical results

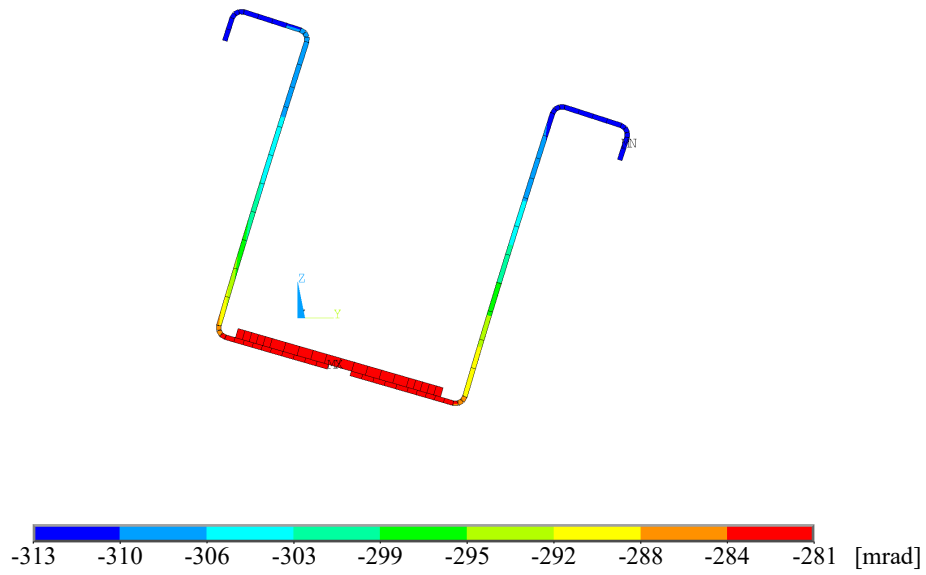


Figure 5.21 – Rotation of the section of the FEM at the measurement n° 18

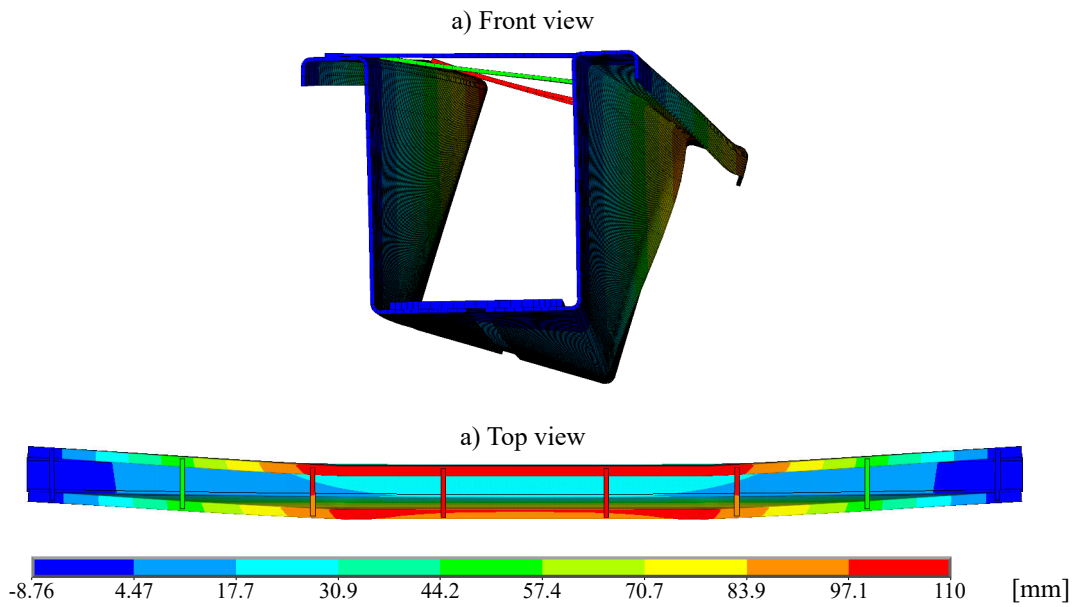


Figure 5.22 – Lateral displacement of the nodes of the FEM at the measurement n° 18

5.7 Comparison to EN 1993

In EN 1993, the cross-section is classified as “other sections” referring to the buckling curve “d” for hot rolled sections (EN 1993-1-1, 2005) or curve “b” for cold-formed sections (EN 1993-1-3, 2007). As the studied section is an assembly of plates from two different methods of fabrication, the calculation of the buckling resistance moment $M_{b,R}$ is carried out on the basis of the two buckling curves.

The non-dimensional slenderness for LTB is generally determined by Equation 5.4 (EN 1993-1-1, 2005).

$$\bar{\lambda}_{LT} = \sqrt{\frac{M_{el,R,m}}{M_{cr,FE,final}}} \quad (5.4)$$

$M_{el,R,m}$ is the elastic moment resistance of the cross-section determine by Equation 5.1. $M_{cr,FE,final}$ is the elastic critical moment determined by the numerical simulations.

The reduction factor for LTB is then obtained by Equation 5.5 (EN 1993-1-1, 2005):

$$\chi_{LT} = \frac{1}{\Phi_{LT} + \sqrt{\Phi_{LT}^2 - \bar{\lambda}_{LT}^2}} \quad (5.5)$$

Where:

$$\Phi_{LT} = \frac{1}{2} [1 + \alpha_{LT}(\bar{\lambda}_{LT} - 0.2) + \bar{\lambda}_{LT}^2] \quad (5.6)$$

$\bar{\lambda}_{LT}$ is the non-dimensional slenderness for LTB previously determined by Equation 5.4. α_{LT} is the imperfection factor defined by EN 1993-1-1 (2005) depending on the buckling curve (see Table 5.6).

Table 5.6 – Imperfection factors for LTB curves according to EN 1993-1-1 (2005)

Buckling curve	a ₀	a	b	c	d
Imperfection factor α_{LT}	0.13	0.21	0.34	0.49	0.76

Finally, the buckling resistance moment calculated with the mean values from the tensile tests and with the elastic critical moment determined with numerical simulations is determined by Equation 5.7 (EN 1993-1-1, 2005).

$$M_{b,R} = \chi_{LT} M_{el,R,m} \quad (5.7)$$

The elastic moment resistance $M_{el,R,m}$ is calculated by Equation 5.1 with the material mean values of the steel parts given in Table 4.1. The elastic critical bending moment ($M_{cr,FE,final}$) was taken from the FE analysis with the assumptions of the real boundary conditions of the test (see § 5.5.4). As it is a comparison with an experimental test, no partial safety factor is considered, that means $\gamma_{M0} = \gamma_{M1} = 1.0$.

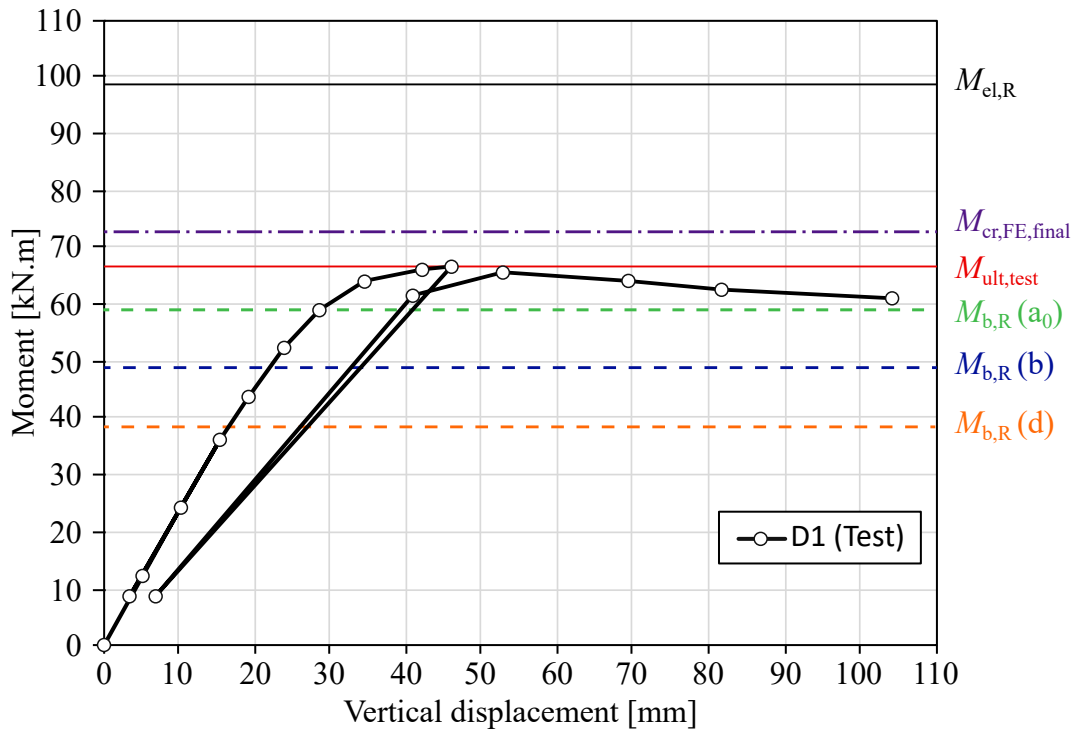


Figure 5.23 – Comparison between the different buckling moments of EN 1993 and the test result

The analytical results obtained from the two buckling curves “b” and “d” are respectively $M_{b,R}(b) = 49.0\text{ kN.m}$ and $M_{b,R}(d) = 38.5\text{ kN.m}$. For comparison purposes, the most favourable buckling moment resistance determined with the curve “a₀” is $M_{b,R}(a_0) = 59.0\text{ kN.m}$. These buckling resistance moments, according to EN 1993, are compared with the test curves, see Figure 5.23.

It can be observed that the two buckling resistant moments calculated with the curves “b” ($M_{b,R}(b)$) and “d” ($M_{b,R}(d)$) according to EN 1993-1-1 (2005) are below the ultimate resistance moment of the test ($M_{ult,test} = 66.9\text{ kN.m}$) about 26% for the curve “b” and 42% for the curve “d”. For comparison purposes, the buckling resistant moment calculated with the curves “a₀” is about 10% below the ultimate resistance moment of the test.

In an ideal case, the test result would lie only slightly above the analytical result $M_{b,R}$, which is not the case for the recommended buckling curves by EN 1993 for the studied section. This indicates, that the recommendation for the studied section are far on the safe (and uneconomic) side. Even the use of the curve “a₀” would give a more suitable result, see Figure 5.23.

Thanks to this comparison, it appears that the use of the curve “b” for the evaluation of the buckling resistance moment, according to EN 1993, for the developed U-shaped section, is placing on the safe side. The use of the curve “d” for “other section” according to EN 1993-1-1 (2005) would lead to an uneconomic design with an important underestimation of the buckling resistance moment.

5.8 Parametric study on the LTB of the U-shaped steel section

The test underlined that for the evaluation of the buckling resistance moment of the U-shaped steel section, the use of the buckling curve “b” with the design methods of EN 1993-1-1 (2005) would lead to a realistic result with security (see § 5.7). In order to confirm this assumption, a parametric study was carried out with numerical simulations on 200 geometrical configurations of the developed U-shaped steel beam.

5.8.1 The finite element model

The numerical model validated with the test in § 5.6 reproduced the particular boundary conditions of the test. In this parametric study, the beam is considered only simply supported between two ideal fork supports as described in § 5.5.2. Therefore in the FE model dedicated to the parametric study, the special other boundary conditions of the test like the welds at the support (§ 5.5.3) or the load introduction warping restraint (§ 5.5.4) are not reproduced.

5.8.2 The varied parameters

The U-shaped section developed is very slender due to the thin plates. The geometrical parameters were varied in order to cover realistic configurations for the solution.

- The span was varied from: $4\text{ m} \leq L \leq 8\text{ m}$
- The total height of the U-shaped section was varied from: $200\text{ mm} \leq h \leq 500\text{ mm}$
- The thickness of the cold-formed side plates was varied from: $4\text{ mm} \leq t_{cf} \leq 6\text{ mm}$
- The top flanges of the cold-formed side plates were varied from: $50\text{ mm} \leq b_{cf,top} \leq 100\text{ mm}$

The variation of the total height (h) of the section was linked to the variation of the webs height. The other main dimensions stayed constants and are presented in Table 5.7.

5.8.3 Methodology

For each geometrical configuration, the methodology followed for the parametric study was:

1. The elastic critical moment $M_{cr,FE,ideal}$ is calculated by LBA analysis with ANSYS. The material laws for the steel parts are only elastic.
2. The elasto-plastic bending resistant moment $M_{epl,R}$ is calculated by GMNIA analysis with ANSYS. The material laws for the steel parts followed the elasto-plastic curves as recommended by ECCS-TC8 (1984) and shown in Figure 5.12 **including strength hardening**. The model includes initial local imperfections in buckling shapes in the steel plates in order to obtain plate buckling for slender section (see Figure 5.13). The local imperfection’s magnitudes are defined by $e_{0w} = \min(a/200; b/200)$ where a and b are the sides of the panels as recommended by EN 1993-1-5 (2007). Thus for compact section, the elasto-plastic bending resistance obtained could be superior to the plastic bending resistance moment calculated according to EN 1993-1-1 (2005) due to strength hardening ($M_{epl,R} > M_{pl,R}$). Furthermore, for higher slender section (class 3),

Table 5.7 – The dimensions of the cross-section specimen that stayed constants

Designation	Symbol	Values
Hot rolled central plate (1)		
- Thickness	t_{hr}	8 mm
- Width	b_{hr}	180 mm
- Mean measured yield strength	$f_{y,hr,m}$	417 MPa
- Mean measured tensile strength	$f_{u,hr,m}$	558 MPa
Cold-formed side plates (2, 3)		
- Bottom flanges width	$b_{cf,inf}$	100 mm
- Edge stiffeners height	c_{cf}	30 mm
- Mean measured yield strength	$f_{y,cf,m}$	322 MPa
- Mean measured tensile strength	$f_{u,cf,m}$	406 MPa
Steel battens (5)		
- Thickness	t_{bat}	4 mm
- Width	b_{bat}	30 mm
- Length	l_{bat}	320 mm

the elasto-plastic bending resistance can be inferior to the plastic bending resistance moment and for very slender sections (class 4) inferior to the elastic bending resistance of a full effective section $M_{el,R}$.

3. The ultimate bending resistant moment $M_{ep1,ult}$ considering the effect of LTB is calculated by GMNIA analysis with ANSYS. The FE models were similar to the ones used in (2.) and include an additional initial global equivalent imperfection in a bow shape in order to induce the LTB of the beam. Although the FE model of the test was validated compared to the test results with a magnitude for the global imperfection of $e_0 = L/500$, for the parametric study the magnitude is fixed to $e_0 = L/200$ as recommended for a plastic analysis by EN 1993-1-1 (2005) table 5.1. In fact, for the parametric study, the model does not reproduce the conditions of the test, but a more realistic use and a higher global imperfection is giving more security on the analysis. In this study, the ultimate bending resistant moment $M_{ep1,ult}$ is taken at the peak of the applied moment versus displacement curve. However, for very slender beams in regards to the span, when $2.0 \leq \bar{\lambda}_{LT} \leq 3.0$, the rotations were so important that the initial second moment of area of the beam along the minor axis (I_z) is playing a role in the bending resistance at very high displacements. Therefore, the applied moment never decreases, rather, after the instability and the high rotation, the applied moment could even increase as shown in Figure 5.24. Outside numerical simulation, this phenomenon could not occur because the applied load would never follow such a rotation. Nevertheless, the stiffness of the beam K decreases with the LTB instability and increases again at very high displacement and rotation in this particular case (see Figure 5.24). Thus, for this particular case, it was decided to define the ultimate bending resistant moment $M_{ep1,ult}$ at the last step before the new increase of stiffness. In other words, the maximum resistant moment $M_{ep1,ult}$ is the applied moment when the derivative of the stiffness $\frac{dK}{dU_z}$ is changing sign (see the green curve in Figure 5.24). This is giving the calculation step of the maximum resistant moment $M_{ep1,ult}$ (see the blue curve in Figure 5.24).

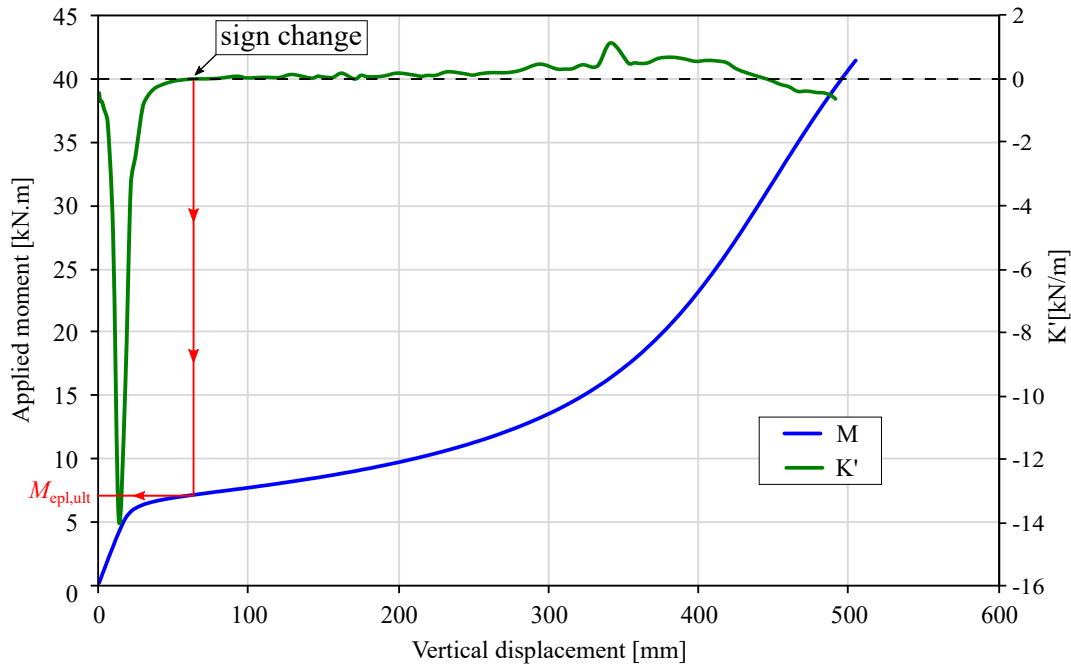


Figure 5.24 – Definition of the ultimate bending resistant moment $M_{epl,ult}$ for particular cases very slender

4. Finally, the non-dimensional slenderness for lateral torsional buckling (λ_{LT}) is calculated by Equation 5.8 and the reduction factor for lateral-torsional buckling is calculated by Equation 5.9.

$$\bar{\lambda}_{LT} = \sqrt{\frac{M_{epl,R}}{M_{cr,FE,ideal}}} \quad (5.8)$$

$$\chi_{LT} = \frac{M_{epl,ult}}{M_{epl,R}} \quad (5.9)$$

5.8.4 Results

The results of the parametric study are presented in Figures 5.25 and 5.26. The detailed results for each configuration are presented in Annex D. Each geometrical configuration is represented in these Figures by a single point. As the main varied parameters were the thickness of the cold-formed side plates (t_{cf}) and the span (L), the results are shown with a particular legend. The points are in the form of a circle for $t_{cf} = 4$ mm, a triangle for $t_{cf} = 5$ mm and a square for $t_{cf} = 6$ mm. Additionally, the color of each point depends on the span studied (red: $L = 4$ m, green: $L = 4.5$ m, blue: $L = 5$ m and brown: $L \geq 6$ m). In fact, due to the high slenderness of the studied beam, for the span between 7 and 8 meters, only very few points were below $\bar{\lambda}_{LT} = 3.0$ and are represented.

As shown in Figures 5.25 and 5.26, most of the configurations are above the limit of the curve “b” defined in EN 1993-1-1 (2005). The initial geometrical imperfection in a bow shape was inserted with magnitude of $e_0 = L/200$ corresponding to a plastic analysis according to the

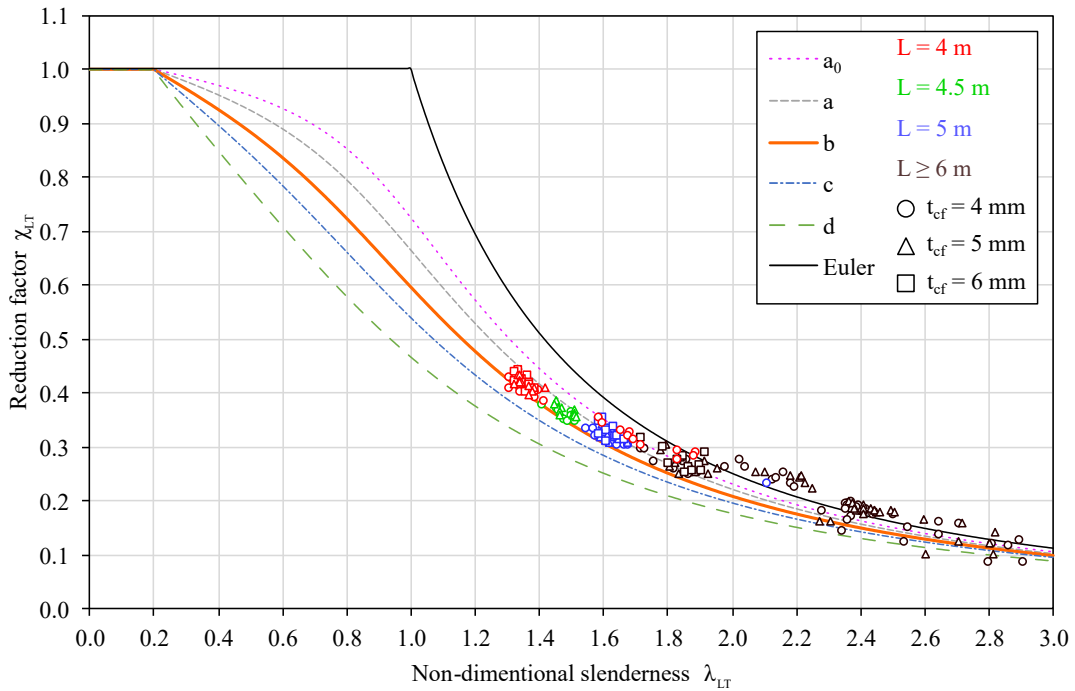


Figure 5.25 – χ_{LT} vs. $\bar{\lambda}_{LT}$ for LTB with the configurations of the parametric study

curve “b” (EN 1993-1-1 (2005)). It can be concluded that the results are in accordance with the recommendation for almost every configuration. The tests underlined that the use of the curve “b” for the design of the buckling resistance moment for LTB placed in the safe side. This parametric study with extend geometrical configurations confirms that the mechanical behaviour of the beam is predictable with the use of the curve “b” in the design methods proposed in EN 1993-1-1 (2005).

For very slender beams, when $2.0 \leq \bar{\lambda}_{LT} \leq 3.0$, some of the results are beyond the Euler curve, normally this is not realistic, whereas some of the results are lower than the curve “d”. This dispersion of the results probably comes from the way to define the ultimate bending resistant moment $M_{epl,ult}$ as described in the Methodology (§ 5.8.3 3.). In fact, for these particular cases, the value of $M_{epl,ult}$ is not at the peak load and the criteria defined on the variation on the stiffness leads to less precision.

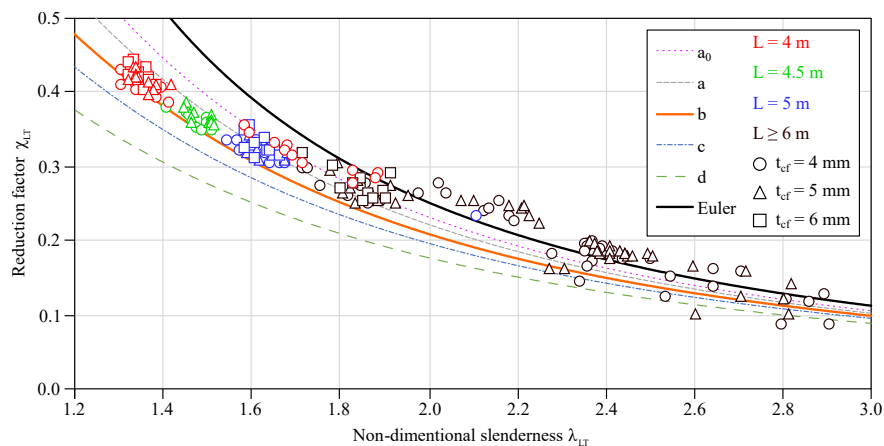


Figure 5.26 – χ_{LT} vs. $\bar{\lambda}_{LT}$ for LTB with the configurations of the parametric study (Zoom)

5.9 Modeling of the lateral restraint provided by perpendicular steel decks

Although the use of the buckling curve "b" seems to best describe the LTB instability of this type of section, with a certain security, the beam is very slender and thus very sensitive to the global instability of LTB leading to important reduction factors $0.2 \leq \chi_{LT} \leq 0.4$ (see Figure 5.26). Therefore, to overcome the problem of instability in the construction stage, the effect of the lateral restraint provided by perpendicular steel decks is investigated in this paragraph. This study has been already presented in the International Conference on Engineering Research and Practice for Steel Construction 2018 (ICSC2018) (Turetta, Khelil, Odenbreit, and Martin, 2018).

The beam solution developed in this project is for traditional secondary beams of composite floor in buildings, this type of floor is often made with steel decks. In many cases, they are fixed perpendicularly to those beams and provide a restraint against LTB. This restraint can be evaluated analytically as described in ECCS-TC7 (1995). In our situation, the steel decks are discontinuous (to let the place for concrete casting) and the U-shaped beam sections are not standard profiles. Thus, it was decided to numerically model the steel decks with shell elements (SHELL181) in the FE model to see the effect of the restraint. The FE model is now composed of three beams of that type and two commercial steel decks (with the size of COFRAPLUS60) as described in Figure 5.27.

In order to not overestimate the restraint, the modelling assumptions on the connection between the steel decks and the steel flanges are less constraining than in reality (See Figure 5.28):

1. The contact steel-steel between the steel decks and the section flanges is modelled sliding without friction whereas in real situation, the contact is rough.
2. The nailing is modelled with an articulated link whereas in real situation, the nailing rigidly connects the common nodes.

Additionally to the assumptions made on the connection of the steel decks on the top flanges of the U-shaped beam, the magnitude of the initial global geometrical imperfection retained for the comparison is the most unfavourable case, that means $e_0 = L/100$. This is the most unfavorable equivalent imperfection according to EN 1993-1-1 (2005). This give an additional security; if the beams are stabilised by the steel decks with this imperfection, it can

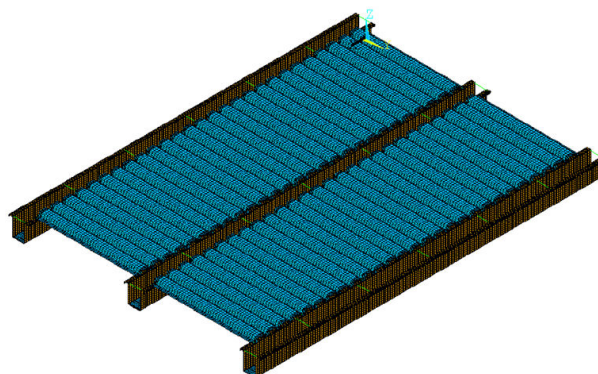


Figure 5.27 – FE model with three beams and two perpendicular steel decks not continuous

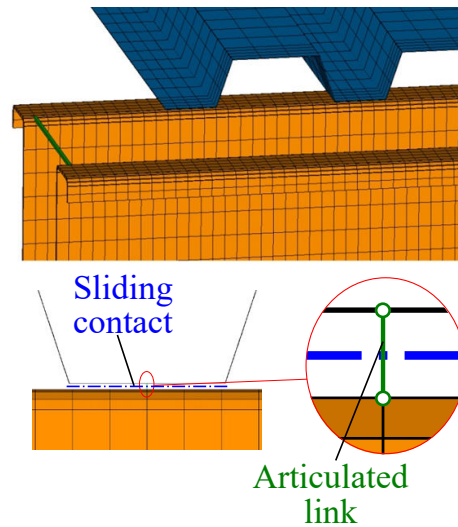


Figure 5.28 – Model of the connection between the steel deck and a top flange of the steel section

be concluded that the stabilisation provided does not depend on the beam buckling curve classification for LTB (curve a_0 , a, b, c, d). This imperfection, in a bow shape, is introduced in the three beams as represented in Figure 5.27.

For a better understanding, the load bearing capacity of the beam is expressed by the coefficient $\alpha_{ULS,c}$ (see Equation 5.10) which is the ratio of the applied loading on the loading in the construction stage combined with the ULS combination according to EN 1990 (2003). When $\alpha_{ULS,c} \geq 1.0$, the U-shaped steel beam is able to resist the loading in the construction stage at ULS.

$$\alpha_{ULS,c} = \frac{q_{load}}{q_{ULS,c}} \quad (5.10)$$

The results of the carried out simulations underlined that the perpendicular steel decks, **nailed in each rib of the steel decking**, provide a full restraint to the U-shaped steel beam. For instance, a comparison is made with the U-shaped beam of the same geometrical configuration tested at the laboratory of Luxembourg as described in § 4.2.1 with and without the presence of perpendicular steel decks in the FE model (with the same span of 6 m). It can be clearly seen in Figure 5.29 that the U-shaped beam without restraint is not resisting alone the loading in the construction stage combined at ULS ($\alpha_{ULS,c} < 1.0$), whereas the same beam with the perpendicular steel deck modeled is resisting the ULS_c loads with a great security ($\alpha_{ULS,c} > 2.0$). The mechanical behaviour of the beam restrained by steel decking is linear and started to be non-linear only at $\alpha_{ULS,c} \approx 2.1$.

Considering the lateral restraint provided by perpendicular steel decks, the failure mode of the beam is no more a LTB instability but a plate buckling instability. In fact, the section resistance is reached at mid-span and one of the top flanges yielded and started to buckle. This failure mode appears with twice the loading of the combination for the construction stage. Therefore, the developed solution should work in a real situation with sufficient security if it is used with perpendicular steel decks.

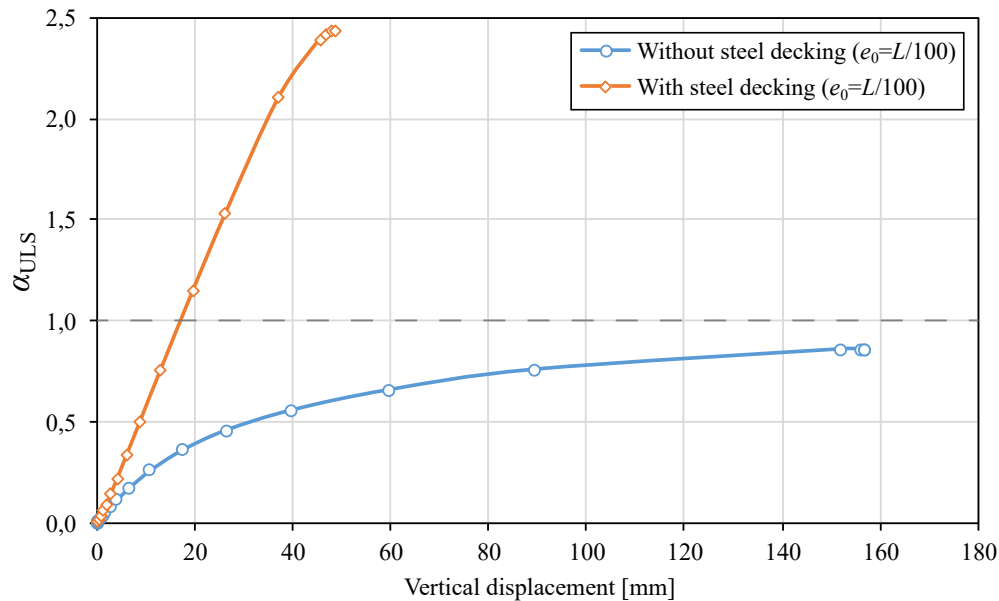


Figure 5.29 – Comparison of the load bearing capacity of the U-shaped beam in the construction stage with or without the steel decks restraint

5.10 Conclusions

The numerical studies to investigate the LTB behaviour of the U-shaped steel beam leads to the following conclusions:

- The numerical studies reproduced the global instability of LTB of the U-shaped steel beam which was shown in the test with good accuracy.
- The loading system designed for the test had a warping restraint effect onto the section at their locations. This effect could have been reduced with only one point load at mid-span because the warping restraint at mid-span has a lessened effect on the critical elastic moment. This can be chosen for further LTB tests.
- The FE analysis performed with ANSYS with an equivalent imperfection in a bow shape with a magnitude of $e_0=L/500$ fits within a certain tolerance with the tests curves.
- The section is an assembly of different steel plates made with two different fabrication processes (hot rolled and cold-formed). According to EN 1993-1-1 (2005), the design buckling resistance moment of a member susceptible to LTB should be determined using the lateral buckling curve “b” for cold-formed sections or “d” for “other” hot rolled sections. From the test results and from numerical simulations, it can be concluded that the use of the curve “b” for the evaluation of the buckling resistance moment according to EN 1993-1-1 (2005) of the tested U-section is on the safe side.
- The U-shaped beam is very slender and prone to the LTB instability leading to high reduction factors even with the use of the buckling curve "b". Therefore, in the construction stage, the beam has to be restrained against this global instability. One solution is to consider the effect of the lateral restraint provided by the perpendicular steel decking as recommended by ECCS-TC7 (1995). In this case, the steel decking is not continuous but numerical simulations carried out confirm that this effect is really strong and allow to avoid the LTB to occur if the steel decks are **nailed in each rib**.

Chapter 6

Conducted composite beam test

Contents

6.1	Objectives of the test	152
6.2	Test specimen	152
6.2.1	Geometry	152
6.2.2	Material	154
6.2.3	Fabrication	156
6.3	Layout	163
6.4	Test setup	164
6.5	Measurements	165
6.5.1	Displacement sensors	165
6.5.2	Strain gauges	169
6.6	Test procedure	169
6.7	Test results	170
6.7.1	Observations during the test and failure mode	170
6.7.2	Effect of the self-weight	172
6.7.3	Moment-displacement curve	174
6.7.4	Evolution of the deflection	174
6.7.5	Slip at the steel-concrete interface	176
6.7.6	Strain	179
6.8	Investigation on the failure mode of the composite beam	183
6.9	Conclusions	186

6.1 Objectives of the test

Once the concrete hardened, the U-shaped steel beam is connected to the reinforced concrete part. The composite behaviour is activated through the shear connection. In this project, the connection is realized with headed studs welded on the bottom flange of the U-shaped beam. The connection is then located in tension zone in simple bending. Thus, the efficiency of the connection is questionable and therefore the real composite behaviour of the proposed solution. A full-scale test was then carried out at the Laboratory of the University of Luxembourg in order to investigate the mechanical behaviour of the composite beam and therefore, the efficiency of the shear connection.

6.2 Test specimen

6.2.1 Geometry

The specimen tested has the same dimensions of the solution proposed for a normal use with the same span. The span of the beam at the laboratory was 6 meters. The total length of the beam was 6.3 meters, the beam extended beyond the supports by 150 mm at each side. The test specimen is a steel U-shaped section connected to a T-shaped reinforced concrete part as described in Figure 6.1.

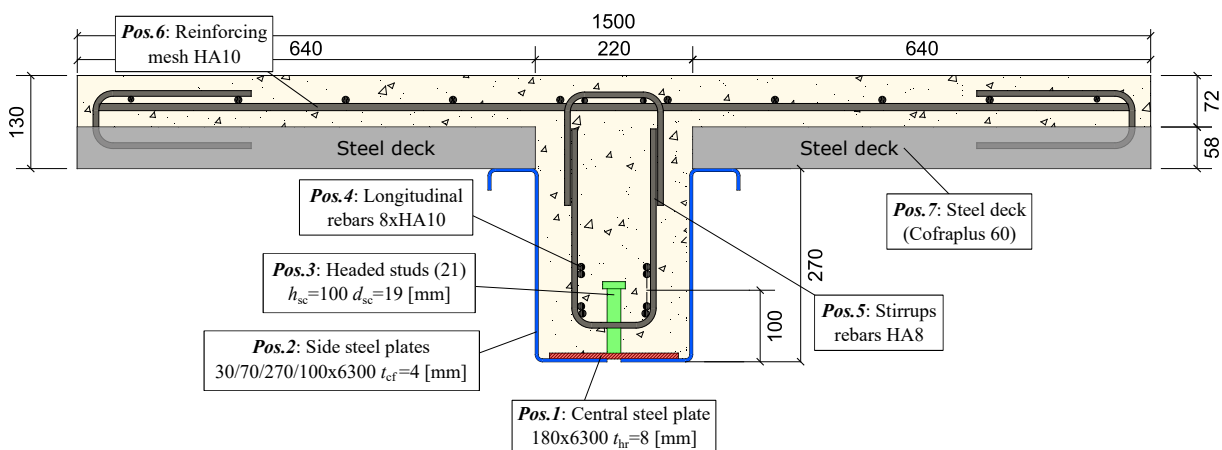


Figure 6.1 – Cross-section of the composite beam specimen tested

The U-shaped steel section is composed of three steel parts assembled together, a hot rolled steel plate (*Pos. 1* in Figure 6.1) and two cold-formed steel plates (*Pos. 2* in Figure 6.1), assembled together. The hot rolled central steel plate forms the bottom of the steel section. The cold-formed steel plates are folded in an asymmetric Z section with an edge stiffener on their top flanges. These side folded plates constitute the webs and the top flanges of the steel section. Eight steel battens connect the top flanges of the section, they are regularly spaced 828 mm along the beam. These battens prevent the section from too much opening. The steel section is 270 mm high and 220 mm wide without considering the width of the top flanges or 352 mm in total.

The reinforced T-shaped concrete section comprises a composite slab and a downstand beam. The composite slab is made with the steel deck COFRAPLUS60® (*Pos. 7* in Figure 6.1). The height of the steel deck is 58 mm with a thickness of 0.75 mm. The height of the concrete on top of the steel deck is 72 mm and this leads to a total height of the composite slab of 130 mm.

The width of the slab is 1.5 m limited by the effectiveness slab width (b_{eff}) according to EN 1994-1-1 (2005) (see Eq. 6.1). The composite slab was reinforced with a wire mesh (type ST25C, $A_{s,\text{slab}}$ see Table 6.1, **Pos.6** in Figure 6.1) whereas the downstand part was reinforced with longitudinal rebars (8xHA10, A_s see Table 6.1, **Pos.4** in Figure 6.1) and stirrups (HA8, **Pos.5** in Figure 6.1). The amount of longitudinal rebars was determined for the fire situation with the required cover (here $c = 45$ mm), as it would be the case for a real use.

$$b_{\text{eff}} = 2 \times \frac{L_e}{8} \quad (6.1)$$

In order to prevent an uplifting failure between the slab and the downstand beam like that found by Liu et al. (2018) (see § 2.3.5), the stirrups were divided in two folded U-shaped parts (**Pos.5** in Figure 6.1). The first part at the bottom linked the longitudinal rebars. The second part connected the reinforcing mesh of the slab to the first part and therefore to the longitudinal rebars. The shear connection was realised by welding headed studs (**Pos.3** in Figure 6.1) on the bottom plate. The bottom plate (**Pos.1** in Figure 6.1) was thicker than the cold-formed plates (**Pos.2** in Figure 6.1) for two reasons. First, the plate located at the extreme fibre of the section would significantly contribute to the bending resistance of the composite beam. Second, according to the 42 tests carried out by Goble (1968) (see § 2.4.3), the thickness of the steel flange cannot be lower than $0.37d_{sc}$ (were d_{sc} is the diameter of the shear studs, here $d_{sc} = 19$ mm) in order to avoid the pull-out of the headed studs from the steel plate.

The main dimensions of the steel-concrete composite section are presented in Table 6.1 and a more detailed representation of the U-shaped steel section is given in Figure 4.1a.

Table 6.1 – Main dimensions of the composite section

Definition	Symbol	Value	Units
Effective width of the composite slab	b_{eff}	1.5	m
Height of the concrete slab	h_c	72	mm
Height of the steel deck	h_p	58	mm
Area of the reinforcement in the composite slab in both direction	$A_{s,\text{slab}}$	3.35	cm ² /m
Width of the downstand reinforced concrete beam	b_{rc}	212	mm
Height of the downstand reinforced concrete beam	h_{rc}	258	mm
Area of the longitudinal reinforcement	A_s	6.283	cm ²
Thickness of the hot rolled central plate	t_{hr}	8	mm
Width of the hot rolled central plate	b_{hr}	180	mm
Thickness of the cold-formed side plates	t_{cf}	4	mm
Cold-formed edge stiffeners height	c_{cf}	30	mm
Cold-formed top flanges width	$b_{cf,\text{sup}}$	70	mm
Cold-formed webs height	$h_{cf,w}$	270	mm
Cold-formed bottom flanges width	$b_{cf,\text{inf}}$	100	mm

6.2.2 Material

The tensile and compression tests on the materials were performed by the technical team at the laboratory of the University of Luxembourg (see Appendix A and B for the reports). The main results are presented in this paragraph.

Tensile test on the steel parts

For the steel beam, the same steel plates with the same steel grades used for the steel beam test were used for the composite beam test. Therefore, their material characteristics were already presented in Chapter 4 (see § 4.2.2). The main results of the tensile tests are presented in Table 4.3 and Table 4.4.

The steel rebars class was B500 B, their minimum expected yield strengths were $f_s = 500$ MPa. From remaining bars, 10 coupons were cut (R1 to R10) and tested (see Figure 6.2). The main results of the tensile tests performed on the rebars are presented in Table 6.2. For each steel grade, the experimental values were in accordance with the recommended values of EN 10025-2 (2005).

The mean measured values of the steel parts are used to reproduce the results of the tests in numerical simulations and analytical calculations. The mean measured values are presented in Table 6.4 (see Appendix A for the detailed reports).



Figure 6.2 – Tensile specimens of the rebars (R1 to R10)

Compression test on the concrete part

The concrete ordered for the test was a C35/45 with a limit size of the maximum granulates of $D_{\max} = 8$ mm with a consistency class F2. In total, six concrete cubes (CUB1 to CUB6) and six cylinders (CYL1 to CYL6) were prepared for compression tests at the same time as the concreting of the composite beam. The compression tests were carried out 34 days after the concreting. The compression strength results are presented in Table 6.3 (see Appendix B for the detailed reports). From these results, the experimental mean value for the concrete is $f_{c,m} = 53.4$ MPa.

Table 6.2 – Tensile tests results of the rebars

Specimens	Grade	ReH [MPa]	Rm [MPa]
R1	Fe500	585	681
R2	Fe500	583	681
R3	Fe500	583	689
R4	Fe500	582	682
R5	Fe500	580	684
R6	Fe500	576	682
R7	Fe500	581	681
R8	Fe500	582	682
R9	Fe500	574	676
R10	Fe500	580	686

Table 6.3 – Compression strength of the concrete specimens

Specimens	Class	RH [MPa]
CYL1	C35/45	54.1
CYL2	C35/45	52.6
CYL3	C35/45	50.9
CYL4	C35/45	55.1
CYL5	C35/45	53.4
CYL6	C35/45	54.1
CUB1	C35/45	61.3
CUB2	C35/45	59.3
CUB3	C35/45	60.3
CUB4	C35/45	61.7
CUB5	C35/45	62.9
CUB6	C35/45	60.4

Finally, all the mean material values are presented in Table 6.4.

Table 6.4 – Characteristic, design and mean ultimate material values of the different parts

Designation	Symbol	Value	Unit
Mean measured yield strength of the cold-formed steel plates	$f_{y,cf,m}$	322	MPa
Mean measured ultimate strength of the cold-formed steel plates	$f_{u,cf,m}$	407	MPa
Mean measured yield strength of the hot rolled steel plates	$f_{y,hr,m}$	417	MPa
Mean measured ultimate strength of the hot rolled steel plates	$f_{u,hr,m}$	559	MPa
Mean measured yield strength of the steel rebars	$f_{s,m}$	581	MPa
Mean measured ultimate strength of the steel rebars	$f_{t,m}$	682	MPa
Mean measured compressive strength of the concrete	$f_{c,m}$	53	MPa

6.2.3 Fabrication

The steel beam

The same steel beam used for the steel beam test (described in Chapter 4) is used for the composite beam test. The same fabrication procedure is followed as described in § 4.2.3. This time, the central plate has shear studs already welded on it (see Figure 4.3a).

The steel decks

The steel beam was then placed in a timber formwork that was able to bear the two steel decks on both sides of the steel beam (see Figure 6.3). The steel decks (COFRAPLUS60®) were placed on the formwork and nailed on the top flanges of the steel beams in every steel deck rib (see Figure 6.4).



Figure 6.3 – The steel beam placed in the formwork



(a) Positioning of the steel decks

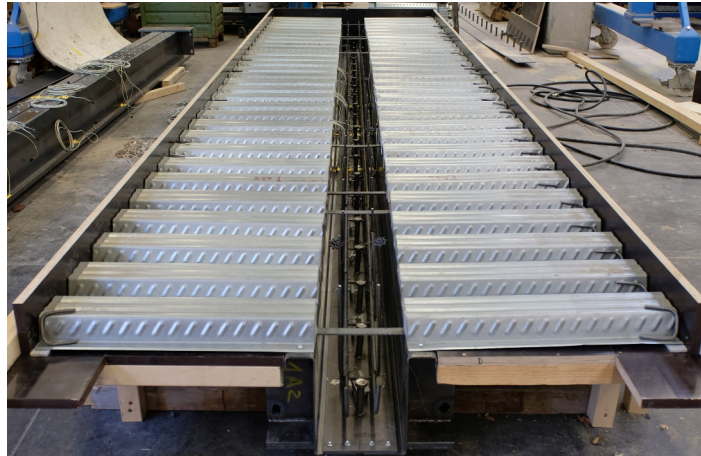
(b) Nailing of the steel decks

Figure 6.4 – Steel decks assembly on the steel beam and the formwork

The reinforcement bars (rebars)

In order to have a simplified fabrication process, the stirrups were made in two parts. The longitudinal rebars were assembled outside of the beam with the first half part of the stirrups.

The cage of rebars was then placed inside the U-shaped section and the steel battens were screwed into the top flanges. In fact, it was easier to make the cage from outside of the beam, so the steel battens had to be fixed after placing the cage inside the section (see Figure 6.5).



(a) General view



(b) Local view around the studs

Figure 6.5 – The cage of rebars inside the U section

The longitudinal rebars used at the bottom of the reinforced concrete section were HA10 (see Figure 6.6). The rebars used for the stirrups were HA8 (see Figure 6.7).

After nailing the steel decks on the steel beam, the reinforcing mesh was placed on the top of steel decks with the correct space between the steel deck ribs and the top of the slab. The second half of the stirrups was inserted to link the reinforcing mesh to the cage composed of the first half of the stirrups and the longitudinal rebars. The transversal spacing of the reinforcing mesh was 150 mm, it was too large for the second half of the stirrups, so additional top longitudinal rebars were inserted between the reinforcing mesh and the second half of the stirrups. A representation of the disposition of the rebars in the composite cross-section is represented in Figure 6.8.

In order to prevent cracks at the edge of the composite slabs, rebars bended in “U” were

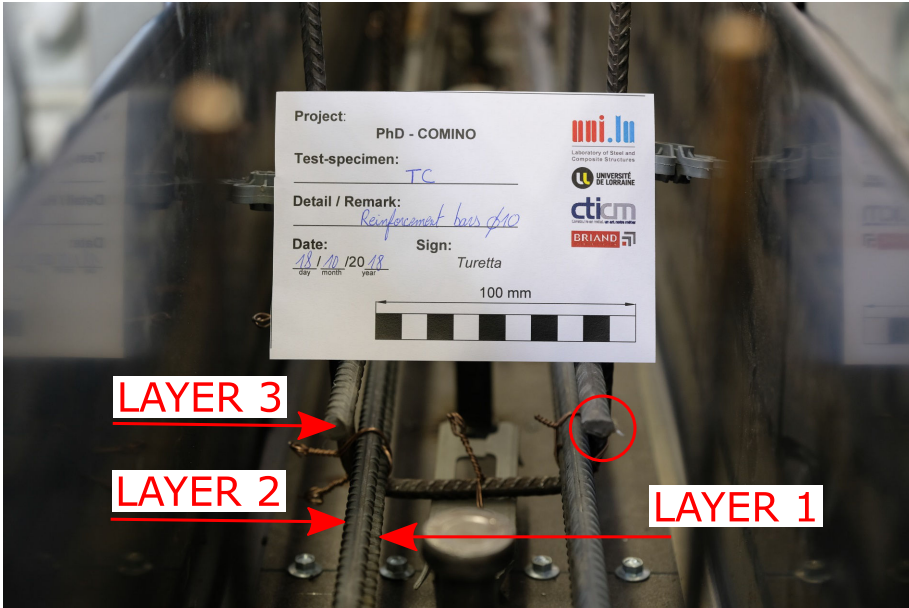


Figure 6.6 – Longitudinal rebars at the bottom of the section (HA10)

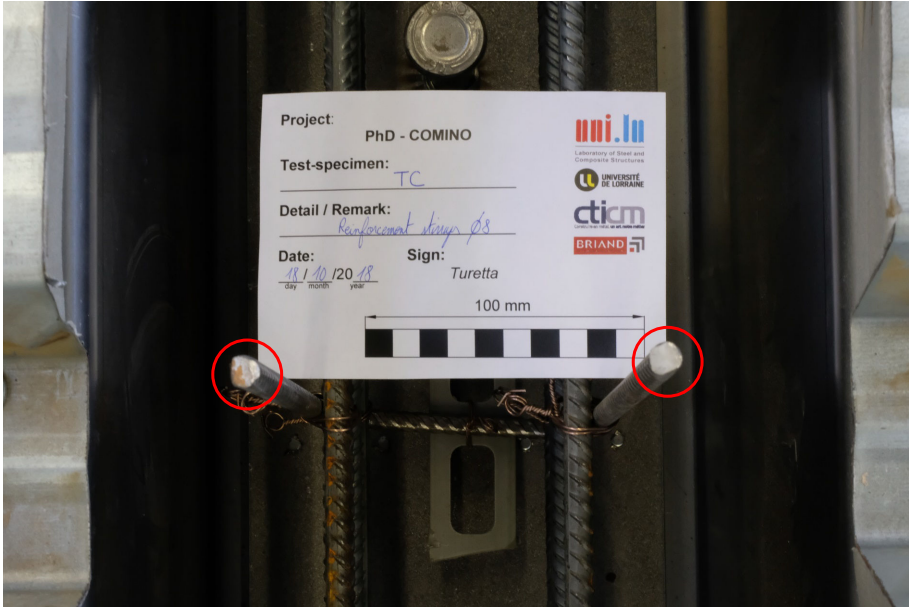


Figure 6.7 – First half of the stirrups rebars (HA8)

added at the edge of the slabs in every rib (see Figure 6.12).

The concreting

The concrete arrived quite dry at the laboratory, a higher class of consistency would have been better (more than F2). With this type of solution, the filling of the U-shaped section was done easily. The concrete has been carefully vibrated and cured for 2 weeks (see Figure 6.14 and Figure 6.15).

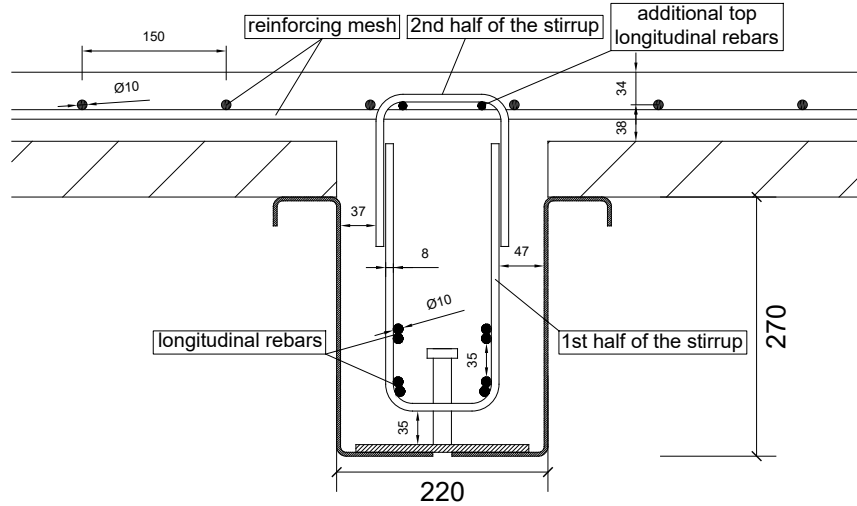


Figure 6.8 – Disposition of the rebars in the composite cross-section

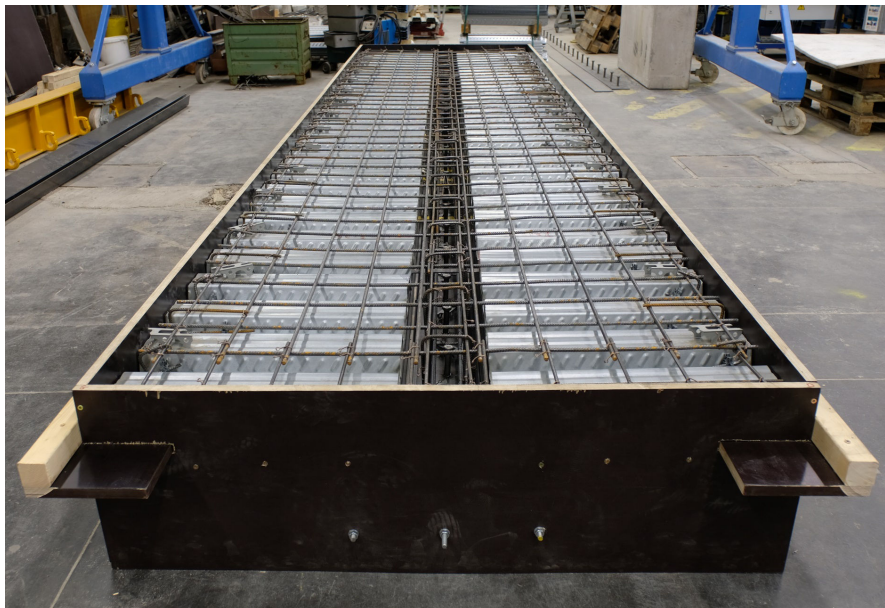


Figure 6.9 – General view of the rebars in the formwork before concreting



Figure 6.10 – The stirrups linked to the reinforcing mesh

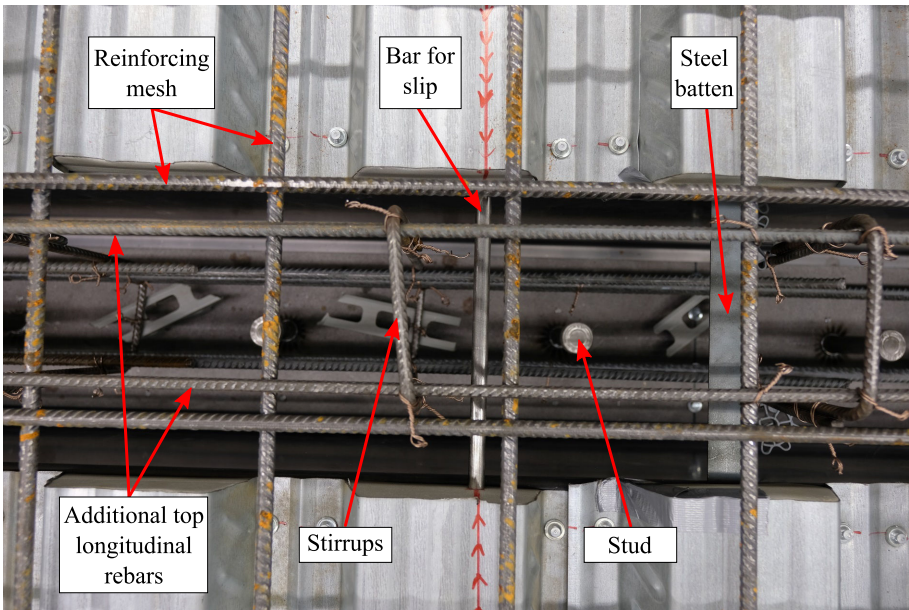


Figure 6.11 – Detailed top view of the rebars before concreting



Figure 6.12 – Rebars folded in U at the edge of the composite slab (HA10)



Figure 6.13 – Concreting



Figure 6.14 – Concrete vibrated



Figure 6.15 – Concrete cured

6.3 Layout

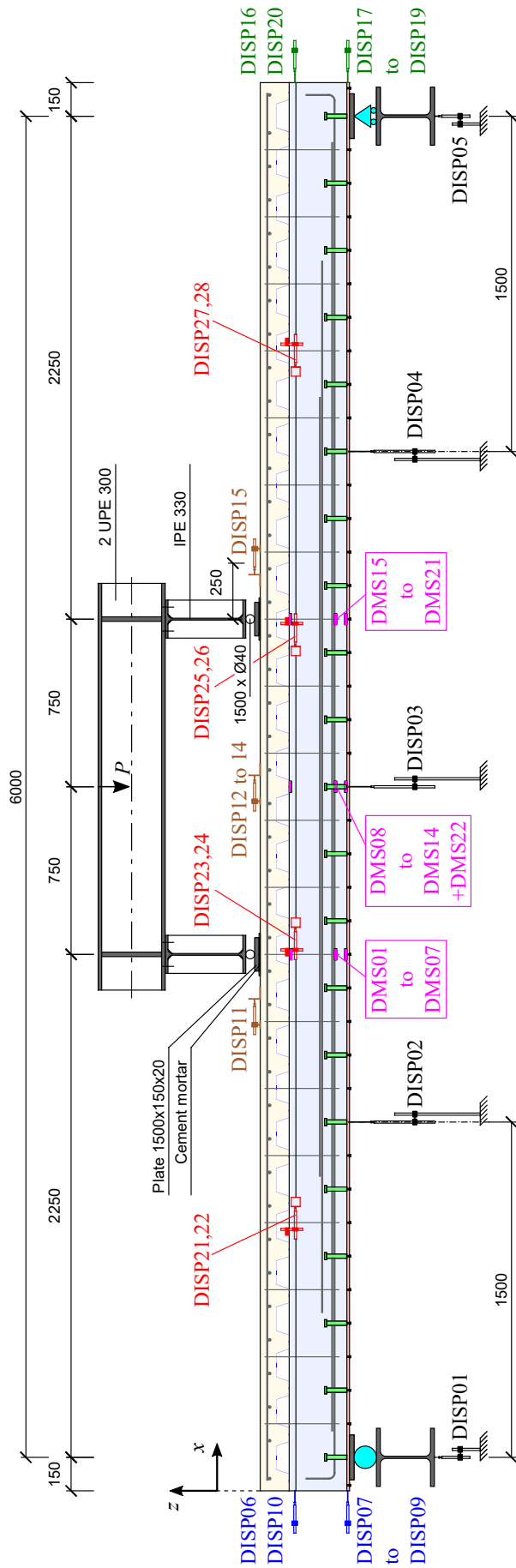


Figure 6.16 – Layout of the composite beam specimen with the measurements devices

6.4 Test setup

The test conducted at the laboratory of the University of Luxembourg was a 4-point bending test as shown in Figure 6.16. The beam was on roller supports (see Figure 6.17), the span was six meters. The load was applied symmetrically at two points, at 2.250 m from the supports. The loading system consisted of a main beam (2xUPE300) that spreads the force on two transverse beams (IPE330) (see Figure 6.18). Under the bottom flange of these transverse beams, circular bars (1500xØ40mm) were welded. These circular bars applied the load on the plates (1500x50x20mm) by contact. The load was distributed through this plate and a cement mortar underneath (see Figure 6.19). The maximum available force of the hydraulic actuator was 1000 kN, the force and the stroke were measured throughout the test.



Figure 6.17 – One roller support and the displacements sensors for the end-slip

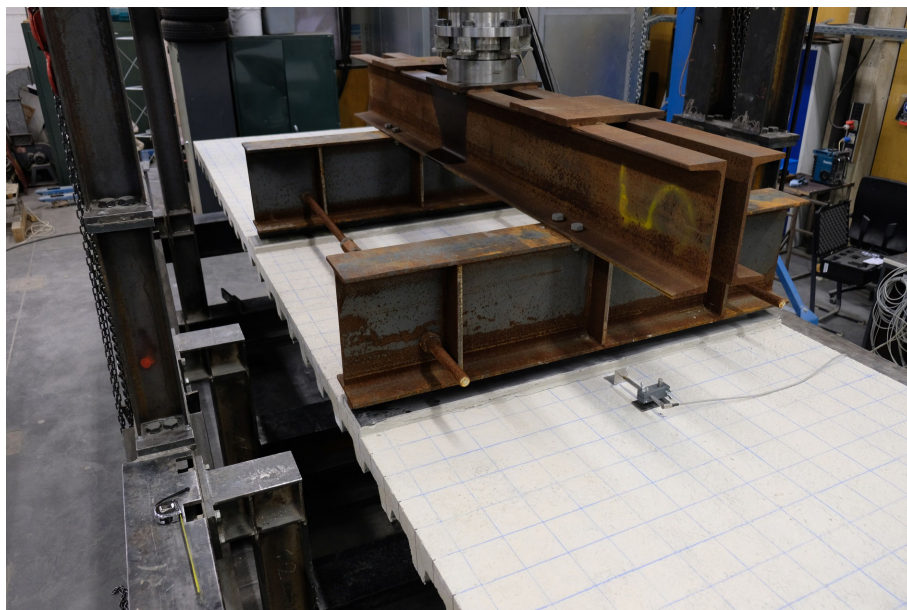


Figure 6.18 – The distribution of the loading



Figure 6.19 – Detail of the loading introduction

6.5 Measurements

6.5.1 Displacement sensors

A total of 28 Linear Variable Differential Transducers (LVDT) were used to record the deflection, the shortening on the top of the composite slab and the slip between concrete and steel. The deflection of the beam specimen was measured in three points, one at mid-span (DISP03) and two at quarter span from each support (DISP02 and DISP04) (see Figure 6.20 (b)). With high loading, the support beams (HEB260) had small deflections. These deflections of the support beams were also measured during the test by one LVDT for each support (DISP01 and DISP05) (see Figure 6.20 (a)). The real deflection of the beam specimen was then obtained by subtracting the measured values with the mean deflection of the two supports.

The shortening on the top of the composite slab was measured in five points, one near each loading point (DISP11 and DISP15) and three at mid-span (DISP12, DISP13 and DISP14). The ratio of these shortening values on the initial distance between the two points measured gives the strain on the top of the composite slab. The three LVTD on the top of the slab at mid-span gives also an information on the uniformity of the compression in the transverse direction.

The slip between the concrete and the steel was measured at both ends of the composite beam and also at four positions along the specimen. At each end, the end-slip was measured in five points (see Figure 6.21 and Figure 6.22). These five measuring points were at the steel-concrete interfaces at the upper part of the steel webs (DISP 06, DISP10, DISP16 and DISP20), the lower part of the steel webs (DISP07, DISP09, DISP17 and DISP19), and the central bottom plate (DISP08 and DISP18).



(a) Deflection at the support

(b) at L/4

Figure 6.20 – Displacement sensors used for record deflections

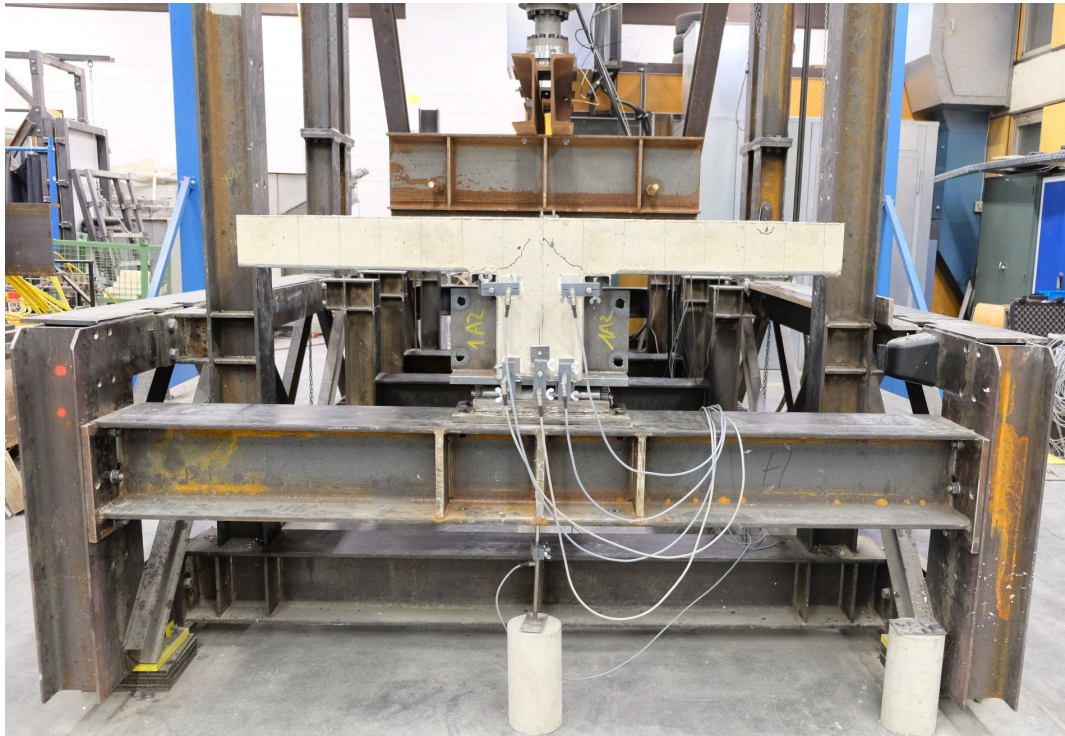


Figure 6.21 – Displacement sensors at one end of the composite beam



(a) Top view



(b) Side view

Figure 6.22 – End-slip measurements

CHAPTER 6. CONDUCTED COMPOSITE BEAM TEST

The slip was also measured at four positions along the beam at one meter from each support (DISP21, DISP22, DISP27 and DISP28) and under the two loading points (DISP23, DISP24, DISP25 and DISP26). At these locations, a bar embedded in the concrete crossed the beam on both sides through the steel deck ribs. A pair of LVDTs was fixed to these bars on each side of the beam specimen and measured the relative displacement between the bars and the top flanges of the U section. As these bars were embedded in the concrete without any contact with the steel beam, the relative displacement measured was the slip between the reinforced concrete beam and the steel beam (see Figure 6.23).

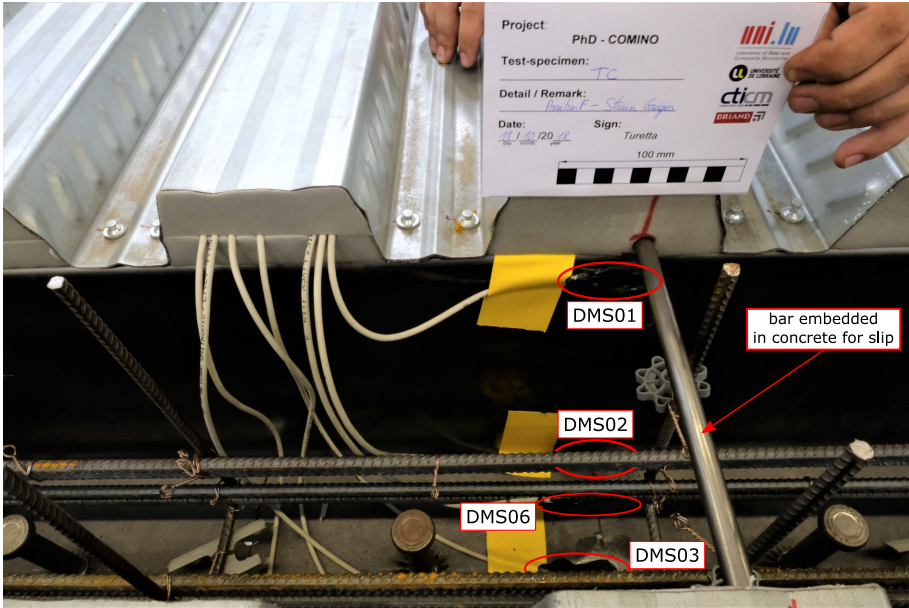


Figure 6.23 – Bar embedded in concrete for slip measurement and positions of strain gauges



Figure 6.24 – Displacement sensor for the slip under one point load (DISP25)

6.5.2 Strain gauges

In total, twenty-two strain gauges (DMS) were used to record the strains in the different steel parts of the composite beam. All the DMS were embedded in concrete and were placed before the concreting. Their positions are presented in Figure 6.25. The strains were measured at three locations, under the two loading points and at mid-span. In order to obtain the strain distribution of the composite cross-section, all the DMSs of one location are at the same longitudinal positions. At each location, the DMS were glued to the steel U section at five positions (DMS01 to DMS05, DMS08 to DMS12 + DMS22, DMS15 to DMS19) and on the two lowest longitudinal rebars (DMS06, DMS07 and DMS13, DMS14 and DMS20 to DMS21). These five positions on the steel beam are the upper part of the steel webs (1 DMS per each), the lower part of the steel webs (1 DMS per each), and the central bottom plate (1 DMS at the load introduction points and 2 DMS at mid-span). In fact, due to the presence of a shear stud at mid-span, an additional DMS was glued to the central bottom plate in order to have a DMS on both sides of this central shear stud. The longitudinal positions of the DMS glued to the rebars were the same as the DMS glued to the U section.

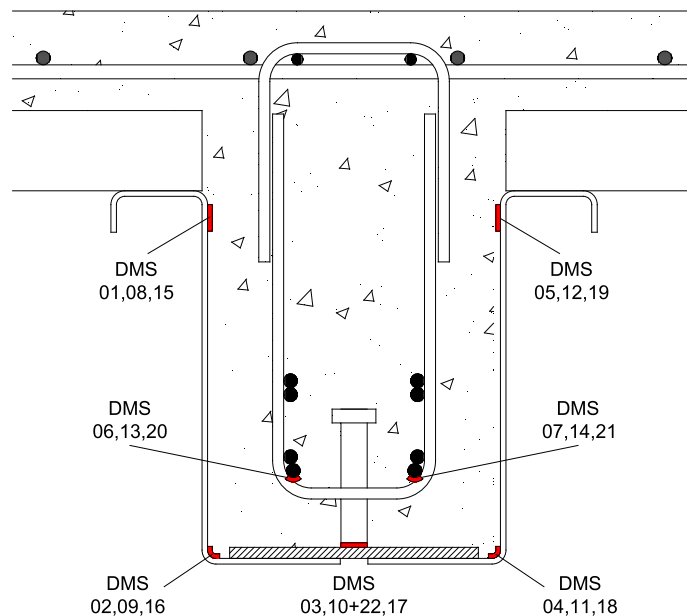


Figure 6.25 – Positions of the DMS in the composite cross-section

6.6 Test procedure

The actuator was controlled in displacement during the test, the speed rate was varying from 2 to 5 mm/min. Before the commencement of the test, the position of the beam on the supports and the position of the loading points on the composite slab were carefully checked. Any lateral movement was prevented during the test by wood plates inserted between the columns of the test frame and the edges of the composite slab. A small load was applied to check the specimen set-up.

The loading procedure was a quasi-static test according to EN 1994-1-1 (2005), Annex B. The load was first increased to 22.5% of the predicted maximum load bearing capacity, this value corresponds to the half of the future cycle's amplitude. Then the load was cycled 25 times between 5% to 40% of the predicted maximum capacity. After the cycles, the beam

was statically loaded. The displacement of the cylinder was increased by 4 mm step by step with waiting times of around 5 minutes at different load levels to have the relaxation of the concrete. The relaxation gives lower force value for a same deflection. During the test, three unloading were done in addition to the 25 cycles. This gave indication on the flexural stiffness of the beam specimen at the time of the unloading. The loading was then increased to the peak load and finally until failure, when no further load could be sustained.

Table 6.5 – Summarized test procedure

Steps	Force reached [kN]	Compared to $P_{ult,test}$	Speed rate [mm/min]
Loading	98	22%	5
25 cycles	Unloading	26	6%
	Loading	169	38%
Loading	211	47%	2
Unloading n° 1	27	6%	5
Loading	430	97%	2
Unloading n° 2	57	13%	5
Loading	437	98%	2
Unloading n° 3	356	80%	5
Loading to $P_{ult,test}$	446	100%	2
Loading to failure	437	98%	5

6.7 Test results

6.7.1 Observations during the test and failure mode

At the beginning of the loading, the beam deflected vertically with a very small deflection. The 25 cycles were conducted without any apparent problem, the composite beam behaved quite ductile. After the cycles, at a load of $P_{test} = 368$ kN (80% of the ultimate load) that corresponds to the end of the linear mechanical behaviour, a loud sound was heard without any visible default. The steel decks, near the supports, took a bit off the concrete of the composite slab. The end-slip increased and started to be visible (1-2mm). The load kept increasing until the biggest noise was heard at $P_{test} = 424$ kN (95% of the ultimate load). Some cracks started to be visible in the concrete of the composite slab. The cracks were visible on the sides of the slab, as the force kept increasing the cracks were developing in the concrete slab, see Figure 6.26.

The load kept increasing to the failure load accompanied with a loud sound. The failure was finally obtained by a shear mechanism characterized by the breaking and lifting of the composite slab in the shear span. The shear span is the distance between the end support and the next load introduction. At this place, important concrete cracks were developing on the top of the composite slab. At the same position, underneath the slab, a high opening crack appeared in the downstand concrete part from each side with an inclination of approximately 45° as it shown in Figure 6.28.

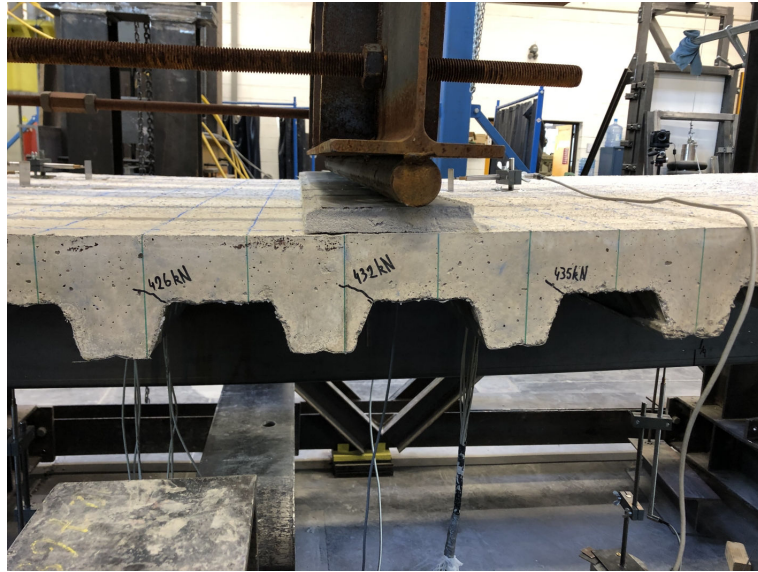


Figure 6.26 – Visible cracks under the load introduction at a high load level ($P_{\text{test}} = 435\text{kN}$)

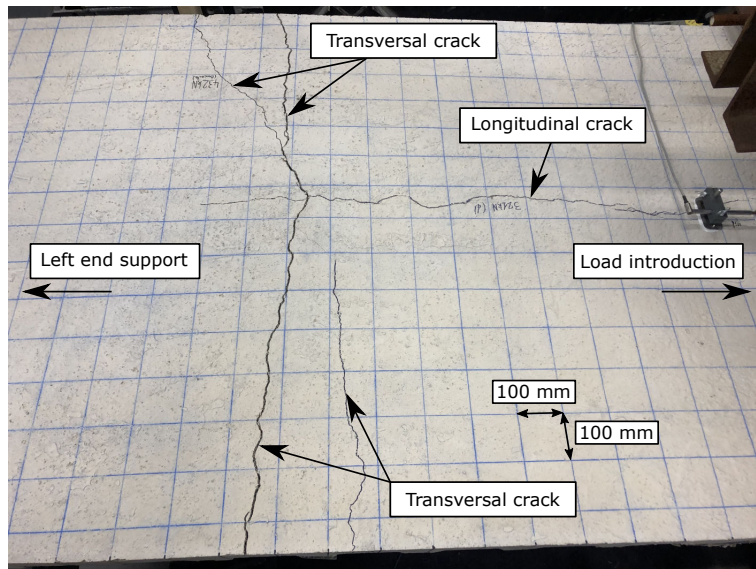


Figure 6.27 – Visible cracks on the top of the composite slab at the failure

At failure, under the zone of the top concrete cracks as shown in Figure 6.27, the composite slab was separated from the composite beam. The most important crack was visible in the downstand composite beam. It was possible to see through the crack as it is shown in Figure 6.28. Further investigations were conducted on the reason of the beam opening and the failure mode in § 6.8.

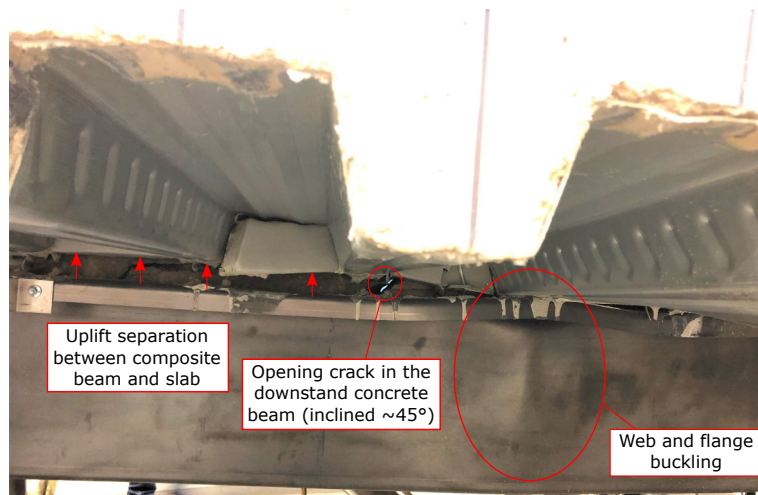


Figure 6.28 – Visible crack opening on the downstand concrete part at the failure

6.7.2 Effect of the self-weight

The record of measurement data started after placing the composite beam on the roller supports. Therefore, the effect of the self-weight was not taken into account in the measured values. The self-weight of the composite beam is estimated to 5.387 kN/m. The loading introduction system is applied in tow point loads and its self-weight is estimated at 2.407 kN per point load. The loading due to the self-weight and the associated bending moment is represented in Figure 6.29.

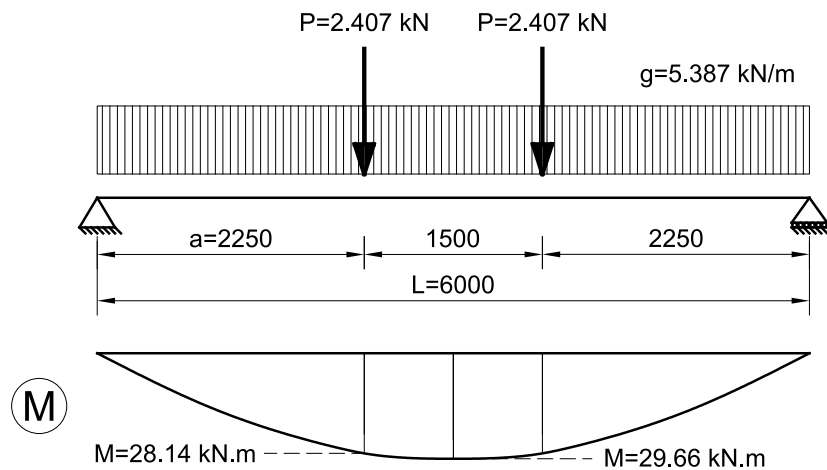


Figure 6.29 – Loading and associated bending moment due to the self-weight

The maximum deflection due to the self-weight (at mid-span) is obtained by:

$$\delta_{sw} = \frac{1}{2EI} \left[Pa \left(\frac{L^2}{4} - \frac{a^2}{3} \right) + \frac{5gL^4}{192} \right] \quad (6.2)$$

Where:

a is the distance from the support (here, $a = 2.25$ m)

L is the span of the beam (here, $L = 6$ m)

Table 6.6 – Estimated flexural stiffness associated to measured points at the beginning of the test

Applied load P_{test} [kN]	Measured deflection δ_{test} [mm]	Estimated initial flexural stiffness $EI_{\text{ini,test}}$ [MN m ²]
5.635	0.267	86.81
9.764	0.413	97.24
19.754	0.819	99.21
30.109	1.386	89.36
41.978	2.107	81.95

The deflection at mid-span of a beam subjected to a symmetrical two-point loading is obtained by the following formulation:

$$\delta = \frac{Pa}{2EI} \left(\frac{L^2}{4} - \frac{a^2}{3} \right) \quad (6.3)$$

The force applied by the hydraulic cylinder (P_{test}) and the deflection at mid-span (δ_{test}) were recorded during the test. The force applied by the hydraulic cylinder is divided in two-point load. Therefore, the initial flexural stiffness of the composite beam can be obtained by:

$$EI_{\text{ini,test}} = \frac{aP_{\text{test}}}{4\delta_{\text{test}}} \left(\frac{L^2}{4} - \frac{a^2}{3} \right) \quad (6.4)$$

Thanks to the formulation 6.4 and the recorded results at the beginning of the test, it is possible to estimate the initial stiffness of the composite beam specimen. The estimated flexural stiffness associated to the measured points at the beginning of the test are represented in Table 6.6. The mean value of the initial flexural stiffness of the composite beam specimen is then estimated to $EI_{\text{ini,test}} = 90.91 \text{ MN m}^2$ (based on the results presented in Table 6.6).

Finally, the additional moment due to the self-weight is estimated to be $M_{\text{sw}} = 29.66 \text{ KN m}$ and the deflection at mid-span due to the self-weight is estimated to be $\delta_{\text{sw}} = 1.22 \text{ mm}$. These values are added to the record values, the curves presented here are offset by these values.

As the loading is a symmetrical four-point bending test with two points load at 2.25 meters each from the support ($3L/8$), the flexural bending moment is estimated by Equation 6.5.

$$M_{\text{test}} = \frac{3L}{16} P_{\text{test}} = 1.125 P_{\text{test}} \quad (6.5)$$

Finally, the moment applied during the test is estimated by Equation 6.6.

$$M_{\text{tot}} = M_{\text{test}} + M_{\text{sw}} \quad (6.6)$$

The deflection at mid-span during the test is estimated by Equation 6.7.

$$\delta_{\text{tot}} = \delta_{\text{test}} + \delta_{\text{sw}} \quad (6.7)$$

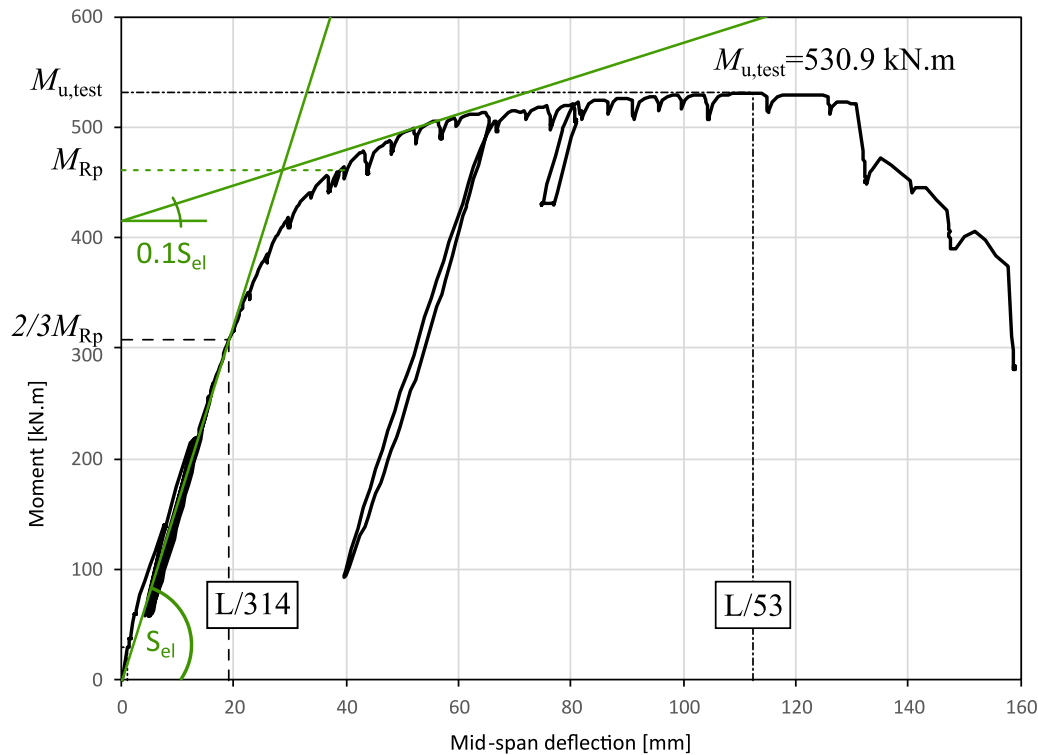


Figure 6.30 – Moment-displacement curve of the composite beam tested

6.7.3 Moment-displacement curve

The force of the hydraulic cylinder and the displacement of the composite beam at mid-span were recorded during the test. The experimental moment is estimated as described in § 6.7.2. The evolution of this moment with the increase of the mid-span deflection is presented in Figure 6.30.

The ultimate bending capacity of the composite beam tested is $M_{ult,test} = 530.9 \text{ kN.m}$. The deflection obtained at this failure load is $\delta_{ult,test} = 112.3 \text{ mm}$ ($L/53$).

The elastic stiffness (S_{el}) of the composite beam tested is estimated by fitting with the first elastic part of the test curve. Then 10% of this elastic stiffness is retained and offset to approach the plastic plateau as shown in Figure 6.30. The pseudo-plastic moment resistance is obtained at the intersection between these two lines.

The pseudo-plastic moment resistance is estimated at $M_{R,p} = 461.1 \text{ kN.m}$ (87% of $M_{ult,test}$).

According to the combination of actions recommended in EN 1990 (2003), the loads for serviceability limit state (SLS) would be around 2/3 the loads for ultimate limit state (ULS). If we consider that the resistance moment for ULS is the pseudo-plastic moment resistance, the deflection at SLS can be estimated at $2/3 M_{R,p} = 307.4 \text{ kN.m}$. The deflection at mid-span corresponding to this moment and the assumed SLS state is $\delta_{SLS,test} = 19.1 \text{ mm}$ ($L/314$).

6.7.4 Evolution of the deflection

The deflection of the composite beam tested was measured in 3 points ($\delta_{L/4}$, $\delta_{L/2}$ and $\delta_{3L/4}$). The displacements of the supports were also measured during the test (δ_A and δ_B). The supports had non-negligible vertical displacement with high loading (3.0 mm and 5.3 mm

for each support at the failure load). It also appeared that the vertical displacement recorded at the supports was not symmetrical, in fact one support displaced around two times more than the other one. In order to estimate the real deflection, the beam is considered simply supported on two springs with different stiffness (K_A and K_B) see Figure 6.31.

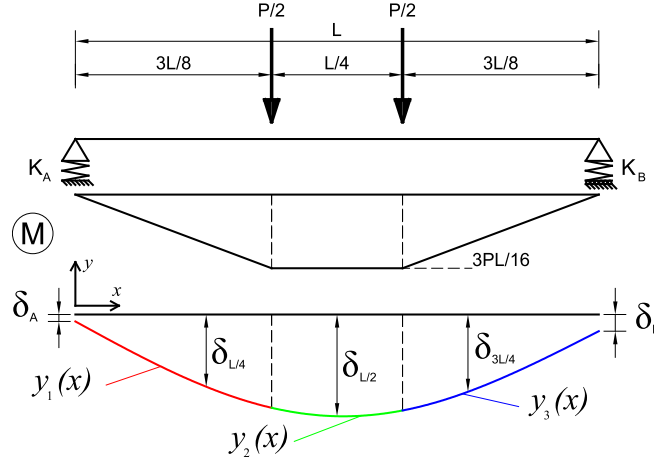


Figure 6.31 – Deflection of the composite beam tested under two springs supports

From the assumptions made, the deflection is obtained by the following formulations :

For $0 \leq x \leq \frac{3L}{8}$:

$$y_1(x) = \frac{P}{2EI} \left(\frac{x^3}{6} + C_1x + C_2 \right) \quad (6.8)$$

Where: $C_1 = \frac{-15L^2}{128} + \frac{EI}{L} \left(\frac{1}{K_A} + \frac{1}{K_B} \right)$; $C_2 = \frac{-EI}{K_A}$

For $\frac{3L}{8} \leq x \leq \frac{5L}{8}$:

$$y_2(x) = \frac{3PL}{16EI} \left(\frac{x^2}{2} + C_3x + C_4 \right) \quad (6.9)$$

Where: $C_3 = \frac{-L}{2} + \frac{8EI}{3L^2} \left(\frac{1}{K_A} + \frac{1}{K_B} \right)$; $C_4 = \frac{3L^2}{128} - \frac{8EI}{3LK_A}$

For $\frac{5L}{8} \leq x \leq L$:

$$y_3(x) = \frac{P}{2EI} \left(-\frac{x^3}{6} + \frac{Lx^2}{2} + C_5x + C_6 \right) \quad (6.10)$$

Where: $C_5 = \frac{-49L^2}{128} + \frac{EI}{L} \left(\frac{1}{K_A} + \frac{1}{K_B} \right)$; $C_6 = \frac{19L^3}{384} - \frac{EI}{K_A}$

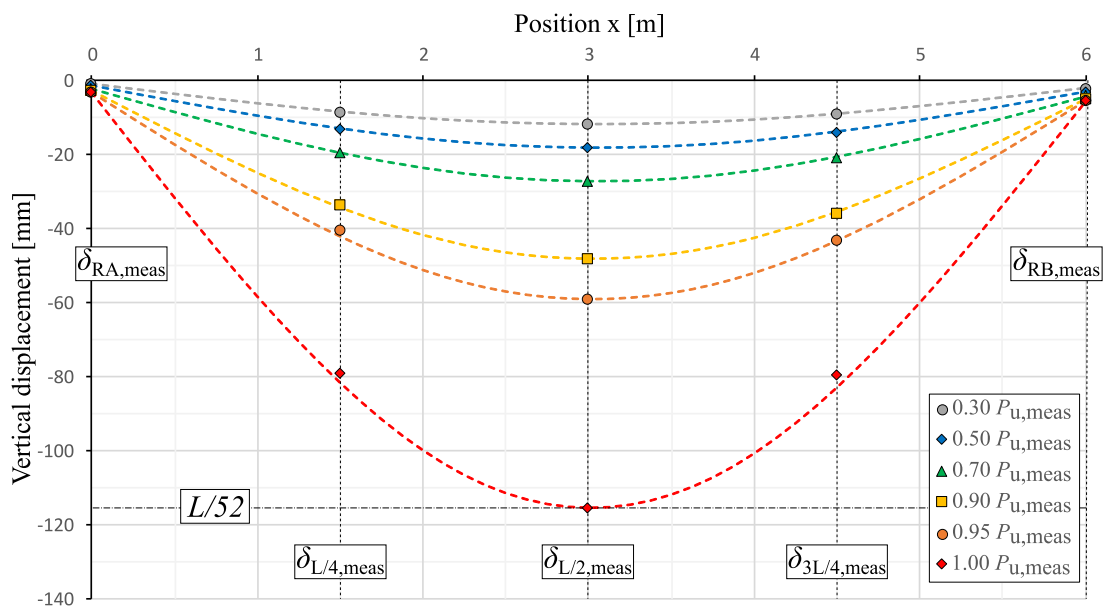
The evolution of the vertical displacements measured during the test with the increase of the loads is represented in Figure 6.32. The deflection curves calculated according to (Equations 6.8, 6.9 and 6.10) are well fitting with the measured points. The assumptions made with a simply supported beam on two springs in order to estimate the real deflection of the beam are verified. At the failure load, the deflection calculated overestimate the real vertical displacements (about 3%) for the intermediate measured points at $L/4$ and $3L/4$.

The mechanical behaviour of the composite beam is ductile, that is why there is a high difference in vertical displacement between $0.95P_{ult,test}$ and $P_{ult,test}$. The maximum deflection

Table 6.7 – Associated calculated flexural stiffness with the loading

Time	P_{test} [kN]	$\delta_{L/2,\text{test}}$ [mm]	EI_{test} [MN m ²]
0.30 $P_{\text{ult,test}}$	134.82	-11.67 (L/514)	53.8
0.50 $P_{\text{ult,test}}$	222.52	-18.14 (L/331)	57.4
0.70 $P_{\text{ult,test}}$	311.14	-27.01 (L/222)	53.3
0.90 $P_{\text{ult,test}}$	401.02	-48.15 (L/125)	37.2
0.95 $P_{\text{ult,test}}$	423.15	-59.00 (L/105)	31.6
$P_{\text{ult,test}}$	445.55	-115.18 (L/52)	16.5

recorded at L/2 was two times higher at the failure load compared to $0.95P_{\text{ult,test}}$. Thanks to the calculated deflection, it is possible to estimate the flexural stiffness (EI_{test}) of the composite beam during the test. The results are presented in Table 6.7. The flexural stiffness of the composite beam was reduced during the test until reaching failure. The initial flexural stiffness of the composite beam was estimated in § 6.7.2 to $EI_{\text{ini,test}} = 90.91 \text{ MN m}^2$. Then the flexural stiffness decreased to reach at the failure load the value $EI_{\text{ult,test}} = 16.5 \text{ MN m}^2$. That is due to the yielding of the steel parts and the deterioration of the concrete.


Figure 6.32 – Evolution of the deflection during the test

6.7.5 Slip at the steel-concrete interface

The slip was measured at the interface between steel and concrete at the ends of the composite beam in 5 points for each end (see § 6.5.1 and Figure 6.33).

The evolution of the end-slip with the increase of the applied load (without considering the effect of the self-weight) is shown in Figure 6.34 and in Figure 6.35 for both ends, respectively $x = 0 \text{ mm}$ and $x = 6300 \text{ mm}$. As it can be seen, for a same steel-concrete interface, there is no significant difference in the measurements of the slip. That is why for the next figure, for a better readability, only one slip curve is present for one interface. That means:

- DISP08 represents also DISP07 and DISP09

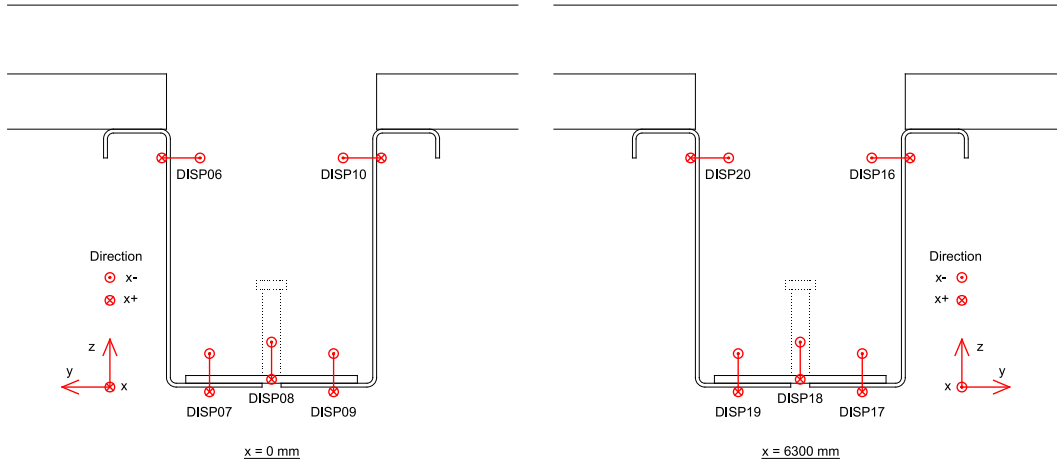


Figure 6.33 – Position of the slip measurement devices at the ends

- DISP18 represents also DISP17 and DISP19
- DISP10 represents also DISP06
- DISP20 represents also DISP16

The failure of the composite beam appeared on the side near $x = 0$ mm. At the end of the test, a concrete part of the composite beam went out of the steel section. The concrete part which went out was more following a vertical direction (see § 6.7.1), this is why the slip recorded at the failure is much higher at the top of the section. In Figure 6.34, after reaching the peak load, the end-slip at $x = 0$ mm, exceeded 6 mm and this is due to the failure mode of the composite beam. It is not due to the failure of the shear connection. This will be confirmed later in § 6.8.

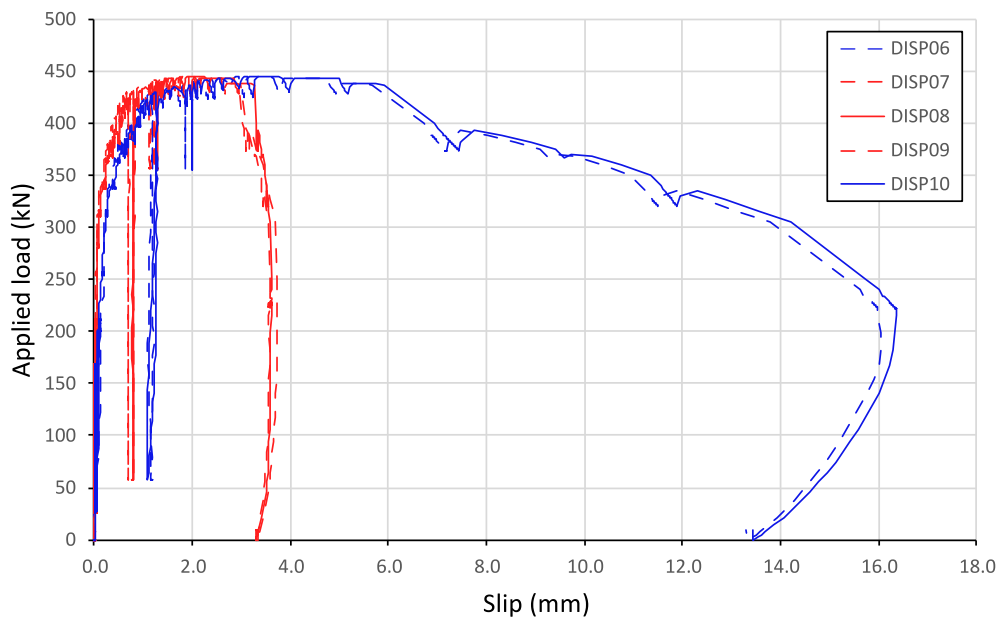


Figure 6.34 – Applied load versus end-slip at $x = 0$ mm

Before the failure, before the breaking of the concrete part, the end-slips are presented in Figure 6.36. The mechanical behaviour is quite symmetric until high load. In fact, closer to the failure load, the side where the failure of the beam would happen started to have more

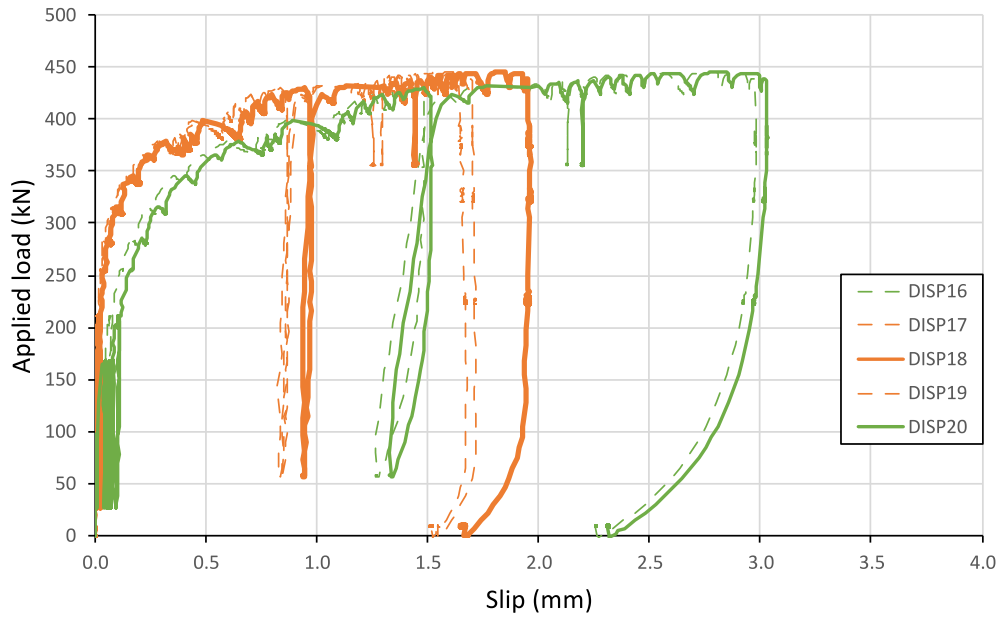


Figure 6.35 – Applied load versus end-slip at $x = 6300$ mm

slip. On this side (at $x = 0$ mm), the slip recorded by DISP10 is nearly reaching 6 mm at the interface between the top of the webs and the top of the concrete downstand beam. However, on both side, before the failure, the slip at the interface where the stud is welded is always below 4 mm. A ductile shear connection is often considered able to sustain 6 mm of slip [Réf Aribert]. This can confirmed that the failure was not due to a lack of shear connection.

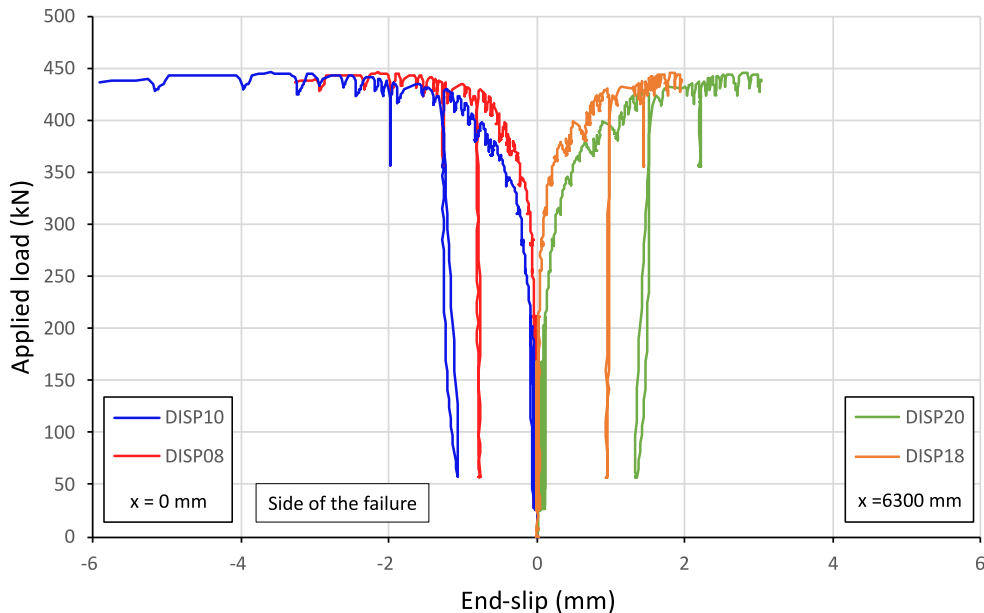


Figure 6.36 – Applied load versus end-slip at $x = 6300$ mm

The slip was also measured underneath the slab through the ribs of the steel decks at 4 positions along the longitudinal direction of the beam (DISP21 to DISP28, see § 6.5.1). The height of these sensors corresponds approximatively to the height of the sensors at the ends of the beam at the top of the section (DISP06-DISP10 and DISP16-DISP20). Thank to these intermediate measured points, the evolution of the slip with the increase of the force along the composite beam is represented in Figure 6.37. The distribution of the slip is symmetrical

until $0.95 P_{ult, test}$. At the failure load, there is more slip on the side where the failure happened (around 4 mm against 3 mm). At failure, before the concrete downstand beam broke, there was an important difference in the slip (around 6 mm against 3 mm).

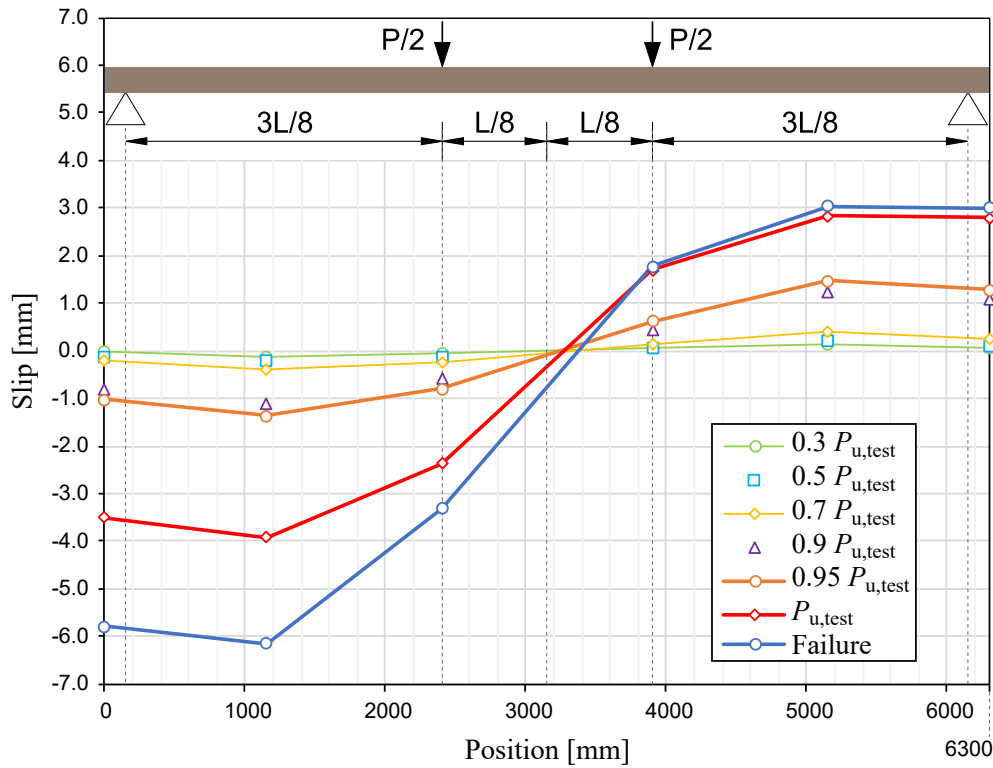


Figure 6.37 – Evolution of the slip along the beam during the test

6.7.6 Strain

The strain gauges were placed in three cross-sections along the beam at the two loads introduction and at mid-span. From the tensile test results (see § 6.2.2), the elastic limit strain for steel can be estimated by Equation 6.11. The elastic limit strain for the three different steel parts used in the composite beam are presented in Table 6.8. For the concrete part, the compressive strain at the peak stress (obtained from the compression tests) can be estimated by Equation 6.12.

$$\epsilon^{el} = \frac{f_{y,m}}{E} \quad (6.11)$$

$$\epsilon_{c1} = 0.7 f_{c,m}^{0.31} \leq 2.8 \quad (6.12)$$

From the compression test carried out, the mean value of concrete strength is $f_{c,m} = 53.4 \text{ MPa}$, thus the associated compressive strain is $\epsilon_{c1} = 0.24\%$.

The strain gauges were all embedded in the concrete, even the ones use to measure the strain in the steel beam. In fact, during the fabrication, it was easier to glue the DMS on the steel beam from inside because the steel beam was already placed in the formwork and the

Table 6.8 – Estimated elastic limit strain for the three steel parts

Material	Grade	f_{ym} [MPa]	ϵ^{el} [%]
Side plates	S235	322	0.15
Central plate	S355	417	0.20
Rebars	Fe 500	581	0.28

steel decks were already nailed. The strains recorded on the steel beam section are not all usable and they are perturbed, whereas the strain measured in the rebars worked fine. This is certainly due to the slip at the interface between steel and concrete. In fact, the strain gauges embedded in concrete could have been peeled off the steel because of the slip. It would have been better to have the strain record from outside the concrete. However, some selected data ranged can be post-treated, that is why there is no strain results presented after the peak load ($P_{ult,test}$) for the strain in the steel. Whereas, the strain recorded in the rebars was fine until $P_{ult,test}$ but not after the peak load.

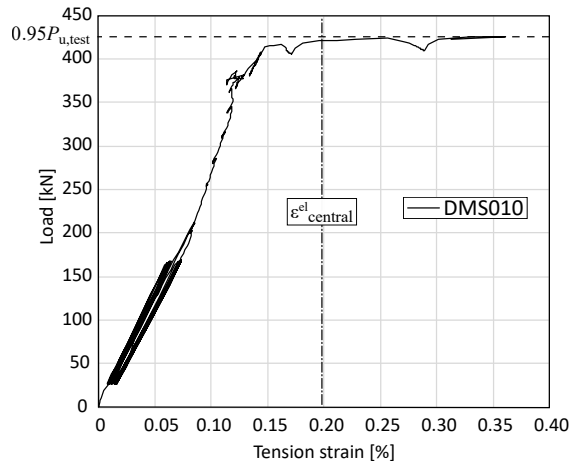
For the compressive strain in the concrete, displacement sensors were placed on the top of the slab to measure the shortening of the concrete (see § 6.5.1).

The evolution of the strain in the bottom central plate at mid-span with the increase of the applied load until $0.95 P_{ult,test}$ is represented in Figure 6.38 (a). In the elastic part, the stiffness obtained increases a bit with the loading, this was not expected. The signal was probably a bit perturbed but the global shape is not far from expected. The central plate has yielded and the last recorded measurements corresponds to the plastic plateau of the steel material used.

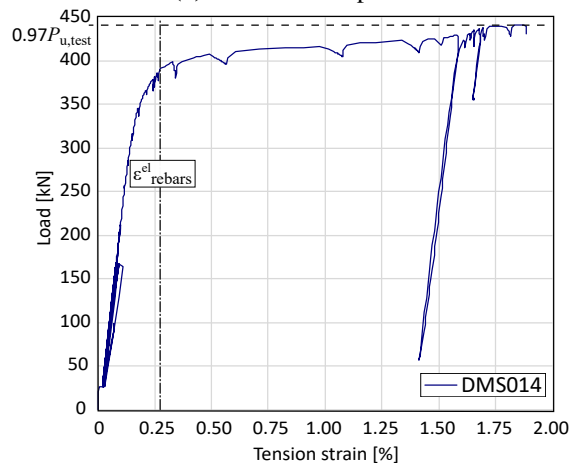
The evolution of the strain in the bottom rebars at mid-span with the increase of the applied load until $P_{ult,test}$ is represented in Figure 6.38 (b). The rebars were even more yielded than the central plate, the last recorded measurements corresponds to the beginning of the strength hardening.

The evolution of the compression strain in the concrete at mid-span with the increase of the applied load is represented in Figure 6.39. The strain is estimated by the shortening of the displacement sensors at the top of the composite slab. The value is not very precise and depends on the initial length. It can be seen that the estimated compressive strain ϵ_{c1} is exceeded near $P_{ult,test}$.

From the strain values measured in the top and bottom fibers of the composite section, the strain distribution with the loading in the composite beam is represented in Figures 6.40 and 6.41. For a better readability, the strain distribution is separated in two parts: in the reinforced concrete part (Figures 6.40) and in the U-shaped steel beam (Figures 6.41). For the reinforced concrete part, the Elastic Neutral Axis (ENA) is located near the top of the steel beam until $0.8P_{u,test}$. With higher loading (like $0.95P_{u,test}$), due to the yielding of the bottom longitudinal steel rebars, the neutral axis is moving to an Elasto-Plastic Neutral Axis (EPNA) located in the composite slab. For the U-shaped steel beam, every part was in tension. At $0.95P_{u,test}$, the bottom plate and a part of the cold-formed side plate had yielded.



(a) In the central plate



(b) In the rebars

Figure 6.38 – Evolution of the tensile strain at mid-span with the applied load

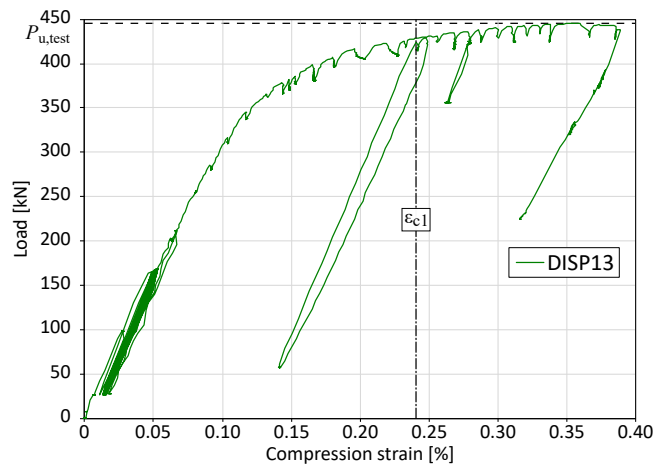


Figure 6.39 – Evolution of the compression strain at mid-span with the applied load in the concrete

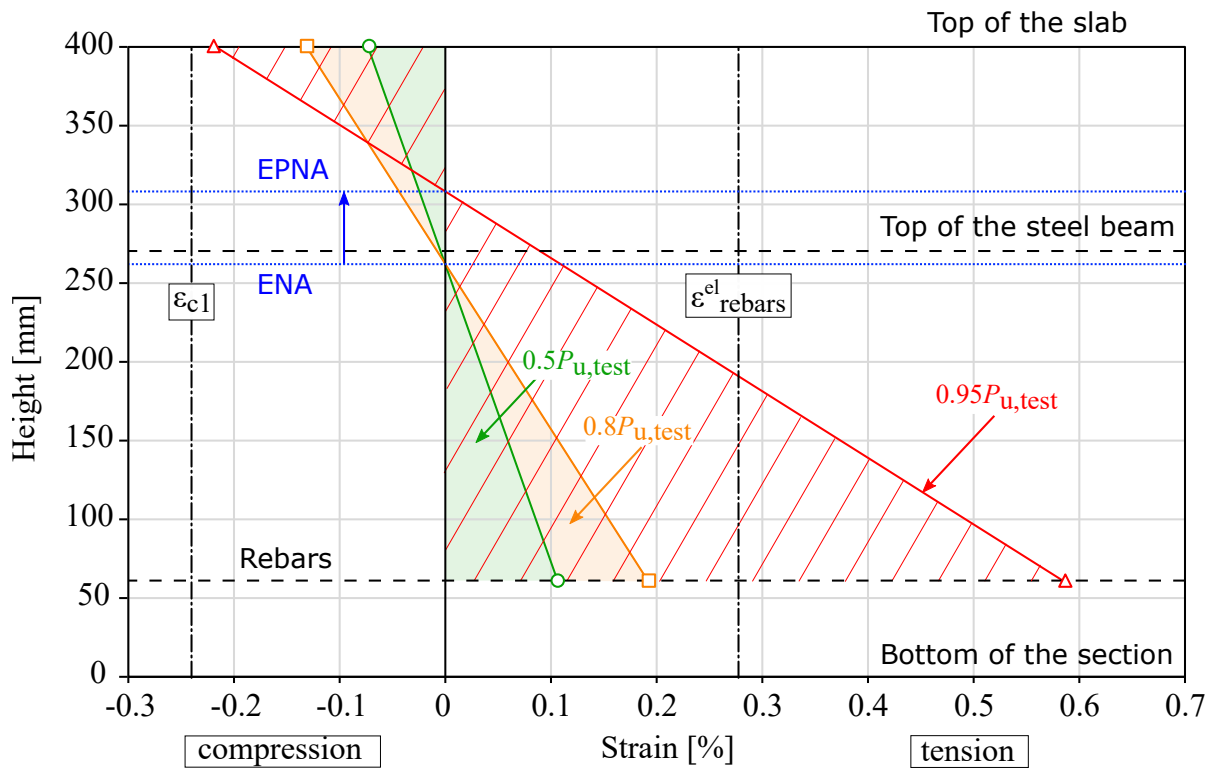


Figure 6.40 – Distribution of the strain in the reinforced concrete

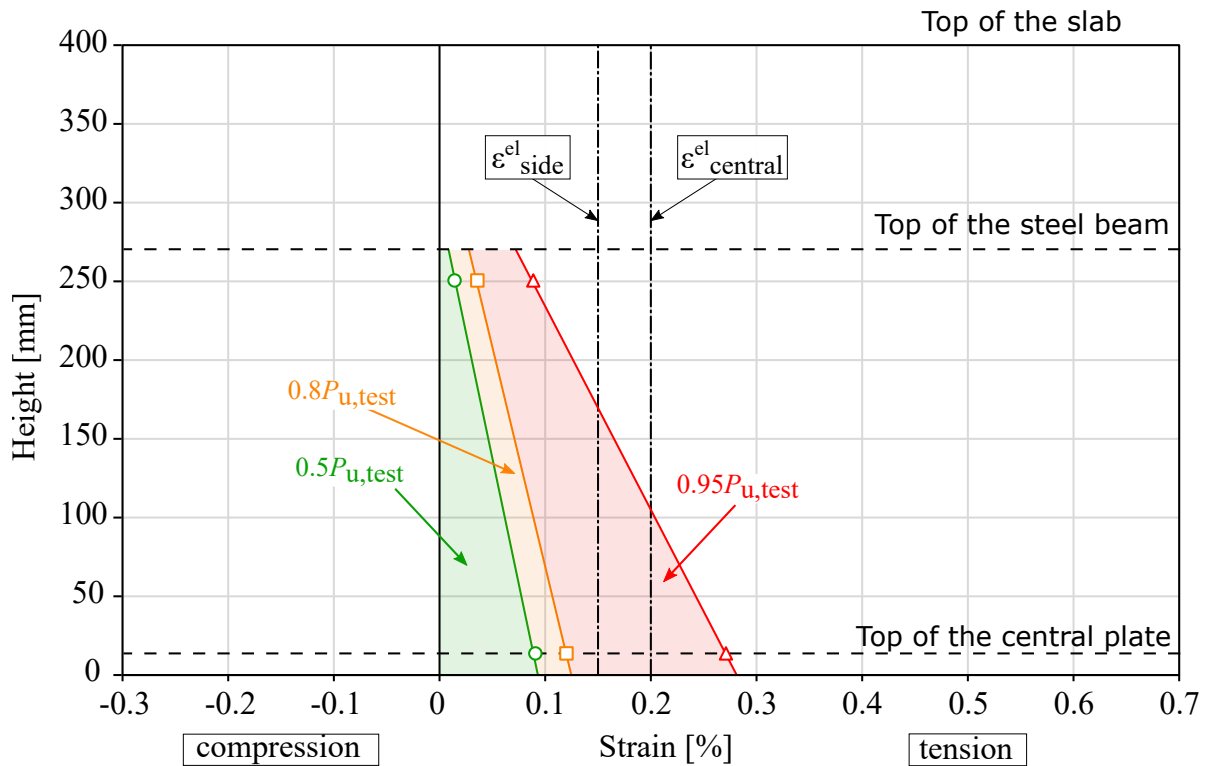


Figure 6.41 – Distribution of the strain in the steel beam

6.8 Investigation on the failure mode of the composite beam

The test ended by a separation of the composite slab to the composite beam at the failure, at very high displacements, as it was presented in § 6.7.1. After the test, the beam was taken out from the test setup and investigations were carried out on the composite beam specimen reversed and laid on the ground (see Figure 6.42). It was decided to open the composite beam in the region where there was the most visible cracks (see Figure 6.28). The steel U-shaped section was cut out in this region to let appeared the reinforced concrete part.

After cutting out one side of the steel section, the severely cracked concrete was removed manually in order to see the reinforcement and the studs. In Figure 6.43, it can be seen that the longitudinal reinforcement bars are bent between the stirrups, they were not straight as they were at the origin before the test. This highlights that there was an important tension force in the stirrups and they were pulled in the direction of the composite slab. The studs inside the concrete and between the longitudinal rebars were visible and they are highlighted in yellow in Figure 6.43.

The cracks in the downstand concrete beam were inclined between 30° and 45° in the shear span (see Figure 6.43). This is typically relevant of a shear failure mechanism. Step by step, the concrete was very carefully removed at the open crack with a small pneumatic hammer. After removing enough concrete, it was possible to see the failure of the stirrup at this position (see Figure 6.44 and 6.45). In Figure 6.45, it is possible to see the necking of the ductile steel of the stirrups. That means the tension force applied induced a stress which exceeded the ultimate tensile strength of the steel material that composed the stirrup. This highlights that they were probably not enough shear resistance provided by the composite specimen. As a reminder, the diameter of the stirrups used for the test were 8 mm.

More concrete was removed and the steel U section of the other side was also taken off. Finally, it appeared that the same stirrup failed on its both sides as shown in Figure 6.45. Except for this stirrup, no other steel failure was found in the composite specimen.

The bottom central plate of the steel section where the studs were welded on it was also cut and taken out from concrete. This was done to see how the headed shear studs were deformed due to the longitudinal shear flow induced by the composite connection. The deformation of the two shear studs close to the supports are shown in Figure 6.46. The shear stud 1 (at the support, (a)) is deformed about 1 mm at the head whereas the second shear stud 2 (300 mm from the support, (b)) was not really deformed.

From this obtained failure, for the design of shear resistance of the composite beam, it would be recommended to not consider the participation of the steel beam. In fact, for the design of the tested specimen, the contribution of the steel webs were considered and this seems to be too optimistic. It should be noted that this failure mechanism only appeared at very high displacements, the flexural behaviour of the composite beam specimen stayed ductile until this failure.

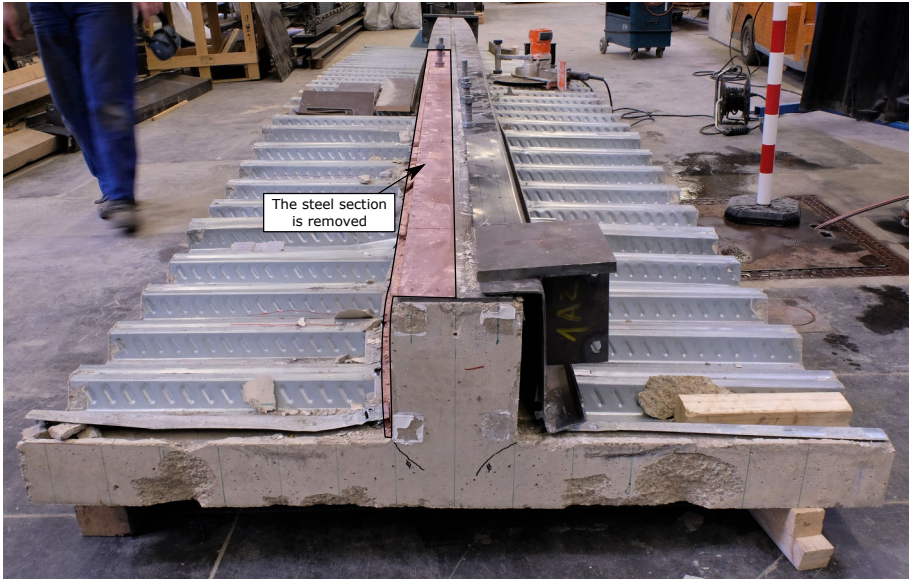


Figure 6.42 – Preparation of the beam for investigation on the failure

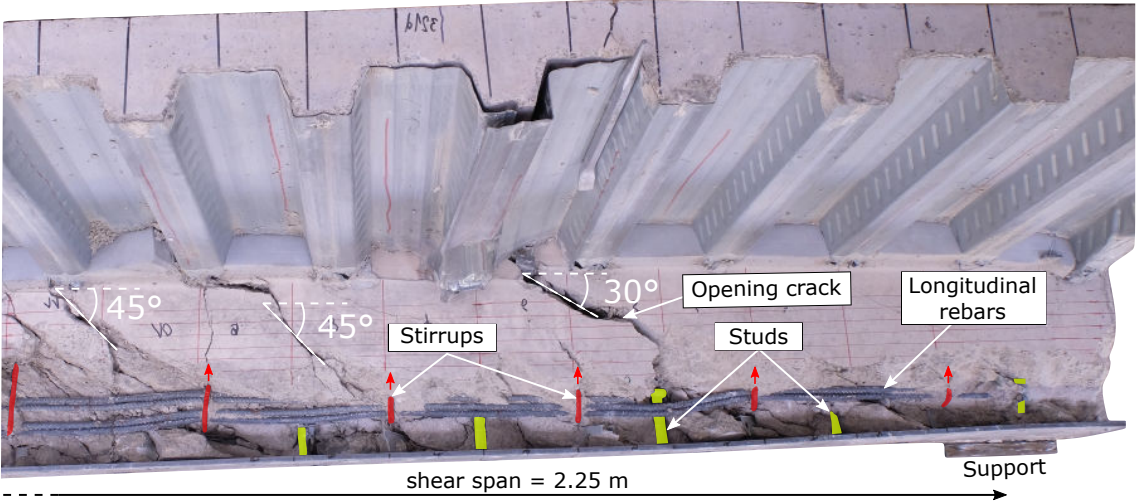


Figure 6.43 – Lateral view of the composite beam specimen after the test without the steel side plate

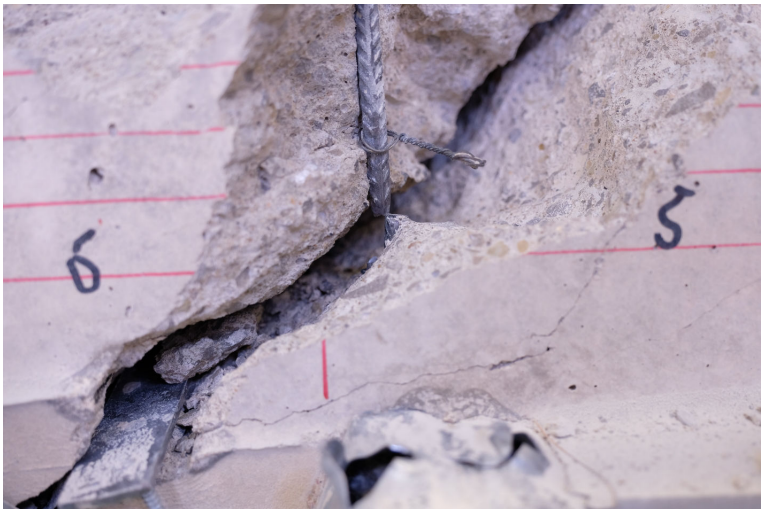


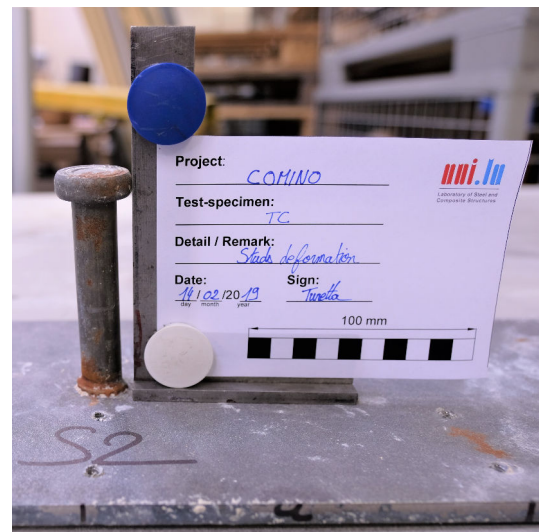
Figure 6.44 – Failure of the stirrup in the major crack



Figure 6.45 – Failure on both sides of the steel stirrup



(a) Stud 1 (at support)



(b) Stud 2 (300 mm from support)

Figure 6.46 – The deformation of the shear stud with the longitudinal shear flow

6.9 Conclusions

The four point bending test carried out on the composite steel-concrete composite beam leads to the following conclusions:

- The load-slip response of the composite beam is characterised by an elastic part followed by an elasto-plastic part and finally a high plastic plateau until the failure. Thus, an elasto-plastic bending resistance (M_{Rp}) is determined as a reference value for the bending resistance of the beam instead of the maximum bending moment of the test ($M_{u,test}$).
- The developed composite beam achieved high ductility (up to $L/53$). The bending capacity ($M_{Rp} = 461.1 \text{ kNm}$) was highly improved by composite action of about 2.2 times compared to the same beam without connection.
- The evolution of the measured slip between steel and concrete showed a classical response with no particular failure of the connection (located in tension zone).
- The strain distribution underlined that both the longitudinal rebars and the bottom central plates were yielded before the failure. However, only a part of the cold-formed steel side plates were yielded, the rest was in tension but not yielded. According to the measured strain values, only the concrete was subjected to compression forces during the test.
- The shear connection subjected to tension forces induced by the bending seems to be efficient. However, the concrete surrounding the connector was highly crushed. The shear connectors were reasonably deformed.
- The failure was obtained by a shear mechanism at very high displacement inducing a high open crack in the downstand concrete beam. The shear resistance of the composite beam might have been overestimated by taking into account the resistance of the cold-formed steel side plates.

Chapter 7

Analytical and numerical investigations of the composite beam

Contents

7.1	Objective of the investigations	188
7.2	Analytical evaluation of the flexural stiffness	188
7.3	Analytical evaluation of the bending resistance	190
7.3.1	Elasto-plastic bending moment resistance by integrating the stress distribution	190
7.3.2	Plastic bending resistance considering a full plastic distribution	193
7.3.3	Plastic bending resistance considering a full plastic distribution neglecting the contribution of the cold-formed part	197
7.3.4	Plastic bending resistance with a full plastic distribution limited by the maximum shear force of the connection	198
7.3.5	Compared to the test curve	200
7.4	Numerical study	202
7.4.1	Model	202
7.4.2	Elements	205
7.4.3	Materials properties	206
7.4.4	The boundary conditions	213
7.4.5	Local geometrical imperfection	213
7.4.6	Validation of the FEM compared to the test	214
7.5	Conclusions	217

7.1 Objective of the investigations

In the present chapter, analytical and numerical investigations of the U-shaped steel-concrete composite beam are presented. First, the test results are compared to analytical methods to evaluate the flexural stiffness and the bending resistance of the beam based on the standards (Eurocodes). Then, a FE model is developed and results from numerical simulations are compared to the test results in order to characterize the mechanical behaviour of the beam and, in particular, the efficiency of the shear connection located in tension zone.

7.2 Analytical evaluation of the flexural stiffness

The loading of the test is assimilated as a short-term action, therefore the modulus of elasticity of the concrete (E_c) is equal to the secant modulus of elasticity of the concrete for short-term loading (E_{cm}).

According to EN 1992-1-1 (2005), the secant modulus of elasticity of concrete is determined as :

$$E_{cm} = 22000 [f_{c,m}/10]^{0.3} = 36365 \text{ MPa} \quad (7.1)$$

The flexural stiffness of the composite cross-section can be evaluated by transforming the section into a single material thanks to the modular ratio (n_0):

$$n_0 = \frac{E_a}{E_{cm}} = 5.77 \quad (7.2)$$

In order to determine the flexural stiffness of the composite section, the position of the Elastic Neutral Axis (ENA) has to be previously determined. The composite cross-section is transformed into an equivalent steel section thanks to the modular ratio (see Figure 7.1). The section considered is a composite “cracked” section where the concrete in tension is neglected. The position of the ENA is by definition defined by Equation 7.3.

$$z_{ENA} = \frac{\sum_i A_i z_i}{\sum_i A_i} \quad (7.3)$$

Finally, the position of the ENA of the composite “cracked” section (the concrete is not considered in the tensile zone) is obtained by solving the second order equation 7.2.

$$z_{ENA}^2 \left(\frac{-b_r}{2n} \right) + z_{ENA} \left((h_{tot} - h_c) \frac{b_r}{n} + \frac{A_{c,slab}}{n} + A_a + A_s \right) - \left(\frac{b_r}{2n} (h_{tot} - h_c)^2 + \frac{A_{c,slab}}{n} z_{c,slab} + A_a z_a + A_s z_s \right) = 0 \quad (7.4)$$

Finally, $z_{ENA} = 302.51$ mm. The ENA is at the beginning of the concrete beam, at the height of the steel decks.

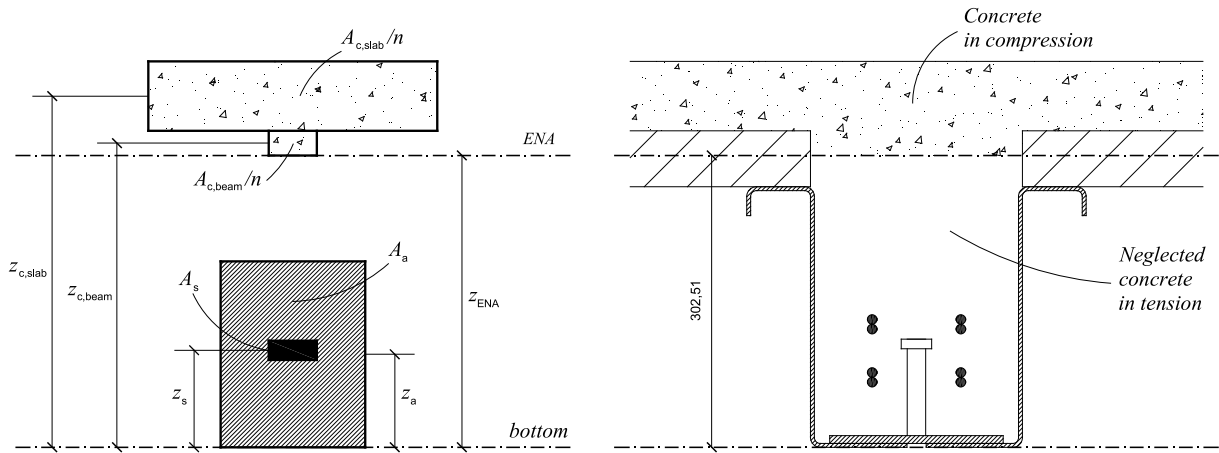


Figure 7.1 – Equivalent cross-section to determine the ENA

From this transformed section, the second moment of area of the composite section is determined as $I_m = 37\,167\text{ cm}^4$. The composite bending stiffness is $EI_{\text{com}} = E_a I_m = 78.05\text{ MN m}^2$

Compared to the test, an initial flexural stiffness was determined to take into account the effect of the self-weight (see § 6.7.2) and its value was : $EI_{\text{ini,test}} = 90.91\text{ MN m}^2$. This initial flexural stiffness was determined with the first measured values of the test at low loads, the concrete in tension was probably not even cracked, this may explain the increase of 16% of the stiffness.

Other flexural stiffness, depending on the load level, were determined by the evolution of the deflection during the test (see Table 6.7 of § 6.7.2). Thanks to the equations of the deflection (Equations 6.8, 6.9 and 6.10), the flexural stiffness of the composite beam (EI) can be isolated and determined for the associated applied load. The evolution of the flexural stiffness with the applied load is represented in Figure 7.2. The noticeable values of Table 6.7 are indicated on the Figure. The stiffness EI_{com} calculated analytically is also represented in the figure by an horizontal line.

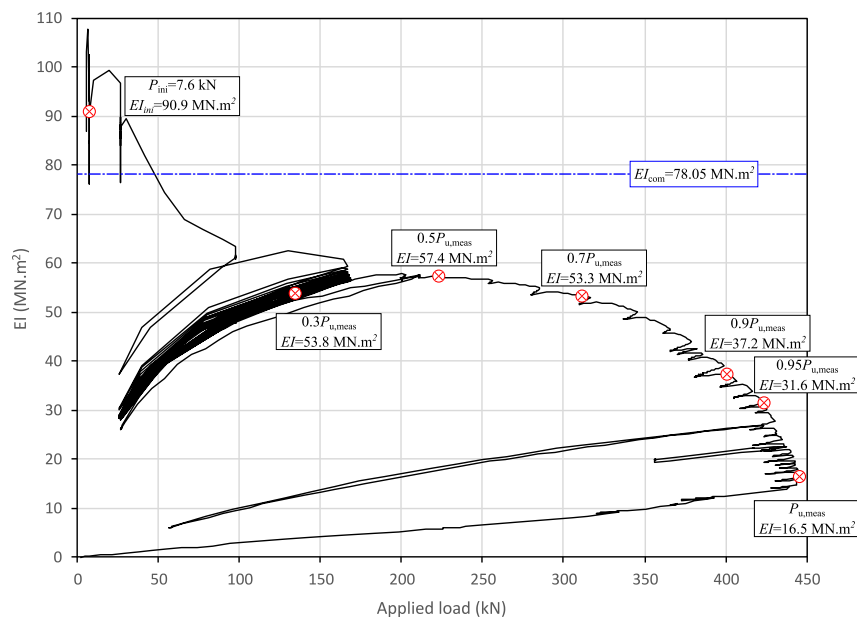


Figure 7.2 – Evolution of the flexural stiffness with the applied loading

It can be seen that the analytical value is lower than the initial value but overestimates the average flexural stiffness about 30%. In fact, the average stiffness should be around $EI_{\text{average}} = 55 \text{ MN m}^2$ comprised between $EI_{0.5P_{\text{ult,test}}} = 57.4 \text{ MN m}^2$ and $EI_{0.7P_{\text{ult,test}}} = 53.3 \text{ MN m}^2$. The gap between (EI_{com}) and the stiffness at the peak load ($EI_{P_{\text{ult,test}}}$) (around 80%) is principally due to the yielding of the steel parts (rebars and central plate) at this high load level and the stiffness of the concrete is also reduced at high load level.

7.3 Analytical evaluation of the bending resistance

In this section, the analytical results are compared to the test results. That is why all the partial safety factor for the different materials are not considered :

$\gamma_C = 1.0$, the partial factor for concrete.

$\gamma_S = 1.0$, the partial factor for reinforcing steel.

$\gamma_{M0} = 1.0$, the partial factor for structural steel.

$\gamma_V = 1.0$, the partial factor for design shear resistance of a headed stud.

7.3.1 Elasto-plastic bending moment resistance by integrating the stress distribution

The bending resistance moment is first evaluated by integrating the stress distribution obtained from the strain distribution at $0.95P_{\text{ult,test}}$ which corresponds almost at the ultimate resistance and at this load step the strain distribution was well measured by the strain gauges (see § 6.7.6).

The strains were measured during the test in three sections including at mid-span as related in § 6.7.6. The distribution of the strain in the reinforced concrete part is presented in Figure 6.40. The distribution of the strain in the steel part is presented in Figure 6.41.

For this evaluation of the ultimate bending resistance, it is assumed that after exceeding the yield strain of a steel part, the resulting stress is the yield strength of the material without taking into account any strength hardening. That means all the parts of a steel section at a strain value higher to the yield strain are considered plastic and the stresses in these parts are limited to the yield strength. This assumption is the same as for a fully plastic analysis according to EN 1994-1-1 (2005). The estimated yield strains for each steel part are presented in Table 6.8.

From this assumption and from the distribution of the strain in the different parts at $0.95P_{\text{ult,test}}$, it can be easily considered that the steel of the rebars and the steel of the hot rolled bottom central plate have a plastic distribution with their respecting yield strengths ($f_{y,hr,m}$ and $f_{s,m}$ see Table 6.4).

When looking at the distribution of the strain in the steel cold-formed sides plates in Figure 6.41, it can be seen that the strains exceeds the elastic limit only on a part at the bottom of the section. The stresses in this part are also limited to the yield strengths of the material ($f_{y,cf,m}$). The height of this plastic zone is estimated to be $h_{cf,pl} = 164 \text{ mm}$ (see in Figure 7.4). The stresses in the rest of the steel cold-formed sides plates are considered to be elastic. Therefore the stresses are linearly distributed from the end of the plastic bottom

part to the top of the steel section at a stress value σ_a . According to the strain measured at $0.95P_{ult,test}$ (see Figure 7.3), the top of the steel section is subjected to a tensile strain.

Since the stresses are considered elastically in this part, it is possible to estimate the stress value at the top of the steel section by Hook's law : $\sigma_{a,1} = E_a \epsilon_{a,1} = 150 \text{ MPa}$. For the detailed calculation, the stress in the side plates at the height of the begin of the edge stiffener is also estimated by elastic distribution to the value $\sigma_{a,2} = 199 \text{ MPa}$. Two other heights are considered in the calculation method :

$h_{cf,el,1} = 30 \text{ mm}$, the height of the edge stiffener

$h_{cf,el,2} = 76 \text{ mm}$, the remaining height where the stress is elastically distributed

At $0.95P_{ult,test}$, the strain distribution in the composite section is shown in Figure 7.3. In red, it is the strain distribution of the reinforced concrete part. In green, it is the strain distribution of the structural steel part. The elastic limit strain of all the material are represented in Figure 7.3 as a limit of the strain. For all the parts, when the strain is exceeding this limit, the stress is limited to the yield strength of each material. This gives the elasto-plastic stress distribution in the composite section as represented in Figure 7.4.

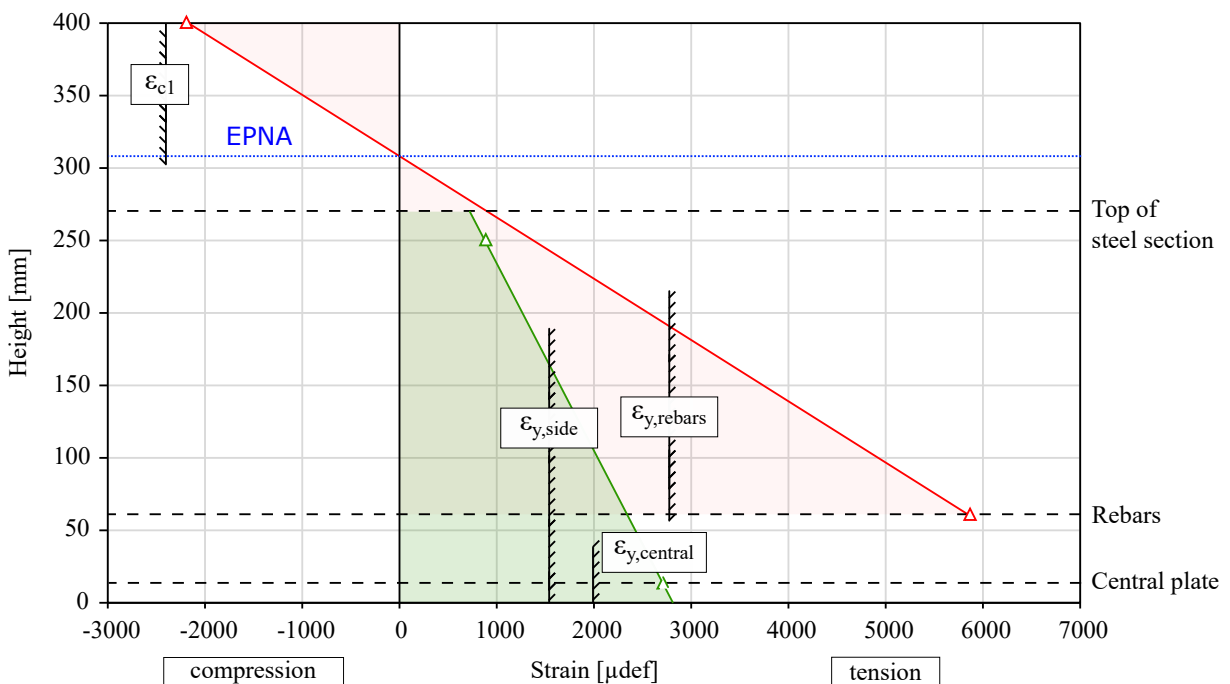


Figure 7.3 – Distribution of the strain in the composite section at $0.95P_{ult,test}$

For the concrete, only a rough estimation of the strains could be extracted from the measurements at the top of the concrete slab (with LVTD). Therefore, the stress values were not obtained directly from the measured strain values of the slab but by solving the horizontal equilibrium between resulting tension and compression forces integrated from the stress distribution.

During the test, the steel rebars yielded first and the concrete strains stayed below the compressive strain at the peak stress (ϵ_{c1}). In order to simplify the calculation, instead of a parabolic distribution of the stress in the concrete, an elastic distribution is assumed as shown in Figure 7.4. The stress distribution in the concrete slab was assumed linear from the Elasto-Plastic Neutral Axis (EPNA) to the top of the slab.

The position of the EPNA in Figure 7.4 is obtained by linking with a straight line the strain in the rebars to the strain in the top concrete slab. This assumes that normals to the neutral surface remains normal during the deformation and that deflections are small (Euler–Bernoulli theory). The strain measured in the rebars were done with DMS (see § 6.5.2) whereas as the strain measured in the top concrete slab is only an estimation. Therefore the position of the EPNA is also not exact but only an approximation.

Finally, with all the assumptions made, the stress at the top of the concrete slab (σ_c) is estimated by equilibrating all the resulting forces (see Equation 7.5) from the integration of the stress distribution presented in Figure 7.4.

$$F = \int_S \sigma_i dS = F_t + F_c = 0 \quad (7.5)$$

Where:

$F_t = F_s + F_{a,hr} + F_{a,cf}$, the sum of the resulting tension forces of the steel parts

$F_s = A_s f_{s,m}$, the resulting tension force of the steel rebars (plastic)

$F_{a,hr} = t_{hr} b_{hr} f_{y,hr,m}$, the resulting tension force of the bottom central plate (plastic)

$F_{a,cf}$, the resulting tension force of the cold-formed side plates (elasto-plastic)

F_c , the resulting compression force of the concrete (elasto-plastic)

The compressive stress in the concrete slab, is determined by Equation 7.6 according to EN 1992-1-1 (2005) :

$$\sigma_c = f_{cd} \left[1 - \left(1 - \frac{\epsilon_c}{\epsilon_{c2}} \right)^n \right] \leq f_{cd} \quad (7.6)$$

Where:

f_{cd} , the design value of concrete compressive strength

ϵ_c , the compressive strain in the concrete

ϵ_{c2} , the strain at reaching the maximum strength (here 0.2%)

n , is the exponent (here 2.0)

The elasto-plastic bending resistance moment of the tested composite cross-section, at $0.95P_{ult,test}$, is then obtained by Equation 7.7.

$$M_{epI,R} = \int_S z_i \sigma_i dS = 484.0 \text{ kNm} \quad (7.7)$$

At the load step $0.95P_{ult,test}$, the associated applied moment during the test was $M_{0.95,ult,test} = 504.4 \text{ kNm}$. Compared to the test results, the elasto-plastic bending resistance moment obtained by integrating the strain distribution is 4.0% inferior to the applied bending during the

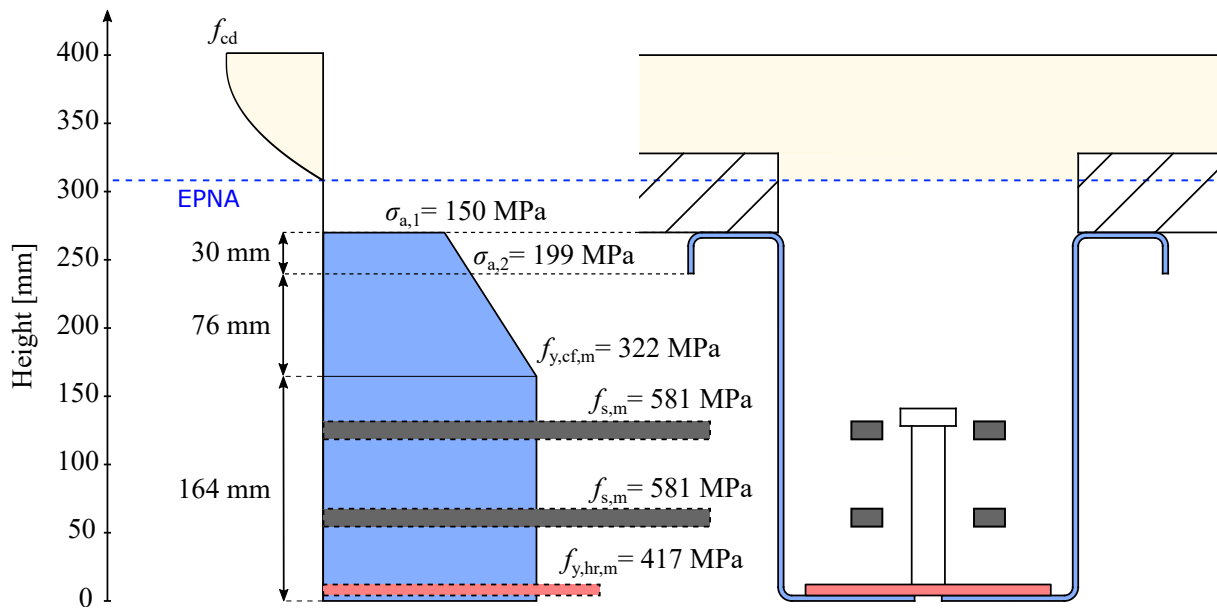


Figure 7.4 – Elasto-plastic stress distribution in the composite section at $0.95P_{ult,test}$

test. The distribution of the stress underlined well that the cold-formed side plates were not entirely yielded as shown in Figure 7.4.

It can be noted that the degree of shear connection was not needed in this method. This is because the stress distribution was already known from the measurements. Although this calculation is accurate, the method used was only possible because the strain was measured in the composite section during the test. The stress distribution was then found from the strain measured at different points of the composite section. There would be too many unknown parameters and the method would be too complicated for a classical method of design for such a composite beam. That is why in the following paragraphs, three other methods of design, that are still accurate and on the safe side, are presented in order to find a simplified method of design.

7.3.2 Plastic bending resistance considering a full plastic distribution

From the calculation made by integrating the real stress distribution of the test in the previous paragraph (§ 7.3.1), it is known that the cold-formed side plates were not entirely yield at the ultimate moment. Anyway, in this paragraph, it is assumed a full plastic distribution in all the parts of the composite section with stress blocks. This method of design is the same as proposed in EN 1994-1-1 (2005), in sagging moment, for a class 1 or 2 section, or when the Plastic Neutral Axis (PNA) is located in the concrete slab or even in the top flanges of the section if they are prevented from buckling by the shear connectors.

Evaluation of the degree of shear connection

The degree of shear connection is calculated according to EN 1994-1-1 (2005) with the assumption that all the steel parts of the beam were participating in the mechanical composite behaviour. The shear studs connect the steel beam to the bottom of the reinforced concrete beam. The maximum tensile stress resultant passing through the connection ($N_{a,max}$) is the

sum of the tensile stress resultant of the central plate and of the two side plates :

$$N_{a,max} = A_{a,cf} \frac{f_{y,cf,m}}{1.0} + A_{a,hr} \frac{f_{y,hr,m}}{1.0} = 1753.75 \text{ kN} \quad (7.8)$$

Where:

$A_{a,cf}$ is the area of the cold-formed steel parts (here, $A_{a,cf} = 35.82 \text{ cm}^2$)

$A_{a,hr}$ is the area of the hot rolled steel part (here, $A_{a,hr} = 14.40 \text{ cm}^2$)

Whereas, the maximum compressive stress resultant passing through the connection in case of full connection ($N_{c,max}$) is determined by :

$$N_{c,max} = 0.85 [b_{eff}h_c + b_r(h_r + h_p)] \frac{f_{c,m}}{1.0} - A_s \frac{f_{sm}}{1.0} = 7577.83 \text{ kN} \quad (7.9)$$

As it can be seen, the maximum available compressive stress ($N_{c,max}$) would always be much greater compared to the maximum available tensile stress ($N_{a,max}$). The shear connection would always be designed with the available stress resultant of the steel parts.

The number of connectors is taken on the shear length $L_s = 3 \times L/8 = 2.25 \text{ m}$ and the number is $N_{sc} = 8$. The parameters of the shear studs used in the test were :

$d_{sc} = 19 \text{ mm}$, diameter of the shear studs

$h_{sc} = 100 \text{ mm}$, height of the shear studs

$f_{u,sc,m} = 500 \text{ MPa}$, the estimated ultimate tensile strength of the shear studs¹

The shear resistance of the headed stud is determined from :

$$P_R = \min \left(\frac{0.8f_{u,sc,m}\pi d_{sc}^2/4}{1.0}; \frac{0.29\alpha d_{sc}^2 \sqrt{f_{ck}E_{cm}}}{1.0} \right) = 113.41 \text{ kN} \quad (7.10)$$

Where:

$\alpha = 1$ because the ratio $\frac{h_{sc}}{d_{sc}} = 5.3 > 4$

E_{cm} secant modulus of elasticity of concrete, (here $E_{cm} = 36365 \text{ MPa}$)

The degree of shear connection is then estimated by :

$$\eta = \frac{N_{sc}P_R}{\min(N_{a,max}; N_{c,max})} \quad (7.11)$$

Finally, $\eta = 0.52 \geq 0.4$, the connection is partial.

¹This value is obtained from the results given by the supplier and is limited by EN 1994-1-1 (2005)

Evaluation of the bending resistance

In the previous chapter concerning the test on the steel beam only, the class of the U steel section was determined according to EN 1993-1-5 (2007). The steel section was determined to be at least a class 3 section without any risk of plate buckling. For the composite section, the steel section is principally in tension and even if a part is in compression, the possibility to develop a plastic bending resistance is assumed. Which is normally allowed only for a class 1 and 2.

Since the available compression stress resultant ($N_{c,max}$) is greater than the tension stress resultant ($N_{a,max}$), a first equilibrium is established as if the connection was full in order to determine the maximum compression height of the composite slab ($h_{c,full}$) :

$$h_{c,full} = \frac{A_{a,hr}f_{y,hr,m} + A_{a,cf}f_{y,cf,m} + A_s f_{sm}}{0.85b_{eff}f_{c,m}} = 31.1 \text{ mm} \quad (7.12)$$

The connection of the composite beam is partial ($\eta = 0.52$), thus the height of the compressed concrete is reduced by multiplying it by η :

$$h_{c,part} = \eta h_{c,full} = 16.1 \text{ mm} \quad (7.13)$$

Therefore, the stress resultant of the concrete slab in partial shear connection becomes:

$$N_{c,part} = \eta N_{c,full} = \eta 0.85b_{eff}h_{c,full} \frac{f_{c,m}}{1.0} = 1096.15 \text{ kN} \quad (7.14)$$

A new equilibrium is made between the stress resultants and a second plastic neutral axis appears in the steel section due to partial shear connection. In order to find the position of the second plastic neutral axis (PNA 2), the steel cross-section is decomposed into different stress blocks with their stress resultants (see Figure 7.5). The position of PNA 2 is assumed to be in the steel web of the section². That means the steel parts above are in compression ($N_{a,com}$) and the steel parts below are in tension ($N_{a,ten}$). The portion of the steel web in compression is $\rho h_{a,cf,w}$ where ρ is determined by:

$$\rho = \frac{N_{a,cf,w} + N_{a,ten} - (N_{c,part} - N_r + N_{a,com})}{2N_{a,cf,w}} = 0.36 \quad (7.15)$$

Where:

$N_{a,cf,w} = 592.48 \text{ kN}$, stress resultant of the “simplified” steel webs (see note 2)

$N_{a,ten} = 864.69 \text{ kN}$, stress resultant of all the rest of the steel parts in tension (except the web)

²In order to simplify the method, the webs are only the parts below the edges stiffeners and the edges stiffeners comprise the part of the webs at the same height

$N_{a,com} = 296.58 \text{ kN}$, stress resultant of all the rest of the steel parts in compression (except the web)

$N_{c,part} = 1096.15 \text{ kN}$, stress resultant of the concrete in compression in partial shear connection calculated by Equation 7.14.

$N_s = 365.05 \text{ kN}$, stress resultant of the rebars in tension

Finally, with this method, the plastic bending resistance in partial shear connection evaluated according to EN 1994-1-1 (2005) is $M_{pl,R,1} = 476.27 \text{ kNm}$ (the detailed calculation is presented in Table 7.1). Compared to the test results, the analytical value is 10.3% inferior to the ultimate bending resistance of the test ($M_{ult,test} = 530.90 \text{ kNm}$) and 3.3% superior to the pseudo-plastic resistance evaluated from the test ($M_{R,p} = 461.10 \text{ kNm}$).

According to the distribution of the stress blocks in partial shear connection (see Figure 7.5), the upper part of the steel section should be in compression. This was not recorded by the strain gauges at this location. This method assumed that the cold-formed side plates were yielded. As it was not really the case, the method can overestimate the bending resistance moment. This method would not be recommended for a normal use, other methods are investigated in the following paragraphs.

Table 7.1 – Calculation of the bending resistance

Part	z_i/v' [mm]	N_{ten} [kN]	N_{com} [kN]	$M_{pl,R,i}$ [kNm]
Concrete in compression	392.0		1096.15	429.64
Cold-formed steel in compression	252.8		511.33	120.04
Rebars in tension	100	-365.05		-36.51
Cold-formed steel in tension	72.2	-641.94		-32.09
Hot rolled steel in tension	8	-600.48		-4.80
Sum		-1607.48	1607.48	476.27

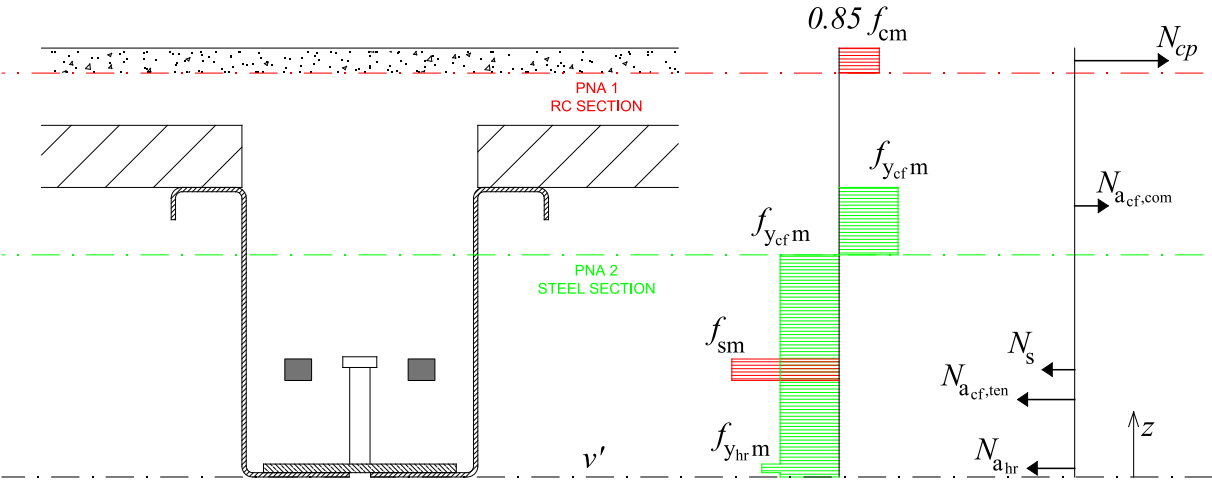


Figure 7.5 – Plastic stress distribution in partial shear connection

7.3.3 Plastic bending resistance considering a full plastic distribution neglecting the contribution of the cold-formed part

In the thesis project, the aim is to develop a composite solution unpropped in construction thanks to the steel beam and fire resistant thanks to the reinforced concrete beam. When these two criteria are respected, the bending resistance in the exploitation stage produced by the composite beam is much greater compared to the loads. There is no need for such resistance, that is why a simplified method of design in accordance with EN 1994-1-1 (2005) is proposed. The method consists in neglecting the contribution of the side plates of the steel beam and to consider only the hot rolled central plate (See Figure 7.6).

Evaluation of the degree of shear connection

The degree of shear connection is calculated according to EN 1994-1-1 (2005) with the assumption that only the hot rolled central plate of the beam was participating in the mechanical composite behaviour. The shear studs connect the central plate to the bottom of the reinforced concrete beam. This means that the maximum tensile stress resultant passing through the connection is the tensile stress resultant of the central plate ($N_{a,max,2}$) :

$$N_{a,max,2} = A_{a,hr} \frac{f_{y,hr,m}}{1.0} = 600.48 \text{ kN} \quad (7.16)$$

Where:

$A_{a,hr}$ is the area of the hot rolled steel part (here, $A_{a,hr} = 14.40 \text{ cm}^2$)

Whereas, the maximum compressive stress resultant passing through the connection ($N_{c,max}$) is not changing (see Equation 7.9).

The degree of shear connection becomes :

$$\eta_2 = \frac{N_{sc} P_R}{\min(N_{a,max,2}; N_{c,max})} = 1.51 \quad (7.17)$$

Finally, $\eta_2 = 1.51 \geq 1.0$, the connection is full.

Evaluation of the bending resistance

The equilibrium between the stress resultant is established in order to determine the maximum compression height of the composite slab ($h_{c,full,2}$) :

$$h_{c,full,2} = \frac{A_{a,hr} f_{y,hr,m} + A_s f_{sm}}{0.85 b_{eff} f_{c,m}} = 14.2 \text{ mm} \quad (7.18)$$

Finally with the proposed simplified method, the plastic bending resistance in full shear connection evaluated according to EN 1994-1-1 (2005) is $M_{pl,R,2} = 338.06 \text{ kNm}$. Compared to the test results, the analytical value is 36.3% inferior to the ultimate bending resistance of the test ($M_{ult,test} = 530.90 \text{ kNm}$) and 26.7% inferior to the pseudo-plastic resistance evaluated from the test ($M_{R,pp} = 461.10 \text{ kNm}$).

Table 7.2 – Calculation of the bending resistance with proposed simplified method

Part	z_i/v' [mm]	N_{ten} [kN]	N_{com} [kN]	$M_{pl,R,i}$ [kNm]
Concrete in compression	392.9		965.53	379.37
Rebars in tension	100	-365.05		-36.51
Hot rolled steel in tension	8	-600.48		-4.80
Sum		-965.53	965.53	338.06

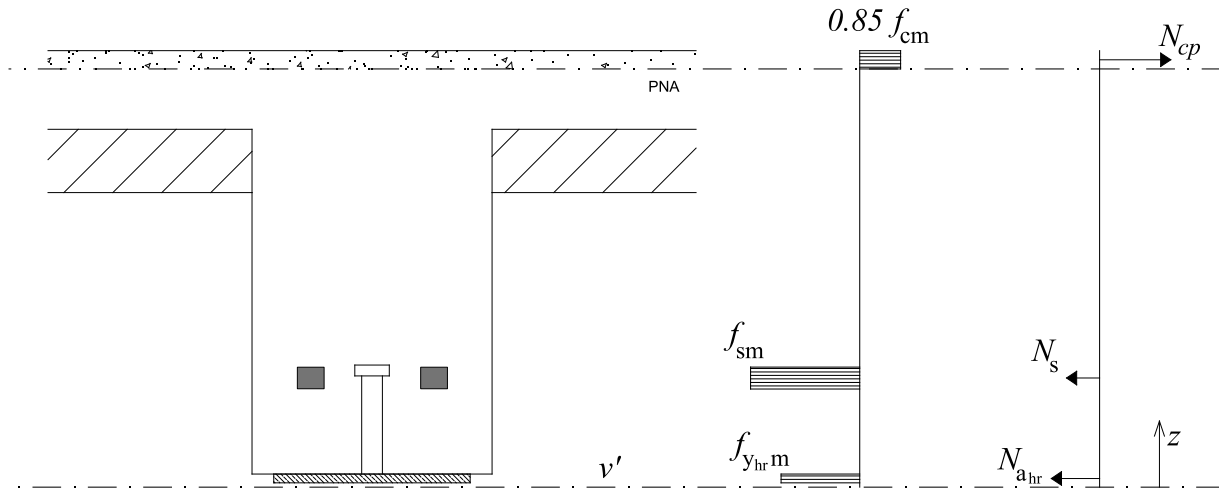


Figure 7.6 – Plastic stress distribution with the simplified model

The proposed simplified method, by neglecting the contribution of the cold-formed part of the steel section in the composite bending resistance, allows a faster resolution and gives an underestimated result about 30%. In the frame of the thesis, this proposed method of design is faster but gives a safe-sided design that is too conservative and uneconomic. A last method of design is proposed to make a compromise between these two last methods.

7.3.4 Plastic bending resistance with a full plastic distribution limited by the maximum shear force of the connection

The proposed method takes into account the yielded parts of the steel plates, as it was the case in reality, but it neglects the steel parts subjected to an elastic stress distribution. First, the maximum shear capacity of the composite connection is determined. Then the quantity of steel parts that can be yielded is estimated by equilibrating the maximum available shear capacity of the connection.

Evaluation of the maximum shear force of the connection

In § 7.3.2, the shear resistance of the headed stud used in the test is determined to be $P_R = 113.41$ kN. The number of connectors used on the shear length were $N_{sc} = 8$. The maximum shear force available through this connection is :

$$V_{l,max} = N_{sc} P_R = 907.3 \text{ kN} \quad (7.19)$$

Evaluation of the available remaining force in the cold-formed side plates

The resulting force integrating from the stress block of the bottom central plate is :

$$N_{a,hr} = t_{hr} b_{hr} f_{y,hr,m} = 600.5 \text{ kN} \quad (7.20)$$

That means, the connection is able to transfer a remaining shear force to the cold-formed side plates of:

$$V_{l,cf} = V_{l,max} - N_{a,hr} = 306.8 \text{ kN} \quad (7.21)$$

Evaluation of the yield parts of the cold-formed side plates

It is then possible to estimate the area of the cold-formed side plates yielded:

$$A_{cf,pl} = \frac{V_{l,cf}}{f_{y,cf,m}} = 9.53 \text{ cm}^2 \quad (7.22)$$

Without taking into account the bending radius for simplification purpose, the height of the last fibre yielded of the cold-formed side plates is determined as:

$$h_{cf,pl} = \frac{A_{cf,pl} - 2t_{cf} b_{cf,inf}}{2t_{cf}} = 29.1 \text{ mm} \quad (7.23)$$

Evaluation of the bending resistance considering a part of the cold-formed side plates yielded

The equilibrium between the stress resultants is established in order to determine the maximum compression height of the composite slab:

$$h_{c,3} = \frac{A_{hr,pl} f_{y,hr,m} + A_s f_{sm} + A_{cf,pl} f_{y,cf,m}}{0.85 b_{eff} f_{c,m}} = 18.7 \text{ mm} \quad (7.24)$$

Table 7.3 – Calculation of the bending resistance with cold-formed side plates partially plastic

Part	z_i/v' [mm]	N_{ten} [kN]	N_{com} [kN]	$M_{pl,R,i}$ [kN m]
Concrete in compression	390.7		1272.35	497.05
Rebars in tension	100.0	-365.05		-36.51
Cold-formed webs	18.6	-74.97		-1.39
Hot rolled steel in tension	8.0	-600.48		-4.80
Cold-formed bottom flanges	2.0	-231.84		-0.46
Sum		-1499.17	1272.35	453.9

Finally with the third method, the plastic bending resistance is evaluated according to EN 1994-1-1 (2005) is $M_{pl,R,3} = 453.9 \text{ kNm}$. Compared to the test results, the analytical value is 14.5% inferior to the ultimate bending resistance of the test ($M_{ult,test} = 530.90 \text{ kNm}$) and 1.6% inferior to the pseudo-plastic resistance evaluated from the test ($M_{R,pp} = 461.10 \text{ kNm}$).

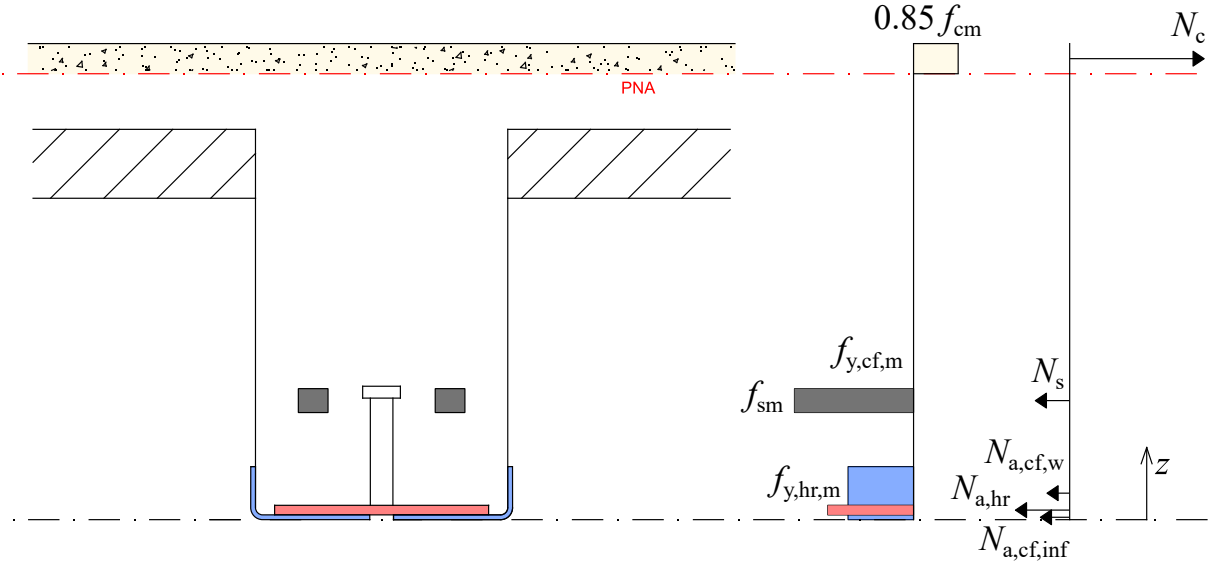


Figure 7.7 – Plastic stress distribution considering only a part of the cold-formed plate yielded

7.3.5 Compared to the test curve

The bending resistances obtained with the fourth analytical method are detailed in the paragraphs above and are recapped in Table 7.4 are compared to the test curve in Figure 7.8.

Table 7.4 – Bending resistance obtained with analytical methods

Designation	Symbol	Value [kN m]	$\frac{M_R}{M_{R,pp}}$	$\frac{M_R}{M_{ult,test}}$
Elasto-plastic resistance by the strain distribution at $0.95P_{ult,test}$	$M_{epI,R}$	484.0	1.04*	0.91*
Plastic resistance with full plastic distribution	$M_{pl,R,1}$	476.3	1.03	0.90
Plastic resistance without side plates	$M_{pl,R,2}$	338.1	0.73	0.64
Plastic resistance limited by the shear connection	$M_{pl,R,3}$	453.9	0.98	0.85

* : The method used to determine the elasto-plastic resistance by integrating the strain distribution was carried out at $0.95P_{ult,test}$. In fact, the accuracy of the method should be obtained with the ratio on $0.95M_{ult,test}$ which is 0.96 instead of 0.91.

For comparison, the results are inserted in the moment-deflection curve of the test in Figure 7.8. The ultimate resistance of the section $M_{ult,test}$ and the pseudo-plastic resistance $M_{R,pp}$ are referred by red points.

The calculation method for $M_{epI,R}$ was accurate and the assumptions made were more realistic compared to the strain measured during the test. However, the resolution without measured values seem to be to complicate with too many unknown parameters.

The calculation method for $M_{pl,R,1}$ was accurate but the assumptions were less realistic. In fact, the assumption that the side plates are able to be fully yielded is not in accordance with the class of the section (class 3 instead of 1 or 2). The stress distribution lead to a

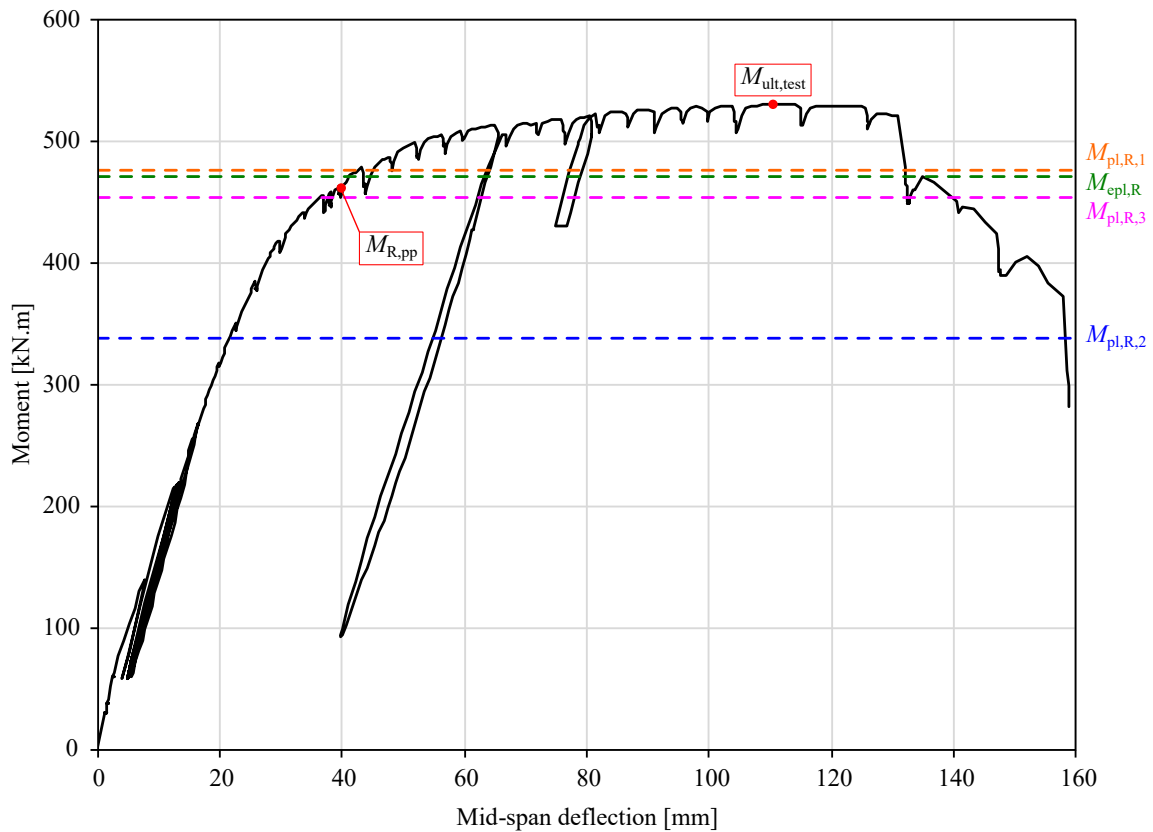


Figure 7.8 – Analytical bending resistance compared to the test curve

compressive part in the top of the cold-formed side plates and this was not recorded during the test. In addition, the method is more complex than the two followings, that is why this method would not be kept for design guidelines.

The calculation method for $M_{pl,R,2}$ was not accurate and the assumptions were less realistic because it is certain that the cold-formed side plates had yielded and they are neglected in the calculation. However, the method is really simple and fast. In the thesis project, after satisfying the construction phase and the fire phase, the association of the steel and concrete often leads to a bigger resistance than needed. This method is not kept because the results are too conservative but due to its simplicity it could be sufficient in some projects for the resistance in the exploitation stage.

The calculation method for $M_{pl,R,3}$ was accurate and the assumptions were realistic because it is sure that the cold-formed side plates had yielded. Additionally, this method is simple and fast. Therefore, this method is kept for the design of the bending resistance in the exploitation phase.

7.4 Numerical study

In order to numerically reproduce the test, a Finite Element (FE) Model is developed with the software ANSYS (2017).

7.4.1 Model

The beam specimen is modelled with the same length (6.3 m) and span (6 m). The plates constitute the U-shaped steel beam and are modelled with shell elements (SHELL181). The 8 steel battens linking the top flanges of the U cross-section together are also modelled with shell elements (SHELL181).

The rebars are modelled explicitly with link elements (LINK180), the amount of rebars and their positions in the test are reproduced in the model. The concrete part is modelled with 3D elements (SOLID185). The shear connection is modelled with spring elements (COMBIN39).

The steel-concrete composite beam is modelled with the exact geometry presented in § 6.2.1 and represented in Figure 7.9 and 7.10.

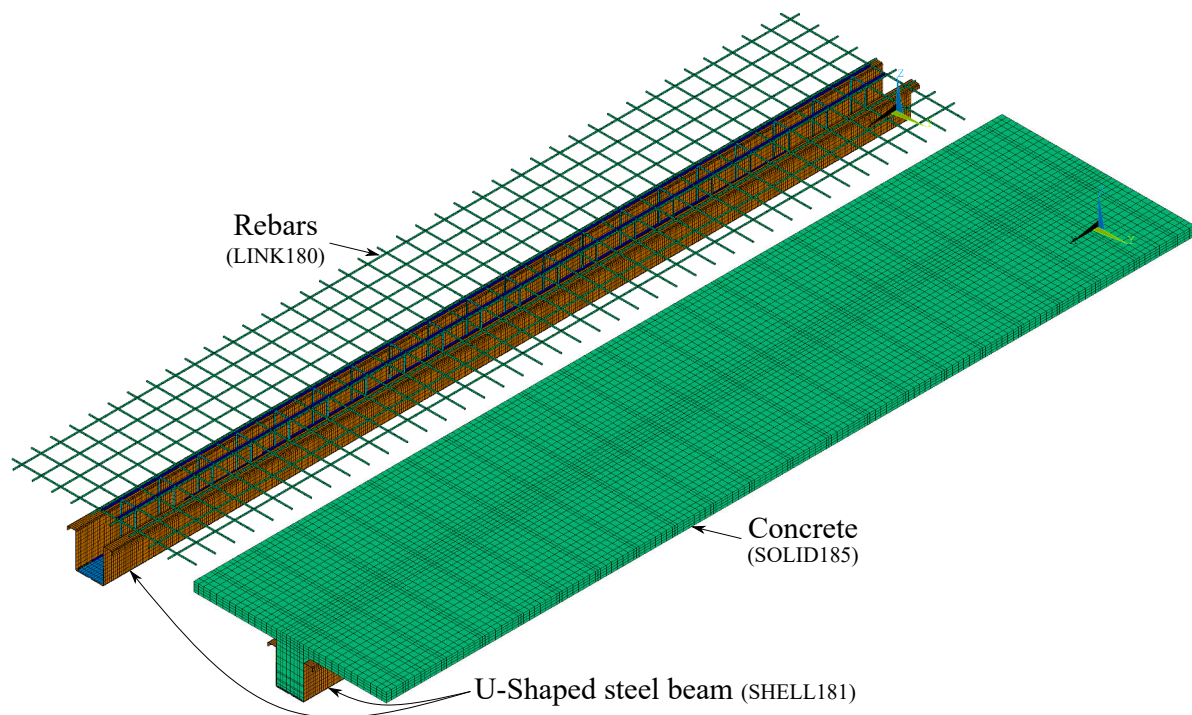


Figure 7.9 – The steel-concrete composite specimen in ANSYS (ISO view)

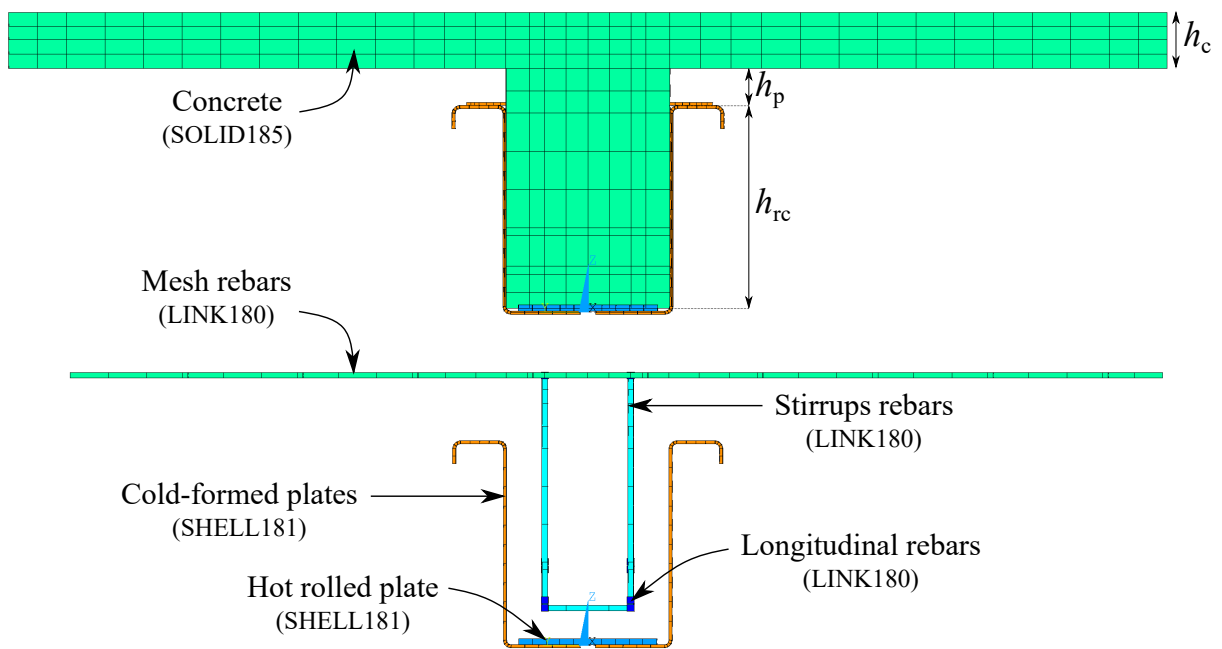


Figure 7.10 – The steel-concrete composite specimen in ANSYS (Front view)

The U-shaped steel beam

The central plate, in reality, is assembled to the side plates with self-drilling screws. Instead of the self-drilling screws, in the model a contact is set between the bottom surfaces of the central plate (CONTA174) and the top surfaces of the folded side plates (TARGE170). The behaviour of this contact surface is always bonded.

The eight steel battens linking the top flanges together along the beam are in reality assembled to the top flanges with self-drilling screws. In the FE model, they are connected to the top flanges with a rigid beam at their connection points. The beams (BEAM188) are linking a node of the top flange to a node of the batten.

The steel-concrete interface

The concrete is in contact with the 3 faces of the interior of the U-shaped steel beam. The contact is also created by the pair CONTA174 (the concrete) and TARGE170 (the steel plates). The nature of the contact is sliding without friction, that means the slip between concrete and steel is allowed. At the bottom face of the concrete rib in contact with the hot rolled central plate of the U-shaped section, the nature of the contact is also sliding without friction but with no separation during the simulations. That means the concrete rib could not be separated from the U-shaped vertically. This assumption helped the solution convergence. In reality, the separation from a concrete slab to the steel beam should be taken into account in the design of the connection with headed shear stud according to EN 1994-1-1 (2005).

The shear connection

In the developed composite solution, the shear connection between steel and concrete is provided by headed stud welded on the central plate at the bottom of the section. This shear connection location is not traditional and not well-covered by the standards. In the FEM, the mechanical shear action of the studs is modelled by non-linear spring elements (COMBIN39)

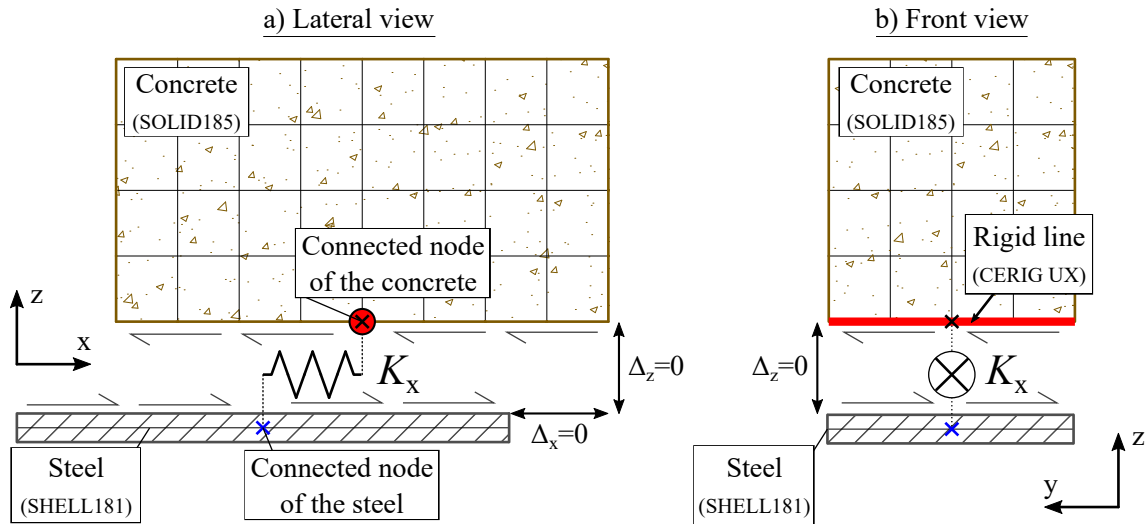


Figure 7.11 – Schematic representation of the shear connection implemented in the FEM

in the longitudinal direction (UX) as represented in Figure 7.11. The spring is linking two coincident nodes of both steel and concrete mesh. There is a spring at each position of the welded studs. In order to avoid local stresses in the concrete around the nodes linked by the springs, all the nodes transversally aligned with the connected node of the concrete are rigidly connected together. Therefore, the longitudinal shear force ($V_{l,x}$) transferred through the spring (K_x) is distributed on the nodes at the bottom of the concrete section aligned with a position of the shear studs. This is done in ANSYS with the command “CERIG”. The command defines a rigid region by generating constraint equations to relates the nodes in the considered region. The constraints are only applied on the longitudinal direction (UX degree of freedom only). This assumption facilitates the convergence by limiting concentrated stresses.

For the mechanical behaviour of the headed shear studs, Ollgaard, Slutter, and Fisher (1971) proposed, after 48 “push-out” tests, the non-linear load-slip relationship given in Equation 7.25.

$$Q = Q_u \left(1 - e^{-18\Delta} \right)^{2/5} \quad (7.25)$$

Where :

Q is the load

Q_u is the ultimate shear strength of the connector

Δ is the slip in inches

The expression 7.25 converted in millimetres and in Eurocode notations becomes :

$$P = P_u \left(1 - e^{-0.7\delta} \right)^{0.4} \quad (7.26)$$

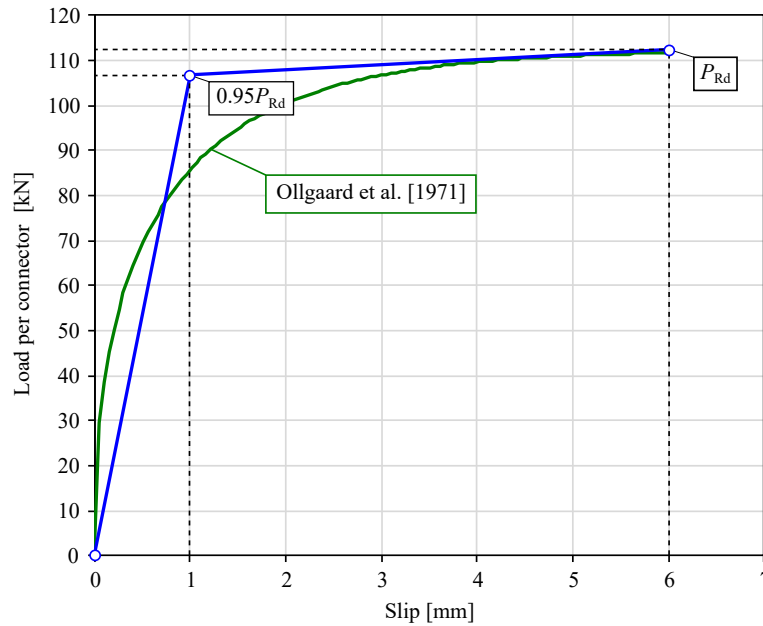


Figure 7.12 – Load-slip curve for the shear studs implemented in the FEM

Where :

P is the load

P_u is the connector shear strength

δ is the slip in mm

The connector shear strength for the headed shear stud was already determined in the analytical studies (see § 7.3) by Equation 7.10 and the values was estimated at $P_u = 112.3$ kN.

The non-linear mechanical behaviour of the shear studs used for the test can be approximated with these values and the Equation 7.26 of Ollgaard et al. (1971), a representation is given in Figure 7.12. In order to simplify the FEM and increase the simulation convergence, the non-linear curve proposed by Ollgaard et al. (1971) is replaced by a bilinear curve as shown in Figure 7.12. The bilinear curve implemented in the model as two characteristics points, at 1 mm of slip the strength of the shear stud is estimated at $0.95P_R$ and at 6 mm of slip the strength of the shear stud is estimated at P_R . The slip value of 6 mm is a common limit defining the ductility of a shear connection (§6.6.1.1(5) in EN 1994-1-1 (2005)).

7.4.2 Elements

Referring to the user guide manual of ANSYS (2017), the definition of the elements used in the FE model are:

- SHELL181 is a four-node element with six degrees of freedom at each node (UX, UY, UZ, ROTX, ROTY, ROTZ). It is well suited for large-deflection effects. Elasticity and plasticity are supported.
- BEAM188 is used as a linear two-node beam element with six degrees of freedom at each node (UX, UY, UZ, ROTX, ROTY, ROTZ). It is well suited for large-deflection effects.

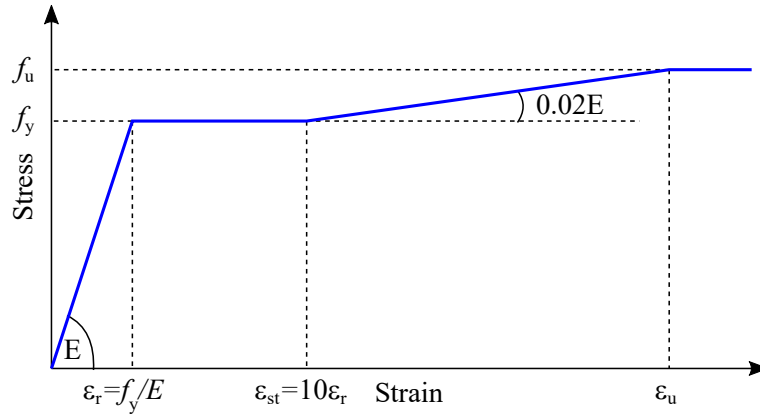


Figure 7.13 – Steel material law for the plates of the U-shaped beam in GMNIA calculations

- CONTA174 is used to represent contact and sliding between 3-D target surfaces and a deformable surface defined by this element. In the case of pair-based contact, the target surface is defined by the 3-D target element type, TARGE170. Contact occurs when the element surface penetrates an associated target surface.
- TARGE170 is used to represent various 3-D target surfaces for the associated contact elements CONTA174.
- SOLID185 is used for 3-D modelling of solid structures. It is defined by eight nodes having three degrees of freedom at each node (UX, UY, UZ). The element has plasticity, large deflection, and large strain capabilities.
- COMBIN39 is an unidirectional element with a non-linear generalized force-deflection capability. The longitudinal option is a uniaxial tension-compression element with up to three degrees of freedom at each node: translations in the nodal x, y, and z directions. No bending or torsion is considered.

7.4.3 Materials properties

Structural steel

For the steel plates of the U-shaped beam, for both steel grades, the numerical simulations are based on the multi-linear law proposed in ECCS-TC8 (1984) for an elasto-plastic material (see Figure 7.13) in both tension and compression. According to the tensile test results, the values used for the laws are presented in Table 7.5.

Table 7.5 – Parameters of the multi-linear laws implemented in the FEM

Components	Grade	E [MPa]	f_y [MPa]	f_u [MPa]	ϵ_r	ϵ_{st}	ϵ_u
Cold-formed plates	S235	210000	322	405	0.15 %	1.53 %	3.51 %
Hot rolled plates	S355	210000	417	558	0.20 %	1.99 %	5.34 %

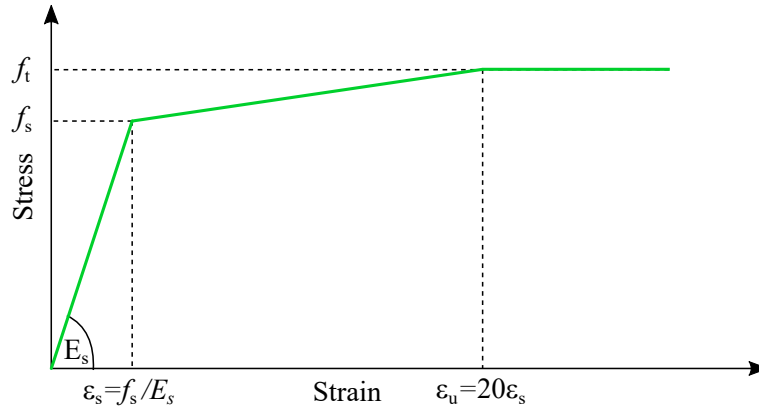


Figure 7.14 – Steel material law for the rebars in GMNIA calculations

Reinforcing steel

For the rebars, the material law used is a bilinear curve, as proposed in EN 1992-1-1 (2005) and represented in Figure 7.14 in both tension and compression. The values used for the bilinear law are those from the tensile tests presented in Table 7.6.

Table 7.6 – Parameters of the bilinear law implemented in the FEM

Components	Grade	E_s [MPa]	f_s [MPa]	f_t [MPa]	ϵ_s	ϵ_u
Rebars	S235	20000	580	680	0.29 %	5.8 %

Concrete

The concrete, composed of aggregates included in a cement matrix, is heterogeneous in its composition and in its structural behaviour. The mechanical behaviour of the concrete is complex and completely different in tension and compression.

In uni-axial compression, the concrete has almost a linear behaviour until 30% of the peak stress (noted $f_{c,m}$ in EN 1992-1-1 (2005)). Then the concrete follows a non-linear hardening phase until reaching the peak stress. After reaching the peak stress, the concrete has a softening phase induced by micro-cracks until reaching the failure.

In tension, the mechanical behaviour is totally different. The tensile strength is around 13 times smaller in comparison to the compressive strength for standard concrete. In uni-axial tension, the behaviour is quasi-linear until reaching the tensile limit strength characterized by the cracking of the concrete. Then, the stress decreased in a tension softening phase until the failure.

For normal concrete, EN 1992-1-1 (2005) proposes a non-linear stress-strain relation (see Equation 7.27) for the behaviour in compression represented in Figure 7.15. The expression is valid until the strain (ϵ_c) is positive and inferior to the ultimate compressive strain for the concrete (ϵ_{cu1}) according to EN 1992-1-1 (2005). The non-linear mechanical behaviour of the concrete in tension is not presented in the Eurocode.

$$\sigma_c = \frac{k\eta - \eta^2}{1 + (k - 2)\eta} f_{c,m} \quad (7.27)$$

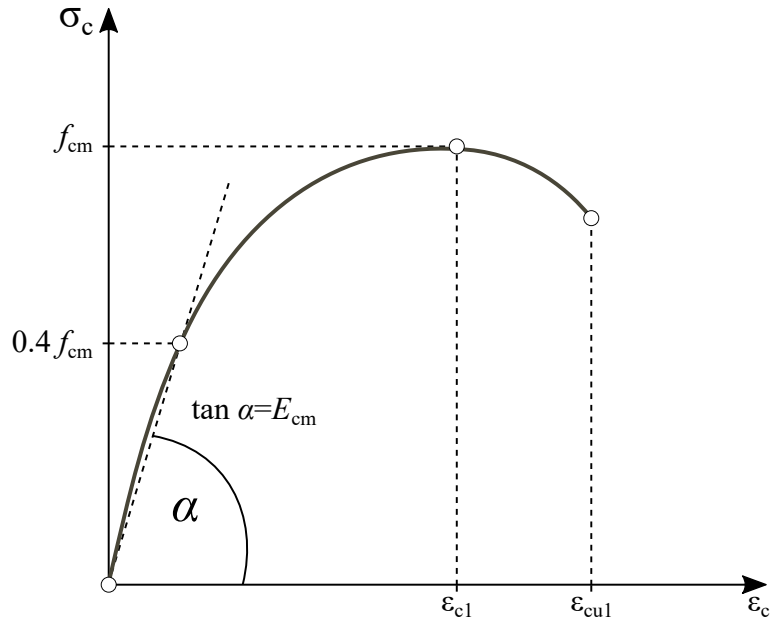


Figure 7.15 – Stress-strain relation in compression according to EN 1992-1-1 (2005)

Where :

$$\eta = \varepsilon_c / \varepsilon_{c1}$$

$$k = 1.05 E_{cm} |\varepsilon_{c1}| / f_{c,m}$$

The stress-strain relationship suggested in CEB-FIP Model Code 1990 (1993) is more general for describing the concrete behaviour in both tension and compression. The model proposed gives a compression curve in two parts on both sides of the limiting strain $\varepsilon_{c,lim}$ given in Equation 7.28. The first part (when $\varepsilon_c \leq \varepsilon_{c,lim}$) is similar to the curve proposed by Equation 7.27, it is composed of an ascending branch until the peak stress ($f_{c,m}$) and a descending branch until $\varepsilon_{c,lim}$ (which is closed to ε_{cul} of EN 1992-1-1 (2005)). The second part (when $\varepsilon_c > \varepsilon_{c,lim}$) is a compression softening until failure where the remaining stress is not null.

$$\frac{\varepsilon_{c,lim}}{\varepsilon_{c1}} = \frac{1}{2} \left(\frac{k}{2} + 1 \right) + \left[\frac{1}{4} \left(\frac{k}{2} + 1 \right)^2 - \frac{1}{2} \right]^{1/2} \quad (7.28)$$

In compression, for the first part, when $\varepsilon_c \leq \varepsilon_{c,lim}$, the stress-strain relationship for short-term loading is given by Equation 7.29.

$$\sigma_{c,1} = \frac{k\eta - \eta^2}{1 + (k-2)\eta} f_{c,m} \quad (7.29)$$

It can be noted that Equation 7.27 proposed by EN 1992-1-1 (2005) and Equation 7.29 proposed by CEB-FIP Model Code 1990 (1993) are equivalent, the only difference is in the definition of the coefficient k (the ratio of the modulus). According to Eurocode 2, the secant modulus (E_{cm}) is around 1.02 greater than the secant modulus (E_{ci}) and the coefficient $k = 1.05 E_{cm} / E_{ci}$ in Eurocode 2, whereas $k = E_{ci} / E_{c1}$ in CEB-FIP Model Code 1990 (1993).

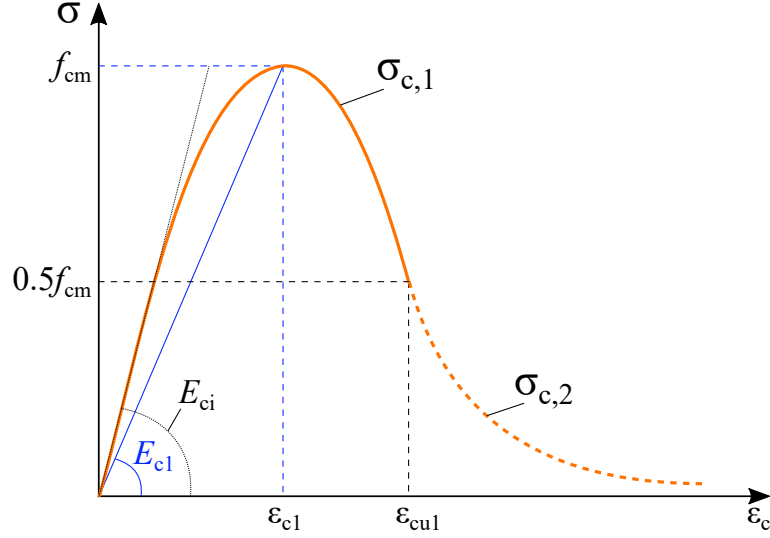


Figure 7.16 – Stress-strain diagram for uniaxial compression according to CEB-FIP Model Code 1990 (1993)

The difference is very minor in the first part of the curve in compression, this is shown in Figure 7.18.

In compression, for the second part, when $\varepsilon_c > \varepsilon_{c,lim}$, the stress-strain relationship for short-term loading is given by Equations 7.30 and 7.31.

$$\sigma_{c,2} = \left[\left(\frac{1}{\varepsilon_{c,lim}/\varepsilon_{c1}} \xi - \frac{2}{(\varepsilon_{c,lim}/\varepsilon_{c1})^2} \right) \eta^2 + \left(\frac{4}{\varepsilon_{c,lim}/\varepsilon_{c1}} - \xi \right) \eta \right]^{-1} f_{c,m} \quad (7.30)$$

$$\xi = \frac{4 \left[\left(\frac{\varepsilon_{c,lim}}{\varepsilon_{c1}} \right)^2 (k-2) + 2 \frac{\varepsilon_{c,lim}}{\varepsilon_{c1}} - k \right]}{\left[\frac{\varepsilon_{c,lim}}{\varepsilon_{c1}} (k-2) + 1 \right]} \quad (7.31)$$

Where :

$$\eta = \varepsilon_c / \varepsilon_{c1}$$

$$k = \frac{E_{ci}}{E_{c1}}$$

$E_{ci} = 21500 \alpha_E (f_{cm}/10)^{1/3}$ is the tangent modulus of elasticity in MPa ($\alpha_E = 1.0$ for most aggregates)

$E_{c1} = f_{cm} / \varepsilon_{c1}$ is the secant modulus from the origin to the peak compressive stress in MPa

In tension, for uncracked concrete, **fib** Model Code 2010 (2013) suggest a bilinear law given by Equations 7.32 and 7.33.

For $\sigma_{ct} \leq 0.9 f_{ctm}$:

$$\sigma_{ct,1} = E_{ci} \varepsilon_{ct} \quad (7.32)$$

For $0.9f_{ctm} < \sigma_{ct} \leq f_{ctm}$:

$$\sigma_{ct,2} = f_{ctm} \left(1 - 0.1 \frac{0.00015 - \varepsilon_{ct}}{0.00015 - 0.9f_{ctm}/E_{ci}} \right) \quad (7.33)$$

Where :

ε_{ct} is the strain in tension

f_{ctm} is the tensile strength in MPa

In tension, **fib** Model Code 2010 (2013) also proposed a bilinear stress-crack opening relation given by the Equations below.

For $w \leq w_1$:

$$\sigma_{ck,1} = f_{ctm} \left(1 - 0.8 \frac{w}{w_1} \right) \quad (7.34)$$

For $w_1 < w \leq w_c$:

$$\sigma_{ck,2} = f_{ctm} \left(0.25 - 0.05 \frac{w}{w_1} \right) \quad (7.35)$$

Where :

w is the crack opening in mm

$w_1 = G_F/f_{ctm}$ in mm is the crack opening at $\sigma_{ct} = 0.2f_{ctm}$

$w_c = 5G_F/f_{ctm}$ in mm is the crack opening at $\sigma_{ct} = 0$

G_F is the fracture energy in N/m, the energy required to propagate a tensile crack of unit area

fib Model Code 2010 (2013) propose Equation 7.36 for estimating the fracture energy for ordinary normal weight concrete.

$$G_F = 73f_{ctm}^{0.18} \quad (7.36)$$

The stress-strain curve for the concrete in uniaxial compression as proposed in CEB-FIP Model Code 1990 (1993) is represented in Figure 7.16 Whereas, the stress-strain and stress-crack relation for uniaxial tension are represented in Figure 7.17. The models are compared with a real case and with the material law implemented in ANSYS described below (see Figures 7.18 and 7.19).

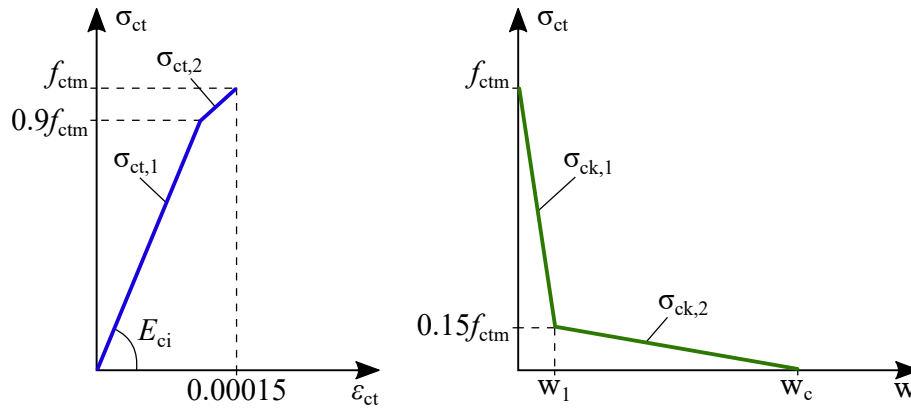


Figure 7.17 – Stress-strain and stress-crack diagrams for uniaxial tension according to CEB-FIP Model Code 1990 (1993)

In ANSYS (2017), this physical phenomena are taken into account in the FEM by a Drucker-Prager concrete exponential hardening/softening/dilatation (HSD) behaviour (called HSD2). The concrete material law implemented in the FE model and the input parameters defining the hardening and softening are presented in Annex E. The code ANSYS (2017) proposes also three others HSD behaviour (HSD4, HSD5 and HSD6) to characterize the hardening and softening of the material, the differences are mainly in the form of the functions. The parameters used for the concrete material law described above are presented in Table E.1. The value $f_{cm} = 53.4 \text{ MPa}$ is the average compressive strength measured on the concrete cylinders made during the concreting. For the other parameters needed to define the concrete law (f_{ctm} , E_{cm} , ϵ_{c1} , ϵ_{cu}), they have been chosen according to EN 1992-1-1 (2005) for a concrete that has this mean value of concrete cylinder compressive strength (f_{cm}). In this case, the values retained are those for a concrete class C45/55 (it is not the concrete class ordered which was C35/45). From the compressive test results, it appeared that the concrete was quite stronger, therefore in order to reproduce the test with the FEA those values were chosen.

Numerical simulations were performed on a simple element of concrete to compare the result of the implemented material law in the FE model (DP-HSD2) to the model proposed by EN 1992-1-1 (2005) and CEB-FIP Model Code 1990 (1993). The comparisons are represented in Figure 7.18 for compression and in Figure 7.19 for tension behaviour. The results are very similar until high stress level. Therefore it can be concluded that this material law (DP-HSD2) proposed by ANSYS (2017) would be adequate for the reproduction of the test.

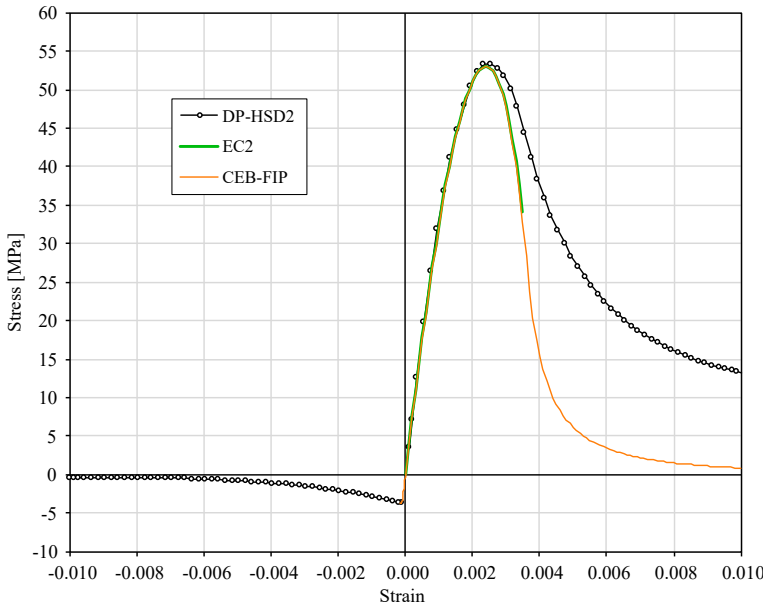


Figure 7.18 – Stress-strain curve of the concrete

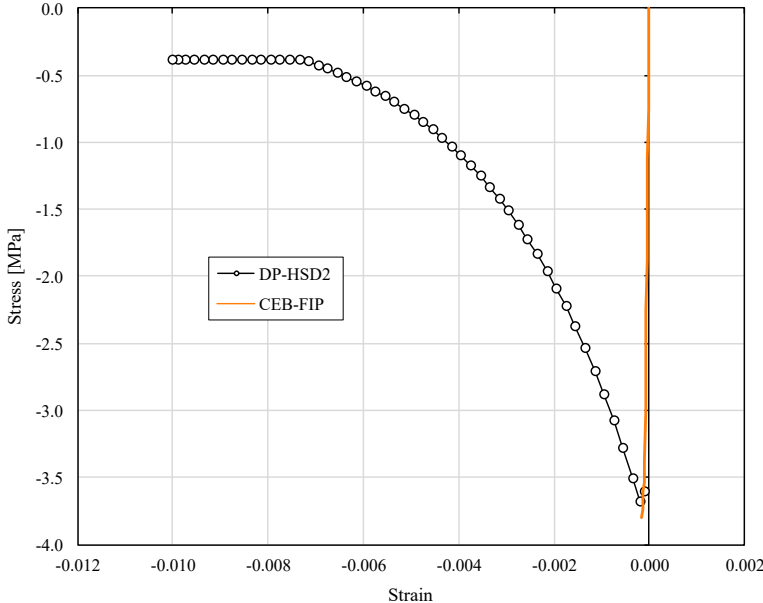


Figure 7.19 – Stress-strain curve of the concrete in tension

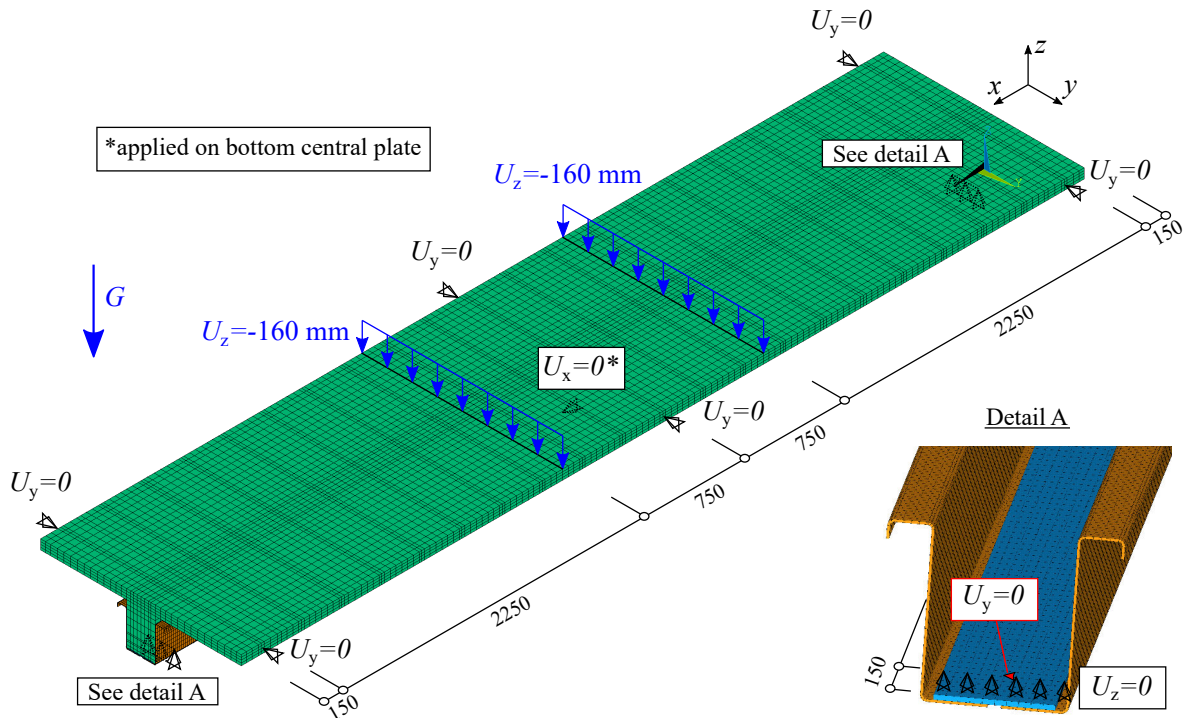


Figure 7.20 – Boundary conditions of the numerical model

7.4.4 The boundary conditions

The boundary conditions of the numerical model are represented in Figure 7.20. Like for the test, the numerical simulation is controlled in displacement. Vertical displacements ($U_z = -160\text{ mm}$) are applied at the top of the slab at the same position as the loads introduction of the test setup. That means the imposed vertical displacements are applied at 2500 mm from the supports. This value was chosen to be superior to the maximum displacement recorded during the test at this location. The gravity force is also included in the numerical model by an acceleration of $G = 9.81\text{ m/s}^2$.

At the supports, the vertical displacements (U_z) are restrained on the line of nodes of the bottom central plate, which in reality, is in contact with the rollers (see detail A in Figure 7.20). Like it was the case for the test, the composite beam exceeds by 150 mm this lines of restrained nodes on each side. For “numerical” stability reasons of the steel beam, the lateral displacements (U_y) are restrained only at the middle nodes of the bottom central plate at the supports and the longitudinal displacement (U_x) is restrained at the middle of the steel beam on one node of the bottom central plate. This was not the case in the test, but in the numerical simulation this restraint does not affect the result and keeps the model perfectly symmetric. Finally, the slab is transversally restrained by blocking three nodes in lateral displacement (U_y) on both sides of the composite slab. The three positions are at the two supports and at mid-span. In reality, this same restraints were near the supports.

7.4.5 Local geometrical imperfection

Since the cold-formed plates are slender and could be subjected to compression force, they are prone to plate buckling. In order to take this potential effect into account, local imperfections in buckling shapes were introduced in the cold-formed plates. The local imperfection is introduced similarly as it was already done for the previous FE model reproducing the first

test on the steel beam only. According to EN 1993-1-5 (2007) § C.5, the local imperfections are in plate buckling shape with a magnitude $e_{0w} = \min(a/200; b/200)$, where a and b are the sides of the panels (see Figure 5.13).

7.4.6 Validation of the FEM compared to the test

The numerical analysis, with the FE model presented in the paragraphs below, is performed with material non-linearities considering geometrical imperfection (GMNIA). Since the shear connection capacity is only an estimation, two simulations were carried out with two values of shear strength $P_{Rd} = 112.3 \text{ kN}$ and $0.75P_{Rd} = 84.2 \text{ kN}$. The evolution of the mid-span deflection with the increase of the applied load is shown in Figure 7.21.

First, it can be seen that the numerical results are very accurate compared to the test result. The FE model is able to reproduce the test with a good precision, this confirms that the assumptions made on the material laws and the boundary conditions were correct. This also underlines that the single full-scale test carried out at the Laboratory was well done.

It can be seen that the moment-deflection responses of the simulations with the two configurations fit with the test curve at different load step. The stiffness of the composite beam is almost identical (2.5% of gap) between the test and the FE model with the assumption of the shear capacity of the connection (P_{Rd}). However, after a mid-span deflection of $\delta_{L/2} = 40 \text{ mm}$ ($L/150$), the bending resistance of the FE model is starting to be superior to the bending resistance of the tested composite beam. Approaching the failure at $\delta_{L/2} = 120 \text{ mm}$ ($L/50$), the resistance determined by the FE model is superior to the real resistance of the test by 7.0%.

For the second FE model with a reduced shear connection capacity ($0.75P_{Rd}$), after the elastic part, the stiffness of the beam modelled differs from the test. At $\delta_{L/2} = 30 \text{ mm}$ ($L/200$), the bending resistance of the second FE model is inferior to the real resistance of the test by 11.4%. However, approaching the failure, this time, the resistance determined by the second FE model is only inferior to the real resistance of the test by 1.7%.

It can be observed in Figure 7.21, that the loss of stiffness in the second model occurs after a slip of $\delta_x = 1 \text{ mm}$ for the first connector next to the support. In fact, in the FE model, the shear stud yielded and reached a plastic plateau after 1 mm of slip with a very low corresponding stiffness (see Figure 7.12). For both FE model, the slip of 1 mm was reached almost at the same time. However, for the model without reduction of P_{Rd} the mechanical behaviour of the composite beam is closer to the test until the pseudo-plastic resistance $M_{R,pp}$. After the second model with a reduced P_{Rd} gave a closer result compared to the test. The reason might come from a loss of shear strength in the connection at very high displacement near the failure load. In fact, in the investigation on the failure mode of the composite beam after the test in § 6.8, it was found that the concrete surrounding the connectors was crushed and could have reduced the shear strength at this load level. In order to potentially reduce this effect, additional stirrups rebars would be recommended in design guidelines (see § 8.3) next to each connector.

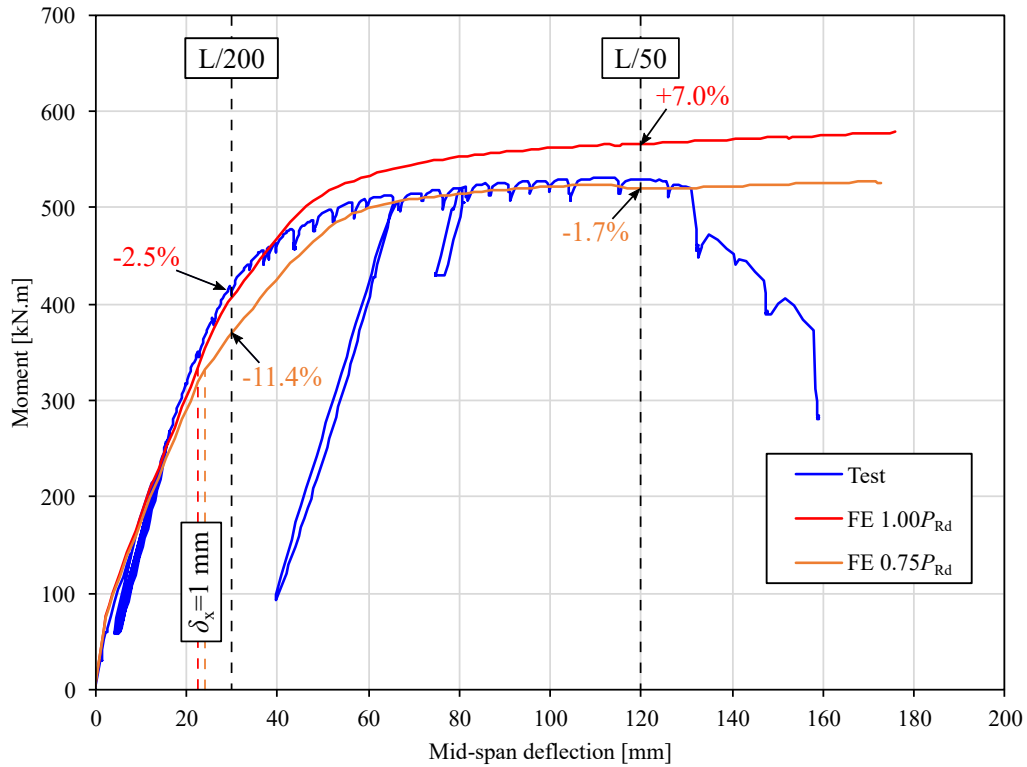


Figure 7.21 – Comparison between FE results and test result

The vertical displacements of the nodes of the FE model with full strength connection ($1.0P_{Rd}$) at $L/50$ (approximately the failure) are shown in Figure 7.22. The deflection obtained is similar to the test until the failure, the FE model is not able to reproduce the deflection after the failure.

The longitudinal displacements of the nodes of the FE model with full strength connection ($1.0P_{Rd}$), at one end of the beam, at $L/50$ (approximately the failure) are shown in Figure 7.23. The end-slip (δ_{sx}) is obtained from the differential in longitudinal displacement between the steel and concrete parts as shown in Figure 7.23.

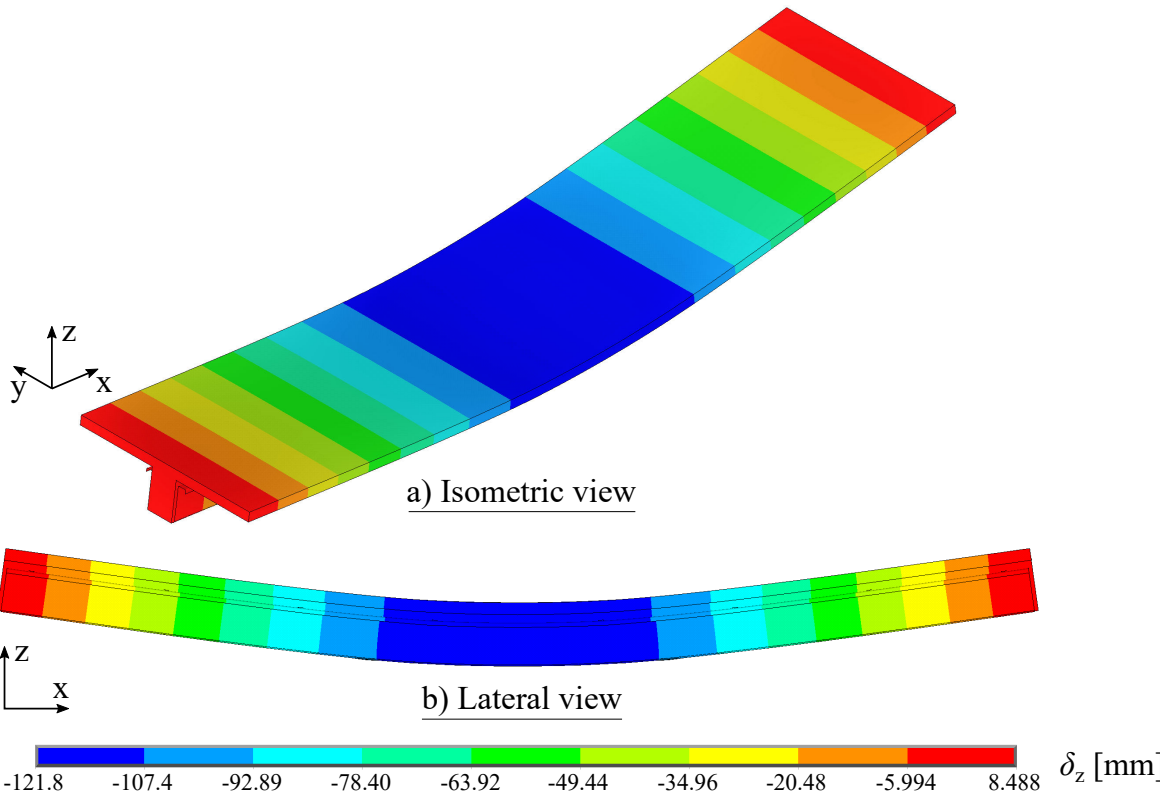


Figure 7.22 – Vertical displacement δ_z of the nodes in the FE model at L/50

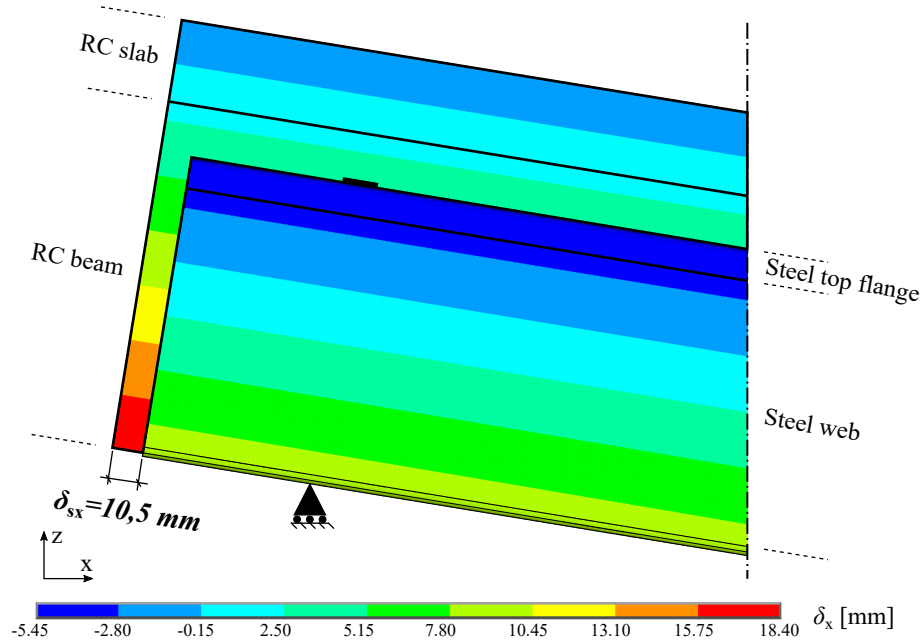


Figure 7.23 – Longitudinal displacement δ_x of the nodes at one end in the FE model at L/50

7.5 Conclusions

The analytical and numerical studies to investigate the mechanical behaviour of the composite beam leads to the following conclusions:

- A partial shear connection can be adopted and the determination of the bending resistance of the composite beam can follow the third method proposed. In this method the cold-formed side plates of the U-shaped section are partially yielded depending of the available shear capacity of the connection.
- A 3D finite element model was created and validated with the test with assumptions on the shear strength of the connection (1.0 or $0.75P_{Rd}$). The comparison of the results underlined that the connection, located in tension zone, had a shear strength fully efficient, until the pseudo-plastic bending resistance (M_{Rp}). However, a slight reduction of the shear capacity was found at high load level. Therefore, additional stirrup reinforcements are recommended to be placed at the position of the shear connectors to limit a potential reduction of the connection strength.

Chapter 8

Design and constructional guideline

Contents

8.1	Construction stage	220
8.2	Fire situation	220
8.3	Exploitation stage	221
8.4	Real case example	222
8.4.1	Case study	222
8.4.2	Section properties	222
8.4.3	Design in the construction stage	222
8.4.4	Design in the fire situation	228
8.4.5	Design in the exploitation stage	230
8.4.6	Summary	235

8.1 Construction stage

In the construction stage, the U-shaped steel beam withstands the construction loads alone without additional temporary propping systems.

1. The assembly between the two cold-formed side plates and the hot rolled bottom plate can be done with self-drilling screws (S-MD 25 GZ were used for the experimental tests). They have to be designed with the shear flow at ULS in the construction stage.
2. The U-shaped cross-section is made of cold-formed thin plates. In order to take into account the possible effects of local and distortional buckling, the calculation of the section properties must follow the recommendation of § 5.5 in EN 1993-1-3 (2007). An effective cross-section based on the effective widths must be calculated following the recommendations of EN 1993-1-5 (2007).
3. The bending moment resistance of the U-shaped steel beam is the elastic moment resistance ($M_{el,Rd}$) of the effective section previously determined.
4. The global stability of the beam has to be carefully checked, in fact, the beam is subjected to lateral torsional buckling. The verifications for LTB followed the recommendations of § 6.3.2.1 and § 6.3.2.2 in EN 1993-1-1 (2005). The buckling curve for LTB recommended to use is the curve “b”, as recommended by EN 1993-1-3 (2007) for cold-formed members, leading to the imperfection factor ($\alpha_{LT} = 0.34$). This assumption was verified by the test conducted at the Laboratory of the University of Luxembourg and confirmed by analytical and numerical investigations in the thesis.
5. The stabilisation against LTB by perpendicular profiled steel sheeting is possible if the steel decks are correctly nailed with fasteners as recommended by ECCS-TC7 (1995). That means each rib of the steel decks must be nailed to the top flanges of the U-shaped beam. All four sides of the steel decks constituting a shear panel should be fastened. The adjacent sheets should be also fastened together by seam fasteners. The fasteners should carry shear forces produced by the shear diaphragm; examples of suitable fasteners are self-drilling screws.
6. The deflection should also be controlled carefully. Once the concrete hardened, the deflection would be fixed.
7. Steel battens should link the two top flanges of the U-shaped section in order to prevent the beam from too much opening while the concrete is still not hardened. The battens can be nailed with the same self-drilling screws used for the assembly of the U-shaped beam. The battens should be used every meter.

8.2 Fire situation

1. To limit the heating of the steel rebars during the fire situation, it is advised to place them with a cover of 45 mm from the edges of the downstand beam.
2. The design of the bending resistance in the fire situation ($M_{Rd,fi}$) should follow the tabulated data method as proposed in EN 1992-1-2 (2005). The results are conservative and can be improved by combined thermal and mechanical numerical analysis.

8.3 Exploitation stage

In the exploitation stage, the U-shaped steel beam is connected to the reinforced concrete part by a shear connection.

1. According to Goble (1968), in order to prevent the pull-out failure of the shear studs, the bottom plate thickness of the U-shaped section, where the studs are welded, must be superior to 0.4 times the diameters of the welded headed studs ((Goble, 1968), (AISC 360-16, 2016), (EN 1994-1-1, 2005)).
2. The shear connection in the tension zone due to the bending is efficient. After satisfying the requirements in the construction stage (for the steel part) and in the fire situation (for the concrete part), the composite section is often sufficiently resistant with full shear connection. A partial shear connection can be adopted, the plastic bending resistance can be then evaluated through the method proposed in § 7.3.4. In this method, the area of the U-shaped steel yielded is determined with the shear capacity of the composite connection.
3. The calculation of the shear resistance of the composite section is not taking into account the contribution of the steel webs of the U-shaped section. In fact, due to the shear failure obtained during the composite flexural test (see § 6.7.1) and the investigations carried out on the specimen after the test (see § 6.8), it seems that the shear resistance of the composite beam is strongly dependent on the shear resistance of the reinforced concrete part. Thus, in a conservative approach, the contribution of the steel beam to the shear resistance of the composite section is neglected. Therefore, the design of the composite beam shear resistance is carried out according to § 6.2 in EN 1992-1-1 (2005) considering only the reinforced concrete part.
4. The investigations carried out on the beam specimen after failure also underlined that the concrete under the concrete cone above the headed shear stud might be not sufficiently armed. In fact the concrete was severely crushed around the headed shear stud. It is proposed to add stirrups at each location of shear stud in addition to the stirrups already used for the shear resistance of the composite beam, except if the stirrups for the shear resistance of the beam is also located at the position of the shear studs. In order to ensure a proper load transfer between the compression induced by the shear stud into the composite beam, a strut-and-tie model is proposed as described in Figure 8.1 according to the method explained by Schlaich, Schafer, and Jennewein (1987).

In fact, as related by Nellinger (2015), Lungershausen (1988) proposed a model describing the load-bearing behaviour of the headed shear studs embedded in concrete solid slab. Resulting from the initial longitudinal shear force (V_l) applied to the concrete, the force is applied on the weld collar of the studs with an angle β . Then with increasing load, the force located at the lower stud shank induced plastic bending and shear deformation of the stud causing a vertical tension force in the stud shank. Finally, these tension forces are equilibrated by compression forces in the concrete cone below the head of the stud. In Figure 8.1, only the initial shear force (V_l), the resulting inclined force (with an angle β) and the concrete cone are represented.

For the developed solution, it is recommended to equilibrate these compression forces by placing shear stirrups in the concrete cones, as described in Figure 8.1, in order to limit the concrete crushing in this region and ensure a proper loads transfer.

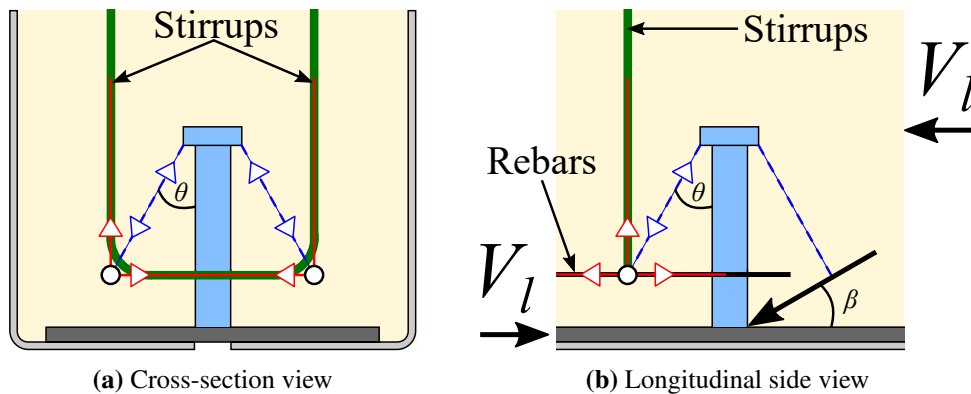


Figure 8.1 – Additional stirrups for a proper load transfer by strut-and-tie model

8.4 Real case example

8.4.1 Case study

The building is a shopping centre (category D according to EN 1991-1-1 (2003)), the beam is supporting a composite floor with a thickness of $h_{\text{slab}} = 150$ mm, the span is $L = 8$ m and the beam spacing is $e = 2$ m.

The composite slab is made with steel decks (Cofraplus60) perpendicular to the beam studied, with the following dimensions:

- The height of the concrete on top of the steel decks: $h_c = 92$ mm
- The height of the steel decks ribs: $h_p = 58$ mm
- The space between the steel decks ribs: $e_0 = 207$ mm
- The minimum width of the steel decks ribs: $b_1 = 62$ mm
- The maximum width of the steel decks ribs: $b_2 = 101$ mm
- The average width of the steel decks ribs: $b_0 = \frac{b_1+b_2}{2} = 81.5$ mm
- The nominal thickness of the steel decks ribs: $t_d = 0.75$ mm
- The weight of the steel decks: $\Gamma_d = 8.53$ daN/m²

8.4.2 Section properties

The U-shaped steel-concrete composite cross-section studied is shown in Figure 8.2.

The dimensions of the U-shaped steel-concrete composite beam are presented in Table 8.1. The mechanical properties of the U-shaped steel beam studied are presented in Table 8.2.

8.4.3 Design in the construction stage

a. Loadings

In the construction stage, the U-shaped steel beam withstands the construction loads alone without additional temporary propping system. The construction loads are:

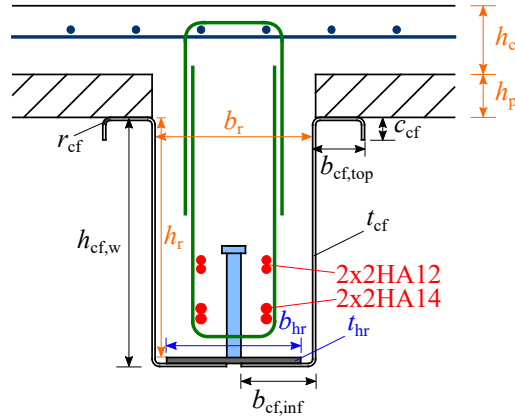


Figure 8.2 – U-shaped steel-concrete composite cross-section studied

Table 8.1 – Dimensions of the U-shaped steel-concrete composite beam

Designation	Symbol	Values
Hot rolled central plate (1)		
- Thickness	t_{hr}	8 mm
- Width	b_{hr}	180 mm
- Steel grade	S355	
- Characteristic strength	$f_{hr,yk}$	275 MPa
Cold-formed side plates (2, 3)		
- Thickness	t_{cf}	4 mm
- Top flanges width	$b_{cf,top}$	70 mm
- Webs height	$h_{cf,w}$	335 mm
- Bottom flanges width	$b_{cf,inf}$	100 mm
- Edge stiffeners height	c_{cf}	30 mm
- Bending radius	r_{cf}	8 mm
- Steel grade	S235	
- Characteristic strength	$f_{cf,yk}$	235 MPa
Steel battens (5)		
- Thickness	t_{bat}	4 mm
- Width	b_{bat}	30 mm
- Length	l_{bat}	320 mm
Reinforced concrete downstand beam (6)		
- Height	h_r	323 mm
- Width	b_r	200 mm
- Concrete class	C30/37	
- Characteristic strength	f_{ck}	30 MPa

- The permanent load of the self-weight of the reinforced concrete not hardened:

$$g_c = \rho_c \left[eh_c + (e - b_r) \frac{b_0}{e_0} h_p + (h_r + h_p) b_r \right] = 7.42 \text{ kN/m}$$

- The permanent load of the self-weight of steel beam :

$$g_a = \rho_a A_a = 0.43 \text{ kN/m}$$

Table 8.2 – Mechanical properties of the U-shaped steel **gross** section

Definition	Symbol	Value	Units
Total area of the section	A	55.4	cm ²
Vertical position of the gravity centre (G) in yOz	z_G	123.7	mm
Second moment of area /GY (major axis)	I_{gy}	8888.4	cm ⁴
Second moment of area /GZ (minor axis)	I_{gz}	5406.3	cm ⁴
Young's modulus	E	210 000	MPa
Shear modulus	G	80 769	MPa
Torsion constant	I_t	10.771	cm ⁴
Warping constant	I_ω	507 179	cm ⁶
Vertical position of the shear centre (S) in yGz	z_S	-247.95	mm
Wagner's coefficient	β_z	30.227	-

- The permanent load of the self-weight of steel decks :

$$g_d = e\Gamma_d = 0.17 \text{ kN/m}$$

- The construction load for “Personnel and hand tools” according to EN 1991-1-6 (2005):

$$q_{ca,k} = 1.0 \text{ kN/m}$$

First, the U-shaped steel beam is installed on supports without any restraints, its stability is verified when the personnel is fixing the steel decks on the section. Thus the loads considered for this preliminary phase are the self-weight of the beam, self-weight of the steel decks and the construction load for “Personnel and hand tools” according to EN 1991-1-6 (2005). These loads are combined according to EN 1990 (2003) in an Ultimate Limit State of design in construction (ULS_{c1}).

When the steel decks are **fixed in each rib** to the two top flanges of the U-shaped steel beam, the beam is stabilised as proved in § 5.9. The rebars are then placed inside the section and the concreting is realised. The loads are combined according to EN 1990 (2003) in an ULS_{c2} of design.

The combinations of actions in the construction stage are calculated according to EN 1990 (2003) as followed :

- For the first Ultimate Limit State (ULS_{c1}):

$$q_{ULS,c1} = 1.35(g_a + g_d) + 1.5q_{ca,k} = 2.31 \text{ kN/m}$$

- For Serviceability Limit State (SLS_{c2}):

$$q_{SLS,c2} = g_c + g_a + g_d + q_{ca,k} = 9.02 \text{ kN/m}$$

- For the second Ultimate Limit State (ULS_{c2}):

$$q_{ULS,c2} = 1.35(g_c + g_a + g_d) + 1.5q_{ca,k} = 12.33 \text{ kN/m}$$

b. Beam assembly

The maximum shear force in the construction stage is obtained by:

$$V_{Ed,ULS,c2} = \frac{q_{ULS,c2} \times l}{2} = 49.3 \text{ kN} \quad (8.1)$$

The maximum shear flow at the location of the assembly is then calculated by:

$$\Phi = \frac{V_{Ed,ULS,c2} \times S_{y,plate}}{I_{gy}} = 98.0 \text{ kN/m} \quad (8.2)$$

Where $S_{y,plate}$ is the first moment of area of the bottom central plate simply calculated by:

$$S_{y,plate} = t_{hr} b_{hr} \times (z_g - t_{cf} - t_{hr}/2) = 178.1 \text{ cm}^3 \quad (8.3)$$

In the cross-section, 4 rows of screws are used. Along a meter, the shear forces in the assembly per rows is then $V_{Ed,row} = 24.5 \text{ kN}$.

The screws used are S-MD 25 GZ, for the thickness assembled, the resistance per screw is : $V_{Rd,screw} = V_{Rk,screw}/1.33 = 5.7 \text{ kN}$.

Consequently, in a row, 5 screws are needed along 1 meter, the spacing between them is then $s_{p,screw} = 200 \text{ mm}$.

The number of screws were calculated with the maximum shear flow. It is possible to reduce the number of screws by decomposing linearly the repartition (like every meter) and repeat the calculation with a reduced shear flow. This is not done in this example, so the assembly of the U-shaped section between cold-formed side plates and hot rolled bottom plate, will need 160 screws divided in 4 rows spaced by 200 mm between each line of assembly.

The assembly must also verify the end distances, edge distances and spacings according to EN 1993-1-3 (2007).

The welding can avoid the number of the screw but a particular attention has to be paid on the galvanisation. In fact, the galvanisation has to be done after this assembly and this could be difficult for such thin plates.

c. Cross-section resistance

In order to take into account the possible effects of local and distortional buckling, the cross-section resistance is evaluated according to § 5.5 of EN 1993-1-3 (2007) combined with EN 1993-1-5 (2007). An effective cross-section is determined with the method already presented in the thesis in § 5.2. Only the main results are presented in this section. The geometrical properties of the cold-formed plates used in this example are presented in Table 8.3.

Table 8.3 – Geometrical properties of the cold-formed plates

Definition	Symbol	Dimensions [mm]
Width of the top flanges	b	70
Notional width of the top flanges	b_p	61.3
Width of the edge stiffeners	c	30
Notional width of the edge stiffeners	$b_{p,c}$	25.7
Height of the webs	h_w	335
Notional height of the webs	$b_{p,hw}$	326.3

- Effect of the local buckling of the edge stiffeners

- $b_{p,c}/b_p = 0.42$
- $k_\sigma = 0.64$
- $\bar{\lambda}_p = 0.283 < 0.748$
- $\rho = 1.0$
- $c_{\text{eff}} = b_{p,c} = 25.7 \text{ mm}$

There is no reduction of the edge stiffeners due to local buckling.

- Effect of the local buckling of the top flanges

- $\psi = 1.0$
- $k_\sigma = 4.0$
- $\bar{\lambda}_p = 0.270 < 0.673$
- $\rho = 1.0$
- $b_{\text{eff}} = b_p = 61.3 \text{ mm}$

There is no reduction of the top flanges due to local buckling.

- Effect of the local buckling of the webs

- $\sigma_1 = 235 \text{ MPa}$
- $\sigma_2 = -137.1 \text{ MPa}$
- $\psi = -0.58$
- $k_\sigma = 14.81$
- $\bar{\lambda}_p = 0.746 > 0.673$
- $\rho = 1.0$
- $b_{\text{eff},w} = b_{p,w} = 326.3 \text{ mm}$

There is no reduction of the webs due to local buckling.

- Effect of distortional buckling

- $A_s = 2.25 \text{ cm}^2$
- $I_s = 1.861 \text{ cm}^4$
- $k_f = 0$ in bending about y-y axis
- $b_1 = 56.48 \text{ mm}$
- $K = 3.024 \text{ MN m}^{-1} \text{ ml}^{-1}$
- $\sigma_{\text{cr},s} = 965 \text{ MPa}$
- $\bar{\lambda}_d = 0.49 < 0.65$
- $\chi_d = 1.0$

The is no reduction due the distortional buckling.

Finally, according to EN 1993-1-3 (2007), there is **no reduction applied to the section**, the section is fully effective, considered as a class 3 cross-section according to EN 1993-1-1 (2005). That means the mechanical properties of the cross-section are equal to the characteristic of the gross section (see Table 8.2). The section is able to develop an elastic distribution of stresses and is allowed to reach the yield strengths with the respective elastic bending resistance. The bending resistance of the section is determined as $M_{el,R,m} = 98.8 \text{ kNm}$ according to Equation 8.4.

$$M_{el,Rd} = f_{yd} \frac{I_{gy}}{h_{cf,w} - z_g} \quad (8.4)$$

d. Member stability without restraint

For the installation of the steel deckings, the stability of the U-shaped steel beam is first verified at ULS_{c1} without any restraint. The elastic critical moment (M_{cr}) is evaluated with equation Equation 5.3 as the precision was confirmed in § 5.3 with the given parameters in Table 8.2 and 8.4: $M_{cr} = 35.6 \text{ kNm}$.

The investigations performed on the stability behaviour of the U-shaped steel beam (including the flexural test at the University of Luxembourg) described in the previous chapters (3 and 4) allow the use of the buckling curve “b” for the lateral torsional buckling moment resistance. Thus the imperfection factor is $\alpha_{LT} = 0.34$.

Table 8.4 – Geometrical properties of the cold-formed plates

Definition	Symbol	Dimensions [mm]	
Factors depending on the loading and end restraint conditions	C_1	1.04	-
	C_2	0.42	-
	C_3	0.562	-
Effective length factors (no restraint at the end)	k_z, k_ω	1.0	-
Coordinate of the point of load application/G	z_a	211.35	mm
Distance between load and shear centre	z_g	459.30	mm

The non-dimensional slenderness for LTB is determined by Equation 8.5.

$$\bar{\lambda}_{LT} = \sqrt{\frac{M_{el,Rd}}{M_{cr}}} = 1.67 \quad (8.5)$$

The reduction factor for LTB is then obtained by Equation 8.6 (EN 1993-1-1, 2005):

$$\chi_{LT} = \frac{1}{\Phi_{LT} + \sqrt{\Phi_{LT}^2 - \bar{\lambda}_{LT}^2}} = 0.29 \quad (8.6)$$

Where:

$$\Phi_{LT} = \frac{1}{2} [1 + \alpha_{LT}(\bar{\lambda}_{LT} - 0.2) + \bar{\lambda}_{LT}^2] = 2.14 \quad (8.7)$$

Finally the lateral torsional buckling moment resistance is obtained by Equation 8.8: . The bending moment at ULS_{c1} is $M_{c1,Ed} = 18.8 \text{ kNm}$

$$M_{b,Rd} = \chi_{LT} M_{el,Rd} = 28.4 \text{ kNm} [0.65] \quad (8.8)$$

The beam is auto-stabilized during its installation on the supports and during the nailing of the steel decks.

e. Member resistance with full restraint

The U-shaped steel beam is fixed to the supports, the perpendicular steel decks are nailed in each rib. The beam is verified for the concreting at ULS_{c2} , the bending moment is $M_{c2,Ed} = 98.6 \text{ kNm}$. The buckling moment resistance ($M_{b,Rd}$) of the beam without any restraint is not sufficient for this phase. It has been demonstrated in § 5.9, that the perpendicular steel decks **nailed in each rib to the top flanges** of the U-shaped beam provide a complete lateral restraint against Lateral Torsional Buckling. Thus the elastic moment resistance of the section is not reduced. If the steel decks are not perpendicular to the beam, the stabilisation has to be done by additional members and the critical bending moment has to be calculated with these restraints.

$$M_{el,Rd} = 98.8 \text{ kNm} [0.99] \quad (8.9)$$

f. Vertical deformation at SLS in the construction stage

The vertical deformation of the beam under the construction loads is controlled to be lower than $L/300$ at SLS. It is advised to use a restrictive criterion on the vertical deformation in the construction stage because when the concrete will harden the deflection would be fixed to this position. Assuming that the loads are mainly distributed, the deflection of the simply supported beam is verified by Equation 8.10.

$$w_c = \frac{5q_{SLS,c2}L^4}{384EI_a} = 25.8 \text{ mm} < L/300 (= 26.7 \text{ mm}) [0.97] \quad (8.10)$$

The U-shaped steel beam is satisfying the main requirements in the construction stage (deformation, stability and bending resistance).

8.4.4 Design in the fire situation

In the fire situation, the resistance of the composite beam is ensured by the reinforced concrete part. As investigated in Chapter 3, the thermal heating of the U-shaped steel beam is too important to consider a participation of the unprotected steel in the bending resistance in this phase.

The actions in a fire design are combined for an accidental situation as recommended by EN 1990 (2003) and presented in Equation 8.11 (adapted for the case study), the loads considered are only the permanent loads ($G_{k,j}$) and the single live load ($Q_{k,1}$). In the case study, the

category of the building is D, thus $\psi_1 = 0.7$. Thus, the linear load for Accidental Limit State (ALS) are determined by Equation 8.12.

$$E_{fi} = \sum_{j \geq 1} G_{k,j} + \psi_1 Q_{k,1} \quad (8.11)$$

$$p_{fi} = g_c + g_a + g_d + 0.7q_{D,k} = 15.02 \text{ kN/m} \quad (8.12)$$

The design bending moment in the fire situation is then calculated to: $M_{fi,Ed} = 120.2 \text{ kNm}$

The investigations made in Chapter 3 validate the use of the design methods proposed in EN 1992-1-2 (2005) for the developed composite solution in the fire situation.

Considering the reinforced T-shaped section (the downstand beam plus the slab), the height of the concrete is $h_{rc} = h_c + h_p + h_r = 473 \text{ mm}$.

The arrangement of the rebars is 4 layers, with 2xHA14 for the two lower layers and 2xHA12 for the two upper layer as described in Figure 8.2.

The area of longitudinal rebars is then : $A_s = 10.68 \text{ cm}^2$. The cover between the bottom edge of the reinforced concrete part and the first layer is $c_{fi} = 45 \text{ mm}$. The vertical spacing between the two groups of layers is $c_v = 40 \text{ mm}$. Therefore the position of the gravity centre of the first group of layer (HA14) from the bottom of the reinforced concrete part is $z_{g,s,G1} = 59 \text{ mm}$ and the position of the gravity centre of the second group of layer (HA12) from the bottom is $z_{g,s,G2} = 125 \text{ mm}$. Finally, the gravity centre of the longitudinal rebars from the bottom is $z_{g,s} = 87 \text{ mm}$.

In order to use the tabulated data method proposed by EN 1992-1-2 (2005), a combination of the minimum dimension of a and b_{min} must be respected, there were already presented in the thesis in Table 3.3. In this example, for R90, the combination $a = 45 \text{ mm}$ and $b_{min} = 200 \text{ mm}$ is chosen. The width of the reinforced concrete downstand beam is $b_r = 200 \text{ mm} \geq b_{min}$. The cover between the edges of the reinforced concrete part and the rebars is $c_{fi} = 45 \text{ mm} \geq a$.

The maximum resistance in tension of the heated longitudinal rebars, in the fire situation, $F_{s,fi}$ is then obtained by :

$$F_{s,fi} = \frac{k_{y,\theta} A_s f_{yk}}{\gamma_{s,fi}} = 320.4 \text{ kN} \quad (8.13)$$

Where $k_{y,\theta} = 0.6$ assumes that the rebars are heated to the critical temperature $\theta = 500^\circ\text{C}$.

In order to determine the height of the concrete in compression (x_{fi}), the equilibrium between tension and compression is made:

$$F_c = F_{s,fi} \quad (8.14)$$

Assuming that the stress distribution in the concrete is rectangular instead of parabolic, the resultant design value of the compressive normal force in the concrete flange is:

$$F_c = 0.8 b_{eff} x_{fi} f_{cd,i} \quad (8.15)$$

The effective width of the concrete slab is calculated by Equation 3.9, $b_{\text{eff,fi}} = 2.0\text{ m}$. The fire design concrete strength is $f_{\text{cd,i}} = f_{\text{ck,i}}/1.0 = 30\text{ MPa}$, (see § 3.3 for the partial safety factors in the fire situation). Then the height of compression in the slab in the fire situation is obtained : $x_{\text{fi}} = 6.7\text{ mm}$

Finally the lever arm, in the fire situation, between the concrete compressive resultant and the steel rebars tension resultant is :

$$z_{\text{fi}} = h_{\text{rc}} - z_{\text{g,s}} - x_{\text{fi}}/2 = 382.7\text{ mm} \quad (8.16)$$

The resistance moment of the reinforced concrete section can be obtained by :

$$M_{\text{Rd,fi}} = F_{\text{s,fi}} \times z_{\text{fi}} = 122.6\text{ kNm} [0.98] \quad (8.17)$$

The reinforced concrete part of the U-shaped composite beam studied is resisting during an ISO fire of 90 minutes. The beam studied is R90 without any additional protection.

8.4.5 Design in the exploitation stage

In this stage, the concrete is hardened, the beam has a composite behaviour thanks to the shear connection provided by headed stud welded on the bottom plate. The efficiency of the composite connection in tension zone due to the simple bending was demonstrated through experimental, analytical and numerical investigations (see Chapters 6 and 7).

a. Loadings

In the exploitation stage, the U-shaped steel-concrete composite beam withstands the following loads:

- The permanent load of the self-weight of the reinforced concrete:

$$g_c = \rho_c \left[eh_c + (e - b_r) \frac{b_0}{e_0} h_p + (h_r + h_p) b_r \right] = 7.42\text{ kN/m}$$

- The permanent load of the self-weight of steel beam :

$$g_a = \rho_a A_a = 0.43\text{ kN/m}$$

- The permanent load of the self-weight of steel decks :

$$g_d = e\Gamma_d = 0.17\text{ kN/m}$$

- An additional permanent load to take into account non-structural permanent element (like flooring, movable partitions): $g_2 = 2.4\text{ kN/m}$

- The live load depending on the building category (here D): $q_{\text{D,k}} = 10.0\text{ kN/m}$

The combination of actions in the exploitation stage are calculated according to EN 1990 (2003) as followed : For the first Ultimate Limit State (ULS_{c1}):

$$q_{\text{ULS,exp}} = 1.35 \times (g_c + g_a + g_d + g_2) + 1.5 \times q_{\text{D,k}} = 29.07\text{ kN/m}$$

b. Internal forces

- The design value of the applied internal bending moment is $M_{Ed,exp} = 232.5 \text{ kN m}$ at $x = L/2 = 4 \text{ m}$
- The design value of the applied internal shear force is: $V_{Ed,exp} = 116.3 \text{ kN}$ at $x = 0 \text{ m}$ and $x = L = 8 \text{ m}$.

c. Plastic bending moment resistance

The method of design proposed in § 7.3.4 is followed in this example:

- Evaluation of the maximum shear force of the connection

The headed stud connectors, used in the example, have the following parameters:

N_{sc} : number of connectors used on the shear length ($N_{sc} = 8$)

s_{sc} : longitudinal spacing of the connectors ($s_{sc} = 500 \text{ mm}$)

h_{sc} : overall nominal height of the stud ($h_{sc} = 150 \text{ mm}$)

d_{sc} : diameter of the shank of the stud ($d_{sc} = 19 \text{ mm}$)

$f_{u,sc}$: ultimate tensile strength of the stud ($f_{u,sc} = 500 \text{ MPa}$)

The design shear resistance of the headed stud used are determined by:

$$P_{Rd} = \min \left(\frac{0.8 f_{u,sc} \pi d_{sc}^2 / 4}{\gamma_v}; \frac{0.29 \alpha d_{sc}^2 \sqrt{f_{ck} E_{cm}}}{\gamma_v} \right) = 83.1 \text{ kN} \quad (8.18)$$

Where:

$\gamma_v = 1.25$ the partial safety factor

$\alpha = 1$ for $h_{sc}/d_{sc} > 4$

$E_{cm} = 22000 [(f_{ck} + 8) / 10]^{0.3} = 32837 \text{ MPa}$

The design value of the normal force in the structural steel bottom central plate is :

$$N_{a,hr} = t_{hr} b_{hr} f_{y,hr} = 396 \text{ kN} \quad (8.19)$$

The maximum shear capacity of the composite connection is calculated on the shear span as follow:

$$V_{l,max} = N_{sc} P_{Rd} = 665 \text{ kN} > N_{a,hr} \quad (8.20)$$

The shear connection capacity ($V_{l,max}$) must be greater than the design value of the normal force in the structural steel bottom central plate ($N_{a,hr}$).

- Evaluation of the available remaining force in the cold-formed side plates

The connection is able to transfer a remaining shear force to the cold-formed side plates of:

$$V_{l,cf} = V_{l,max} - N_{a,hr} = 269 \text{ kN} \quad (8.21)$$

- Evaluation of the yield parts of the cold-formed side plates

It is then possible to estimate the area of the cold-formed side plates yielded:

$$A_{cf,pl} = \frac{V_{l,cf}}{f_{y,cf,m}} = 11.4 \text{ cm}^2 \quad (8.22)$$

Without taking into account the bending radius for simplification purpose, the height of the last fibre yielded of the cold-formed side plates is determined as:

$$h_{cf,pl} = \frac{A_{cf,pl} - 2t_{cf} b_{cf,inf}}{2t_{cf}} = 43.1 \text{ mm} \quad (8.23)$$

- Evaluation of the bending resistance considering a part of the cold-formed side plates yielded

The equilibrium between the stress resultants is established in order to determine the maximum compression height of the composite slab:

$$N_a = N_c \quad (8.24)$$

Where:

$$N_a = A_s f_{sk} / 1.15 + A_{cf,pl} f_{yk,cf} / 1.0 + A_{hr,pl} f_{yk,hr} / 1.0$$

$$N_c = 0.85 h_{comp} b_{eff} f_{ck} / 1.5$$

Finally, the compression height of the composite slab is obtained by :

$$h_{comp} = \frac{A_{hr,pl} f_{yk,hr} / 1.0 + A_s f_{sk} / 1.15 + A_{cf,pl} f_{yk,cf} / 1.0}{0.85 b_{eff} f_{ck} / 1.5} = 33 \text{ mm} \quad (8.25)$$

It can be noted that $h_{comp} < h_c$, so the position of the Plastic Neutral Axis (PNA) is in the concrete of the slab above the steel decking.

Table 8.5 – Calculation of the bending resistance with cold-formed side plates partially plastic

Part	z_i/v' [mm]	N_{ten} [kN]	N_{com} [kN]	$M_{pl,R,i}$ [kNm]
Concrete in compression	468.5		1129.4	529.1
Second bundle of bars (2x2HA12)	137.0	-196.7		-26.9
First bundle of bars (2x2HA14)	71.0	-267.7		-19.0
Cold-formed webs	21.5	-81.0		-1.7
Hot rolled steel in tension	8.0	-396.0		-3.2
Cold-formed bottom flanges	2.0	-188.0		-0.4
Sum		-1129.4	1129.4	477.9

Finally, the plastic bending resistance is evaluated to $M_{pl,Rd} = 477.9 \text{ kNm}$ [0.49].

d. Determination of the shear resistance and the arrangement of stirrups

Based on the observed shear failure obtained in the experimental test carried out at the Laboratory of the University of Luxembourg (see § 6.8), it is recommended to not consider the shear resistance of the steel beam in the calculation. The shear resistance of the composite beam is then provided only by the reinforced concrete part. The calculation procedure then follows the recommendations of EN 1992-1-1 (2005).

- Design shear resistance

The shear reinforcements are vertical, thus $\alpha = 90^\circ$. The angle between the concrete compression strut and the beam axis is chosen to have $\cot(\theta) = 2.5$, thus $\theta = 21.8$ deg. According to § 6.2.3(3) of EN 1992-1-1 (2005), the shear resistance (V_{Rd}) is obtained by :

$$V_{Rd,s} = \frac{A_{sw}}{s} 0.9d f_{ywd} \cot(\theta) \quad (8.26)$$

- Reduced design value of the applied internal shear force

It is possible to reduce the value of the applied internal shear force for the calculation of the shear resistance. For a simply supported beam, the design value of the shear force (V_{Ed}) can be limited to the shear force at the distance d for the support:

$$V_{Ed,red} = q_{ULS,exp} \frac{(L - 2 \times d)}{2} = 105.1 \text{ kN} \quad (8.27)$$

- Determination of the cross-sectional area of the shear reinforcement

The design shear resistance ($V_{Rd,s}$) must be greater than the reduced design value of the applied internal shear force ($V_{Ed,red}$). Therefore, the ratio of cross-sectional area of the shear reinforcement on the spacing is determined by :

$$\frac{A_{sw,min}}{s} \geq \frac{V_{Ed,red}}{0.9d f_{ywd} \cot(\theta)} = 2.78 \text{ cm}^2/\text{ml} \quad (8.28)$$

In this example, the shear reinforcement is a rebar stirrup of diameter 8 mm (HA8). An horizontal spacing near the supports of $s_1 = 250$ mm is retained.

Therefore: $\frac{A_{sw}}{s} = 4.02 \text{ cm}^2/\text{ml} > \frac{A_{sw,min}}{s}$.

- Optimisation of the stirrups spacing with the spacing of the headed studs

For a simply supported beam, far from the supports, when the applied internal shear force decreased sufficiently, the spacing of the stirrups is increased to the spacing of the headed stud.

The user is free to optimise the spacing of the stirrups at his convenience but it is recommended to place a stirrup close to a shear stud (inside the concrete cone below the head of the stud, see Figure 8.1).

For example, the applied internal shear force at $x = L/4 = 2\text{ m}$ is $V_{Ed} = 58.1\text{ kN}$. Following the previous calculation, with the same cross-sectional area of shear reinforcement, the minimum spacing obtained from Equation 8.28 is $s_{1,max} = 653\text{ mm}$. In this example, the longitudinal spacing of shear stud is $s_{sc} = 500\text{ mm}$ ($< s_{1,max}$). Therefore, after $x = L/4 = 2\text{ m}$, the spacing of the stirrups is equal to the spacing of the shear studs.

The shear reinforcement of the studied composite beam finally looks like as represented in Figure 8.3.

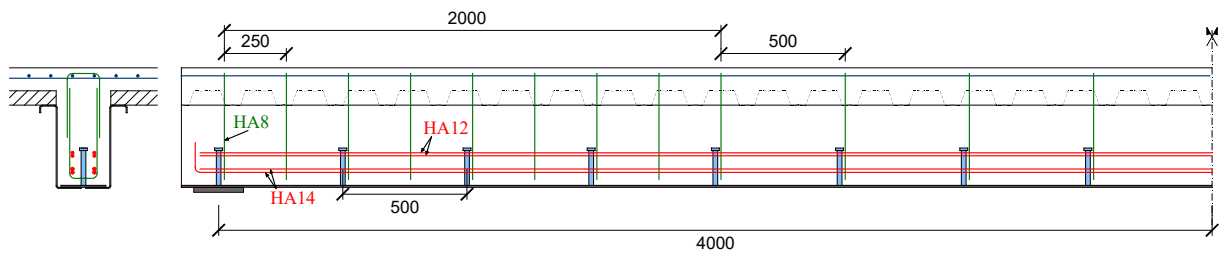


Figure 8.3 – Representation of the reinforcement bars in the composite beam studied

e. Vertical deformation at SLS

- Loading considered

The self-weights of the composite parts were already supported by the steel beam in the construction stage. The vertical deformation of the steel beam was already considered with this effects in § 8.4.3. Therefore these loads are not taken into account for the verification of the vertical deformation of the beam at SLS. In this example, only the additional permanent load for non-structural permanent element (like flooring, movable partitions) and live load depending on the building category (here D) are considered. The flexural stiffness of the composite beam varies depending on the duration of the applied actions, to consider this effect EN 1994-1-1 (2005) separates the effect in short term loading and long term loading, as followed :

- $q_{SLS,exp,LT} = g_2 = 2.4\text{ kN/m}$
- $q_{SLS,exp,ST} = q_{D,k} = 10.0\text{ kN/m}$

- Evaluation of the flexural stiffness

The flexural stiffness of the composite beam is evaluated as related in § 7.2.

According to EN 1992-1-1 (2005), the secant modulus of elasticity of concrete is determined as :

$$E_{cm} = 22000 [(f_{c,k} + 8)/10]^{0.3} = 32837\text{ MPa} \quad (8.29)$$

The composite cross-section is transformed into a single material because of the modular ratio for short-term actions (n_0):

$$n_0 = \frac{E_a}{E_{cm}} = 6.4 \quad (8.30)$$

In buildings, the modular ratio for long term actions can be approximated by $n_{eq} = 3 \times n_0$ according to EN 1994-1-1 (2005).

For short and long term actions, the Elastic Neutral Axis (ENA) located in the down-stand part is determined according to Equation 7.2. Then the equivalent second moment of area of the composite beam is determined as well as the flexural stiffness for short and long term actions (see Table 8.6).

- Deflection for short and long term actions

Assuming that the loads are mainly distributed, the deflection of the simply supported beam is obtained by:

$$w_{exp} = \frac{5q_{SLS,exp}L^4}{384EI_{comp}} \quad (8.31)$$

For short and long term actions, the results are presented in Table 8.6.

Table 8.6 – Calculation of the deflection in the exploitation stage for short and long term actions

	q [kN/m]	n	z_{ENA} [mm]	EI_{com} [MN m ²]	w [mm]
Short term actions	10	6.4	379.4	138.1	3.9
Long term actions	2.4	19.2	310.9	104.4	1.2
				w_{exp} [mm] =	5.1

- Total deflection of the composite beam

The vertical deformation of the composite beam in the exploitation stage is controlled to be lower than $L/250$ at SLS. Finally, the total deflection of the composite beam is the sum of the deflection previously calculated :

$$w_{tot} = w_c + w_{exp} = 30.9 \text{ mm} < L/250 (= 32 \text{ mm}) [0.97] \quad (8.32)$$

The U-shaped steel-concrete composite beam is satisfying the main requirements in the exploitation stage (deformation, bending and shear resistance).

8.4.6 Summary

The example studied was dedicated to the structural floor a shopping centre (category D according to EN 1991-1-1 (2003)). The span was $L = 8$ m and the beam spacing was $e = 2$ m. The requirement for the fire situation was R90.

The example chosen perfectly meets all the requirements imposed by the case study, as summarized in Table 8.7.

The beam also fulfils the objectives of the thesis, which means a composite beam without any propping system in the construction stage and is fire resistant without any additional protection.

Table 8.7 – Summary of the verifications made in the example

Construction stage		Ratio
- Verification of the steel plates assembly of the U-shaped cross-section (see § 8.4.3.b)		
- No reduction of the cross-section resistance (see § 8.4.3.c)		
- Steel beam stability before the nailing of the perpendicular steel decking (see § 8.4.3.d)	$M_{b,Rd}$	0.65
- Steel beam bending resistance after the nailing of the perpendicular steel decking (see § 8.4.3.e)	$M_{el,Rd}$	0.99
- Vertical deformation of the steel beam (L/300) (see § 8.4.3.f)	w_c	0.97
Fire situation		
- Composite beam resistance for R90 (see § 8.4.4)	$M_{Rd,fi}$	0.98
Exploitation stage		
- Composite beam bending resistance (see § 8.4.5.c)	$M_{b,Rd}$	0.49
- Determination of the shear resistance and the arrangement of stirrups (see § 8.4.5.d)		
- Vertical deformation of the composite beam (L/250) (see § 8.4.5.e)	w_{exp}	0.97

Chapter 9

Conclusions and outlooks

9.1 Conclusions

The objective of this research was to develop a steel-concrete beam solution fire resistant and stable in the construction stage. From a state of the art on previous international research, a solution of U-shaped steel-concrete composite beams was chosen. The beam developed is innovative by the arrangement of the steel plate, its resistance in the construction stage and the location of the composite connection.

In the fire situation, the resistance of the unprotected external U-shaped steel part is negligible and the resistance is provided by the concrete part. Analytical studies according to the standard were performed to determine the required height coupled with a reinforcement area to ensure sufficient bending resistance. The required height of the downstand beam clearly influences the global height of the composite beam. Thermomechanical numerical analysis were conducted and underlined that an optimisation of the beam height was possible, particularly if the rebars are placed sufficiently far from the edges of the beam (≈ 45 mm).

The mechanical behaviour of the steel beam in the construction stage, in particular its stability against LTB was investigated. In order to characterize the LTB of the steel beam without lateral restraint, a four-point bending test was carried out at the Laboratory of the University of Luxembourg on a full-scale specimen. The loading introduction system was developed especially for the test to unrestrain the movements of LTB. For this type of section, which is a mix of cold-formed steel plates and hot rolled, the lateral-torsional buckling curve was not clearly defined by the standard between "b" and "d". The test results showed the LTB instability of the section at mid-span as expected. The test also indicated that the beam behaved monolithic with no slip or damage in the assembly of the three steel plates together to form the U-shaped beam. The results were compared to analytical calculation and the use of the curve "b" appeared to be conservative. Numerical simulations were validated on the tests and were extended through a parametric study to see the effect of varied geometrical parameter on the LTB behaviour. Most of the configurations were lying above the curve "b" and confirm that the use of this curve for the U-shaped section developed with cold-formed side plates is safe sided.

From the literature review, it was found that the headed studs must be welded on a sufficiently thick plate to prevent pull-out failure modes. It was decided to develop a solution divided in three parts with two thin cold-formed side plates and a thicker bottom plate. The

shear connection ensured by headed studs are welded on this thicker bottom plate. Thus the connectors are embedded in concrete subject to tension forces in simple bending causing micro-cracks. From literature review, no particular shear resistance reduction were found for beams subjected to similar situation like in negative bending. Although it is similar for the aspect of concrete cracking in the connection location, the arrangement of the beam is completely different and the mechanical behaviour of the composite beam has to investigate. Therefore, in this research, a full-scale flexural test was also performed on the steel-concrete composite beam. This time, the test is a more classical four-point bending test. The test results showed a great ductility and high bending capacity. However, the failure mode, at very high deformations, was a shear failure of the stirrups after the complete yielding of the bottom plate and the rebars. The cold-formed side plates were partially yield. It was concluded that with this configuration, the steel webs of the beam were not participating in the shear resistance as expected. The test results are then compared to analytical and numerical simulations. Different simplified analytical methods of design are compared to the test results and a simplified method assuming the partial yielding of the side plates is proposed. A 3D finite element model was created and validated with the test with assumptions of the shear strength capacity of the connection. Comparisons of results underlined that the connection, located in tension zone, had a shear strength fully efficient, equivalent to a classic connector located in a solid slab in compression zone. A slight reduction of the shear capacity could be visible at high load level and therefore it is proposed to place stirrups rebars at each shear stud location to prevent eventual crushing of the concrete.

Finally, based on the research investigations performed in the frame of the thesis, for each critical phase (construction, fire and exploitation), design recommendations and constructional guideline are given for a use of this solution in buildings. A detailed real case example is proposed and fulfills all the objectives of the thesis.

9.2 Outlooks

The structural fire resistance seems to be more and more required for many buildings. Although this beam solution can work only for structural floor, it seems that this kind of solution can increase the market share of steel and steel-concrete composite construction in the future. In fact, thanks to the composite behaviour, the structure can take most benefits of the different material (here steel and concrete).

In order to optimize the cost, this innovative solution can be combined with the FRACOF method proposed by Vassart and Zhao (2011). Thus, the structural floor can be composed of the developed solution for the peripheral beams and the inward beams can be unprotected steel profile connected to the slab.

The thermomechanical simulations in the fire situation also showed that the height or the area of reinforcement can be reduced if the rebars are correctly placed inside the downstand beam. Actually, this is not taken into account in the design guideline because it is specific for each configuration. However, it could be interesting for a later use to build database and abacus with these simulations for different configuration giving the optimisation in the fire situation without using complicated numerical simulations.

The assembly of the three plates is actually done by self-drilling screws to avoid welding on the pre-galvanized cold-formed steel plates. This assembly takes time and increases the cost. In fact, the side plates are folded in the asymmetric Z-shaped section after galvanization.

The welding is then not recommended. An optimization of the solution could be a change in the fabrication process to allow a welding of the three steel plates together and thus avoid the use of self-drilling screws.

Finally, further full-scale experimental tests are needed on the steel and on the composite beam to increase the knowledge on the mechanical behaviour of U-shaped steel concrete composite beam. A fire test could also be interesting for the validations of the analytical model and the thermomechanical simulations performed.

9.3 Scientific publications

In the frame of the thesis project, four publications have been prepared:

- Maxime Turetta. “Développement d’une poutre mixte acier-béton innovante répondant à une problématique de mise en oeuvre et de résistance au feu” – *Séminaire de l’Ecole Doctorale EMMA (Poster)*, 2018
- Maxime Turetta, Abdelouahab Khelil, Christoph Odenbreit. “Numerical study on the load bearing capacity of a steel U section beam used as a formwork in the construction stage” – *International Conference on Engineering Research and Practice for Steel Construction (ICSC2018) (Proceeding)*, 2018
- Maxime Turetta, Christoph Odenbreit, Abdelouahab Khelil, Pierre-Olivier Martin. “Investigations on the lateral-torsional buckling of an innovative U-shaped steel beam” – *Journal of Constructional Steel Research (Article under review)*, 2019
- Maxime Turetta, Christoph Odenbreit, Abdelouahab Khelil and Pierre-Olivier Martin. “Investigation on the flexural behavior of an innovative U-shaped steel-concrete composite beam” – *Steel and Composite Structures (Article under review)*, 2019

Appendix A

Tensile tests reports

A.1 Coupon B1

Table A.1 – Parameters

Client	COMINO PhD
Tester	Ralph Reiter
Standard	EN ISO 6892-1(2016)
Material	Steel S235
Specimen	Specimen B1
Machine	DUPS-H WN:807289 Displacement transducer WN:807289 Force sensor ID:0 WN:807290 400 kN

Table A.2 – Results

	S0	E	ReH	Rm	Fm	Agt	Ag	RB	FB	At	A
Nr	mm^2	kN/mm^2	N/mm^2	N/mm^2	kN	%	%	N/mm^2	kN	%	%
1	80.08	11	325	410	32.8	20.7	17.1	-	-	-	-

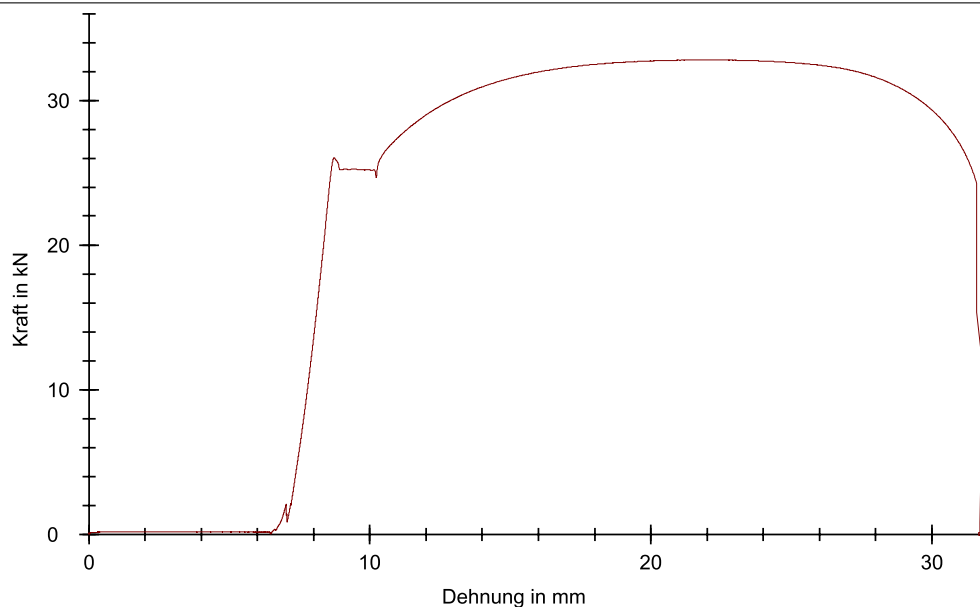


Figure A.1 – Tensile test curve of B1

A.2 Coupon B2

Table A.3 – Parameters

Client	COMINO PhD
Tester	Ralph Reiter
Standard	EN ISO 6892-1(2016)
Material	Steel S235
Specimen	Specimen B2
Machine	DUPS-H WN:807289 Displacement transducer WN:807289 Force sensor ID:0 WN:807290 400 kN

Table A.4 – Results

	S0	E	ReH	Rm	Fm	Agt	Ag	RB	FB	At	A
Nr	mm^2	kN/mm^2	N/mm^2	N/mm^2	kN	%	%	N/mm^2	kN	%	%
2	80.08	10	338	410	32.8	20.7	16.7	-	-	-	-

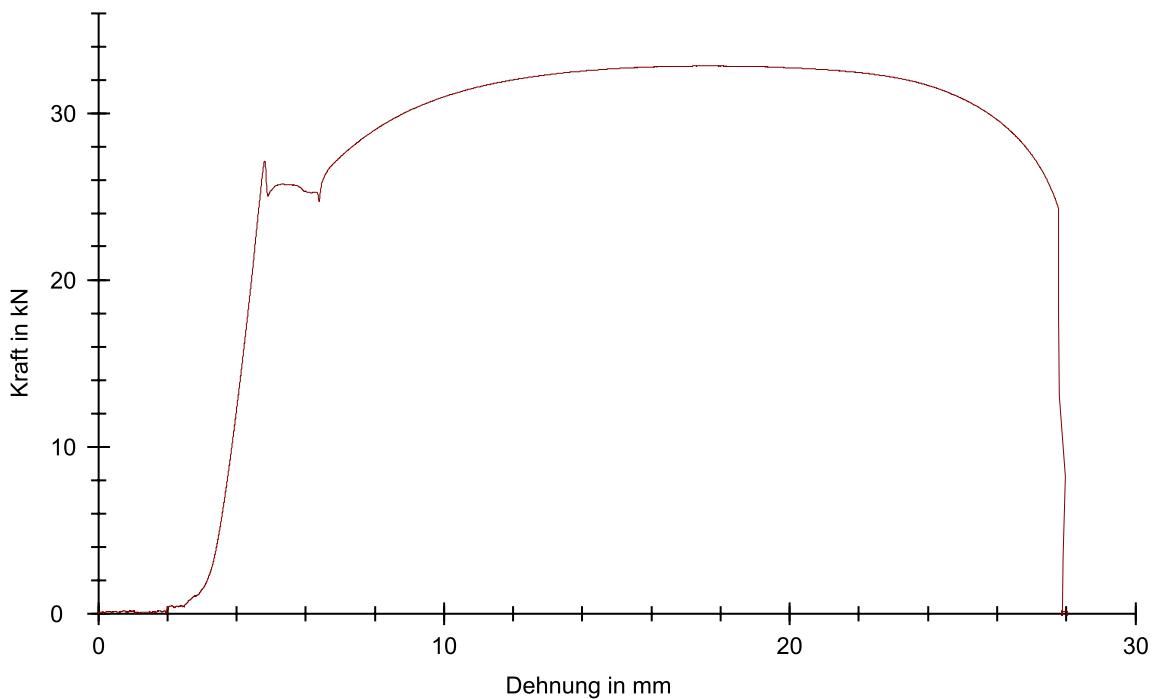


Figure A.2 – Tensile test curve of B2

A.3 Coupon B3

Table A.5 – Parameters

Client	COMINO PhD
Tester	Ralph Reiter
Standard	EN ISO 6892-1(2016)
Material	Steel S235
Specimen	Specimen B3
Machine	DUPS-H WN:807289 Displacement transducer WN:807289 Force sensor ID:0 WN:807290 400 kN

Table A.6 – Results

	S0	E	ReH	Rm	Fm	Agt	Ag	RB	FB	At	A
Nr	mm^2	kN/mm^2	N/mm^2	N/mm^2	kN	%	%	N/mm^2	kN	%	%
3	80.08	12	331	409	32.7	21.5	17.9	-	-	-	-

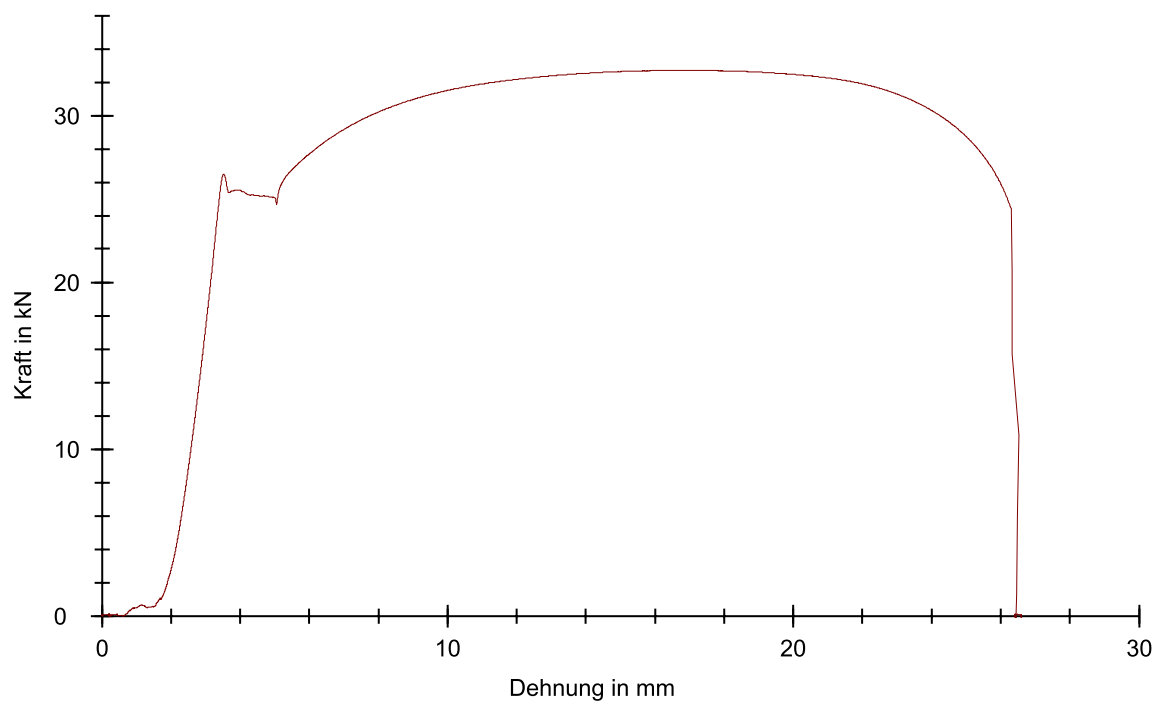


Figure A.3 – Tensile test curve of B3

A.4 Coupon W1

Table A.7 – Parameters

Client	COMINO PhD
Tester	Ralph Reiter
Standard	EN ISO 6892-1(2016)
Material	Steel S235
Specimen	Specimen W1
Machine	DUPS-H WN:807289 Displacement transducer WN:807289 Force sensor ID:0 WN:807290 400 kN

Table A.8 – Results

	S0	E	ReH	Rm	Fm	Agt	Ag	RB	FB	At	A
Nr	mm ²	kN/mm ²	N/mm ²	N/mm ²	kN	%	%	N/mm ²	kN	%	%
1	79.20	10	316	407	32.3	21.6	17.7	-	-	-	-

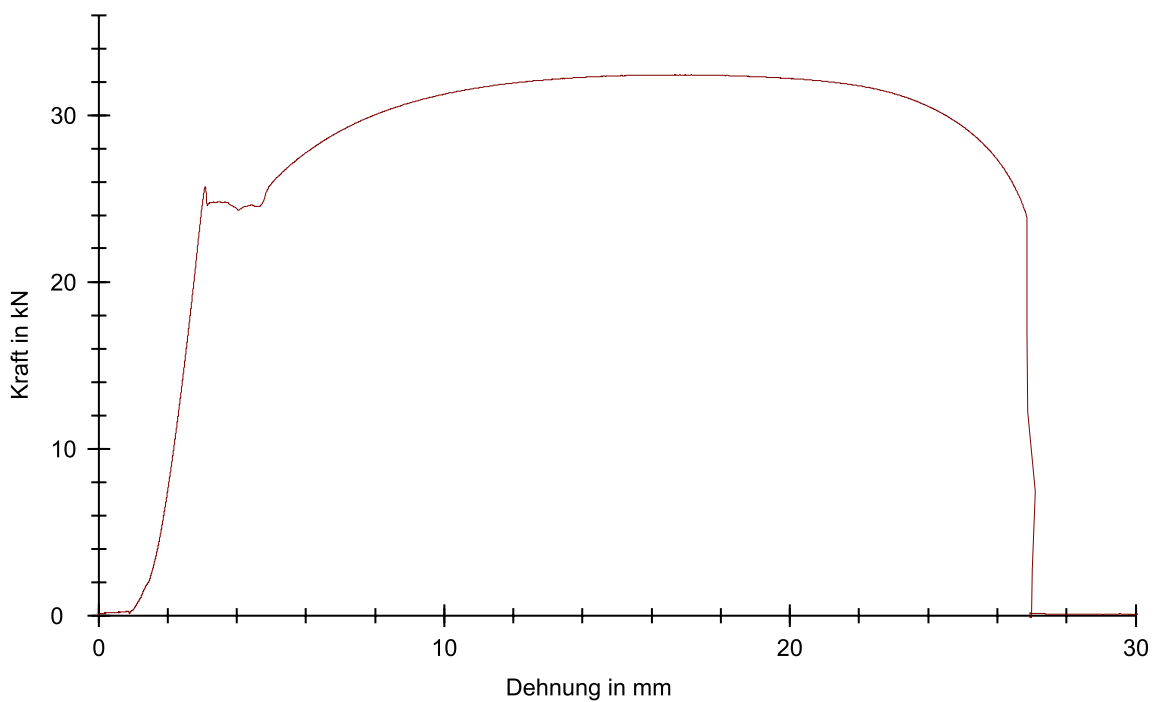


Figure A.4 – Tensile test curve of W1

A.5 Coupon W2

Table A.9 – Parameters

Client	COMINO PhD
Tester	Ralph Reiter
Standard	EN ISO 6892-1(2016)
Material	Steel S235
Specimen	Specimen W2
Machine	DUPS-H WN:807289 Displacement transducer WN:807289 Force sensor ID:0 WN:807290 400 kN

Table A.10 – Results

	S0	E	ReH	Rm	Fm	Agt	Ag	RB	FB	At	A
Nr	mm^2	kN/mm^2	N/mm^2	N/mm^2	kN	%	%	N/mm^2	kN	%	%
2	80.28	11	316	402	32.2	20.9	17.2	-	-	-	-

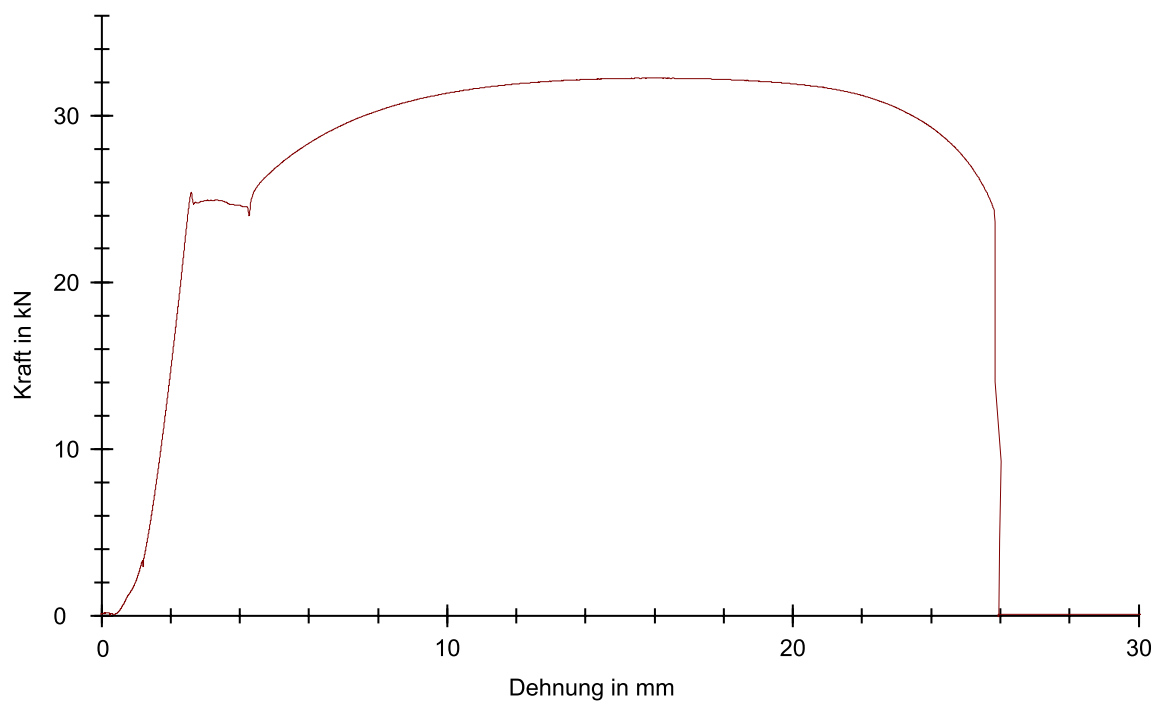


Figure A.5 – Tensile test curve of W2

A.6 Coupon W3

Table A.11 – Parameters

Client	COMINO PhD
Tester	Ralph Reiter
Standard	EN ISO 6892-1(2016)
Material	Steel S235
Specimen	Specimen W3
Machine	DUPS-H WN:807289 Displacement transducer WN:807289 Force sensor ID:0 WN:807290 400 kN

Table A.12 – Results

	S0	E	ReH	Rm	Fm	Agt	Ag	RB	FB	At	A
Nr	mm ²	kN/mm ²	N/mm ²	N/mm ²	kN	%	%	N/mm ²	kN	%	%
3	79.88	11	314	406	32.5	22.0	18.4	-	-	-	-

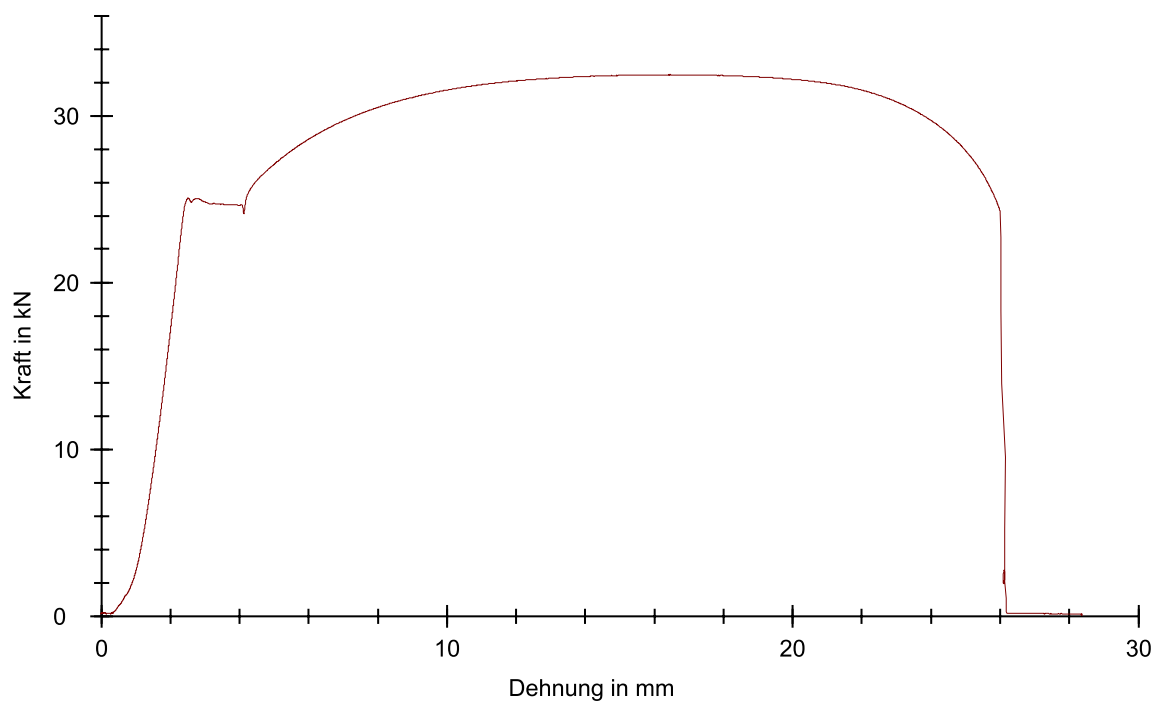


Figure A.6 – Tensile test curve of W3

A.7 Coupon T1

Table A.13 – Parameters

Client	COMINO PhD
Tester	Ralph Reiter
Standard	EN ISO 6892-1(2016)
Material	Steel S235
Specimen	Specimen T1
Machine	DUPS-H WN:807289 Displacement transducer WN:807289 Force sensor ID:0 WN:807290 400 kN

Table A.14 – Results

	S0	E	ReH	Rm	Fm	Agt	Ag	RB	FB	At	A
Nr	mm^2	kN/mm^2	N/mm^2	N/mm^2	kN	%	%	N/mm^2	kN	%	%
1	80.16	11	320	404	32.4	21.8	18.1	-	-	-	-

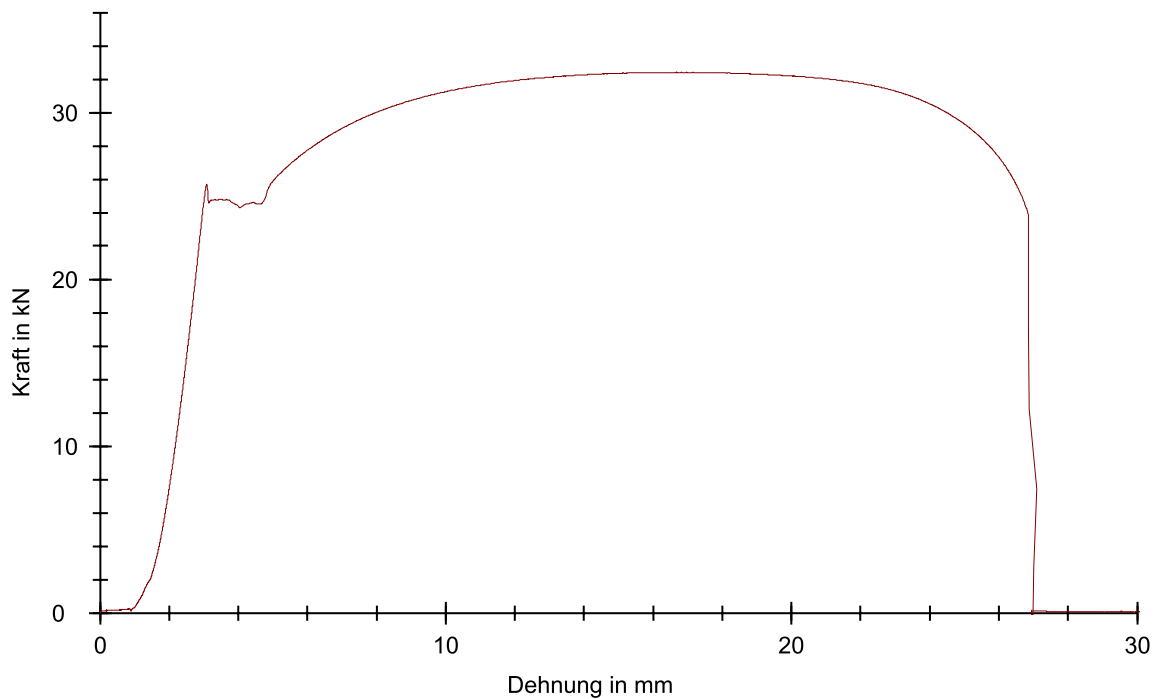


Figure A.7 – Tensile test curve of T1

A.8 Coupon T2

Table A.15 – Parameters

Client	COMINO PhD
Tester	Ralph Reiter
Standard	EN ISO 6892-1(2016)
Material	Steel S235
Specimen	Specimen T2
Machine	DUPS-H WN:807289 Displacement transducer WN:807289 Force sensor ID:0 WN:807290 400 kN

Table A.16 – Results

	S0	E	ReH	Rm	Fm	Agt	Ag	RB	FB	At	A
Nr	mm ²	kN/mm ²	N/mm ²	N/mm ²	kN	%	%	N/mm ²	kN	%	%
2	79.6	11	317	407	32.4	22.1	18.4	-	-	-	-

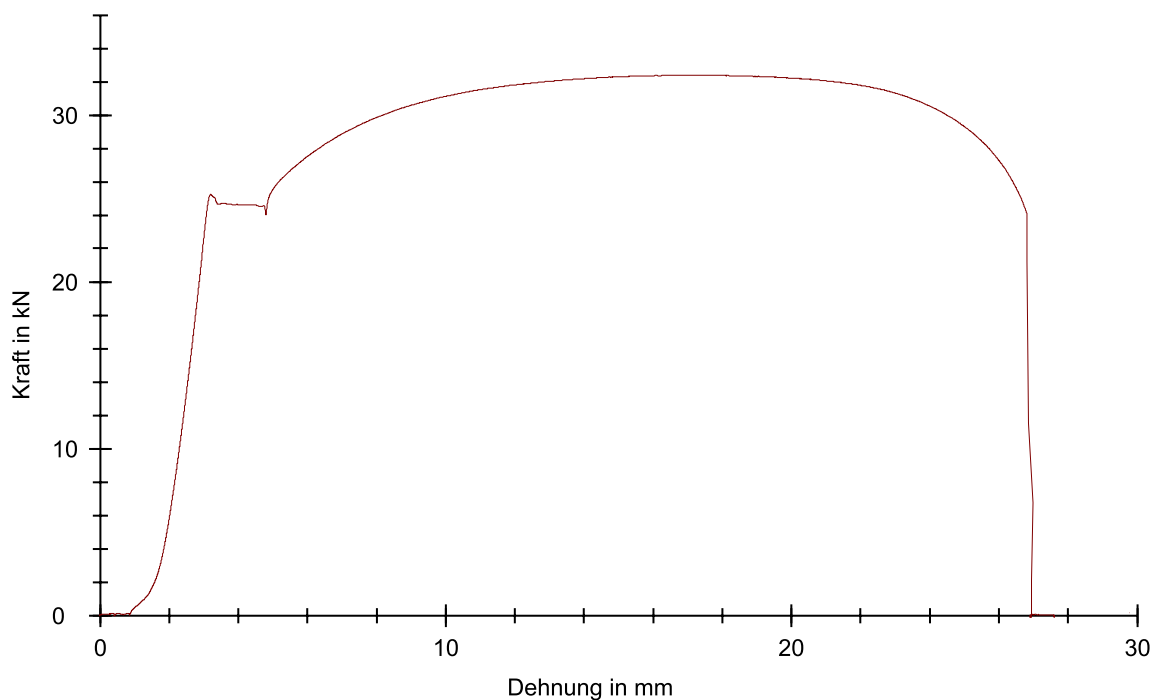


Figure A.8 – Tensile test curve of T2

A.9 Coupon T3

Table A.17 – Parameters

Client	COMINO PhD
Tester	Ralph Reiter
Standard	EN ISO 6892-1(2016)
Material	Steel S235
Specimen	Specimen T3
Machine	DUPS-H WN:807289 Displacement transducer WN:807289 Force sensor ID:0 WN:807290 400 kN

Table A.18 – Results

	S0	E	ReH	Rm	Fm	Agt	Ag	RB	FB	At	A
Nr	mm^2	kN/mm^2	N/mm^2	N/mm^2	kN	%	%	N/mm^2	kN	%	%
3	79.76	11	323	405	32.3	20.9	17.4	-	-	-	-

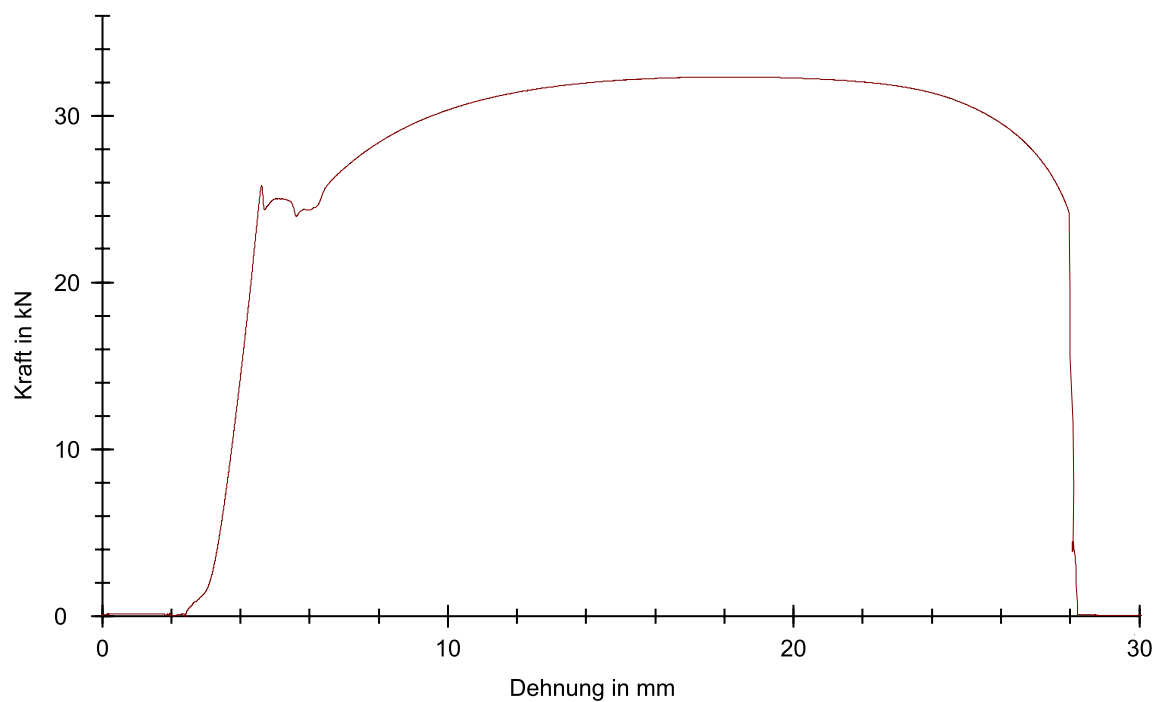


Figure A.9 – Tensile test curve of T3

A.10 Coupon C1

Table A.19 – Parameters

Client	COMINO PhD
Tester	Ralph Reiter
Standard	EN ISO 6892-1(2016)
Material	Steel S355
Specimen	Specimen C1
Machine	DUPS-H WN:807289 Displacement transducer WN:807289 Force sensor ID:0 WN:807290 400 kN

Table A.20 – Results

	S0	E	ReH	Rm	Fm	Agt	Ag	RB	FB	At	A
Nr	mm ²	kN/mm ²	N/mm ²	N/mm ²	kN	%	%	N/mm ²	kN	%	%
1	159	10	413	560	89.0	18.4	13.1	-	-	-	-

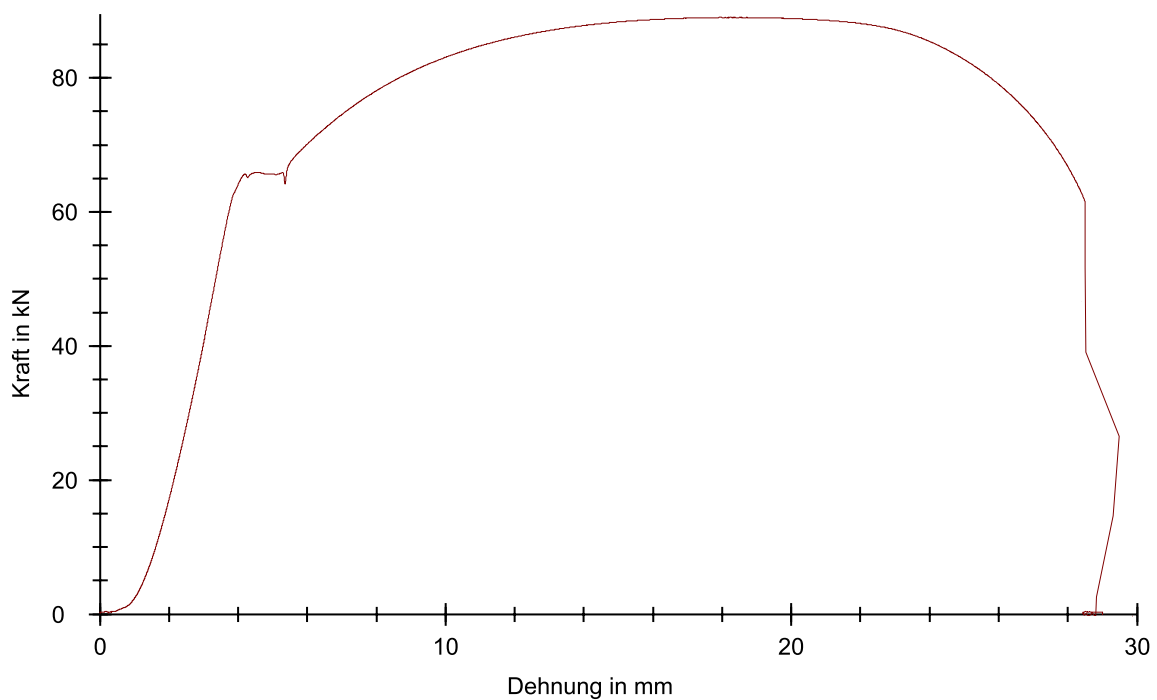


Figure A.10 – Tensile test curve of C1

A.11 Coupon C2

Table A.21 – Parameters

Client	COMINO PhD
Tester	Ralph Reiter
Standard	EN ISO 6892-1(2016)
Material	Steel S355
Specimen	Specimen C2
Machine	DUPS-H WN:807289 Displacement transducer WN:807289 Force sensor ID:0 WN:807290 400 kN

Table A.22 – Results

	S0	E	ReH	Rm	Fm	Agt	Ag	RB	FB	At	A
Nr	mm ²	kN/mm ²	N/mm ²	N/mm ²	kN	%	%	N/mm ²	kN	%	%
2	160	11	410	558	89.2	18.4	13.2	-	-	-	-

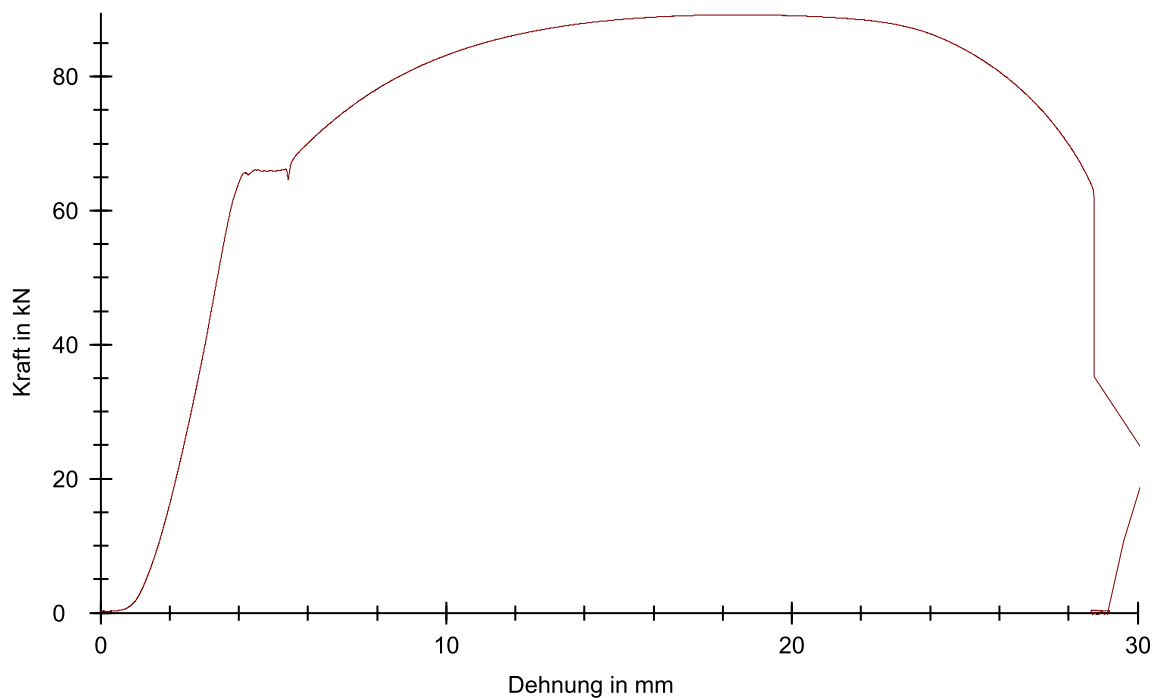


Figure A.11 – Tensile test curve of C2

A.12 Coupon C3

Table A.23 – Parameters

Client	COMINO PhD
Tester	Ralph Reiter
Standard	EN ISO 6892-1(2016)
Material	Steel S355
Specimen	Specimen C3
Machine	DUPS-H WN:807289 Displacement transducer WN:807289 Force sensor ID:0 WN:807290 400 kN

Table A.24 – Results

	S0	E	ReH	Rm	Fm	Agt	Ag	RB	FB	At	A
Nr	mm ²	kN/mm ²	N/mm ²	N/mm ²	kN	%	%	N/mm ²	kN	%	%
3	160	11	420	558	89.2	18.1	13.0	-	-	-	-

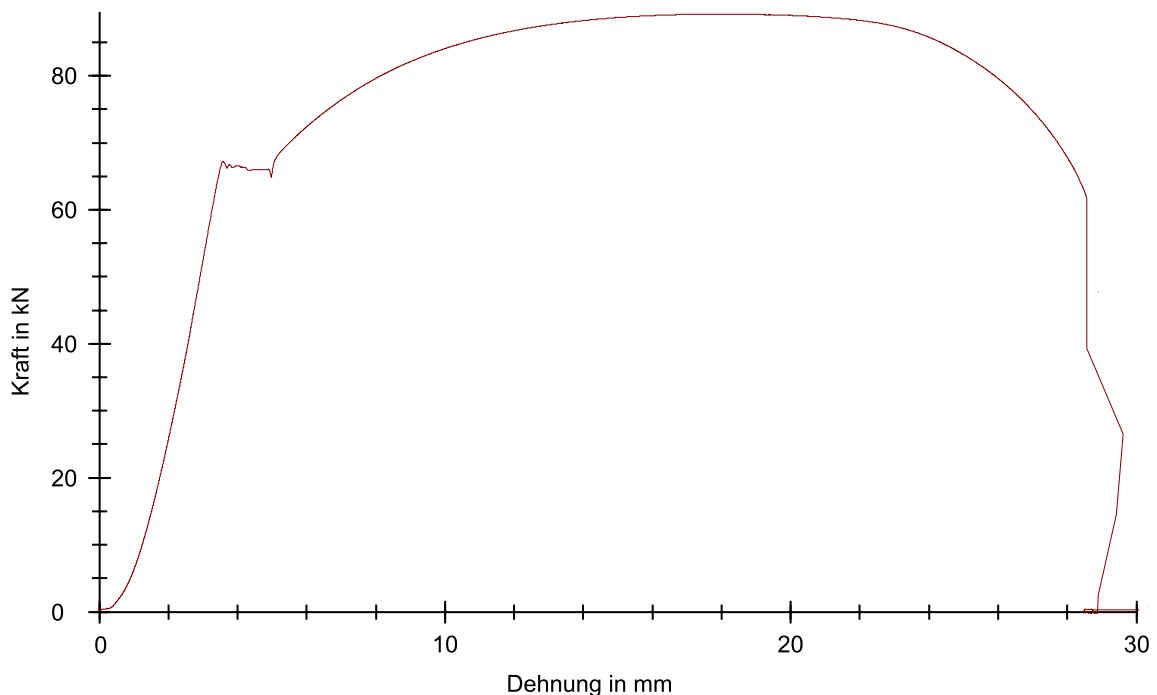


Figure A.12 – Tensile test curve of C3

A.13 Coupon C4

Table A.25 – Parameters

Client	COMINO PhD
Tester	Ralph Reiter
Standard	EN ISO 6892-1(2016)
Material	Steel S355
Specimen	Specimen C4
Machine	DUPS-H WN:807289 Displacement transducer WN:807289 Force sensor ID:0 WN:807290 400 kN

Table A.26 – Results

	S0	E	ReH	Rm	Fm	Agt	Ag	RB	FB	At	A
Nr	mm^2	kN/mm^2	N/mm^2	N/mm^2	kN	%	%	N/mm^2	kN	%	%
4	159.9	11	419	557	89.1	18.2	13.1	-	-	-	-

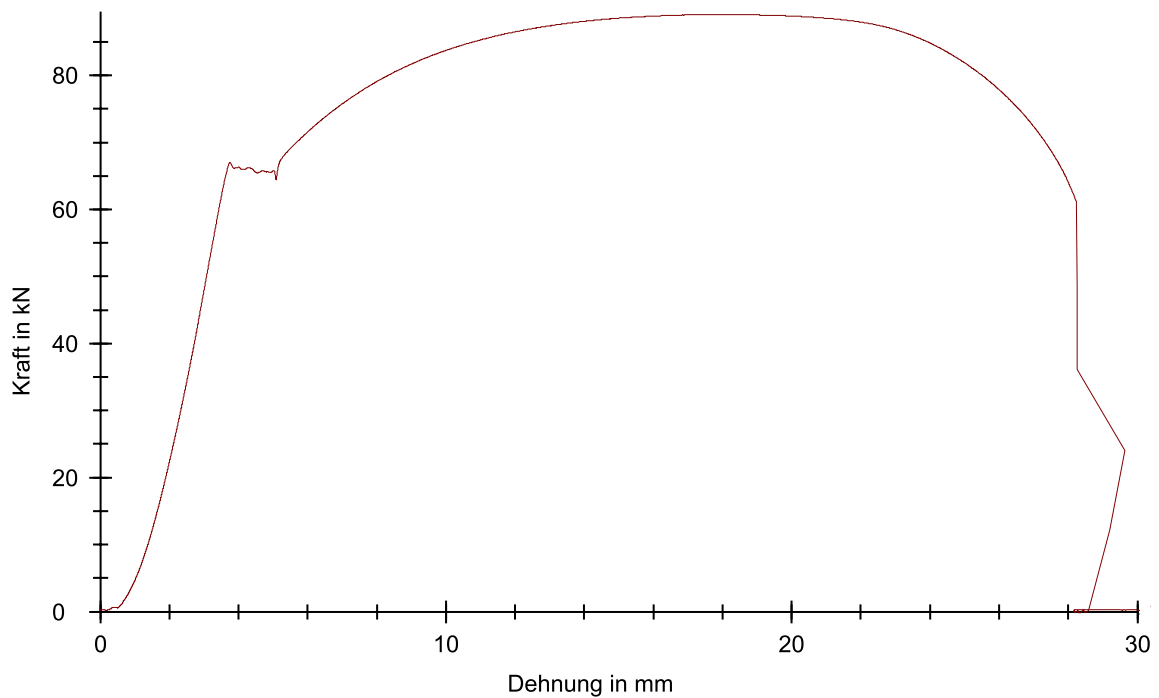


Figure A.13 – Tensile test curve of C4

A.14 Coupon C5

Table A.27 – Parameters

Client	COMINO PhD
Tester	Ralph Reiter
Standard	EN ISO 6892-1(2016)
Material	Steel S355
Specimen	Specimen C5
Machine	DUPS-H WN:807289 Displacement transducer WN:807289 Force sensor ID:0 WN:807290 400 kN

Table A.28 – Results

	S0	E	ReH	Rm	Fm	Agt	Ag	RB	FB	At	A
Nr	mm^2	kN/mm^2	N/mm^2	N/mm^2	kN	%	%	N/mm^2	kN	%	%
5	160.2	10	423	560	89.8	18.3	12.7	-	-	-	-

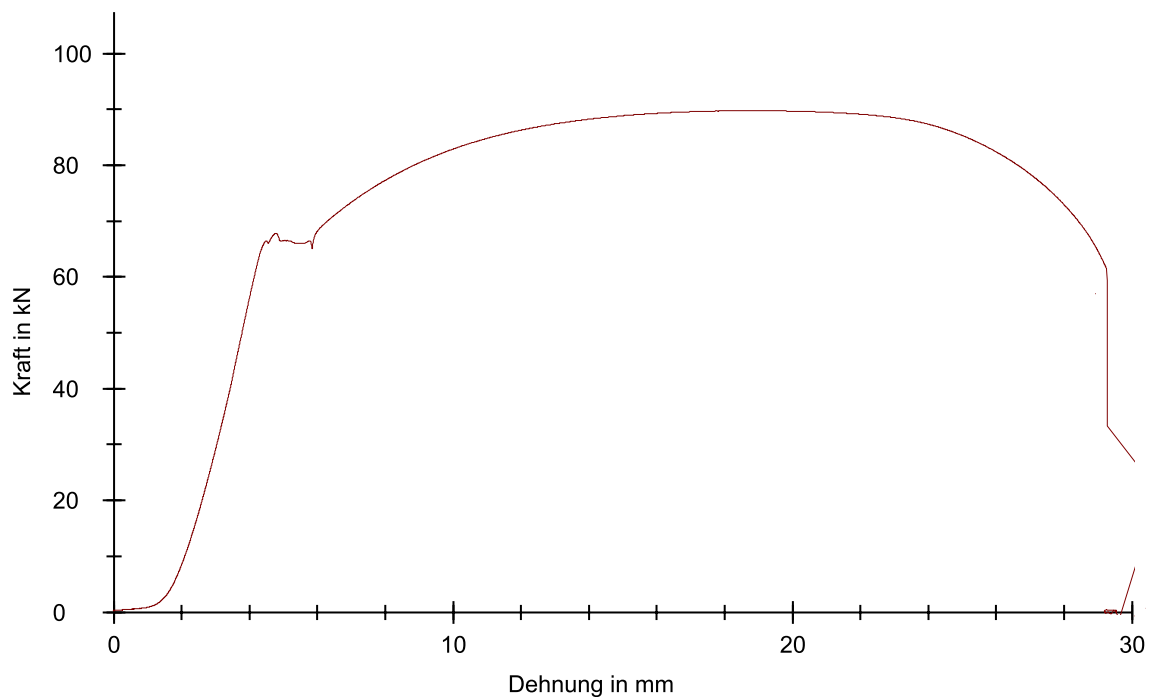


Figure A.14 – Tensile test curve of C5

Appendix B

Compression tests reports

B.1 Test on concrete cylinders

Table B.1 – Test parameters

Test:	Compression test on concrete cylinders
UTM type:	4000kN
Load cell:	4000 kN
Extensometer:	XHead
Clamping device:	no
Test area:	Lower test area
Sample dimensions:	D = 149.82 mm; h = 300.1 mm; m = 12540 g
Length data:	Le = 50 mm; Lc = 100 mm
Test rates:	V0 = 50 mm/min; V1 = 13.5 kN/s
Rate switch points:	F0 = 10 kN
End of test criterions:	Force = 4000 kN; dF = 1 kN

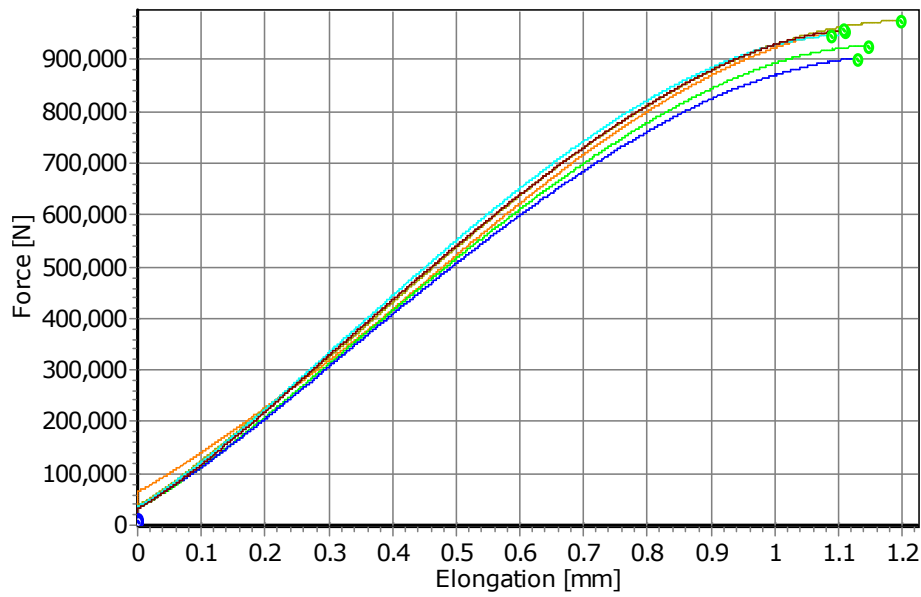


Figure B.1 – Compression test curve on concrete cylinders

Table B.2 – Test results

n	Date	Time	FH [N]	RH [N/mm ²]	Rho [g/cm ³]	D [mm]	h [mm]	m [g]
1	26.11.18	01:33	955880.00	54.09	2.36	150.00	300.00	12490.00
2	26.11.18	01:39	928236.00	52.53	2.36	150.00	300.00	12490.00
3	26.11.18	01:45	902504.00	50.94	2.35	150.20	299.30	12480.00
4	26.11.18	01:49	977252.00	55.08	2.36	150.30	299.40	12535.00
5	26.11.18	01:53	947224.00	53.53	2.36	150.10	299.20	12500.00
6	26.11.18	01:58	957740.00	54.33	2.37	149.82	300.10	12540.00

Table B.3 – Statistics n=6

	FH [N]	RH [N/mm ²]	Rho [g/cm ³]	D [mm]	h [mm]	m [g]
Average	944806.00	53.42	2.36	150.07	299.67	12505.83
Standard deviation	26124.84	1.48	0.01	0.17	0.41	25.38
Median	951552.00	53.81	2.36	150.05	299.70	12495.00
Minimum	902504.00	50.94	2.35	149.82	299.20	12480.00
Maximum	977252.00	55.08	2.37	150.30	300.10	12540.00

B.2 Test on concrete cubes

Table B.4 – Test parameters

Test:	Compression test on concrete cubes
UTM type:	4000kN
Load cell:	4000 kN
Extensometer:	XHead
Clamping device:	no
Test area:	Lower test area
Sample dimensions:	a = 150.56 mm; b = 150 mm; h = 150 mm; m = 8020 g
Length data:	Le = 50 mm; Lc = 100 mm
Test rates:	V0 = 50 mm/min; V1 = 13.5 kN/s
Rate switch points:	F0 = 10 kN
End of test criteria:	Force = 4000 kN; dF = 1 kN

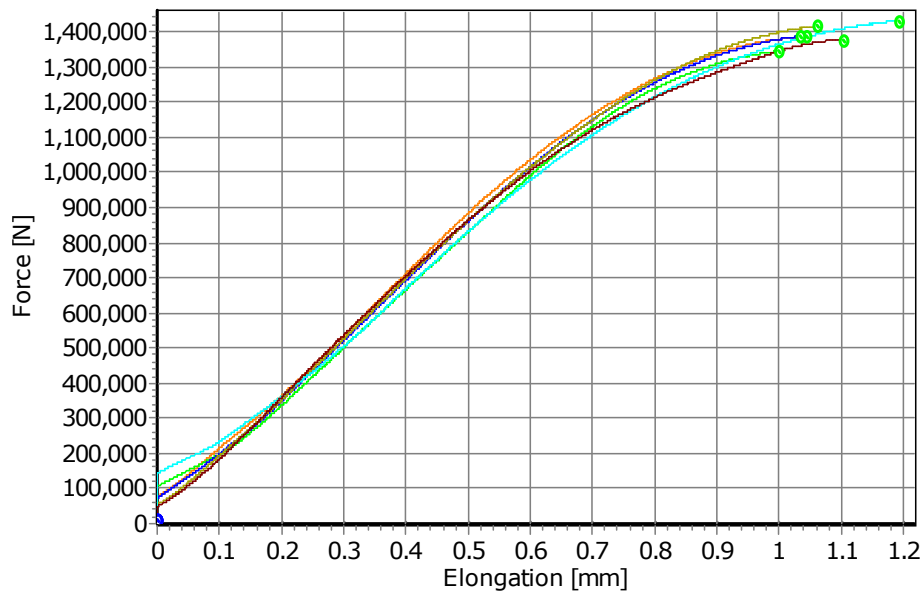


Figure B.2 – Compression test curve on concrete cylinders

Table B.5 – Test results

n	Date	Time	FH [N]	RH [N/mm ²]	Rho [g/cm ³]	a [mm]	h [mm]	m [g]
1	26.11.18	02:14	1390392.00	61.80	2.36	150.00	150.00	7980.00
2	26.11.18	02:20	1345992.00	59.82	2.35	150.00	150.00	7920.00
3	26.11.18	02:24	1388940.00	61.73	2.36	150.00	150.00	7960.00
4	26.11.18	02:27	1417652.00	63.01	2.37	150.00	150.00	7990.00
5	26.11.18	02:32	1432720.00	63.68	2.38	150.00	150.00	8020.00
6	26.11.18	02:38	1379472.00	61.08	2.37	150.56	150.00	8020.00

Table B.6 – Statistics n=6

	FH [N]	RH [N/mm ²]	Rho [g/cm ³]	a [mm]	h [mm]	m [g]
Average	1392528.00	61.85	2.36	150.09	150.00	7981.67
Standard deviation	30331.85	1.37	0.01	0.23	0.00	38.17
Median	1389666.00	61.76	2.37	150.00	150.00	7985.00
Minimum	1345992.00	59.82	2.35	150.00	150.00	7920.00
Maximum	1432720.00	63.68	2.38	150.56	150.00	8020.00

Appendix C

Effective Cross-section calculation of the specimen

The effective cross-section of the U-shaped beam is determined according to EN 1993-1-3 (2007) combined with EN 1993-1-5 (2007). The effects of local and distortional buckling are taken into account to determine the effective cross-section. In order to follow the methods proposed in EN 1993-1-3 (2007), the notional widths of the plates have to be defined as described in Figure C.1 and this leads to the parameters presented in Table C.1.

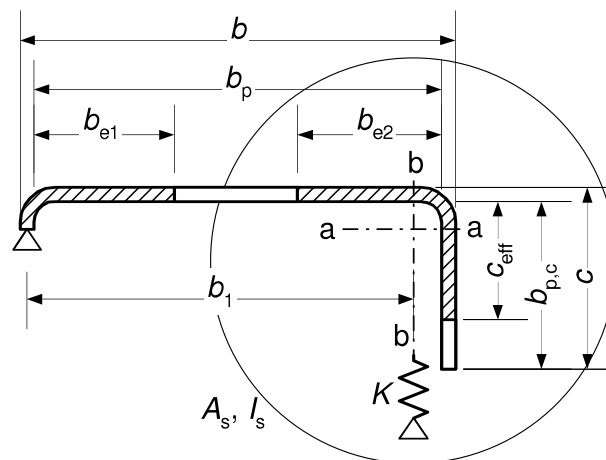


Figure C.1 – Effective cross-section of a plate with an edge stiffener (EN 1993-1-3, 2007)

Table C.1 – Geometrical properties of the cold-formed plates

Definition	Symbol	Dimensions [mm]
Width of the top flanges	b	70
Notional width of the top flanges	b_p	61.3
Width of the edge stiffeners	c	30
Notional width of the edge stiffeners	$b_{p,c}$	25.7
Height of the webs	h_w	270
Notional height of the webs	$b_{p,hw}$	261.3

C.0.1 Effect of the local buckling of the edge stiffeners

According to § 5.5.3.2 EN 1993-1-3 (2007), for a single edged fold stiffener:

$$c_{\text{eff}} = \rho b_{p,c} \quad (\text{C.1})$$

With ρ obtained from EN 1993-1-5 (2007), with a value of the buckling factor given by:

$$k_{\sigma} = 0.5 + 0.83 \sqrt[3]{(b_{p,c}/b_p - 0.35)^2} \quad (\text{C.2})$$

with $0.35 < b_{p,c}/b_p < 0.6$

With the given values: $k_{\sigma} = 0.64$

According to EN 1993-1-5 (2007), the plate slenderness is obtained by:

$$\bar{\lambda}_p = \sqrt{\frac{f_{y,m,s}}{\sigma_{cr}}} = \frac{\bar{b}/t}{28.4\varepsilon\sqrt{k_{\sigma}}} \quad (\text{C.3})$$

According to the tensile test results (see § 2.2): $f_{y,m,s} = 322 \text{ MPa}$

$$\varepsilon = \sqrt{\frac{235}{f_{y,m,s}}} \quad (\text{C.4})$$

With the given values and $\bar{b} = b_{p,c}$:

$$\varepsilon = 0.85$$

$$\bar{\lambda}_p = 0.331 < 0.748$$

$$\rho = 1.0$$

$$c_{\text{eff}} = b_{p,c}$$

There is no reduction of the edge stiffeners due to local buckling.

C.0.2 Effect of the local buckling of the top flanges

According to § 5.5.3.2(4) EN 1993-1-3 (2007), the effective width of the top flanges are calculated according to EN 1993-1-5 (2007) by assuming that the plane element is doubly supported (internal compression elements).

The stress ratio (ψ) is equal to 1.0, $k_{\sigma} = 4$, with the given values and $\bar{b} = b_c$:

$$\bar{\lambda}_p = 0.317 < 0.673$$

$$\rho = 1.0$$

$$b_{\text{eff}} = b_p \text{ and } b_{e1} = b_{e2} = 0.5b_p$$

There is no reduction of the top flanges due to local buckling.

C.0.3 Effect of the local buckling of the webs

According to § 5.5.2 EN 1993-1-3 (2007), the effective width of the webs are calculated according to EN 1993-1-5 (2007) by assuming that the plane element is doubly supported (internal compression elements).

For the webs, it is assumed that the yield strength is reached at the top, thus: $\sigma_1 = f_{y,m,s}$ and at the bottom $\sigma_2 = \frac{-b_{p,hw,t}}{b_{p,hw,c}} \sigma_1 = -175.2 \text{ MPa}$, where $b_{p,hw,t}$ is the width in tension and $b_{p,hw,c}$ is the width in compression of the plate considered.

The stress ratio is: $\psi = -0.54$

The buckling factor is: $k_\sigma = 7.81 - 6.29\psi + 9.78\psi^2 = 14.13$

The plate slenderness of the web is: $\bar{\lambda}_p = 0.720 > 0.673$

$$\rho = 1.0$$

$$b_{p,hw,eff} = b_{p,hw}$$

There is no reduction of the webs due to local buckling.

C.0.4 Effect of distortional buckling

According to § 5.5.3.2(6) EN 1993-1-3 (2007), the effective cross-sectional area of the edge stiffener should be:

$$A_s = t(b_{e2} + c_{eff}) \tag{C.5}$$

With the given values:

$$A_s = 2.25 \text{ cm}^2$$

According to § 5.5.3.1(4) EN 1993-1-3 (2007), the stiffness of the equivalent spring can be determined by:

$$K = K_1 = \frac{Et^3}{4(1-\nu^2)} \frac{1}{b_1^2 h_w + b_1^3 + 0.5b_1 b_2 h_w k_f} \tag{C.6}$$

With:

$$k_f = 0 \text{ in bending about y-y axis}$$

$$b_1 = 56.48 \text{ mm (Distance from the web-to-flange junction to the gravity centre of } A_s, \text{ see Figure C.1)}$$

$$K = 3.589 \text{ MN m}^{-1} \text{ ml}^{-1}$$

According to § 5.5.3.2(7) EN 1993-1-3 (2007), the elastic critical buckling stress for and edge stiffener is:

$$\sigma_{cr,s} = \frac{2\sqrt{KEI_s}}{A_s} \tag{C.7}$$

With $I_s = 1.861 \text{ cm}^4$, the effective second moment of area of the stiffener about the axis “a-a” of its effective cross-section (see Figure C.1).

$$\sigma_{cr,s} = 1052 \text{ MPa}$$

According to 5.5.3.1(7) EN 1993-1-3 (2007), the plate slenderness is obtained by:

$$\bar{\lambda}_d = \sqrt{f_{y,m,s}/\sigma_{cr,s}} \tag{C.8}$$

$$\bar{\lambda}_d = 0.55 < 0.65$$

The reduction factor for the distortional buckling resistance is obtained:

$$\chi_d = 1.0$$

Finally, according to EN 1993-1-3 (2007), there is **no reduction applied to the section**, the section is fully effective, considered as a class 3 cross-section according to EN 1993-1-1 (2005).

Appendix D

Parametric study – Data and results

n^o	Dimensions [mm]				Results				
	L [m]	h_{tot}	t_{cf}	$b_{cf,sup}$	$M_{epI,R}$ [kNm]	M_{cr} [kNm]	$M_{epI,ult}$ [kNm]	λ_{LT}	χ_{LT}
1	4.0	270	4	50	161.989	48.354	47.7	1.830	0.295
2	5.0	270	4	50	160.783	36.214	37.6	2.107	0.234
3	6.0	270	4	50	160.778	28.956	31.3	2.356	0.195
4	7.0	270	4	50	160.895	23.220	26.6	2.632	0.165
5	8.0	270	4	50	161.114	19.408	22.9	2.881	0.142
6	9.0	270	4	50	161.097	16.836	20.1	3.093	0.125
7	10.0	270	4	50	160.802	14.558	18.3	3.323	0.114
8	11.0	270	4	50	161.116	12.945	16.7	3.528	0.104
9	12.0	270	4	50	161.348	12.083	15.6	3.654	0.097
10	13.0	270	4	50	160.770	11.020	14.0	3.820	0.087
11	6.0	200	4	50	107.79	26.431	29.7	2.019	0.275
12	6.0	210	4	50	115.26	27.713	30.2	2.039	0.262
13	6.0	220	4	50	122.27	27.075	29.3	2.125	0.240
14	6.0	230	4	50	129.69	27.845	32.6	2.158	0.252
15	6.0	240	4	50	136.83	29.939	33.4	2.138	0.244
16	6.0	250	4	50	145.49	30.514	33.6	2.184	0.231
17	6.0	260	4	50	152.37	31.705	34.2	2.192	0.225
18	6.0	270	4	50	160.78	28.956	31.3	2.356	0.195
19	6.0	280	4	50	168.21	28.868	31.2	2.414	0.185
20	6.0	290	4	50	176.49	29.754	31.1	2.435	0.176
21	6.0	300	4	50	184.98	33.369	36.4	2.354	0.197
22	6.0	310	4	50	191.72	34.186	37.9	2.368	0.198
23	6.0	320	4	50	198.86	35.491	34.4	2.367	0.173
24	6.0	330	4	50	207.82	36.331	40.1	2.392	0.193

APPENDIX D. PARAMETRIC STUDY – DATA AND RESULTS

n^o	Dimensions [mm]				Results				
	L [m]	h_{tot}	t_{cf}	$b_{cf,sup}$	$M_{epI,R}$ [kNm]	M_{cr} [kNm]	$M_{epI,ult}$ [kNm]	λ_{LT}	χ_{LT}
25	6.0	340	4	50	214.29	38.470	40.9	2.360	0.191
26	6.0	350	4	50	223.06	39.087	42.0	2.389	0.188
27	6.0	360	4	50	229.95	41.574	42.9	2.352	0.186
28	6.0	370	4	50	236.89	37.919	41.5	2.499	0.175
29	6.0	380	4	50	246.69	47.426	44.5	2.281	0.180
30	6.0	390	4	50	253.09	46.128	36.5	2.342	0.144
31	6.0	400	4	50	260.14	40.180	39.3	2.544	0.151
32	6.0	410	4	50	269.17	41.873	33.5	2.535	0.124
33	6.0	420	4	50	276.52	33.852	32.1	2.858	0.116
34	6.0	430	4	50	284.00	36.256	24.5	2.799	0.086
35	6.0	440	4	50	290.67	34.432	25.0	2.905	0.086
36	6.0	450	4	50	298.23	53.712	49.1	2.356	0.164
37	6.0	460	4	50	311.01	44.565	50.0	2.642	0.161
38	6.0	470	4	50	317.82	37.974	40.1	2.893	0.126
39	6.0	480	4	50	324.77	44.321	51.4	2.707	0.158
40	6.0	490	4	50	335.23	42.448	40.7	2.810	0.121
41	6.0	500	4	50	342.96	49.081	47.1	2.643	0.137
42	4.0	200	6	100	204.86	115.46	90.8	1.332	0.443
43	4.0	210	6	100	218.65	124.85	96.4	1.323	0.441
44	4.0	220	6	100	233.07	126.12	100.6	1.359	0.432
45	4.0	230	6	100	248.76	138.12	106.2	1.342	0.427
46	4.0	240	6	100	261.83	145.68	111.3	1.341	0.425
47	4.0	250	6	100	276.42	158.84	116.6	1.319	0.422
48	4.0	260	6	100	291.38	159.13	121.8	1.353	0.418
49	4.0	270	6	100	308.20	164.22	129.0	1.370	0.419
50	4.0	280	6	100	322.68	172.49	134.3	1.368	0.416
51	4.0	290	6	100	336.23	175.77	137.9	1.383	0.410
52	4.0	300	6	100	354.49	192.27	143.1	1.358	0.404
53	4.0	200	4	50	107.42	42.72	38.0	1.586	0.354
54	4.0	210	4	50	114.47	45.09	39.5	1.593	0.345
55	4.0	220	4	50	123.19	45.09	40.9	1.653	0.332
56	4.0	230	4	50	129.99	45.88	42.4	1.683	0.326
57	4.0	240	4	50	136.51	48.55	43.8	1.677	0.321
58	4.0	250	4	50	144.24	50.34	45.2	1.693	0.313
59	4.0	260	4	50	152.39	51.94	46.4	1.713	0.305
60	4.0	270	4	50	161.99	48.35	47.7	1.830	0.295
61	4.0	280	4	50	168.32	47.40	49.1	1.884	0.292
62	4.0	290	4	50	175.62	49.83	49.9	1.877	0.284

APPENDIX D. PARAMETRIC STUDY – DATA AND RESULTS

n^o	Dimensions [mm]				Results				
	L [m]	h_{tot}	t_{cf}	$b_{cf,sup}$	$M_{epl,R}$ [kNm]	M_{cr} [kNm]	$M_{epl,ult}$ [kNm]	λ_{LT}	χ_{LT}
63	4.0	300	4	50	183.44	54.87	51.0	1.828	0.278
64	4.0	200	4	100	133.40	78.20	57.1	1.306	0.428
65	4.0	210	4	100	141.99	78.24	60.5	1.347	0.426
66	4.0	220	4	100	148.60	84.97	62.9	1.322	0.423
67	4.0	230	4	100	159.32	85.50	65.9	1.365	0.414
68	4.0	240	4	100	167.49	93.54	68.8	1.338	0.411
69	4.0	250	4	100	176.86	103.59	72.2	1.307	0.408
70	4.0	260	4	100	185.04	103.40	74.5	1.338	0.403
71	4.0	270	4	100	192.47	98.45	78.1	1.398	0.406
72	4.0	280	4	100	200.68	104.49	80.8	1.386	0.402
73	4.0	290	4	100	211.62	109.95	83.1	1.387	0.393
74	4.0	300	4	100	223.83	112.34	86.3	1.412	0.385
75	4.0	200	5	100	170.51	95.83	73.8	1.334	0.433
76	4.0	210	5	100	181.72	101.61	78.4	1.337	0.432
77	4.0	220	5	100	193.15	107.84	81.7	1.338	0.423
78	4.0	230	5	100	205.67	113.52	86.1	1.346	0.418
79	4.0	240	5	100	215.82	119.90	90.2	1.342	0.418
80	4.0	250	5	100	227.75	130.10	94.6	1.323	0.415
81	4.0	260	5	100	239.04	128.08	98.4	1.366	0.411
82	4.0	270	5	100	252.91	125.76	103.7	1.418	0.410
83	4.0	280	5	100	263.88	137.87	107.7	1.383	0.408
84	4.0	290	5	100	274.64	144.22	110.7	1.380	0.403
85	4.0	300	5	100	289.97	155.48	114.9	1.366	0.396
86	6.0	200	5	50	140.31	32.66	35.4	2.073	0.252
87	6.0	210	5	50	150.74	34.05	38.2	2.104	0.254
88	6.0	220	5	50	160.71	33.85	39.6	2.179	0.247
89	6.0	230	5	50	171.64	35.14	41.6	2.210	0.243
90	6.0	240	5	50	182.80	37.22	44.8	2.216	0.245
91	6.0	250	5	50	192.48	38.82	44.8	2.227	0.233
92	6.0	260	5	50	203.60	40.30	45.5	2.248	0.224
93	6.0	270	5	50	213.86	38.29	42.2	2.363	0.197
94	6.0	280	5	50	224.22	37.89	41.3	2.433	0.184
95	6.0	290	5	50	235.13	39.19	42.2	2.449	0.180
96	6.0	300	5	50	244.83	42.27	44.9	2.407	0.183
97	6.0	310	5	50	255.76	45.29	49.6	2.376	0.194
98	6.0	320	5	50	266.36	46.73	48.7	2.387	0.183
99	6.0	330	5	50	277.67	47.76	53.0	2.411	0.191
100	6.0	340	5	50	287.14	48.20	52.0	2.441	0.181

APPENDIX D. PARAMETRIC STUDY – DATA AND RESULTS

n^o	Dimensions [mm]				Results				
	L [m]	h_{tot}	t_{cf}	$b_{cf,sup}$	$M_{epI,R}$ [kNm]	M_{cr} [kNm]	$M_{epI,ult}$ [kNm]	λ_{LT}	χ_{LT}
101	6.0	350	5	50	298.66	52.79	55.8	2.379	0.187
102	6.0	360	5	50	307.97	53.06	57.1	2.409	0.185
103	6.0	370	5	50	318.00	53.34	58.2	2.442	0.183
104	6.0	380	5	50	327.53	52.66	59.5	2.494	0.182
105	6.0	390	5	50	340.67	56.35	60.8	2.459	0.179
106	6.0	400	5	50	349.37	55.52	62.1	2.509	0.178
107	6.0	410	5	50	362.45	62.59	63.4	2.407	0.175
108	6.0	420	5	50	371.48	50.81	46.2	2.704	0.124
109	6.0	430	5	50	382.23	56.46	39.1	2.602	0.102
110	6.0	440	5	50	392.17	49.46	39.9	2.816	0.102
111	6.0	450	5	50	401.45	54.36	63.3	2.718	0.158
112	6.0	460	5	50	416.89	53.01	50.1	2.804	0.120
113	6.0	470	5	50	426.72	63.20	70.5	2.598	0.165
114	6.0	480	5	50	436.77	54.95	62.0	2.819	0.142
115	6.0	490	5	50	452.04	85.15	73.7	2.304	0.163
116	6.0	500	5	50	461.39	89.21	74.7	2.274	0.162
117	5.0	200	4	100	135.85	56.89	45.6	1.545	0.336
118	5.0	210	4	100	140.70	55.98	47.7	1.585	0.339
119	5.0	220	4	100	149.18	60.90	49.9	1.565	0.334
120	5.0	230	4	100	161.00	61.61	51.9	1.616	0.322
121	5.0	240	4	100	168.39	68.20	54.1	1.571	0.321
122	5.0	260	4	100	187.94	70.76	58.3	1.630	0.310
123	5.0	270	4	100	192.47	72.29	61.0	1.632	0.317
124	5.0	280	4	100	205.43	74.40	62.7	1.662	0.305
125	5.0	290	4	100	213.68	79.60	64.7	1.638	0.303
126	5.0	300	4	100	223.84	79.85	67.7	1.674	0.303
127	5.0	200	5	100	174.18	68.26	59.4	1.597	0.341
128	5.0	210	5	100	184.65	70.84	62.1	1.615	0.336
129	5.0	220	5	100	196.98	76.79	64.8	1.602	0.329
130	5.0	230	5	100	208.10	77.75	67.7	1.636	0.325
131	5.0	240	5	100	220.44	84.79	70.7	1.612	0.321
132	5.0	250	5	100	231.35	91.86	73.4	1.587	0.317
133	5.0	260	5	100	243.59	89.81	76.5	1.647	0.314
134	5.0	270	5	100	254.35	90.12	80.7	1.680	0.317
135	5.0	280	5	100	266.73	94.85	82.7	1.677	0.310
136	5.0	290	5	100	278.16	99.13	85.7	1.675	0.308
137	5.0	300	5	100	289.97	110.60	89.2	1.619	0.308
138	5.0	200	6	100	208.17	81.66	73.6	1.597	0.354

APPENDIX D. PARAMETRIC STUDY – DATA AND RESULTS

n^o	Dimensions [mm]				Results				
	L [m]	h_{tot}	t_{cf}	$b_{cf,sup}$	$M_{epI,R}$ [kNm]	M_{cr} [kNm]	$M_{epI,ult}$ [kNm]	λ_{LT}	χ_{LT}
139	5.0	210	6	100	222.19	88.54	77.0	1.584	0.346
140	5.0	220	6	100	236.56	88.99	79.8	1.630	0.337
141	5.0	230	6	100	250.25	97.23	84.0	1.604	0.336
142	5.0	240	6	100	265.45	102.99	87.7	1.605	0.330
143	5.0	250	6	100	279.09	111.35	90.4	1.583	0.324
144	5.0	260	6	100	294.54	110.13	94.8	1.635	0.322
145	5.0	270	6	100	309.13	113.11	100.5	1.653	0.325
146	5.0	280	6	100	324.02	120.03	104.4	1.643	0.322
147	5.0	290	6	100	339.10	122.61	106.5	1.663	0.314
148	5.0	300	6	100	354.27	137.66	110.2	1.604	0.311
149	6.0	200	4	100	134.89	45.95	40.0	1.713	0.297
150	6.0	210	4	100	139.35	46.71	41.4	1.727	0.297
151	6.0	220	4	100	152.83	44.22	42.4	1.859	0.278
152	6.0	230	4	100	160.70	47.10	43.9	1.847	0.273
153	6.0	240	4	100	165.15	53.49	45.3	1.757	0.274
154	6.0	260	4	100	186.92	56.55	48.6	1.818	0.260
155	6.0	270	4	100	192.07	49.29	50.4	1.974	0.263
156	6.0	280	4	100	204.05	57.09	52.0	1.890	0.255
157	6.0	290	4	100	213.24	60.58	53.8	1.876	0.252
158	6.0	300	4	100	222.61	64.08	55.4	1.864	0.249
159	6.0	200	5	100	172.27	53.65	52.6	1.792	0.305
160	6.0	210	5	100	184.42	58.39	53.9	1.777	0.292
161	6.0	220	5	100	194.94	57.67	54.9	1.839	0.282
162	6.0	230	5	100	206.56	56.28	56.8	1.916	0.275
163	6.0	240	5	100	218.01	65.68	58.8	1.822	0.270
164	6.0	250	5	100	230.20	70.60	60.7	1.806	0.264
165	6.0	260	5	100	242.36	68.92	62.8	1.875	0.259
166	6.0	270	5	100	253.54	66.45	65.9	1.953	0.260
167	6.0	280	5	100	265.38	74.49	67.3	1.887	0.254
168	6.0	290	5	100	278.33	75.11	69.9	1.925	0.251
169	6.0	300	5	100	289.77	86.06	72.2	1.835	0.249
170	6.0	200	6	100	206.70	70.35	65.7	1.714	0.318
171	6.0	210	6	100	221.02	69.41	66.7	1.784	0.302
172	6.0	220	6	100	235.18	64.09	68.5	1.916	0.291
173	6.0	230	6	100	249.50	73.35	70.7	1.844	0.283
174	6.0	240	6	100	264.03	79.18	73.1	1.826	0.277
175	6.0	250	6	100	279.41	86.34	75.4	1.799	0.270
176	6.0	260	6	100	294.35	84.71	78.0	1.864	0.265

APPENDIX D. PARAMETRIC STUDY – DATA AND RESULTS

n^o	Dimensions [mm]				Results				
	L [m]	h_{tot}	t_{cf}	$b_{cf,sup}$	$M_{epl,R}$ [kNm]	M_{cr} [kNm]	$M_{epl,ult}$ [kNm]	λ_{LT}	χ_{LT}
177	6.0	270	6	100	308.76	85.94	82.1	1.895	0.266
178	6.0	280	6	100	324.02	91.99	83.5	1.877	0.258
179	6.0	290	6	100	338.68	93.84	86.3	1.900	0.255
180	6.0	300	6	100	353.21	103.15	89.3	1.850	0.253
181	4.5	200	4	100	134.01	67.66	50.7	1.407	0.379
182	4.5	210	4	100	142.38	67.25	53.0	1.455	0.372
183	4.5	220	4	100	151.05	71.27	55.5	1.456	0.368
184	4.5	230	4	100	158.59	70.55	58.1	1.499	0.366
185	4.5	260	4	100	185.67	85.47	65.4	1.474	0.352
186	4.5	270	4	100	192.46	85.98	68.6	1.496	0.357
187	4.5	280	4	100	203.48	89.60	71.1	1.507	0.350
188	4.5	290	4	100	211.56	95.50	73.5	1.488	0.348
189	4.5	200	5	100	171.57	81.40	66.4	1.452	0.387
190	4.5	210	5	100	182.28	87.10	68.8	1.447	0.377
191	4.5	220	5	100	194.11	90.08	72.5	1.468	0.373
192	4.5	230	5	100	205.93	90.31	76.1	1.510	0.370
193	4.5	240	5	100	217.85	101.88	79.3	1.462	0.364
194	4.5	250	5	100	230.20	107.04	82.2	1.466	0.357
195	4.5	260	5	100	241.62	107.16	86.2	1.502	0.357
196	4.5	270	5	100	252.27	110.55	91.0	1.511	0.361
197	4.5	280	5	100	263.19	115.11	94.5	1.512	0.359
198	4.5	290	5	100	274.81	119.68	97.5	1.515	0.355

Appendix E

Concrete material law implemented in ANSYS

The concrete law impleted in ANSYS (2017) and retained for the FE model of the composite beam is defined by a Drucker-Prager concrete exponential hardening/softening/dilatation (HSD) behaviour (called HSD2).

The tension and tension-compression Drucker-Prager yield surface is given by:

$$f_{DPt} = \frac{\sigma_e}{\sqrt{3}} + \beta_t \sigma_m - \sigma_{Yt} \quad (E.1)$$

Where β_t and σ_{Yt} are constants defined by the uni-axial tensile strength R_t and uni-axial compressive strength R_c :

$$\beta_t = \frac{\sqrt{3}(R_c \Omega_c - R_t \Omega_t)}{R_c \Omega_c + R_t \Omega_t} \quad (E.2)$$

$$\sigma_{Yt} = \frac{2R_c \Omega_c R_t \Omega_t}{\sqrt{3}(R_c \Omega_c + R_t \Omega_t)} \quad (E.3)$$

The compression Drucker-Prager yield surface is given by:

$$f_{DPC} = \frac{\sigma_e}{\sqrt{3}} + \beta_c \sigma_m - \sigma_{Yc} \Omega_c \quad (E.4)$$

Where β_c and σ_{Yc} are constants defined by the biaxial compressive strength R_b and uni-axial compressive strength R_c :

$$\beta_c = \frac{\sqrt{3}(R_b - R_c)}{2R_b - R_c} \quad (E.5)$$

$$\sigma_{Yc} = \frac{R_b R_c}{\sqrt{3}(2R_b - R_c)} \quad (E.6)$$

Where σ_e and σ_m are respectively the equivalent stress and the average stress defined by :

$$\sigma_e = \sqrt{3I_2} = \sqrt{\frac{3}{2}[(\text{tr}\bar{\sigma})^2 - \text{tr}(\bar{\sigma}^2)]} \quad (E.7)$$

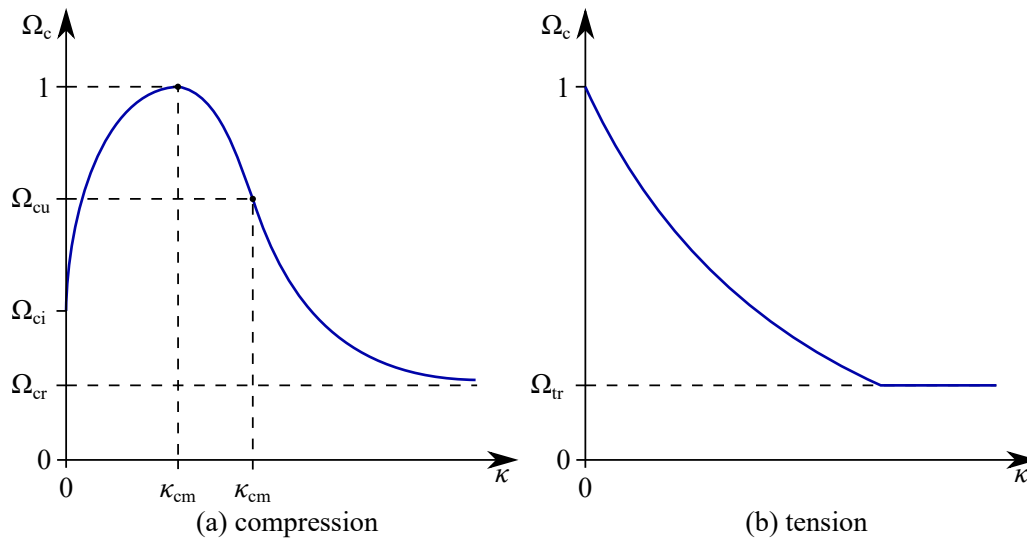


Figure E.1 – Exponential Hardening Softening in Compression and Tension

$$\sigma_m = \frac{I_1}{3} = \frac{1}{3} \text{tr} \bar{\sigma} \quad (\text{E.8})$$

Ω_c and Ω_t are respectively the hardening and softening functions in compression and tension, depending on the HSD behaviour chosen (here HSD2) and given in ANSYS (2017). The code ANSYS (2017) proposes also three others HSD behaviour (HSD4, HSD5 and HSD6) to characterize the hardening and softening of the material, the differences are mainly in the form of the functions.

The parameters used for the concrete material law described above are presented in Table E.1.

Table E.1 – Parameters of the concrete law implemented in the FEM

Designation	Symbol	Value
Uniaxial compressive strength	$R_c = f_{cm}$	53.4 MPa
Uniaxial tensile strength	$R_t = f_{ctm}$	3.8 MPa
Biaxial compressive strength	$R_b = 1.2f_{cm}$	64.1 MPa
Secant modulus of elasticity of concrete	E_{cm}	36 GPa
Compressive strain in the concrete at the peak stress	ϵ_{c1}	0.0024
Ultimate compressive strain in the concrete	ϵ_{cu}	0.0035
Relative stress at start of non-linear hardening	Ω_{ci}	0.4
Residual relative stress at κ_{cu}	Ω_{cu}	0.85
Residual compressive relative stress	Ω_{cr}	0.2
Mode I area-specific fracture energy	G_{ft}	100 N/m
Residual tensile relative stress	Ω_{tr}	0.1
Plastic strain at uniaxial compressive strength	$\kappa_{cm} = \epsilon_{c1} - f_{cm}/E_{cm}$	
Plastic strain at transition from power law to exponential softening	$\kappa_{cu} = \epsilon_{cu} - \Omega_{cu}f_{cm}/E_{cm}$	

Appendix F

Technical drawings

Poutre COMINO (Position 17s et 11c) - Quantité par poutre

Position	Type	Description	Quantité	Dimension	Fournisseur
a	Plat	Plat inférieur	1	180x6300 t=8	Briand
b	Tôle pliée	Tôles pliées à froid	2	450x6300 t=4	Briand
c	Maintien	Maintiens latéraux (position à donner plus tard)	8	30x322 t=4	Briand
d	Vis	Vis auto-perceuse S-MD 25 GZ	164	41 fois 4	HILTI
e	Connecteur	Nelson (Nombre à confirmer) (poutre 11c uniquement)	21	Ø19 h100	Briand
f	Vis	Vis auto-perceuse S-MD 25 GZ	16	8 fois 2	HILTI

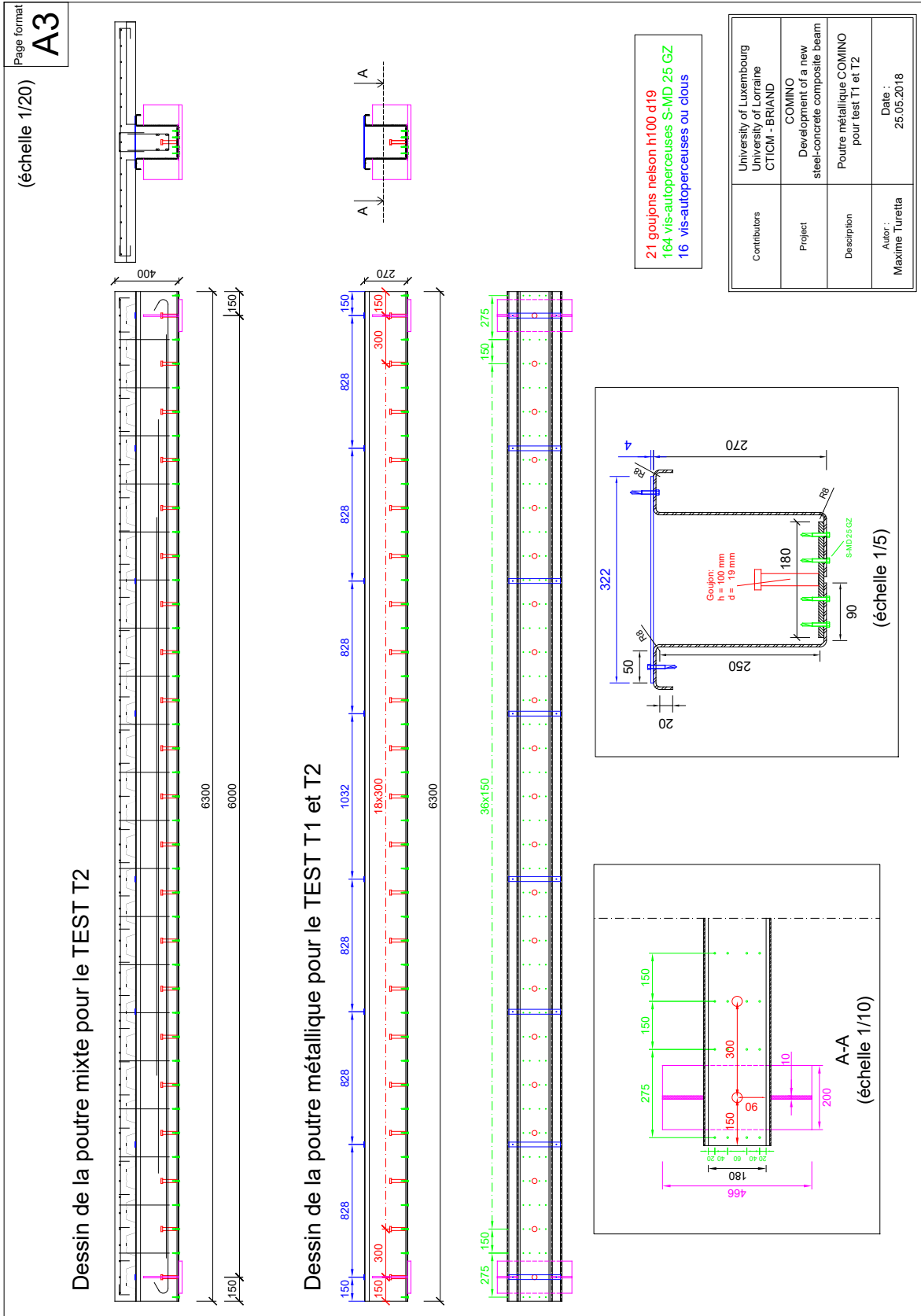
TEST T1 - Test de la poutre métallique en phase de construction

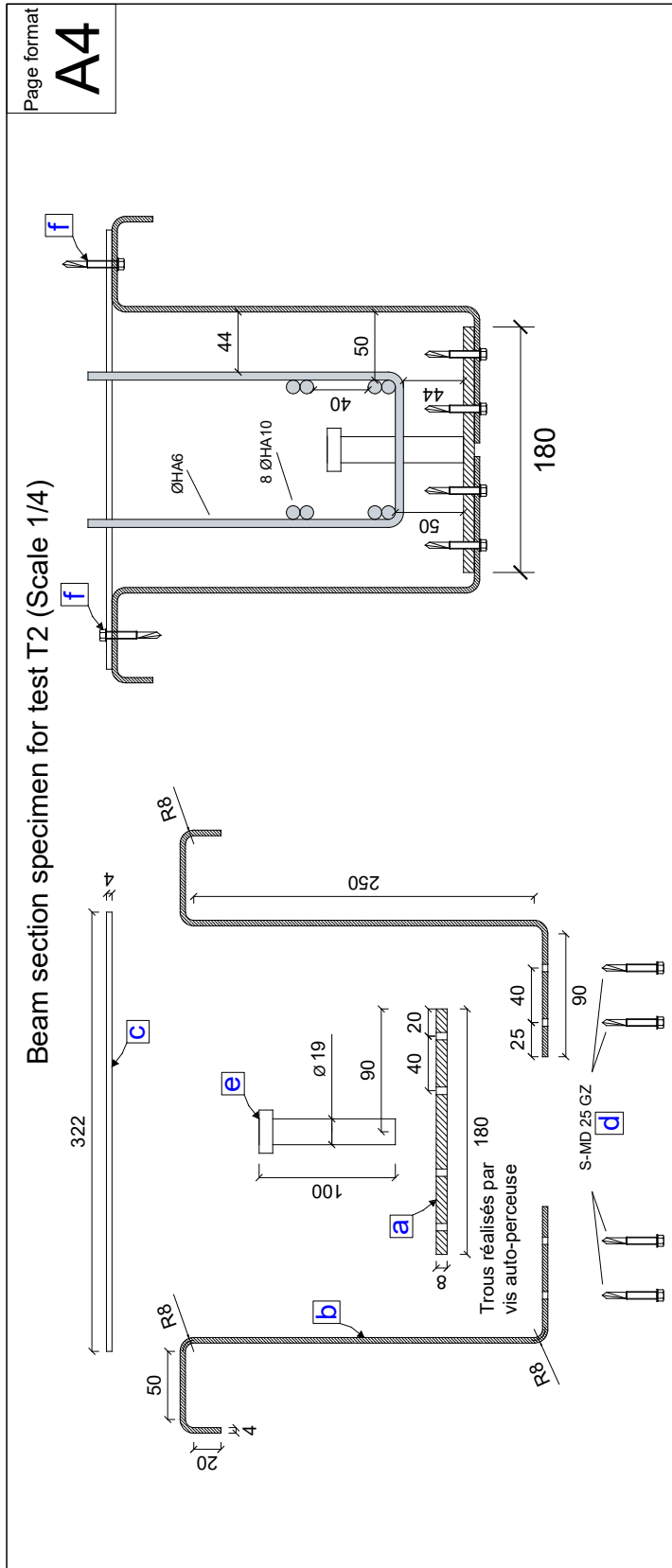
Position	Type	Description	Quantité	Dimension	Fournisseur
1s	Plat	Plat sous le vérin	1	450x450x20	UL Lab
2s	Oreille	Oreille sous vérin	1	128x95x20 Ø57	UL Lab
3s	Chaîne	Chaîne sous le vérin	1	I300 CMU 12T	UL Lab
4s	Oreille	Oreille milieu (sur Poutre 5s)	1	128x95x20 Ø57	UL Lab
5s	Poutre	Poutre répartition longitudinale	1	HEA160 I=2470	Briand
6s	Raidisseur	Raidisseurs de Poutre 5s	6	134x77x20	Briand
7s	Poutre	Poutre Sup répartition transversale	2	UPE 270 I=1000	Briand
8s	Assemblage	Assemblage Poutre 5s - Poutre 7s	-	-	UL Lab
9s	Raidisseur	Raidisseurs de Poutre 7s	6	243x87x10	Briand
10s	Oreille	Oreilles des poutres 7s	4	128x95x20 Ø57	UL Lab
11s	Chaîne	Chaîne reliant les poutres 7s - 15s	4	I630 CMU 3.5T	UL Lab
12s	Crochet	Crochets aux extrémités des chaînes	8	CMU 3.5T	UL Lab
13s	Oreille	Oreilles des poutres 15s	4	128x95x20 Ø57	UL Lab
14s	Assemblage	Assemblage Poutre 15s - COMINO	-	-	UL Lab
15s	Poutre	Poutre Inf répartition transversale	2	UPE 270 I=1000	Briand
16s	Raidisseur	Raidisseurs de Poutre 15s	4	243x87x10	Briand
17s	COMINO	Poutre testée sans goujons	2	I=6300	Briand
18s	Plat	Plat de support aux appuis	2	465x200x20	Briand
19s	Raidisseur	Raidisseurs de COMINO aux appuis	4	220x128x10	Briand
20s	Rouleau	Rouleau aux appuis	2	Ø80 I313	UL Lab
21s	R-Support	Support des rouleaux	2	465x200x20	UL Lab
22s	Poutre	Poutre transversale (appuis)	2	HEB260	UL Lab
23s	Lindapter	Fixation Lindapter	12	Lindapter	UL Lab
24s	Plat	Plat inf. de l'appui à fourche	4	260x150x10	Briand
25s	Plat	Raidisseur de l'appui à fourche	4	330x140x10	Briand
26s	Plat	Plat latéral de l'appui à fourche	4	330x200x10	Briand
27s	Plat	Plat supplémentaire (réserve)	1	2000x300x10	Briand

APPENDIX F. TECHNICAL DRAWINGS

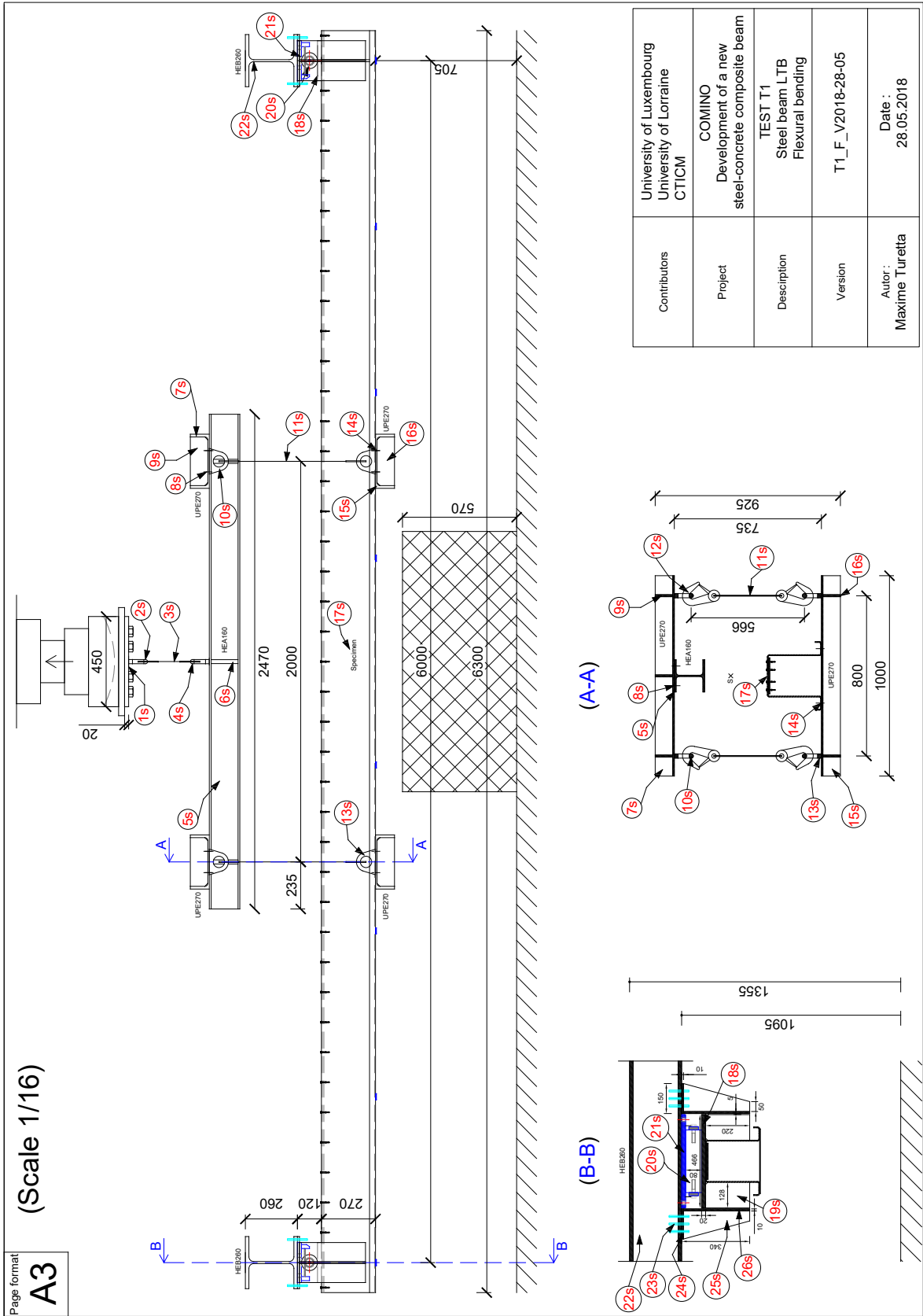
TEST T2 - Test de la poutre mixte

Position	Type	Description	Quantité	Dimension	Fournisseur
1c	Poutre	Poutre répartition longitudinale	1	HEA300 I1820	UL Lab
2c	Raidisseur	Raidisseurs de la poutre 1c	4	145x270x20	UL Lab
3c	Poutre	Poutre répartition transversale	2	IPE360 I1500	UL Lab
4c	Assemblage	Assemblages entre Poutre 1c - 3c	-	-	UL Lab
5c	Raidisseur	Raidisseurs de la poutre 3c	4	334x81x10	UL Lab
6c	Barre	Bar reliant les poutres 3c	1	Ø24 I1520	UL Lab
7c	Rouleau	Rouleaux introduisant la charge	2	Ø50 I1500	UL Lab
8c	Plat	Plat sous les Rouleaux 7c	2	1500x150x20	Briand
9c	Béton	Béton (Dalle + Poutre)	1	1.6 m ³	UL Lab
10c	Bac acier	COFRAPLUS 60	28	l=640 b=640	Briand
11c	COMINO	Poutre testée avec goujons	2	l=6300	Briand
12c	Armature	Armatures longi. lit 1 (+Crossée)	2	Ø10 I6450	Briand
13c	Armature	Armatures longitudinales Lit 2	2	Ø10 I5760	Briand
14c	Armature	Armatures longitudinales Lit 3	2	Ø10 I4700	Briand
15c	Armature	Armatures longitudinales Lit 4	2	Ø10 I3480	Briand
16c	Armature	Cadre partie inférieure	40	Ø8 I600	Briand
17c	Armature	Cadre partie supérieure	40	Ø8 I400	Briand
18c	Armature	Treillis soudés ST50C	1	Ø8 6200x1400	Briand
19c	Armature	Armatures en U pour les bords	86	Ø8 I130	Briand
20c	Plat	Plat support aux appuis	2	465x200x20	Briand
21c	Raidisseur	Raidisseurs de COMINO aux appuis	4	220x128x10	Briand
22c	Rouleau	Rouleau aux appuis	2	Ø80 I313	UL Lab
23c	R-Support	Support des rouleaux	2	465x200x20	UL Lab
24c	Poutre	Poutre transversale (appuis)	2	HEB260	UL Lab
25c	Plat	Raidisseur de l'appui à fourche	4	330x140x10	Briand
26c	Plat	Plat latéral de l'appui à fourche	4	330x200x10	Briand
27c	Plat	Plat inf. de l'appui à fourche	4	260x150x10	Briand
28c	Clou	Clou des bacs acier	N	XENP	HILTI
29c	Armature	Armatures additionnelles (réserve)	4	Ø8 I2000	Briand





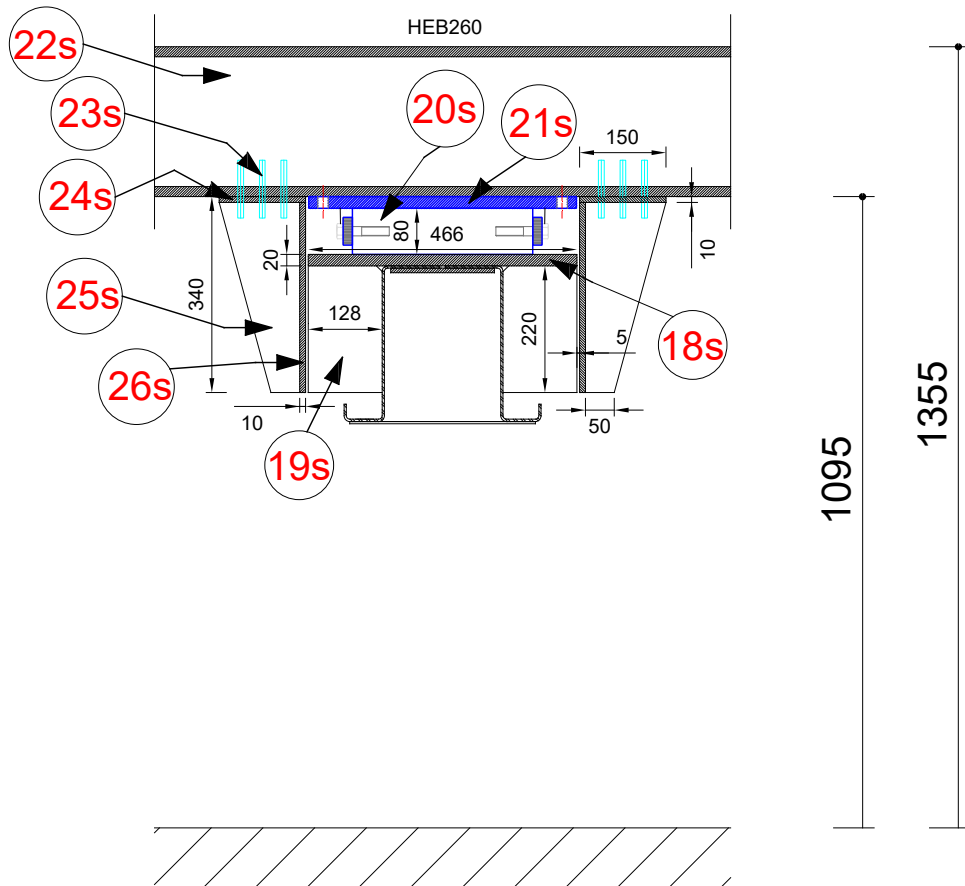
Contributors	University of Luxembourg University of Lorraine CTICM
Project	COMINO Development of a new steel-concrete composite beam
Description	TEST T2 Steel-concrete composite Flexural bending
Version	T2_S_V2018-02-05
Autor :	Date : 02.05.2018
Maxime Turetta	



Page format
A4

Scale 1/10

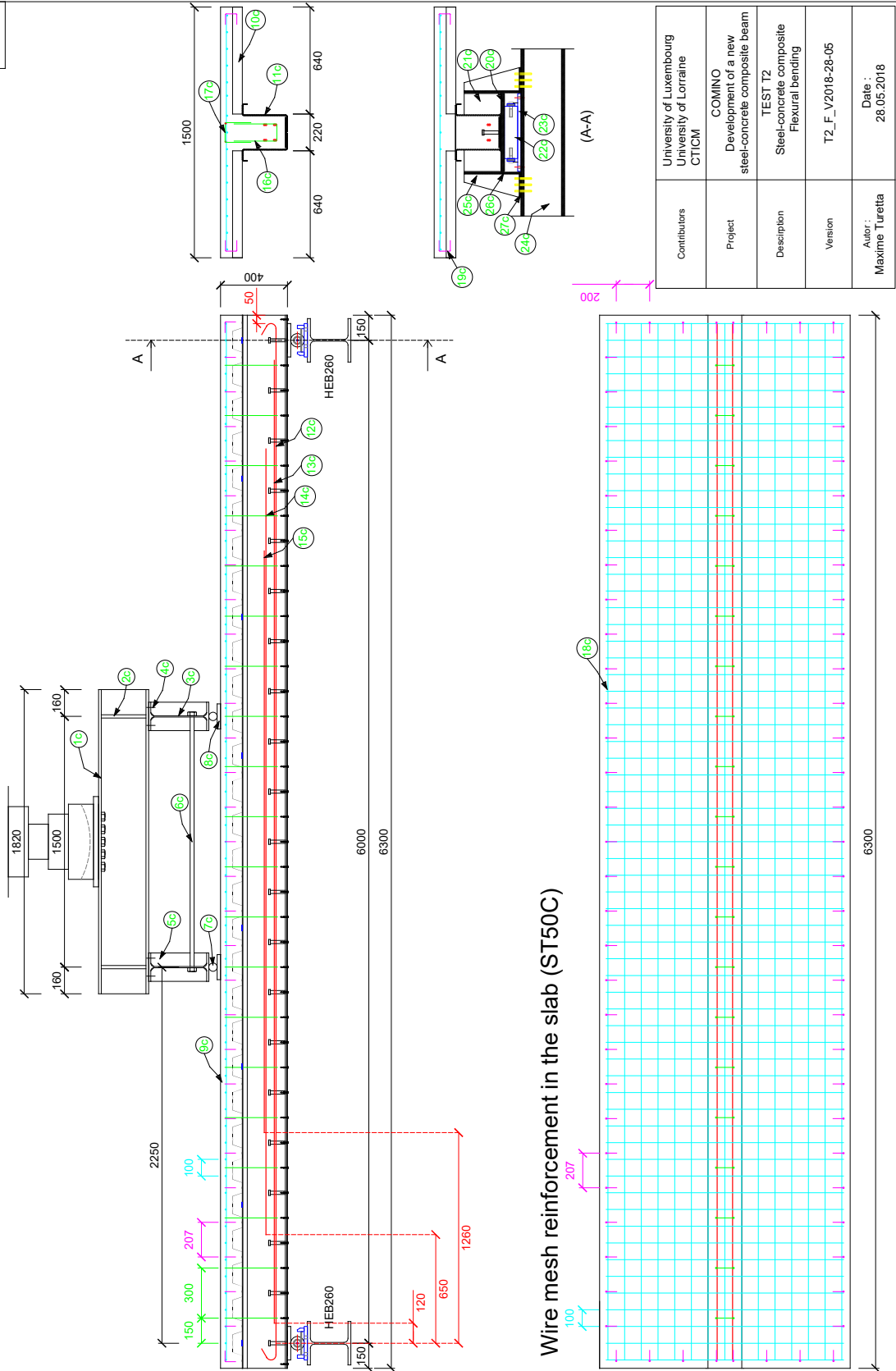
(B-B)

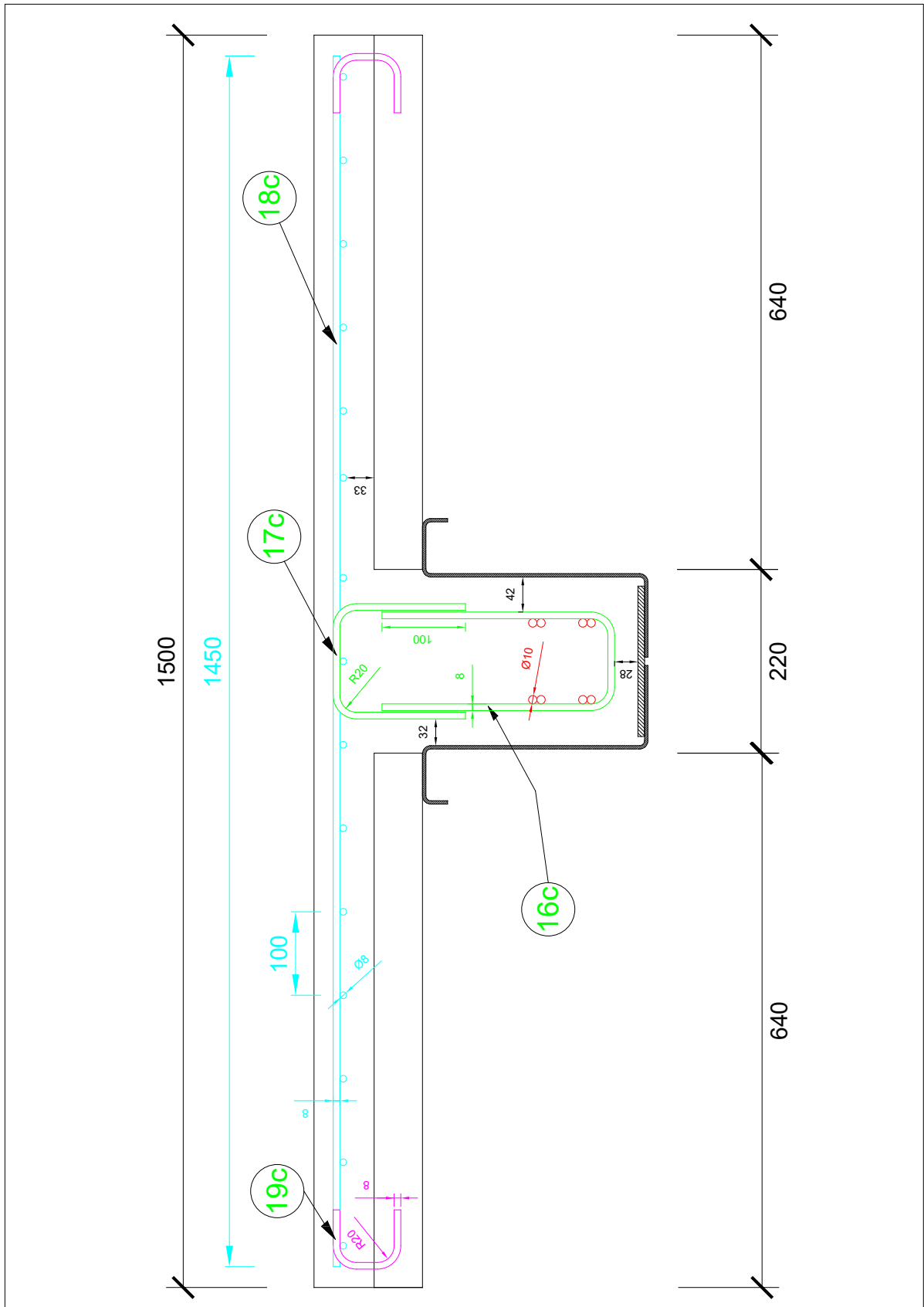


Contributors	University of Luxembourg University of Lorraine CTICM
Project	COMINO Development of a new steel-concrete composite beam
Description	TEST T1 Steel beam LTB Flexural bending
Version	T1_BB_V2018-28-05
Autor : Maxime Turetta	Date : 28.05.2018

General drawing specimen for test T2 - Composite
(Scale 1/20)

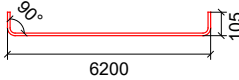
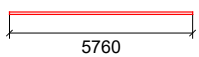
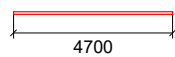
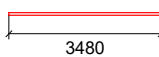
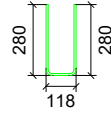
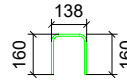
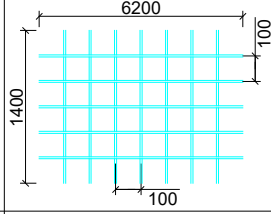
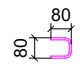
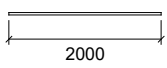
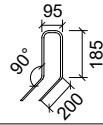
Page format
A3





Page format

A3

Position related to test T2	Quantity	Diameter (mm)	Description / Form	Bending diameter (mm)	Length (mm)	Steel Grade	Mass per unit length (kg/m)	Total mass (kg)
12c	2	Ø10		Ø40	6410	B 500B	0.62	7.95
13c	2	Ø10		-	5760	B 500B	0.62	7.14
14c	2	Ø10		-	4700	B 500B	0.62	5.83
15c	2	Ø10		-	3480	B 500B	0.62	4.32
16c	22	Ø8		Ø32	678	B 500B	0.395	5.89
17c	22	Ø8		Ø32	458	B 500B	0.395	3.98
18c - ST50C	1	Ø8		-	6200 x 1400	B 500B	0.395	162.58
19c	80	Ø8		Ø32	240	B 500B	0.395	7.58
29c	4	Ø8		Ø32	2000	B 500B	0.395	3.16
30c	25	Ø8		Ø32	865	B 500B	0.62	8.54
SUM								216.97

Remarks:

- 1) The indicated dimensions are external dimensions
- 2) All dimensions are indicated in (mm)
- 3) Bending diameter : 4Ø
- 4) All bars have a grade of B 500B
- 5) Concrete grade C30/37

Contributors	University of Luxembourg University of Lorraine CTICM - BRIAND
Project	COMINO
Version	TEST T2 Reinforcement bars
Autor : Maxime Turetta	Date : 16.07.2018

Bibliography

Articles

- H.-J. Ahn and S.-H. Ryu. Experimental study on flexural strength of modular composite profile beams. *Steel and Composite Structures*, 7(1):71–85, 2007. doi:10.12989/scs.2007.7.1.071.
- H.-J. Ahn and S.-H. Ryu. Experimental study on flexural strength of reinforced modular composite profiled beams. *Steel and Composite Structures*, 8(4):313–328, 2008. doi:10.12989/scs.2008.8.4.313.
- A. Beyer, Y. Galéa, and T. Nguyen. Déversement élastique des barres fléchies comprimées - Fondement théorique et validation du logiciel LTBeamN. *Revue Construction Métallique*, 3, 2015.
- A. Beyer, N. Boissonnade, A. Khelil, and A. Bureau. Elastic stability of U-shaped members in bending considering pre-buckling displacements. *Journal of Constructional Steel Research*, 135:230 – 241, 2017. ISSN 0143-974X. doi:10.1016/j.jcsr.2017.04.011.
- A. Beyer, N. Boissonnade, A. Khelil, and A. Bureau. Influence of assumed geometric and material imperfections on the numerically determined ultimate resistance of hot-rolled U-shaped steel members. *Journal of Constructional Steel Research*, 147:103 – 115, 2018. doi:10.1016/j.jcsr.2018.03.021.
- M. Braun, R. Obiala, and C. Odenbreit. Analyses of the loadbearing behavior of deep-embedded concrete dowels, CoSFB. *Steel Construction*, 8(3):167–173, 2015. doi:10.1002/stco.201510024.
- L. Chen, J. Dai, Q. Jin, L. Chen, and X. Liu. Refining bond–slip constitutive relationship between checkered steel tube and concrete. *Construction and Building Materials*, 79:153 – 164, 2015. doi:https://doi.org/10.1016/j.conbuildmat.2014.12.058.
- L.-H. Chen, S.-T. Li, H.-Y. Zhang, and X.-F. Wu. Experimental study on mechanical performance of checkered steel-encased concrete composite beam. *Journal of Constructional Steel Research*, 143:223 – 232, 2018. doi:10.1016/j.jcsr.2017.12.021.
- G. G. Goble. Shear Strength of Thin Flange Composite Specimens. *Engineering Journal - AISC*, 5:62–65, 1968.
- L. Guo, Y. Liu, and B. Qu. Fully composite beams with u-shaped steel girders: Full-scale tests, computer simulations, and simplified analysis models. *Engineering Structures*, 177: 724 – 738, 2018. doi:https://doi.org/10.1016/j.engstruct.2018.09.087.

BIBLIOGRAPHY

- S. Hicks. Current trend in modern floor construction. *New steel construction*, 11:32–33, 01 2003.
- K. M. A. Hossain. Experimental & theoretical behavior of thin walled composite filled beams. *Electronic Journal of Structural Engineering*, 3:117–139, 2003.
- B. Y. Huo and C. A. D’Mello. Push-out tests and analytical study of shear transfer mechanisms in composite shallow cellular floor beams. *Journal of Constructional Steel Research*, 88:191–205, 2013. doi:<https://doi.org/10.1016/j.jcsr.2013.05.007>.
- J. G. James. Ralph dodd, the very ingenious schemer. *Transactions of the Newcomen Society*, 47(1):161–178, 1974. doi:10.1179/tns.1974.012.
- Y. K. Ju, D.-H. Kim, and S.-D. Kim. Experimental assessment of the shear strength of an asymmetric steel composite beam with web openings. *Canadian Journal of Civil Engineering*, 32(2):314–328, 2005. doi:10.1139/104-094.
- P. Keo, C. Lepourry, H. Somja, and F. Palas. Behavior of a new shear connector for U-shaped steel-concrete hybrid beams. *Journal of Constructional Steel Research*, 145:153 – 166, 2018. doi:10.1016/j.jcsr.2018.01.028.
- A. Kozma, C. Odenbreit, M. Braun, M. Veljkovic, and M. Nijgh. Push-out tests on demountable shear connectors of steel-concrete composite structures. *Structures*, 2019. doi:10.1016/j.istruc.2019.05.011.
- R. M. Lawson and H. Taufiq. Partial shear connection in light steel composite beams. *Journal of Constructional Steel Research*, 154:55 – 66, 2019. doi:10.1016/j.jcsr.2018.11.005.
- C. Lepourry, P. Heng, H. Somja, N. Boissonnade, and F. Palas. An innovative concrete-steel structural system for long-span structure allowing a fast and simple erection. *Structures*, in press, 2019. doi:<https://doi.org/10.1016/j.istruc.2019.04.016>.
- J. Liu, Y. Zhao, Y. F. Chen, S. Xu, and Y. Yang. Flexural behavior of rebar truss stiffened cold-formed u-shaped steel-concrete composite beams. *Journal of Constructional Steel Research*, 150:175 – 185, 2018. doi:10.1016/j.jcsr.2018.08.011.
- J. Liu, Y. Zhao, Y. Yang, and Y. F. Chen. Bending capacity and elastic stiffness for a novel configuration of cold-formed u-shaped steel-and-concrete composite beams. *Journal of Structural Engineering*, 145(10):04019106, 2019. doi:10.1061/(ASCE)ST.1943-541X.0002394.
- Y. Liu, L. Guo, B. Qu, and S. Zhang. Experimental investigation on the flexural behavior of steel-concrete composite beams with U-shaped steel girders and angle connectors. *Engineering Structures*, 131:492 – 502, 2017. doi:10.1016/j.engstruct.2016.10.037.
- H. Loh, B. Uy, and M. Bradford. The effects of partial shear connection in the hogging moment regions of composite beams: Part i—experimental study. *Journal of Constructional Steel Research*, 60(6):897–919, 2004a. doi:<https://doi.org/10.1016/j.jcsr.2003.10.007>.
- H. Loh, B. Uy, and M. Bradford. The effects of partial shear connection in the hogging moment regions of composite beams part ii—analytical study. *Journal of Constructional Steel Research*, 60(6):921–962, 2004b. doi:<https://doi.org/10.1016/j.jcsr.2003.10.008>.

- S.-i. Nakamura. New structural forms for steel/concrete composite bridges. *Structural Engineering International*, 10(1):45–50, 2000. doi:10.2749/101686600780620955.
- S.-i. Nakamura. Bending behavior of composite girders with cold formed steel u section. *Journal of Structural Engineering*, 128(9):1169–1176, 2002. doi:10.1061/(ASCE)0733-9445(2002)128:9(1169).
- S. Nellinger, F. Eggert, U. Kuhlmann, C. Odenbreit, and R. Obiala. Short-span composite beam tests to evaluate stud resistances. *Proceedings of the Institution of Civil Engineers - Structures and Buildings*, 171(1):17–28, 2018. doi:10.1680/jstbu.16.00173.
- J. Nie, J. Fan, and C. S. Cai. Stiffness and Deflection of Steel-Concrete Composite Beams under Negative Bending. *Journal of Structural Engineering*, 130(11):1842–1851, 2004. doi:10.1061/(ASCE)0733-9445(2004)130:11(1842).
- D. J. Oehlers. Composite Profiled Beams. *Journal of Structural Engineering*, 119(4):1085–1100, 1993. doi:10.1061/(ASCE)0733-9445(1993)119:4(1085).
- D. J. Oehlers, H. D. Wright, and M. J. Burnet. Flexural Strength of Profiled Beams. *Journal of Structural Engineering*, 120(2):378–393, 1994. doi:10.1061/(ASCE)0733-9445(1994)120:2(378).
- J. G. Ollgaard, R. G. Slutter, and J. W. Fisher. Shear Strength of Stud Connectors in Lightweight and Normal-Weight Concrete. *AISC Engineering Journal*, 8:55–64, 1971.
- S.-H. Ryu. Study on behavior of T-section modular composite profiled beams. *Steel and Composite Structures*, 10(5):457–473, 2010. doi:10.12989/scs.2010.10.5.457.
- J. Schlaich, K. Schafer, and M. Jennewein. Toward a Consistent Design of Structural Concrete. *PCI Journal*, 32(3):74–150, 1987.
- B. Uy and M. Bradford. Elastic local buckling of steel plates in composite steel-concrete members. *Engineering Structures*, 18(3):193 – 200, 1996. doi:https://doi.org/10.1016/0141-0296(95)00143-3.
- B. Uy and M. A. Bradford. Ductility of Profiled Composite Beams. Part I: Experimental Study. *Journal of Structural Engineering*, 121(5):876–882, 1995a. doi:10.1061/(ASCE)0733-9445(1995)121:5(876).
- B. Uy and M. A. Bradford. Ductility of Profiled Composite Beams. Part II: Analytical Study. *Journal of Structural Engineering*, 121(5):883–889, 1995b. doi:10.1061/(ASCE)0733-9445(1995)121:5(883).
- W. E. Ward. Fire-proof building construction. *Popular Science Monthly*, 23:161–178, 1883. doi:10.1179/tns.1974.012.
- B. Yang, S.-B. Kang, G. Xiong, S. Nie, Y. Hu, S. Wang, J. Bai, and G. Dai. Experimental and numerical study on lateral-torsional buckling of singly symmetric Q460GJ steel I-shaped beams. *Thin-Walled Structures*, 113:205 – 216, 2017. doi:10.1016/j.tws.2016.12.009.
- X. Zhou, Y. Zhao, J. Liu, Y. F. Chen, and Y. Yang. Bending experiment on a novel configuration of cold-formed U-shaped steel-concrete composite beams. *Engineering Structures*, 180:124 – 133, 2019. doi:10.1016/j.engstruct.2018.11.001.

Thesis

- M. Braun. *Investigation of the Load-Bearing Behaviour of CoSFB-Dowels*. PhD thesis, Université du Luxembourg, 2018.
- V. de Ville de Goyet. *L'analyse statique non linéaire par la méthode des éléments finis des structures spatiales formées de poutres à section non symétrique*. PhD thesis, Université de Liège, 1989.
- B. Huo. *Experimental and analytical study of the shear transfer in composite shallow cellular floor beams*. PhD thesis, City University London, 2012.
- H. Lungershausen. *Zur Schubtragfähigkeit von Kopfbolzendübeln*. PhD thesis, Ruhr-Universität Bochum, 1988.
- S. Nellinger. *On the behaviour of shear stud connections in composite beams with deep decking*. PhD thesis, Université du Luxembourg, 2015.
- M. Schäfer. *Zum Tragverhalten von Flachdecken mit integrierten hohlkastenförmigen Stahlprofilen*. PhD thesis, Bergische Universität Wuppertal, 2007.
- B. Uy. *Profiled composite beam construction*. PhD thesis, The University of New South Wales, 1995.

Proceedings

- G. Fabbrocino and M. Pecce. Experimental tests on steel-concrete composite beams under negative bending. In *Annual Conference of Canadian Society for Civil Engineering (CSCE 2000)*, page 217, 01 2000.
- K. M. A. Hossain. Designing thin-walled composite-filled beams. In *Proceedings of the Institution of Civil Engineers - Structures and Building*, volume 158, pages 267–278, 08 2005.
- C. Lepourry, H. Somja, P. Keo, P. Heng, and F. Palas. An innovative concrete-steel structural system allowing for a fast and simple erection. In *12th international conference on 'Advances in Steel-Concrete Composite Structures' - ASCCS 2018*, pages 617–624, 06 2018. doi:10.4995/ASCCS2018.2018.7014.
- M. V. Leskela, S. Peltonen, A. Iliopoulos, and P. Kiriakopoulos. Numerical and experimental investigations on the vertical shear resistance of boxed steel cross-sections with concrete infill (Deltabeams). In *EUROSTEEL 2014*, 09 2014.
- P. Nádaský. Steel-concrete composite beams for slim floors—specific design features in scope of steel frames design. In *Steel Structures and Bridges 2012 - 23rd Czech and Slovak International Conference*, volume 40, pages 274–279, 2012. doi:https://doi.org/10.1016/j.proeng.2012.07.093.
- E. Pelke and K.-E. Kurrer. On The Evolution Of Steel-Concrete Composite Construction. In *5th International Congress on Construction History*, pages 107–116, 06 2015.

- S. Peltonen and M. V. Leskelä. Connection Behaviour of a Concrete Dowel in a Circular Web Hole of a Steel Beam. In *Fifth International Conference on Composite Construction in Steel and Concrete*, pages 544–552, 07 2004. doi:10.1061/40826(186)51.
- M. Schäfer. Design rules for slim-floor girders considering the composite behaviour. In *Nordic Steel Construction Conference 2015*, 09 2015.
- M. Turetta, A. Khelil, C. Odenbreit, and P.-O. Martin. Numerical study on the load bearing capacity of a steel U section beam used as a formwork in construction stage. In *International Conference on Engineering Research and Practice for Steel Construction 2018 (ICSC2018)*, 09 2018.

Books

- ANSYS. *Mechanical APDL Theory Reference*. 2017.
- R. M. Lawson, D. L. Mullett, and J. W. Rackham. *Design of Asymmetric Slimflor Beams using Deep Composite Decking*, volume 175. SCI Publication, 1997.
- Leica Geosystems AG. *Leica TS30 - Technical Data*. 2009.
- D. L. Mullett. *Slim Floor Design and Construction*, volume 110. SCI Publication, 1992.
- D. L. Mullett. *Design of RHS Slimflor Edge Beams*, volume 169. SCI Publication, 1997.
- D. J. Oehlers and M. A. Bradford. *17 - Composite Profiled Beams*. Pergamon, Oxford, 1995. ISBN 978-0-08-041919-0. doi:10.1016/B978-0-08-041919-0.50023-5.
- J. A. Purkiss. *Fire Safety Engineering Design of Structures, Second Edition*. Butterworth Heinemann, 2007.
- O. Vassart and B. Zhao. *Fire Resistance Assessment of Partially Protected Composite Floors (FRACOF) - Design Guide*. 2011.

Patents

- G. Dejean and C. Fraud. Structure mixte de construction, 2013. French Patent No. FR3013064 A1.
- R. Dodd. Improved bridge floorings or platforms, fireproof floorings and fireproof roofings for extensive dwelling houses, warehouses and mills, June 1808. British Patent n° 3141.
- J. Kahn. Composite beam construction, August 1926. United States Patent Office No. 1,597,278 - US1597278A.
- J. Monier. Système de caisses-bassins mobiles en fer et ciment applicables à l'horticulture, 1867. French Patent n° 77 165.
- F. Pohlmann. Concrete or like girder, August 1904. United States Patent Office No. 766,899 - US766899A.
- H. Rahimzadeh. Composite structural framing system, June 2002. United States Patent - US 2002/0069598A1.

Recommendations

CEB-FIP Model Code 1990. *CEB-FIP Model Code 1990*. Thomas Telford Limited, 1993.

ECCS. *Rules for Member Stability in EN 1993-1-1 – Background documentation and design guidelines*. European Convention for Constructional Steelwork (ECCS) - TC8, 2006.

ECCS-TC7. *European Recommendations for the Application of Metal Sheeting acting as a Diaphragm*. European Convention for Constructional Steelwork. Technical Committee 7, Thin-walled, Cold Formed Sheet Steel in Building, 1995.

ECCS-TC8. *Ultimate limit state calculation of sway frames with rigid joints*. European Convention for Constructional Steelwork. Technical Committee 8, Structural Stability, 1984.

fib Model Code 2010. *fib Model Code for Concrete Structures 2010*. Ernst & Sohn, 2013.

Standards

AISC 360-16. *Specification for Structural Steel Buildings*. American Institute of Steel Construction (AISC), 2016.

BS 5950-1. *Structural use of steelwork in building, Part 1 : Code of practice for design in simple and continuous construction: hot rolled sections*. British Standards Institution (BSI), 1990.

BS 5950-3. *Structural use of steelwork in building, Part 3, Section 3.1 : Code of practice for design of simple and continuous composite beams*. British Standards Institution (BSI), 1990.

EN 10025-2. *Hot rolled products of structural steels – Part 2 : Technical delivery conditions for non-alloy structural steels*. European Committee for Standardization (CEN), 2005.

EN 1990. *Eurocode 0: Basis of structural design*. European Committee for Standardization (CEN), 2003.

EN 1991-1-1. *Eurocode 1: Actions on structures, Part 1-1: General actions - Densities, self weight, imposed loads for buildings*. European Committee for Standardization (CEN), 2003.

EN 1991-1-2. *Eurocode 1: Actions on structures, Part 1-2: General actions - Actions on structures exposed to fire*. European Committee for Standardization (CEN), 2002.

EN 1991-1-6. *Eurocode 1: Actions on structures, Part 1-6: General actions - Actions during execution*. European Committee for Standardization (CEN), 2005.

EN 1992-1-1. *Eurocode 2: Design of concrete structures, Part 1-1: General rules and rules for buildings*. European Committee for Standardization (CEN), 2005.

EN 1992-1-2. *Eurocode 2: Design of concrete structures, Part 1-2: General rules - Structural fire design*. European Committee for Standardization (CEN), 2005.

- EN 1993-1-1. *Eurocode 3: Design of steel structures, Part 1-1: General rules and rules for buildings*. European Committee for Standardization (CEN), 2005.
- EN 1993-1-3. *Eurocode 3: Design of steel structures, Part 1-3: General rules - Supplementary rules for cold-formed members and sheeting*. European Committee for Standardization (CEN), 2007.
- EN 1993-1-5. *Eurocode 3: Design of steel structures, Part 1-5: Plated structural elements*. European Committee for Standardization (CEN), 2007.
- EN 1994-1-1. *Eurocode 4: Design of composite steel and concrete structures, Part 1-1: General rules and rules for buildings*. European Committee for Standardization (CEN), 2005.
- EN ISO 6892-1. *Metallic materials – Tensile testing – Part 1 : Method of test at room temperature*. International Organization for Standardization (ISO), 2016.
- GB 50017. *Code for Design of Steel Structures*. Ministry of Housing and Urban-Rural Development of the People’s Republic of China, 2017.
- GBJ 17-88. *Code for Design of Steel Structures*. Ministry of Construction of the People’s Republic of China, 1995.
- NF P 06-111-2. *Eurocode 1: Actions on structures, Part 1-1: General actions - Densities, self weight, imposed loads for buildings - French National Annex*. European Committee for Standardization (CEN), 2004.

Résumé

Une solution innovante de poutre mixte acier-béton a été développée en tenant compte des problématiques de résistance au feu et de montage sur chantier. La poutre est composée d'une partie métallique en U connectée à une partie en béton armé. En phase de construction, la poutre métallique supporte la dalle et constitue un coffrage pour la retombée en béton armé. La poutre en U résiste aux charges de construction sans système d'étaie temporaire. Lors du coulage du béton, la poutre en acier est remplie en même temps que la dalle, ce qui permet un gain de temps considérable sur chantier. En phase d'exploitation, la poutre est mixte acier-béton. La connexion entre les deux matériaux est réalisée par des goujons à tête soudée en partie inférieure de la poutre en U. En situation d'incendie, la poutre mixte répond aux durées de stabilité au feu conventionnelles grâce aux armatures longitudinales à l'intérieur de la retombée avec des enrobages suffisants.

Un état de l'art sur les solutions existantes répondant aux critères de la thèse est réalisé afin de proposer une solution innovante et optimisée. En phase de construction, sans présence de maintien, la poutre métallique en U est sujette à l'instabilité globale de déversement. Afin de caractériser la stabilité de la poutre, un test à échelle réelle est effectué au Laboratoire de l'Université du Luxembourg. Les résultats de l'essai sont comparés à des simulations numériques et à des études analytiques. Une étude paramétrique portant sur 200 configurations géométriques de la poutre en U est réalisée afin de valider l'utilisation de la courbe « b » pour le dimensionnement au déversement selon l'Eurocode 3. En phase d'exploitation, une fois le béton durci, la poutre présente un comportement mixte acier-béton assuré par la connexion. Pour des raisons de fabrication, la connexion est située dans une zone où le béton est soumis à des efforts de traction induits par la flexion de la poutre. Le béton dans cette zone est potentiellement fissuré, l'efficacité de la connexion et par conséquent le comportement mixte acier-béton sont étudiés. Un autre test, à échelle réelle, est effectué dans le Laboratoire de l'Université du Luxembourg. La ruine de la poutre mixte, par effort tranchant, se produit à très grands déplacements. Cependant, l'échantillon présente un réel comportement mixte avec une ductilité élevée, la connexion est donc très efficace. Les résultats de l'essai sont comparés à des simulations numériques afin de valider le modèle par éléments finis développé. A partir des résultats numériques et des résultats d'essais, une méthode de conception pour déterminer la résistance à la flexion de cette poutre, basée sur l'Eurocode 4, est proposée en tenant compte de la plastification partielle des parois de la section en U. Une méthode de conception analytique globale est proposée pour la solution développée basée sur les Eurocodes, avec des considérations supplémentaires et des conseils de mise en œuvre.

Mots clés: Poutre mixte acier-béton, Déversement, Connexion en partie tendue, Essais de flexion, Simulations numériques, Dimensionnement en situation d'incendie

Abstract

An innovative solution of steel-concrete composite beam was developed taking into consideration the fire situation and the construction stage. The beam is composed of a U-shaped steel part connected to a reinforced concrete part. In the construction phase, the beam is supporting the slab and constitutes a formwork for the reinforced concrete part. The U-shaped beam withstands the construction loads without any temporary propping system. When casting concrete, the steel beam is filled at the same time as the slab, this allows considerable time-saving on site. In exploitation stage, the beam behaves as a steel-concrete composite beam. The connection between the two materials is made by welded headed studs on the lower part of the U-shaped beam. In fire situations, the composite beam satisfies conventional fire stability durations due to the longitudinal reinforcements inside the concrete downstand part with sufficient covers.

A literature review focuses on modern solutions that fulfils the criteria of the thesis is performed in order to develop an innovative solution optimised. In construction stage, the U-shaped steel beam without restraints is prone to lateral torsional buckling instability. In order to characterise the stability of the beam, a full-scale test is carried out at the Laboratory of the University of Luxembourg. The test clearly showed the lateral torsional buckling of the steel beam. The test results are compared to numerical simulations and analytical studies. A parametrical study, covering 200 geometrical configurations of the U-shaped beam, is carried out to validate the use of the curve "b" for the design of the steel beam for lateral torsional buckling according to Eurocodes 3. In the exploitation phase, once the concrete hardens, the beam has a steel-concrete composite behaviour provided by the shear connection between the two materials. For manufacturing reasons, the connection is located in a zone where the concrete is subjected to tension forces induced by the bending of the beam. The concrete in this zone is potentially cracked, thus the efficiency of the connection and therefore the mechanical steel-concrete composite behaviour is investigated. Another test is therefore carried out in the Laboratory of the University of Luxembourg, this time the specimen tested is made of concrete and steel. The failure mode is a shear mechanism of the composite beam at very large displacements. However, the beam specimen exhibited a real steel-concrete composite behaviour with high ductility, the connection is therefore very efficient. The test results are compared to numerical simulations in order to validate the finite element model developed. From numerical results and test results, an analytical method, based on EN 1994-1-1, is proposed to find the bending resistant of this composite beam by taking into account the partial yield of the side plates of the U-shaped steel section. A global analytical design method is proposed for the developed solution based on the Eurocodes with additional considerations and constructional guidelines.

Keywords: Steel-concrete composite beam, Lateral torsional buckling, Connection in tension zone, Flexural tests, Numerical simulations, Fire design